UNIVERSITÀ DEGLI STUDI DI MILANO

Scuola di Dottorato in Fisica, Astrofisica e Fisica Applicata

Dipartimento di Fisica

Corso di Dottorato in Fisica, Astrofisica e Fisica Applicata

Ciclo XXXII

Amplitude analysis and polarisation measurement of the Λ_c^+ baryon in $pK^-\pi^+$ final state for electromagnetic dipole moment experiment

Settore Scientifico Disciplinare FIS/01, FIS/04

Supervisore: Prof. Nicola NERI

Coordinatore: Prof. Matteo PARIS

Tesi di Dottorato di:

Daniele MARANGOTTO

Anno Accademico 2018-2019

Commissione d'esame finale:

Revisori esterni:
Dr. Alessandro PILLONI
Prof. Tomasz SKWARNICKI

Membri:
Prof. Vincenzo GUIDI
Prof. Fernando MARTINEZ VIDAL
Prof. Guy WILKINSON

Esame finale:

Data 16/03/2020

Università degli Studi di Milano, Dipartimento di Fisica, Milano, Italy

... tutto era così sbagliato che bisognava cominciare a sbagliare in un altro modo.

Piero Chiara, *Il Piatto Piange*

Settori Scientifico-Disciplinari MIUR:

FIS/01, FIS/04

PACS:

13.30.-a, 13.35.Dx, 13.40.Em, 13.88.+e, 14.20.Lq, 14.60.Fg

Contents

Abstract

The Standard Model of particle physics (SM) has demonstrated an amazing predictive power in the last decades of high energy physics experiments, successfully describing electromagnetic electromagnetic, strong and weak forces, and the Higgs interactions providing mass to elementary particles. However, the cosmological observations which uncovered the existence of Dark Matter and Dark Energy, as well as a significant asymmetry between matter and antimatter in the Universe, can not be explained by SM physics. Moreover, theoretical arguments suggests the SM can be a"low energy" approximation, effective up to the TeV energy scale, of a more fundamental theory describing physics at higher energy scales.

The need for physics beyond the Standard Model, for which no clear evidence has been found to date in particle physics experiments[1], has pushed experimental searches in many directions. Among these, the study of the electromagnetic dipole moments of elementary and composite particles have a special importance, being excellent probes for both Standard Model and beyond the SM physics. The CP-violating electromagnetic dipole moments provide null tests for the SM, in which flavour-diagonal CP-violation effects are extremely suppressed. The measured magnetic dipole moments of elementary particles, like leptons, are used as precision tests for the SM, while those associated to composite particles, give precious information on the particle structure; in the case of baryons, they are exploited to benchmark low-energy Quantum Chromo Dynamics (QCD) models. The measurement of the electromagnetic dipole moments of short-lived charm and beauty baryons, and of the τ lepton, has never been performed to date due to technological limitations.

The first part of the thesis discusses an experiment proposal for short-lived heavy baryon dipole moments measurement, exploiting spin precession of very high energy particles channeled in bent crystals, produced from fixed-target collisions of multi-TeV energy protons extracted from the main beam of the Large Hadron Collider accelerator. The LHCb detector is considered to measure the baryon polarisation from its decay distribution. The spin precession equations for ultra-relativistic positive and negative particles in bent crystals have been derived, as well as the expected precision on the dipole moments.

The same methodology is further extended to the measurement of τ^+ lepton electromagnetic dipole moments, which is complicated by the presence of undetectable neutrinos. It is demonstrated that the kinematic requirements given by the channeling acceptance of bent crystals are able to select τ^+ leptons with significant polarisation, which

[1] Actually, the presence of neutrino masses is already beyond the SM physics, but it may be described by a minimal modification of the SM.

can be exploited to extract dipole moments from spin precession. A novel method is explored to determine the τ^+ polarisation from partially reconstructed $\tau^+ \to \pi^+\pi^-\pi^+\bar{\nu}_\tau$ decay distributions. The achievable precision on the τ^+ dipole moments is estimated for a prospective dedicated experiment.

The second part of the thesis presents the current status of the amplitude analysis of $\Lambda_c^+ \to pK^-\pi^+$ decays from $\Lambda_b^0 \to \Lambda_c^+\mu X$ production recorded by the LHCb experiment, including the extraction of the Λ_c^+ polarisation vector. This analysis, which is an essential tool in light of the Λ_c^+ baryon dipole moments measurement, enables an unprecedented knowledge of the main Λ_c^+ decay mode, Λ_c^+ polarisation determination, parity and CP-violation studies. Order one million $\Lambda_c^+ \to pK^-\pi^+$ events are selected from the LHCb dataset with negligible background contributions. The $\Lambda_c^+ \to pK^-\pi^+$ decay model for generic polarisation has been written in the helicity formalism and fitted to experimental data. An amplitude model for $\Lambda_c^+ \to pK^-\pi^+$ decays has been obtained from two-dimensional Dalitz plot fits, giving valuable information on the main intermediate resonances, including the observation of new Λ^* resonant contributions. A problem in the implementation of the model preventing the extraction of the polarisation from full phase space amplitude has been found and carefully studied.

The third part of the thesis deals with the Λ_c^+ polarisation measurement in proton-neon collisions at $\sqrt{s} = 68.6\,\text{GeV}$ recorded by LHCb, which can provide information on the Λ_c^+ baryon structure. A significant Λ_c^+ polarisation is also crucial for the proposed Λ_c^+ baryon dipole moments measurement. The feasibility of the measurement has been proved achieving two essential results. First, a few hundreds $\Lambda_c^+ \to pK^-\pi^+$ decays from fixed-target production have been selected from the proton-neon LHCb data sample, separated from background contributions and overlapping proton-proton collision events. Second, the possibility to measure the Λ_c^+ polarisation from the selected sample has been proved on simulated pseudo-experiments, showing that the associated systematic uncertainty is negligible compared to statistical uncertainties.

CHAPTER 1

Introduction

1.1 Discrete symmetries

A very important role in physics is played by discrete symmetries, in particular parity (P), charge-conjugation (C) and time-reversal (T) transformations as well as their sequential combinations CP and CPT [1].

Parity transformation is the inversion of spatial coordinates, similar to the transformation acted by a mirror[1]. Table 1.1 reports the effect of parity transformation on some physical quantities.

On quantum states parity is represented by a unitary operator P acting as

$$P\,|\psi(\boldsymbol{x},t)\rangle = \eta_P\,|\psi(-\boldsymbol{x},t)\rangle\,. \tag{1.1}$$

The normalisation of quantum states is not changed by parity,

$$\begin{aligned} 1 &= \langle\psi(-\boldsymbol{x},t)\,|\,\psi(-\boldsymbol{x},t)\rangle = \langle\psi(\boldsymbol{x},t)\,|\,\psi(\boldsymbol{x},t)\rangle \\ &= \left\langle\psi(\boldsymbol{x},t)\,\middle|\,P^\dagger P\,\middle|\,\psi(\boldsymbol{x},t)\right\rangle = |\eta_P|^2\,\langle\psi(-\boldsymbol{x},t)\,|\,\psi(-\boldsymbol{x},t)\rangle = |\eta_P|^2, \end{aligned} \tag{1.2}$$

implying η_P to be a phase (complex number with unit modulus $e^{i\theta}$, with real θ). Since a second application of parity transformation restores the initial system, the P operator must satisfy $P^2 = 1$, which, along with its unitarity $PP^\dagger = 1$, implies that P is also an hermitian operator $P = P^{-1} = P^\dagger$. Parity eigenstates are said to be parity-defined states, and their real eigenvalues $\eta_P = \pm 1$ represent a multiplicative quantum number called P-parity.

Charge-conjugation transforms each particle into its own antiparticle, changing sign to all charges associated to the quantum state. Table 1.1 reports the effect of charge-conjugation transformation on some physical quantities.
As parity, it is represented by a unitary and hermitian operator C acting as

$$C\,|\psi\rangle = \eta_C\,\left|\overline{\psi}\right\rangle, \tag{1.3}$$

with η_C being a phase, and a C-parity quantum number can be defined for charge conjugation eigenstates. Existence of P- and C-parity allows to test directly the conservation of these symmetries on physical processes. For instance, if parity is a symmetry of the system, transitions between states with different P-parities are forbidden and any observable A odd under parity (such that $P^\dagger A P = -A$) must have zero expectation value for every state of the system.

[1] The mirror transformation is equivalent to a parity transformation followed by a rotation of angle π. Assuming rotational symmetry, which is regarded as a very fundamental physics principle, symmetry under parity or mirror transformation are equivalent.

Observable		P-transformed	C-transformed	T-transformed
Time	t	t	t	$-t$
Position	$\boldsymbol{x}$	$-\boldsymbol{x}$	$\boldsymbol{x}$	$\boldsymbol{x}$
Momentum	$\boldsymbol{p}$	$-\boldsymbol{p}$	$\boldsymbol{p}$	$-\boldsymbol{p}$
Energy	E	E	E	E
Angular momentum	$\boldsymbol{J}$	$\boldsymbol{J}$	$\boldsymbol{J}$	$-\boldsymbol{J}$
Electric charge	q	q	$-q$	q
Electric field	$\boldsymbol{E}$	$-\boldsymbol{E}$	$-\boldsymbol{E}$	$\boldsymbol{E}$
Magnetic field	$\boldsymbol{B}$	$\boldsymbol{B}$	$-\boldsymbol{B}$	$-\boldsymbol{B}$

Table 1.1: Transformation of some physical quantities under parity, charge-conjugation and time-reversal transformations.

Time-reversal transformation reverses the time direction: it leaves unchanged the spatial coordinates but it reverses the direction of all momenta and swaps initial and final states. From conservation of the canonical commutation relation $[x, p] = i\hbar$ under time reversal operator T follows $TiT^{\dagger} = -i$, meaning that time-reversal is represented by an antiunitary (unitary and antilinear) operator. For this reason, tests of time-reversal symmetry are quite different from tests of parity and charge-conjugation symmetries. For instance, the observation of a non-zero expectation value of a T-odd observable does not necessarily imply T symmetry violation [1]. Time-reversal symmetry is usually tested indirectly, because of the impossibility of building a time-reversed version of a quantum state, apart few simple cases. For example, it is not possible to experimentally implement the time-reversed state of a decaying particle starting from the incoherent superposition of its asymptotic daughter particles states.

Gravity, electromagnetic and strong interaction conserve separately P, C and T symmetries, as far as it is currently known. This is not true for electroweak interaction. The first suggestion that parity could not be a symmetry for weak interaction was put forward in 1956 by Lee and Yang [2] as an explanation of the so-called $\theta - \tau$ puzzle, while the first experimental evidence of parity violation came one year later from the study of cobalt-60 β-decay [3]. Due to the tight link between P and C symmetries in weak interaction, many of the early experiments showing parity violation implied also charge-conjugation violation. It was soon realized that weak interaction maximally violate P and C symmetries, this because weak interaction involves only left-handed fields. Given a left-handed neutrino, from weak interaction perspective does not exist neither the right-handed neutrino (its P-transformed) nor the left-handed antineutrino (its C-transformed). The fact that right-handed antineutrino existed (its CP-transformed) suggested that CP symmetry could be conserved by weak interaction. The discovery of CP-violation (CPV) in kaon decays [4] was as unexpected as inexplicably small, raising a great interest in CP symmetry violation studies, which is still lively now. Indeed, besides being one of the main features of the quark mixing phenomenon, Sec. 1.2.1, the violation of CP symmetry is one of the Sakharov's conditions needed to explain the origin of the observed matter-antimatter asymmetry of the universe if assuming an initially CP symmetric state [5].

The CPT transformation is the only combination of P, C and T transformations which is still observed to be a symmetry of physical laws. The CPT combination has a very special role because CPT symmetry follows from the assumption of a local and Lorentz invariant field theory (CPT theorem [6]). Therefore, a CPT symmetry violation

would imply the breakdown of the current quantum field theory paradigm, on which the SM theory is built.

1.2 The Standard Model of particle physics

The Standard Model of particle physics (SM), the most reliable theory describing strong, weak and electromagnetic interactions to date, is a Lorentz-invariant Yang-Mills quantum field theory based on the $SU(3) \otimes SU(2)_L \otimes U(1)_Y$ gauge group [7]. The $SU(3)$ group acts in the three-dimensional space of color charges giving rise to the strong interaction, mediated by eight massless gluons, involving only quark fields. The $SU(2)_L \otimes U(1)_Y$ group generates the unified electroweak interaction. The $SU(2)_L$ group acts in the two-dimensional space of weak isospin, the L subscript indicating that only left-handed chirality fields transforms under this group. They transform as isospin doublets in which the three neutrinos are paired with their associated leptons and the three up-type quarks with down-type ones,

$$\begin{pmatrix} \nu_e \\ e \end{pmatrix}, \begin{pmatrix} \nu_\mu \\ \mu \end{pmatrix}, \begin{pmatrix} \nu_\tau \\ \tau \end{pmatrix} \qquad \begin{pmatrix} u \\ d_W \end{pmatrix}, \begin{pmatrix} c \\ s_W \end{pmatrix}, \begin{pmatrix} t \\ b_W \end{pmatrix}, \tag{1.4}$$

where d_W, s_W, b_W are combinations of the three down-type quark mass eigenstates, a phenomenon known as quark mixing, presented in Sec. 1.2.1. Similarly, the three neutrino ν_l are not neutrino mass eigenstate, this giving rise to an analogous lepton mixing phenomenon producing neutrino flavour oscillations. The $U(1)_Y$ group acts as a phase transformation on fields, the Y subscript indicating that is not the $U(1)$ gauge group of electromagnetism, but a different one based on hypercharge conservation. The electroweak interaction is mediated by 4 vector fields, corresponding to the 4 generators of the $SU(2)_L \otimes U(1)_Y$ group. The spontaneous symmetry breaking of the electroweak gauge group (Brout-Englert-Higgs mechanism [8]) accounts for the huge mass of $W^\pm$ and Z^0 weak interaction mediator vector fields by means of an interaction with a complex scalar field, called Higgs boson. The residual symmetry group unaffected by the symmetry breaking is the $U(1)_{EM}$ gauge group of the electromagnetic interaction, associated to the massless photon field.

1.2.1 Quark mixing and CP-violation in the Standard Model

The idea of quark mixing aroused in the '60 when it was tried to classify the known u, d and s quarks into weak isospin representations of $SU(2)_L$ group. In fact, the simple classification as a doublet plus a singlet,

$$\begin{pmatrix} u \\ d \end{pmatrix}, \begin{pmatrix} s \end{pmatrix}, \tag{1.5}$$

was not compatible with the observed $s \to u$ transitions. This problem was solved by the seminal idea of Cabibbo [9] who proposed that the isospin eigenstates could be a combination of d and s quark mass eigenstates characterized by a mixing angle θ,

$$\begin{pmatrix} u \\ \cos\theta d + \sin\theta s \end{pmatrix}, \begin{pmatrix} -\sin\theta d + \cos\theta s \end{pmatrix}. \tag{1.6}$$

However, it was later noticed that this classification allowed flavour-changing neutral current processes (FCNC, mediated by the Z^0 field) to proceed with a much higher rate

than observed. This conflict was settled by the introduction of the charm (c) quark (GIM mechanism [10]) and the isospin classification involving two doublets,

$$\begin{pmatrix} u \\ \cos\theta d + \sin\theta s \end{pmatrix}, \begin{pmatrix} c \\ -\sin\theta d + \cos\theta s \end{pmatrix}, \tag{1.7}$$

which correctly predicts the observed FCNC process suppression.

This scheme was not complete because it did not include the observed CP-violation in weak interactions. Indeed, a CP-violating term in the weak interaction Lagrangian must come from the presence of complex coefficients, nevertheless, with two quark generations Eq. (1.7) the only degree of freedom is the real mixing angle θ. In 1973, Kobayashi and Maskawa [11] theorized the existence of a third quark generation introducing bottom (b) and top (t) quarks. This way, the mixing of the three down-type quark isospin eigenstates (d_W, s_W, b_W) in terms of the mass eigenstates (d, s, b) is expressed by a unitary matrix called Cabibbo-Kobayashi-Maskawa (CKM) matrix

$$\begin{pmatrix} d_W \\ s_W \\ b_W \end{pmatrix} = \begin{pmatrix} V_{ud} & V_{us} & V_{ub} \\ V_{cd} & V_{cs} & V_{cb} \\ V_{td} & V_{ts} & V_{tb} \end{pmatrix} \begin{pmatrix} d \\ s \\ b \end{pmatrix}. \tag{1.8}$$

After fixing the arbitrary quark field phases, the three quark generation mixing matrix can be parametrised by three real mixing angles and a complex phase allowing for CP-violation. The CKM matrix features an interesting hierarchical structure[2], captured by the Wolfenstein CKM matrix parametrisation [12]

$$\begin{pmatrix} 1-\lambda^2/2 & \lambda & A\lambda^3(\rho - i\eta) \\ -\lambda & 1-\lambda^2/2 & A\lambda^2 \\ A\lambda^3(1-\rho-i\eta) & -A\lambda^2 & 1 \end{pmatrix}, \tag{1.9}$$

which is an approximation at the third order of the hierarchical parameter $\lambda \sim 0.22$, ruling favoured and suppressed weak interaction processes. The amount of CP-violation provided by the CKM mechanism is very small, as observed, since the only matrix elements containing a complex phase V_{ub} and V_{td} are suppressed by a factor $\lambda^3 \sim 0.01$.

At present, the CKM mechanism successfully accounts for the observed amount of CP-violation in hadron interaction and decays observed at particle physics experiments.

An additional source of CPV should come from the three generations lepton mixing, where CP-violation is given by the complex phase provided by the lepton mixing matrix. Leptogenesis models, aimed at explaining the observed matter-antimatter asymmetry via lepton mixing CPV, have been proposed [13]. However, these models are based on the see-saw mechanism proposed to justify the smallness of the neutrino masses, which envisages the presence of currently unobserved heavy Majorana neutrinos introducing additional CP-violating phases.

Still in the Standard Model domain, the strong interaction Lagrangian admits a CP-violating term,

$$\mathcal{L}_\theta = \theta \frac{g^2}{32\pi^2} \sum_a F_{\mu\nu a} \tilde{F}_a^{\mu\nu}, \tag{1.10}$$

in which g is the strong coupling constant, $F_{\mu\nu a}$ the gluon field strength tensor and $\tilde{F}_a^{\mu\nu} = \epsilon^{\mu\nu\rho\sigma} F_{\rho\sigma a}/2$ its dual. The contribution of this term is proportional to the QCD

[2] Interestingly not observed in the analogous lepton mixing matrix.

vacuum angle θ. The presence of this CPV term would produce a non-zero neutron electric dipole moment, whose current experimental limit [14] constrains the angle θ to a very tiny amount, order 10^{-10}. The discussion on why this term is so suppressed is known as "strong CP problem". This issue has been addressed in different ways, the most appealing being the Peccei-Quinn theory [15] introducing a new particle named axion.

1.3 Spin

One of the key ideas underlying the rise of quantum mechanics was the realisation that particles can possess internal degrees of freedom, called spin, in addition to those related to the motion in the space-time. The spin is interpretable as an intrinsic angular momentum of the particle; in fact, in particle reactions the quantity conserved as a consequence of rotational invariance is the total angular momentum $\boldsymbol{J}$, which is the sum of the orbital angular momentum $\boldsymbol{L}$, describing the orbital motion of particles around each other, and the spin carried by each particle $\boldsymbol{S}$. Therefore, orbital angular momentum and spin are not separately conserved[3].

In non-relativistic quantum mechanics, spin operators $\hat{\boldsymbol{S}} = (\hat{S}_x, \hat{S}_y, \hat{S}_z)$ are introduced by analogy with the orbital angular momentum [16], satisfying the usual commutation relations

$$[\hat{S}_i, \hat{S}_j] = i\epsilon_{ijk}\hat{S}_k. \tag{1.11}$$

The spin states $|s, m\rangle$ are defined as the simultaneous eigenstates of the spin squared modulus $\hat{S}^2$ and $\hat{S}_z$, with eigenvalues $s(s+1)$ and m, respectively. While S^2 is independent of any reference frame, the spin operators are defined with respect to a specific Cartesian system, called quantisation frame. The reference z-axis, defining the spin operator used to express the spin states, is called quantisation axis, and m is the z-component of the spin. The particle spin s can be any non-negative integer or half-integer value, while m belongs to the set of $2s+1$ values differing by integers satisfying the condition $-s \leq m \leq s$. A particle of spin s is therefore described by an internal Hilbert space of dimension $2s+1$, its state defined by $2(2s+1) - 2 = 4s$ real numbers.

The state of a statistical ensemble of particles, describing a not precisely known particle state, is defined by the associated density operator $\hat{\rho}$ [16]. Given an ensemble of states $|\psi_i\rangle$, each one occurring with probability p_i, the density operator is

$$\hat{\rho} = \sum_i p_i \left|\psi_i\right\rangle \left\langle\psi_i\right|, \tag{1.12}$$

so that the expectation value of any operator $\hat{X}$ can be expressed as

$$\langle\hat{X}\rangle = \sum_i p_i \left\langle\psi_i \,|\, X \,|\, \psi_i\right\rangle = \mathrm{Tr}\left[\hat{\rho}\hat{X}\right]. \tag{1.13}$$

Since the density operator determines the expectation value of any operator, it is the most fundamental description of a statistical ensemble. In fact, different statistical ensembles corresponding to the same density operator are physically indistinguishable. The density operator definition Eq. (1.12) implies that $\hat{\rho}$ is hermitian and with unit trace

[3]The separation between orbital and intrinsic angular momentum depends on the definition of the system called "particle". For instance, the spin of a composite particle can be seen as the composition of orbital angular momentum and spin carried by its constituents.

$\mathrm{Tr}\hat{\rho} = 1$, while the quantity $\mathrm{Tr}\hat{\rho}^2$, called purity, is smaller or equal to one. It is possible to prove that $\mathrm{Tr}\hat{\rho}^2 = 1$ only if $\hat{\rho}$ describes a perfectly defined (pure) state ψ, that is if $\hat{\rho} = |\psi\rangle\langle\psi|$; when $\mathrm{Tr}\hat{\rho}^2 < 1$ it is said the state is mixed.

The spin density operator for a particle of spin s describes a statistical ensemble of spin states $|s, m_i\rangle$. Once a quantisation axis is chosen, the density operator can be written as a $(2s+1) \times (2s+1)$ density matrix $\rho_{mm'} = \langle s, m \,|\, \hat{\rho} \,|\, s, m'\rangle$. A mixed spin s state is therefore defined by $(2s+1)^2 - 1$ real parameters.

For spin $1/2$ particles, the most general spin density matrix can be written as [16]

$$\rho = \frac{1}{2}\left(I + \boldsymbol{s}\cdot\boldsymbol{\sigma}\right), \tag{1.14}$$

in which $\boldsymbol{\sigma}$ are the Pauli matrices and $\boldsymbol{s}$ is the spin-polarisation vector [4],

$$\boldsymbol{s} = \mathrm{Tr}\left[\rho\boldsymbol{\sigma}\right] = \frac{2}{\hbar}\langle\hat{\boldsymbol{S}}\rangle, \tag{1.15}$$

since for $s = 1/2$ the spin operator matrices can be expressed by Pauli matrices, $\boldsymbol{S} = \hbar\boldsymbol{\sigma}/2$. The three polarisation components completely define the state of a spin $1/2$ statistical ensemble. From Eq. (1.14) follows that $\mathrm{Tr}\rho^2 = P^2$, therefore one has a fully polarised state if and only if it is a pure spin state, that is if exist a quantisation axis such that $\hat{\rho} = |s, m\rangle\langle s, m|$.

The existence of the spin has consequences also for electromagnetic interactions, allowing even fundamental, point-like particles to have not only an electric charge, but also higher order electromagnetic multipole moments (multipoles, in the following). The electromagnetic multipoles correspond to electromagnetic radiation with non-zero total angular momentum $\boldsymbol{J}$, which can be considered as the composition of the photon spin $s = 1$ and an orbital angular momentum $\boldsymbol{L}$, having eigenstates j or $j \pm 1$. These states correspond to magnetic and electric multipoles, respectively [1]. The total angular momentum determines the parity of the radiation: magnetic multipoles have parity eigenvalues $\eta_P(M, j) = (-1)^{j+1}$, electric multipoles have opposite parity $\eta_P(E, j) = (-1)^j$. A particle with spin s can have up to 2^{2s} electromagnetic multipoles: for instance a spin $1/2$ particle can only have electromagnetic dipole moments, while a spin $3/2$ particle like the Ω^- can also have quadrupole and octupole moments.

For elementary particles, which only have spin as internal degree of freedom, the expectation values of the magnetic and electric dipole moment operators, $\hat{\boldsymbol{\mu}}$ and $\hat{\boldsymbol{\delta}}$, respectively, must be proportional to the spin S ones, since S is the only preferred direction in space in an otherwise rotationally symmetric system. More formally, this follows from the Wigner-Eckart theorem, implying

$$\left\langle s, m \left| \hat{\boldsymbol{\delta}} \right| s, m \right\rangle = \left\langle s, m \left| \hat{\boldsymbol{S}} \right| s, m \right\rangle \frac{\left\langle s, m \left| \hat{\boldsymbol{\delta}}\cdot\hat{\boldsymbol{S}} \right| s, m \right\rangle}{s(s+1)}. \tag{1.16}$$

This argument is no longer valid for composite systems featuring degenerate states, like atoms and molecules.

[4] Hereafter the spin-polarisation vector will be called equivalently spin or polarisation, differing from the spin vector $\boldsymbol{S} \equiv \langle\hat{\boldsymbol{S}}\rangle$ just by a normalisation factor.

1.3.1 Electromagnetic dipole moments

Magnetic (MDM) and electric (EDM) dipole moments can be written as (in Gaussian units)

$$\hat{\boldsymbol{\mu}} = g\frac{\mu_B}{\hbar}\hat{\mathbf{S}}, \qquad\qquad \hat{\boldsymbol{\delta}} = d\frac{\mu_B}{\hbar}\hat{\mathbf{S}}, \tag{1.17}$$

respectively, in which $\mu_B = e\hbar/(2mc)$ is the particle magneton, m its mass. The g and d dimensionless factors are called the gyromagnetic and gyroelectric ratios, respectively.

In non-relativistic approximation, the interaction of electromagnetic dipoles with external electromagnetic fields is described by the Hamiltonian

$$\hat{H} = -\hat{\boldsymbol{\mu}}\cdot\boldsymbol{B} - \hat{\boldsymbol{\delta}}\cdot\boldsymbol{E} = -g\frac{\mu_B}{\hbar}\hat{\mathbf{S}}\cdot\boldsymbol{B} - d\frac{\mu_B}{\hbar}\hat{\mathbf{S}}\cdot\boldsymbol{E}, \tag{1.18}$$

Under parity and time-reversal transformations, see Sec. 1.1 and Table 1.1, $\hat{\boldsymbol{S}}$ and $\boldsymbol{B}$ transform in the same way as axial vectors, making the magnetic dipole interaction invariant under P and T. On the contrary, the electric field transform as a polar vector while $\hat{\boldsymbol{S}}$ as an axial vector, and the electric dipole interaction violates both parity and time-reversal symmetries, separately. This means that if parity and time-reversal transformations are symmetries of the physical laws, fundamental particles must have zero electric dipole moment. In general, it can be shown that parity and time reversal symmetry separately imply that elementary (non-degenerate) particles can only have even electric and odd magnetic multipoles [17].

In quantum electrodynamics, the most general form of the electromagnetic coupling of a spin 1/2 Dirac fermion with an electromagnetic field is written as [18]

$$\begin{aligned}\langle p' \,|\, J^{\mu}_{EM} \,|\, p\rangle\, A_\mu = \bar{u}(p')\Big\{ & F_1(q^2)\gamma^\mu - \frac{iF_2(q^2)}{2m}\sigma^{\mu\nu}q_\nu - \frac{F_3(q^2)}{2m}\sigma^{\mu\nu}q_\nu\gamma_5 \\ & + iF_A(q^2)\left(q^2\gamma^\mu\gamma_5 - 2mq^\mu\gamma_5\right)\Big\}u(p)A_\mu\end{aligned} \tag{1.19}$$

in which p (p') is the initial (final) fermion four-momenta, q the electromagnetic field (virtual photon) four-momentum, $\bar{u}(p')$ ($u(p)$) the initial (final) spinor, γ^μ the four Dirac matrices. The four form factors $F_i(q^2)$ describe the electromagnetic properties of the particle, in particular $F_1(0)$ represents the charge and the regular (from Dirac's equation) magnetic dipole moment, $F_2(0)$ the anomalous magnetic dipole moment, $F_3(0)$ the parity and time-reversal violating electric dipole moment and $F_A(0)$ the parity odd but time-reversal even anapole moment. The transformation properties of each term follow from those related to spinor bilinears and electromagnetic fields under parity,

$$\begin{aligned}&\left\langle p' \,\middle|\, P^\dagger\gamma^\mu P \,\middle|\, p\right\rangle = \langle p' \,|\, \gamma_\mu \,|\, p\rangle\,, \\ &\left\langle p' \,\middle|\, P^\dagger i\sigma^{\mu\nu}q_\nu P \,\middle|\, p\right\rangle = \langle p' \,|\, i\sigma_{\mu\nu}q^\nu \,|\, p\rangle\,, \\ &\left\langle p' \,\middle|\, P^\dagger\sigma^{\mu\nu}q_\nu\gamma_5 P \,\middle|\, p\right\rangle = -\langle p' \,|\, \sigma_{\mu\nu}q^\nu\gamma_5 \,|\, p\rangle\,, \\ &\left\langle p' \,\middle|\, P^\dagger\left(q^2\gamma^\mu\gamma_5 - 2mq^\mu\gamma_5\right)P \,\middle|\, p\right\rangle = -\left\langle p' \,\middle|\, \left(q^2\gamma_\mu\gamma_5 - 2mq_\mu\gamma_5\right) \,\middle|\, p\right\rangle, \\ &P^\dagger A_\mu P = A^\mu,\end{aligned} \tag{1.20}$$

and time-reversal transformations,

$$\begin{aligned}
&\left\langle p' \left| T^\dagger \gamma^\mu T \right| p \right\rangle = \left\langle p' \left| \gamma_\mu \right| p \right\rangle , \\
&\left\langle p' \left| T^\dagger i\sigma^{\mu\nu} q_\nu T \right| p \right\rangle = \left\langle p' \left| i\sigma_{\mu\nu} q^\nu \right| p \right\rangle , \\
&\left\langle p' \left| T^\dagger \sigma^{\mu\nu} q_\nu \gamma_5 T \right| p \right\rangle = - \left\langle p' \left| \sigma_{\mu\nu} q^\nu \gamma_5 \right| p \right\rangle , \\
&\left\langle p' \left| T^\dagger \left(q^2 \gamma^\mu \gamma_5 - 2mq^\mu \gamma_5 \right) T \right| p \right\rangle = \left\langle p' \left| \left(q^2 \gamma_\mu \gamma_5 - 2mq_\mu \gamma_5 \right) \right| p \right\rangle , \\
&T^\dagger A_\mu T = A^\mu .
\end{aligned} \tag{1.21}$$

The gyromagnetic factor can be expressed in terms of the form factors as [19]

$$g = 2 \left[F_1(0) + F_2(0) \right] . \tag{1.22}$$

At lowest order (tree-level) in perturbation theory, one has $F_1(0) = 1$ as only non-zero form factor, so $g = 2$ coinciding with the prediction of Dirac's equation. At higher orders (loop-level) in quantum electrodynamics an anomalous magnetic dipole moment is produced, of order

$$a = \frac{g-2}{2} \approx \frac{\alpha}{2\pi} \approx 10^{-3}. \tag{1.23}$$

The anomalous magnetic dipole moment of leptons can be very precisely calculated in quantum field theory. For the electron, the extremely precise agreement between the predicted and the measured $g-2$ values [20], at $\delta a/a \approx 10^{-13}$ level, constitutes a spectacular test of quantum electrodynamics. For the muon, a discrepancy between the predicted and the measured [21] $g-2$ values, with statistical significance of about 3.6 standard deviations [22], could be a sign of beyond the standard model physics effects; for this reason a more precise measurement [23] and more precise calculations are planned.

For composite particles, the MDM is sensitive to the inner particle structure and $g-2$ can be of order one. In fact, the direct study of baryon structures can not be performed in low-energy quantum cromodynamics, since the large strong coupling prevents the use of standard perturbation theory methods. The structure of baryons is therefore described by means of phenomenological models which however have limited predictive power and need to be properly tuned from experimental inputs. For instance, the measurement of baryon MDMs contributed to confirm the validity of the quark model [24].

Magnetic dipole moments have been measured for different baryons: proton [25], neutron [26], and most of the strange baryons decaying via weak interaction [24]. No direct measurements of charm baryons, beauty baryons and tau leptons EDMs have been performed to date. See *e.g.* [27] for a summary of experimental data and MDM predictions from different phenomenological models.

The CPT symmetry implies the magnetic dipole moments for particle-antiparticle pairs to be equal and opposite. Thus, if MDMs can be separately measured for a particle and its antiparticle a test of CPT symmetry can be performed. Such tests were performed for the proton [28], electron [29], and muon [30], and a new experiment for the proton is planned [31].

The measurement of heavy baryon dipole moments is of great interest, providing additional information on the structure of heavy flavoured baryons and new, complementary probes for new physics coupled to heavy quarks. Indeed, the structure of heavy baryons is expected to be very different from that of light baryons. In light baryons, the QCD binding energy is much larger than the valence quark masses, resulting in a strongly coupled relativistic bound state. Instead, most of the heavy baryons mass comes

from the heavy quark, which is much larger than the QCD binding energy, and its dynamics can be separated from that of the light quarks and gluons. According to heavy quark effective theory (HQET) [32], which implements this separation, the baryon properties are determined by the heavy quark up to corrections proportional to Λ_{QCD}/m_q, in which $\Lambda_{QCD} \approx 200\,\mathrm{MeV}$ is the typical QCD interaction energy scale and m_q the heavy quark mass. This suggests that the dipole moments of heavy baryons are closely related to the heavy quark ones.

Predictions for charm baryon magnetic dipole moments have been obtained in the quark model [33], from QCD sum rules [34], from QCD spectral sum rules [35], $SU(4)$ chiral constituent quark model [27], chiral perturbation theory [36]. Predictions for the Λ_c^+ baryon MDM are in the range $0.15 - 0.40\mu_N$, where μ_N is the nuclear magneton $\mu_N = e\hbar/2m_p$. A precise charm baryon MDM measurement would allow to discriminate between different phenomenological models. Predictions for beauty baryon magnetic dipole moments have been obtained in quark models [37], in hyper central model [38], in effective quark mass and shielded quark charge scheme [39]. Predictions for the $\overline{\Xi}_b^+$ baryon MDM are in the range $0.050 - 0.066\mu_N$. MDM theoretical predictions for heavy baryons are summarised in Fig. 1.1.

Indirect constrains on heavy quark EDMs have been derived from measured observables sensitive to quark electric (qEDM) and chromoelectric (qCEDM) dipole moments. For the charm quark indirect limits from neutron [41,42] and electron [42] EDM limits, inclusive $B \to X_s\gamma$ branching fraction [41], total $e^+e^- \to c\bar{c}$ cross-section [43] and $Z^0 \to c\bar{c}$ partial decay rate [44] have been derived. For the beauty quark, the following observables have been used: neutron [42, 45] and electron [42] EDM limits, total $e^+e^- \to b\bar{b}$ cross-section [43] and $Z^0 \to b\bar{b}$ partial decay rate [44]. The indirect limits on the charm quark EDM are in the range $\delta < 10^{-17} - 10^{-15} e\,\mathrm{cm}$, while those on the beauty quark EDM are in the range $\delta < 10^{-17} - 10^{-12} e\,\mathrm{cm}$. The different values depend on the different observable sensitivities and model assumptions. Supersymmetric extensions of the Standard Model predicting charm quark EDM with values comparable to the indirect limits have been proposed [46].

An electric dipole moment can be produced only by parity and time-reversal violating interactions. The only known source of time-reversal violation, which is related to CP violation assuming CPT symmetry, comes from the CP-violating phase in the CKM quark mixing matrix in weak nuclear interactions, Sec.1.2.1. However, since the CKM CP-violating phase enters at tree-level only in flavour-changing quark transition, its contribution to the creation of baryon EDMs is extremely small, occurring at high orders of the perturbation theory expansion (3-loop level for quarks and 4-loop level for leptons). Standard Model EDM predictions are at the order of $10^{-31} e\,\mathrm{cm}$ for the neutron [47], $10^{-34} e\,\mathrm{cm}$ for quarks [48] and $10^{-40} e\,\mathrm{cm}$ for the electron [49]. These are orders of magnitude less than the current experimental upper limits $\delta < 3.0 \times 10^{-26} e\,\mathrm{cm}$ for the neutron [14] and $\delta < 1.1 \times 10^{-29} e\,\mathrm{cm}$ for the electron [50].

The allowed CP-violating term of the strong interaction Lagrangian, Sec. 1.2.1, could have produced large baryon EDMs. On the contrary, the absence of neutron EDM at current experimental precision constrain the possible strong CPV contribution to a very small amount. Therefore, the experimental searches for the EDM of fundamental particles provide powerful probes for physics beyond the Standard Model.

Different new physics models introducing new CPV sources predict the appearance of non-zero EDMs, *e.g.* non-standard spontaneous symmetry breaking Brout-Englert-Higgs mechanisms, left-right symmetric models [51], supersymmetric grand unification theories. Some new physics models have been ruled out by current experimental limits on neutron EDM. A phenomenological approach to treat the implications of the mea-

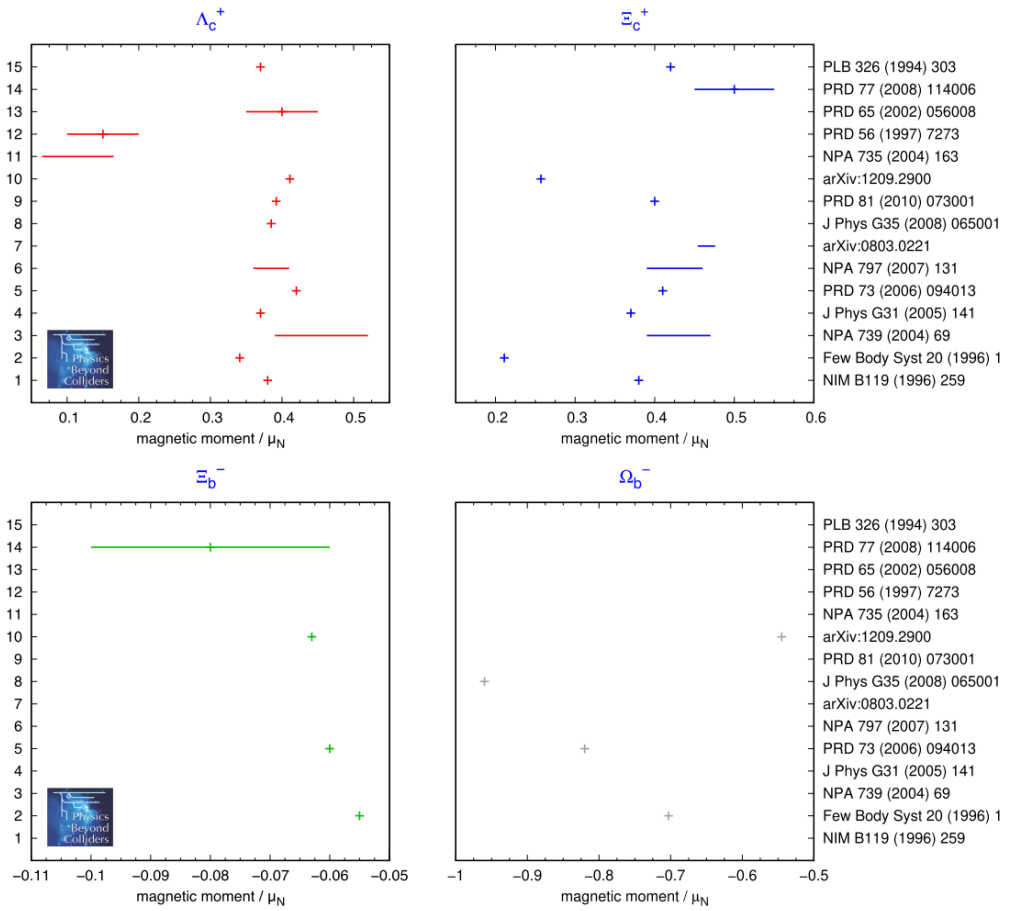

Figure 1.1: from Ref. [40]. Spread of theoretical predictions for the magnetic moments of heavy baryons. Values in rows 1 to 10 are from different quark models, 11 from a soliton approach, 12 to 14 from sum rules, and 15 from chiral perturbation theory.

sured EDM limits based on effective field theory can also be set [52].

A baryon EDM, being a composite particle, can arise from a collective CPV interaction of its constituting quark and gluon fields with the electromagnetic field. It is described by 5 CP-violating operators in an effective CP-odd flavour-diagonal Lagrangian up to dimension six [53]

$$\begin{aligned}
\mathcal{L}_{\text{eff}}^{\not P \not T} =& \bar{\theta} \frac{g^2}{64\pi^2} \epsilon^{\mu\nu\alpha\beta} G^a_{\mu\nu} G^a_{\alpha\beta} && \theta\text{-QCD term} \\
&- \frac{i}{2} \sum_{q=u,d,s,c,b} \delta_q \, \bar{q} \sigma^{\mu\nu} \gamma_5 q \, F_{\mu\nu} && \text{qEDM} \\
&+ i \sum_{q=u,d,s,c,b} \tilde{\delta}_q \, \bar{q} \sigma^{\mu\nu} \gamma_5 t_a q \, G^a_{\mu\nu} && \text{qCEDM} \\
&+ \sum_{i,j,k,l=u,d,s,c,b} C_{ijkl} \, \bar{q}_i \Gamma q_j \, \bar{q}_k \Gamma' q_l && \text{4-quark op.} \\
&+ \frac{d_W}{6} f_{abc} \varepsilon^{\mu\nu\alpha\beta} G^a_{\alpha\beta} G^b_{\mu\rho} G^{c\,\rho}_{\nu} && \text{gCEDM (Weinberg op.)}
\end{aligned} \tag{1.24}$$

The dimension-six gluon chromoelectric dipole moment (gCEDM) and 4-quark operators contribution is suppressed at the baryon energy scale of order $1\,\text{GeV}$ with respect to lower dimension operators: for dimensional analysis, their coupling constants must be proportional to $1/\Lambda^2$, with Λ a large new physics energy scale $\gtrsim 1\,\text{TeV}$. The main contributions to the baryon EDM are expected to come from qEDM and qCEDM operators and the strong interaction CPV term (θ-QCD term). The stringent limit on the neutron EDM put strong constraints on u and d quark q(C)EDMs and the θ-QCD term, the latter being independent of the baryon flavour. Measurements of heavy flavour baryons are therefore able to constrain contributions from heavy quark (chromo)electric dipole moments.

The importance of EDM searches was already recognized in the fifties [54], and since then many measurements have been performed in a variety of systems: electron [50], muon [55], neutron [14], proton (indirect from ^{199}Hg) [56] and Λ baryon [57]. New experiments are ongoing and others are planned, including those based on storage rings for muon [23, 58], proton and light nuclei [59]. No direct measurements of charm baryons, beauty baryons and tau leptons EDMs have been performed to date. The overall status of EDM measurements, indirect limits and SM predictions is reported in Fig. 1.2.

The measurement of EDMs of composite systems like nuclei, atoms or molecules are also interesting because the contribution of the constituent nucleon or electron EDMs can be amplified [52]. For example, in paramagnetic atoms, the electron EDM is enhanced proportionally to $Z^3\alpha^2_{\text{QED}}$, which is larger than unity for heavy atoms. However, care is needed to correctly interpret the measured limits, since the relation between the EDM of a system and that of its constituents depends on the knowledge of the system structure. Moreover, for polar atoms and molecules it is needed to separate the contribution of the "intrinsic" EDM defined for a free particle (*i.e.* in the weak-field limit) from that induced by the orientation of the system in an external field: while the first EDM is a truly time-reversal violating effect the latter is not, because it is not related to free particle states. In fact, a free polar system has no preferred orientation, so states with different orientation are degenerate and its EDM averages to zero in absence of T-violating effects. The

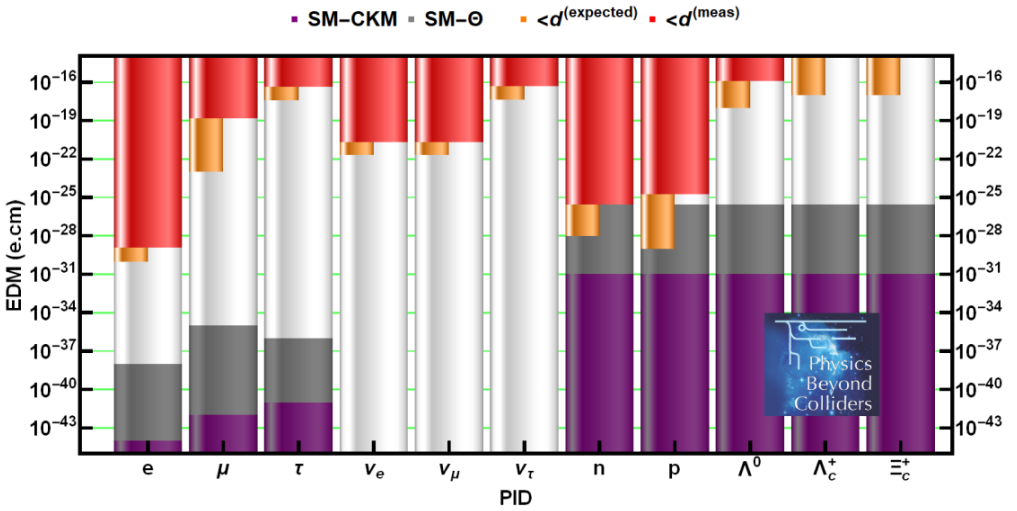

Figure 1.2: from Ref. [60]. Overall status of EDM measurements: current experimental limits on EDMs of fundamental particles are displayed as red bars from the top, indirect limits from other measurements as orange bars. From below are the SM estimates from CKM CP-violation (violet bars) and θ-QCD interaction term (grey bars).

application of a sufficiently strong external field removes the degeneracy modifying the energy associated to different orientations and the eigenstates of the new Hamiltonian turn out to be non-uniform superposition of free states leading to a non-zero EDM which does not violate parity nor time-reversal symmetries [52].

1.3.2 Baryon polarisation

The baryon polarisation is a very interesting probe in high energy physics, since it gives information on the baryon structure and production process, and it influences the angular distributions of decay or scattering processes. Indeed, the spin provide baryons with an additional degree of freedom with respect to mesons, allowing measurements otherwise not possible with spinless particles, like the heavy electromagnetic dipole moment measurement described in Chapter 2.

Baryons produced in parity conserving (strong or electromagnetic) interactions can have polarisation perpendicular to the production plane defined by the beam and heavy baryon momenta [1]. In fact, for an unpolarised, *e.g.* proton-nucleon, interaction there are three vectors available: the proton and heavy baryon momenta $\boldsymbol{p}(p)$, $\boldsymbol{p}(B)$ and the heavy baryon spin $\boldsymbol{s}(B)$. The only scalar, linear term unchanged by parity transformation in the interaction Hamiltonian which can be constructed from these vectors is $\boldsymbol{p}(p) \times \boldsymbol{p}(B) \cdot \boldsymbol{s}(B)$, which is nonzero only if $\boldsymbol{s}(B)$ is orthogonal to the production plane. Instead, an heavy baryon polarisation within the production plane, involving parity-odd scalar products $\boldsymbol{s}(B) \cdot \boldsymbol{p}(p)$, $\boldsymbol{s}(B) \cdot \boldsymbol{p}(B)$, would point to parity symmetry violation in strong interactions.

The production plane defines a natural coordinate system for the polarisation measurement, shown in Fig. 1.3: the heavy baryon momentum defines the z axis, while the production plane defines the x axis, which is taken to be opposite to the component of the beam direction orthogonal to the z axis. The heavy baryon initial polarisation vector

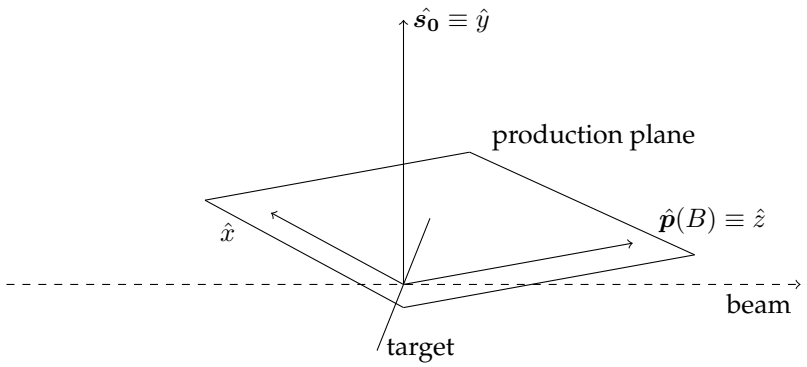

Figure 1.3: Production plane of the heavy baryon defined by the proton and the heavy baryon momenta. The initial polarisation vector $\boldsymbol{s}_0$ must be perpendicular to the production plane, along the y axis, thanks to parity conservation in strong interactions.

must be parallel to the y axis, $\boldsymbol{s}_0 = (0, s_0, 0)$, defined as $\hat{y} \propto \boldsymbol{p}(p) \times \boldsymbol{p}(B)$.

The baryon polarisation produced from strong interaction is very difficult to predict in QCD theory, being related to its non-perturbative low energy regime. Rather, polarisation measurements are useful to discriminate among different QCD models describing the baryon structure.

The spin structure of the nucleons has been extensively studied, especially in polarised deep inelastic scattering experiments, trying to understand how the baryon polarisation arises from spin and orbital angular momentum of its constituents [61]. A notable result is that light quark spins generate only a small fraction of the total baryon polarisation [62]. On the contrary, the main contribution to the polarisation of baryons composed by one heavy quark is expected to come from the heavy quark spin, according to heavy quark effective theory, which is valid in the limit $m_q \gg \Lambda_{\rm QCD} \sim 200\,{\rm MeV}$. This is the case for charm and beauty baryons, in which most of the heavy quark polarisation is expected to be retained by the heavy baryon after hadronisation, allowing polarisation measurements to give information on the heavy quark production mechanism [63, 64].

Focusing on baryon polarisation in proton-nucleon fixed-target collisions, which are of special interest in light of Chapters 2 and 6, different measurements have been performed for strange baryons: Λ and $\overline{\Lambda}$ [65], Σ^- and $\bar{\Sigma}^+$ [66], Ξ^0 [67], Ξ^- and Ξ^+ [68], Ω^- [69], for proton energies within 450 and 920 GeV. Overall, an increasing negative hyperon polarisation with transverse momentum $p_{\rm T}$ and Feynman $|x_F|$ variable is found, the latter defined as $x_F = 2p_l/\sqrt{s}$, p_l being the longitudinal momentum of the baryon relative to beam direction in the centre of mass frame. Negative polarisation means that it is opposite to the y axis defined in Fig. 1.3. Differences between baryon and antibaryon polarisation values have been observed, as expected since baryon and antibaryon production from proton-nucleus collisions are not charge-conjugated processes. For instance, while an heavy quark can form a baryon from the valence quark of the nucleons, the antiquark composing heavy antibaryons have to be produced in the interaction.

Due to the smaller production cross-sections of heavy baryons with respect to light ones, the heavy baryon polarisation in fixed-target collisions has been poorly studied experimentally to date. The only measurements were performed for the Λ_c^+ baryon in $pK^-\pi^+$ decays, showing a trend of increasing negative Λ_c^+ baryon polarisation with $p_{\rm T}$ like strange baryons. A polarisation of $s_0 = -0.65^{+0.22}_{-0.18}$ was measured in 230 GeV π^- col-

lisions on Cu target by the NA32 experiment at CERN-SPS [70]. The E791 experiment at Fermilab [71] colliding 500 GeV π^- on a Pt-diamond target measured the Λ_c^+ polarisation for three $p_{\rm T}$ intervals, finding a significant value $s_0 = -0.67 \pm 0.15$ for $p_{\rm T} > 1.1\,{\rm GeV}/c$. It is important to note that both the Λ_c^+ polarisation measurements included decays from Λ_c^+ and $\overline{\Lambda}_c^-$ baryons together, which should instead be separated since Λ_c^+ and $\overline{\Lambda}_c^-$ may have different polarisation values.

In proton proton symmetric collisions, baryon polarisation measurements were performed for the Λ at $\sqrt{s} = 53$ and $62\,{\rm GeV}$ [72], for Λ and $\overline{\Lambda}$ at $\sqrt{s} = 7\,{\rm TeV}$ [73], and for the Λ_b^0 at 7 and 8 TeV energy [74, 75]. The same trend with baryon $p_{\rm T}$ is observed for Λ at $\sqrt{s} = 53$ and $62\,{\rm GeV}$, while measurements at the TeV energy scale show baryon polarisation compatible with zero at few % level.

A measurement in e^+e^- symmetric collisions was performed for Λ and $\overline{\Lambda}$ at $\sqrt{s} = 10.58\,{\rm GeV}$ by Belle [76]. The leptonic system allows a simpler interpretation of the measured polarisation in terms of polarised fragmentation functions, describing the production of polarised hadrons from unpolarised quarks [77], contrary to hadronic collisions in which initial effects due to the internal dynamics of the colliding hadrons contribute to the baryon polarisation. A trend of increasing negative polarisation with $p_{\rm T}$ and x_F is observed. The Λ and $\overline{\Lambda}$ polarisations have also been measured from $e^+e^- \to J/\psi \to \Lambda\overline{\Lambda}$ processes at BESIII [78], showing a polarisation up to 20% level as a function of the baryon direction in the J/ψ meson rest frame.

Baryon polarisation measurements in ion-ion collisions were performed for Λ and $\overline{\Lambda}$ in Au-Au collisions by STAR [79] and in Pb-Pb collisions by ALICE [80]. In this case, the baryon polarisation can be produced from the orbital angular momentum of the ion-ion systems, and it is a probe for the initial conditions and dynamics of Quark Gluon Plasma, as well as for the hadronisation process.

Baryons produced in weak decays, which violate parity symmetry, can feature polarisation components along their momentum as well. The value of the baryon polarisation depends on the particular weak decay in which it is produced, therefore, results on baryon polarisation can be extracted from the analysis of the angular distribution of the weak decay. In fact, the possibility of including the baryon decay distribution in the angular analysis of a weak decay increases the number of the accessible observables. This is the case for Λ baryons produced in $\Lambda_b^0 \to \Lambda l^+ l^-$ decays [81] (and Refs. therein) or the Λ_c^+ baryon in $\Lambda_b^0 \to \Lambda_c^+ l^- \bar{\nu}_l$ decays [82], for which the presence of a spinful particle increases the sensitivity to possible beyond the SM physics contributions.

1.4 The helicity formalism for baryon amplitude analyses and polarisation measurements

1.4.1 Introduction

Amplitude analyses are a set of formalisms which have been developed for describing multi-body decays with a complex structure characterised by different intermediate states and a non-trivial spin dependence. These formalisms exploit the Lorentz invariance to constrain the functional form of the decay distributions up to a set of free parameters which can be determined from a fit to experimental data.

Amplitude analyses allow to extract the maximum information from the measured decay distributions, therefore providing a wealth of physics results. Amplitude analyses give information on the identity, spin, mass dependence and mutual interferences of the resonant states contributing to the decay, making them a powerful tool also for spec-

troscopic searches. Amplitude analyses of baryon decays enable the measurement of baryon polarisation, and they can provide the best precision for baryons whose two body decay modes are suppressed with respect to multi-body decays, as the case of charm and beauty baryons. Amplitude analyses can be also used to study discrete symmetries violations. The amount of parity violation is particularly interesting since it determines the correlation between decay kinematics and polarisation, while the knowledge of the decay structure can be used to localise *CP*-violation effects in the decay distributions [83].

While many amplitude analyses have been performed for meson decays, only three baryon amplitude analysis have been performed to date: for the $\Lambda_c^+ \to pK^-\pi^+$ decay [71], for the $\Lambda_b^0 \to pK^- J/\psi$ decay [75], which lead to the discovery of the first pentaquark state, and for the $\Lambda_b^0 \to D^0 p\pi^-$ decay [84].

In the following, the helicity formalism for describing relativistic interactions among particles with spin [85] is applied for baryon amplitude analyses and polarisation measurements. After introducing the theoretical bases of the helicity formalism, the general form of the decay amplitude for a baryon three-body decay is derived, along with the differential decay rate for a generic polarisation state. In the end, some useful properties of the polarised decay rate are discussed.

1.4.2 Rotation of reference frames

The rotation of an initial Cartesian reference frame (x, y, z) into a final one (X, Y, Z) can be univocally described by an Euler rotation parametrised by three Euler angles α, β, γ. Taking the z-y-z convention for the rotation axes, the Euler rotation is composed by a first rotation of angle α around the z axis, a second rotation of angle β around the rotated y' axis and a third one of angle γ around the two-times rotated z'' axis,

$$\mathcal{R}(\alpha,\beta,\gamma) = R_{z''}(\gamma)R_{y'}(\beta)R_z(\alpha) = e^{-i\gamma\hat{J}_{z''}}e^{-i\beta\hat{J}_{y'}}e^{-i\alpha\hat{J}_z}. \tag{1.25}$$

The latter equality expresses rotations in terms of the generating angular momentum operators. Here, active rotations are considered, in which the normalised vectors $\hat{\boldsymbol{x}}, \hat{\boldsymbol{y}}, \hat{\boldsymbol{z}}$ defining the initial reference frame are actively rotated to those describing the final reference frame $\hat{\boldsymbol{X}}, \hat{\boldsymbol{Y}}, \hat{\boldsymbol{Z}}$,

$$\hat{\boldsymbol{X}}^i = \mathcal{R}(\alpha,\beta,\gamma)\hat{\boldsymbol{x}}^i. \tag{1.26}$$

The three Euler angles can be computed as follows: given the vector $\boldsymbol{N} = \hat{\boldsymbol{z}} \times \hat{\boldsymbol{Z}}$, α is the angle between $\hat{\boldsymbol{y}}$ and $\hat{\boldsymbol{N}}$, β is the angle between $\hat{\boldsymbol{z}}$ and $\hat{\boldsymbol{Z}}$ axes and γ is the angle between $\hat{\boldsymbol{N}}$ and $\hat{\boldsymbol{Y}}$ axes. In formulae[5],

$$\begin{aligned}
\alpha &= \text{atan2}\left(\hat{\boldsymbol{y}}\cdot\hat{\boldsymbol{Z}}, \hat{\boldsymbol{x}}\cdot\hat{\boldsymbol{Z}}\right) \in [-\pi,\pi],\\
\beta &= \arccos\left(\hat{\boldsymbol{z}}\cdot\hat{\boldsymbol{Z}}\right) \in [0,\pi],\\
\gamma &= \text{atan2}\left(\hat{\boldsymbol{z}}\cdot\hat{\boldsymbol{Y}}, -\hat{\boldsymbol{z}}\cdot\hat{\boldsymbol{X}}\right) \in [-\pi,\pi].
\end{aligned} \tag{1.27}$$

The Euler rotation can be also expressed in terms of rotations around the initial reference frame axes only, by means of the equality, shown in Ref. [86],

$$\mathcal{R}(\alpha,\beta,\gamma) = R_z(\alpha)R_y(\beta)R_z(\gamma) = e^{-i\alpha\hat{J}_z}e^{-i\beta\hat{J}_y}e^{-i\gamma\hat{J}_z}. \tag{1.28}$$

[5]The function $\text{atan2}(y,x) \in [-\pi,\pi]$ computes the signed angle between the x axis and the vector having components (x, y).

The active action of an Euler rotation on a vector $\boldsymbol{v}$ can be written in matrix notation as

$$V_i = \mathcal{R}_{ij}(\alpha, \beta, \gamma) v_j \tag{1.29}$$

in which the vector and matrix components are expressed in the same, but arbitrary, reference frame. Instead, the passive action on vector components, expressed in the initial (v_i) or the final (v_I) reference frames connected by an Euler rotation $\mathcal{R}(\alpha, \beta, \gamma)$, is

$$v_I = v_i \mathcal{R}(\alpha, \beta, \gamma)_{iI} = \mathcal{R}^T(\alpha, \beta, \gamma)_{Ii} v_i = \mathcal{R}(-\gamma, -\beta, -\alpha)_{ij} v_j, \tag{1.30}$$

in which the latter equality follows from $\mathcal{R}^T = \mathcal{R}^{-1}$ and Eq. (1.28).

The action of the rotation operators $\mathcal{R}(\alpha, \beta, \gamma)$ on angular momentum eigenstates $|J, m\rangle$ can be written as

$$\mathcal{R}(\alpha, \beta, \gamma) |J, m\rangle = \sum_{m'=-J}^{J} D^J_{m',m}(\alpha, \beta, \gamma) |J, m'\rangle , \tag{1.31}$$

in which the Wigner D-matrices $D^J_{m'm}(\alpha, \beta, \gamma)$ are the matrix elements of the rotation operator in the given spin reference frame,

$$D^J_{m',m}(\alpha, \beta, \gamma) = \langle J, m' | \mathcal{R}(\alpha, \beta, \gamma) | J, m \rangle . \tag{1.32}$$

From the latter equality of Eq. (1.28), the Wigner D-matrices can be factorised as

$$\begin{aligned} D^J_{m',m}(\alpha, \beta, \gamma) &= \langle J, m' | e^{-i\alpha \hat{J}_z} e^{-i\beta \hat{J}_y} e^{-i\gamma \hat{J}_z} | J, m \rangle \\ &= e^{-im'\alpha} d^J_{m',m}(\beta) e^{-im\gamma}, \end{aligned} \tag{1.33}$$

in which the Wigner d-matrices elements are known combinations of trigonometric functions of β depending on J, m, m' parameters [86].

1.4.3 Spin in relativistic decays

The description of a particle decay into two or more particles with spin is not trivial for relativistic processes, since a covariant definition for the spin operators is not possible [16]. Indeed, while the total angular momentum operators, conserved for rotational invariance, are well defined in any reference frame, the separation between spin and orbital angular momentum is dependent on the reference system. The set of covariant Pauli-Lubanski operators are the most similar to a covariant spin operator,

$$\hat{W}_\sigma = -\frac{1}{2} \epsilon_{\mu\nu\rho\sigma} \hat{M}^{\mu\nu} \hat{P}^\rho, \tag{1.34}$$

defined in terms of the generators of the Poincaré group $\hat{M}^{\mu\nu}$ (Lorentz group) and $\hat{P}^\rho$ (translations). They satisfy the commutation relations

$$\left[\hat{W}_\mu, \hat{W}_\nu \right] = i \epsilon_{\mu\nu\rho\sigma} \hat{W}^\rho \hat{P}^\sigma, \tag{1.35}$$

which reduce to the angular momentum commutation relations only if $\hat{W}_\mu$ operators act on particle states at rest, where the operators $\hat{S}_i = \hat{W}_i / m$ correspond to the non-relativistic spin operators. The expectation values of the Pauli-Lubanski operators on

a particle state form a 4-pseudovector $a^\mu = (a^0, \mathbf{a})$. In the rest frame of the particle $a^\mu = (0, \mathbf{s})$, and $p^\mu = (mc, \mathbf{0})$, so that in any reference frame $a^\mu p_\mu = 0$ and $a_\mu a^\mu = -\mathbf{s}^2$.

The spin-orbit formalism developed to combine angular momenta in non-relativistic quantum mechanics can not be directly applied to relativistic processes because each particle spin is defined only in its rest frame. It is therefore necessary to understand how particle spin states can be represented by observers moving with respect to the particle. Let us consider an observer with a given coordinate system $S = (x, y, z)$, and a particle having momentum $\boldsymbol{p}$ in the system S. To express the particle spin states $|s, m\rangle$, the observer frame S must be Lorentz-transformed to the particle rest frame. However, the choice of the particle spin reference frame is ambiguous, since rest frames obtained by Lorentz-transformations differing by a rotation around $\boldsymbol{p}$, will represent the particle spin with different spin states. There are two main choices for the spin coordinate frame in literature, the canonical choice and the helicity choice [16]:

- The canonical choice corresponds to the reference frame obtained from S by doing a pure Lorentz boost $L(-\boldsymbol{p})$, with no additional rotation, so that the observer describes the particle with the spin states $|s, m\rangle$ defined by its coordinate frame S.

- The helicity choice consists in choosing the particle spin quantisation axis z to be along the particle momentum in the observer frame. Its spin states become helicity states $|s, \lambda\rangle$, with the helicity defined as the spin projection along the particle momentum,

$$\hat{\lambda} = \hat{\boldsymbol{S}} \cdot \frac{\boldsymbol{p}}{p}. \tag{1.36}$$

  The helicity states for $\boldsymbol{p}$ having polar and azimuthal angles θ, ϕ in the observer reference frame are obtained from the observer S system by applying an Euler rotation $R(\phi, \theta, \psi)$ aligning the z axis with $\boldsymbol{p}$, called helicity rotation, followed by a boost $L(-p\boldsymbol{z})$ along the z axis. The advantage of using helicity states is that helicity is invariant under rotations and boosts along $\boldsymbol{p}$. It is important to note that any rotation of the reference frame around the momentum direction, represented by the third Euler angle ψ, would lead to equivalent helicity states $|s, \lambda\rangle$: while the canonical choice fixes all the coordinate axes, the helicity choice does not fix the axes orthogonal to the spin quantisation direction. These axes must be therefore defined by fixing a convention, the two most used in the literature are $\psi = 0$ and $\psi = -\phi$. In the author's opinion, this fact was not stressed enough in the literature, so it worth to point out two things: first, there is no "correct" choice of the angle ψ, but any choice is equivalent; second, once defined, the choice of the orthogonal axes of the helicity frame must be consistently used. Indeed, the effect of the helicity rotation, following from Eq. (1.25), is

$$\begin{aligned} R(\phi, \theta, \psi)\,|s, m\rangle &= e^{-i\psi \hat{J}_{z''}} e^{-i\theta \hat{J}_{y'}} e^{-i\phi \hat{J}_z}\,|s, m\rangle \\ &= e^{-i\psi \hat{J}_{z''}}\,|s, \lambda\rangle = e^{-i\psi\lambda}\,|s, \lambda\rangle \end{aligned} \tag{1.37}$$

  in which z'' is parallel to the particle momentum, showing that the ψ rotation changes the overall phase of the helicity state. Thus, helicity frames with different definitions of the orthogonal axes have different relative phases, which can lead to unphysical quantum interference effect if mixed up.

1.4.4 Helicity amplitudes

To apply the spin-orbit formalism for combining particle spins to relativistic processes the helicity formalism is employed, which was developed in Ref. [85] and reviewed in Ref. [86]. This formalism is based on the definition of two sets of two-particle states: plane-wave helicity states describing propagating particles with well defined momentum and spherical-wave helicity states, describing states of definite total angular momentum.

A single-particle plane-wave helicity state is labelled by the particle momentum $\boldsymbol{p}$, spin s and helicity λ, $|\boldsymbol{p}, s, \lambda\rangle$. A two-particle plane-wave helicity state is just the direct product of the two single-particle states

$$|\boldsymbol{p}_1, s_1, \lambda_1\rangle \otimes |\boldsymbol{p}_2, s_2, \lambda_2\rangle \,. \tag{1.38}$$

In the two-particle centre-of-mass (CM) frame the two momenta are back-to-back, $\boldsymbol{p}_1 = -\boldsymbol{p}_2$, and the same state can be described using the spherical coordinates of $\boldsymbol{p}_1$: its modulus $p = |\boldsymbol{p}_1| = |\boldsymbol{p}_2|$, and the polar and azimuthal angles θ and ϕ with respect to a given coordinate frame.

These states are indicated as $|p, \theta, \phi, \lambda_1, \lambda_2\rangle$, in which s_1 and s_2 labels have been dropped.

Similarly, a two-particle spherical-wave helicity state in its CM frame is denoted by $|p, J, M, \lambda_1, \lambda_2\rangle$, in which J is the total angular momentum of the system and M its projection along the z axis. These states transform irreducibly under rotations according to Eq. (1.31), while plane-wave helicity states do not. The relation between plane- and spherical-wave helicity states is worked out in [86], being

$$|p, \theta, \phi, \lambda_1, \lambda_2\rangle = \sum_{J,M} \sqrt{\frac{2J+1}{4\pi}} D^J_{M,\lambda_1-\lambda_2}(\phi, \theta, \psi)\, |p, J, M, \lambda_1, \lambda_2\rangle \,. \tag{1.39}$$

The crucial point of this derivation is that invariance under rotations of the helicity allows to consider the state $|p, 0, 0, \lambda_1, \lambda_2\rangle$ (in which particles are aligned to the z axis) which is eigenstate of J_z with eigenvalue $\lambda_1 - \lambda_2$. Then, exploiting the invariance of the helicity under rotations, this state is rotated to $|p, \theta, \phi, \lambda_1, \lambda_2\rangle$ with unchanged helicities. Note that, following the discussion of Sec. 1.4.3, the third argument of the D matrix is arbitrary, since any additional rotation around the z axis will lead to equivalent helicity states. In the following, the convention $\psi = 0$ is chosen.

The angular distribution of a two-body decay $A \to 1, 2$ can now be obtained from Eq. (1.39) working in the A rest frame. The initial state is the spin state of the particle A expressed in a given spin reference frame[6], $|i\rangle = |s_A, m_A\rangle$, while the final state is the plane-wave helicity state

$$|f\rangle = |\theta_1, \phi_1, \lambda_1, \lambda_2\rangle \,, \tag{1.40}$$

in which the p label is dropped because fixed by energy-momentum conservation. The angles θ_1 and ϕ_1 represent the spherical coordinates of $\boldsymbol{p}_1$ in the A spin reference (rest) frame; the polar angle is often called the particle 1 helicity angle in the A frame. These

[6]The initial spin reference frame can be chosen arbitrarily, while the helicity frames for the daughter particles are univocally determined starting from the initial frame.

angles are determined as

$$\begin{aligned}\theta_1 &= \arccos\left(\hat{\boldsymbol{z}}\cdot\hat{\boldsymbol{p}}_1\right),\\ \phi_1 &= \operatorname{atan2}\left[\hat{\boldsymbol{y}}\cdot\hat{\boldsymbol{p}}_1, \hat{\boldsymbol{x}}\cdot\hat{\boldsymbol{p}}_1\right].\end{aligned} \tag{1.41}$$

The amplitude for the A particle to decay to the final state $|f\rangle$ is, neglecting constant overall terms,

$$\begin{aligned}\mathcal{A}_{m_A,\lambda_1,\lambda_2}(\theta_1,\phi_1) &= \langle f\,|\,T\,|\,i\rangle\\ &= \langle\theta_1,\phi_1,\lambda_1,\lambda_2\,|\,T\,|\,s_A,m_A\rangle,\end{aligned} \tag{1.42}$$

in which T represents the transition operator describing the decay dynamics. Inserting a basis of two-particle spherical-wave helicity states $|J_f,M_f,\lambda_1,\lambda_2\rangle$ and using Eq. (1.39) one finds

$$\begin{aligned}\mathcal{A}_{m_A,\lambda_1,\lambda_2}(\theta_1,\phi_1) &= \langle\theta_1,\phi_1,\lambda_1,\lambda_2\,|\,T\,|\,s_A,m_A\rangle\\ &= \sum_{J_f,M_f}\langle\theta_1,\phi_1,\lambda_1,\lambda_2\,|\,J_f,M_f,\lambda_1,\lambda_2\rangle\,\langle J_f,M_f,\lambda_1,\lambda_2\,|\,T\,|\,s_A,m_A\rangle\\ &= \sum_{J_f,M_f}\sqrt{\frac{2J_f+1}{4\pi}}D^{*J_f}_{M_f,\lambda_1-\lambda_2}(\phi_1,\theta_1,0)\delta_{J_f,s_A}\delta_{M_f,m_A}\times\\ &\times\langle J_f,M_f,\lambda_1,\lambda_2\,|\,T\,|\,s_A,m_A\rangle\\ &= \mathcal{H}_{\lambda_1,\lambda_2}D^{*s_A}_{m_A,\lambda_1-\lambda_2}(\phi_1,\theta_1,0),\end{aligned} \tag{1.43}$$

in which the term

$$\mathcal{H}_{\lambda_1,\lambda_2}\equiv\langle s_A,m_A,\lambda_1,\lambda_2\,|\,T\,|\,s_A,m_A\rangle, \tag{1.44}$$

called helicity coupling, encodes the decay dynamics and can not depend on m_A for rotational invariance. The possible helicity couplings are determined by angular momentum conservation, requiring

$$|\lambda_1|\le s_1,\qquad |\lambda_2|\le s_2,\qquad |\lambda_1-\lambda_2|\le s_A. \tag{1.45}$$

If the decay conserves parity symmetry helicity couplings for opposite helicities are constrained by the relation shown in Ref. [86],

$$\begin{aligned}\mathcal{H}_{\lambda_1,\lambda_2} &\equiv \langle s_A,m_A,\lambda_1,\lambda_2\,|\,T\,|\,s_A,m_A\rangle\\ &= \langle s_A,m_A,\lambda_1,\lambda_2\,|\,PTP\,|\,s_A,m_A\rangle\\ &= \eta_A\eta_1\eta_2(-1)^{s_1+s_2-s_A}\mathcal{H}_{-\lambda_1,-\lambda_2},\end{aligned} \tag{1.46}$$

in which η are the parity eigenvalues of the particle states.

The helicity formalism can be applied to multi-body particle decays by breaking the decay chain in sequential two-body decays mediated by intermediate particles states. Let us consider a three-body decay $A\to R(\to 1,2),3$, which can be broken in two two-body decays $A\to R,3$ and $R\to 1,2$, with R an intermediate state. The first one can be expressed by Eq. (1.43)

$$\begin{aligned}\mathcal{A}^{A\to R,3}_{m_A,\lambda_R,\lambda_3}(\theta_R,\phi_R) &= \langle\theta_R,\phi_R,\lambda_R,\lambda_3\,|\,T(A\to R,3)\,|\,s_A,m_A\rangle\\ &= \mathcal{H}^{A\to R,3}_{\lambda_R,\lambda_3}D^{*s_A}_{m_A,\lambda_R-\lambda_3}(\phi_R,\theta_R,0).\end{aligned} \tag{1.47}$$

The second decay can be written in the same form by taking the R state as decaying particle, with initial state $|s_R, \lambda_R\rangle$ expressed in the R helicity frame reached from the A reference frame,

$$\begin{aligned}\mathcal{A}^{R\to 1,2}_{\lambda_R,\lambda_1,\lambda_2}(\theta_1,\phi_1) &= \langle \theta_1,\phi_1,\lambda_1,\lambda_2 \,|\, T(R\to 1,2) \,|\, s_R,\lambda_R\rangle \\ &= \mathcal{H}^{R\to 1,2}_{\lambda_1,\lambda_2} D^{*s_R}_{m_R,\lambda_1-\lambda_2}(\phi_1,\theta_1,0),\end{aligned} \tag{1.48}$$

in which θ_1 and ϕ_1 are the spherical coordinates of $\boldsymbol{p}_1$ in the R spin reference frame. The total amplitude is then written introducing R as intermediate state, summing the amplitudes over the allowed R helicity states satisfying the conditions Eq. (1.45),

$$\begin{aligned}&\mathcal{A}^{A\to R,3\to 1,2,3}_{m_A,\lambda_1,\lambda_2,\lambda_3}(\theta_R,\phi_R,\theta_1,\phi_1) = \langle \boldsymbol{p}_1,\boldsymbol{p}_2,\boldsymbol{p}_3,\lambda_1,\lambda_2,\lambda_3 \,|\, T(A\to 1,2,3) \,|\, s_A,m_A\rangle \\ &= \sum_{\lambda_R} \langle \theta_1,\phi_1,\lambda_1,\lambda_2 \,|\, T(R\to 1,2) \,|\, s_R,\lambda_R\rangle \,\langle \theta_R,\phi_R,\lambda_R,\lambda_3 \,|\, T(A\to R,3) \,|\, s_A,m_A\rangle \\ &= \sum_{\lambda_R} \mathcal{A}^{A\to R,3}_{m_A,\lambda_R,\lambda_3}(\theta_R,\phi_R)\mathcal{A}^{R\to 1,2}_{\lambda_R,\lambda_1,\lambda_2}(\theta_1,\phi_1) \\ &= \sum_{\lambda_R} \mathcal{H}^{R\to 1,2}_{\lambda_1,\lambda_2} D^{*s_R}_{\lambda_R,\lambda_1-\lambda_2}(\phi_1,\theta_1,0)\mathcal{H}^{A\to R,3}_{\lambda_R,\lambda_3} D^{*s_A}_{m_A,\lambda_R-\lambda_3}(\phi_R,\theta_R,0) \\ &= \sum_{\lambda_R} \mathcal{H}^{R\to 1,2}_{\lambda_1,\lambda_2}\mathcal{H}^{A\to R,3}_{\lambda_R,\lambda_3} d^{s_R}_{\lambda_R,\lambda_1-\lambda_2}(\theta_1) d^{s_A}_{m_A,\lambda_R-\lambda_3}(\theta_R) e^{i\lambda_R\phi_1} e^{im_A\phi_R}.\end{aligned} \tag{1.49}$$

The latter expression shows the amplitude factorised in helicity couplings, real Wigner d-matrices associated to polar angles θ_1, θ_R and phase factors associated to azimuthal angles ϕ_1, ϕ_R via Eq. (1.33). It is important to stress that helicities and angles are defined in the different and specific reference frames described previously. Usually, the intermediate state R is not a particle state with a definite mass, but a resonant state featuring a non-trivial mass distribution, which is often described by a function of the invariant mass of the $1,2$ particle pair m_{12} called lineshape, $\mathcal{R}(m_{12})$. For most resonances, the lineshape can be chosen to be a relativistic Breit-Wigner function. It is assumed that the dependence on the lineshape is factorised in the amplitude,

$$\begin{aligned}&\mathcal{A}^{A\to R,3\to 1,2,3}_{m_A,\lambda_1,\lambda_2,\lambda_3}(m_{12},\theta_R,\phi_R,\theta_1,\phi_1) \\ &\qquad = \sum_{\lambda_R} \mathcal{H}^{R\to 1,2}_{\lambda_1,\lambda_2} D^{*s_R}_{\lambda_R,\lambda_1-\lambda_2}(\phi_1,\theta_1,0) \\ &\qquad \times \mathcal{H}^{A\to R,3}_{\lambda_R,\lambda_3} D^{*s_A}_{m_A,\lambda_R-\lambda_3}(\phi_R,\theta_R,0)\mathcal{R}(m_{12}),\end{aligned} \tag{1.50}$$

i.e. the helicity couplings Eq. (1.44) are assumed to not depend on the resonance mass.

Now, let us consider an intermediate state contributing to the three-body decay via a different decay channel, *e.g.* $A \to S(\to 1,3),2$. Its associated amplitude is, following Eq. (1.49),

$$\begin{aligned}\mathcal{A}^{A\to S,2\to 1,2,3}_{m_A,\lambda_1',\lambda_2',\lambda_3'}(\theta_S,\phi_S,\theta_1',\phi_1') &= \langle \boldsymbol{p}_1,\boldsymbol{p}_2,\boldsymbol{p}_3,\lambda_1',\lambda_2',\lambda_3' \,|\, T(A\to 1,2,3) \,|\, s_A,m_A\rangle \\ &= \sum_{\lambda_S} \mathcal{H}^{S\to 1,3}_{\lambda_1',\lambda_3'} D^{*s_S}_{\lambda_S,\lambda_1'-\lambda_3'}(\phi_1',\theta_1',0)\mathcal{H}^{A\to S,2}_{\lambda_S,\lambda_2'} D^{*s_A}_{m_A,\lambda_S-\lambda_2'}(\phi_S,\theta_S,0)\end{aligned} \tag{1.51}$$

in which primed quantities have been used to stress that these angles and helicities are

defined in different reference frames with respect to the amplitude for the R intermediate state. To be explicit, quantities related to S and 2 particles are defined in the A reference frame, while those related to $1,3$ particles are expressed in the S helicity frame reached from the A reference frame.

When different intermediate states contribute to the decay, the total amplitude is the sum of the single amplitudes over all the allowed helicity state for each intermediate state, but the helicity frames for the final particles must be the same for each decay channel. Therefore, a reference helicity frame for each final particle must be chosen, and all the different helicity frames must be rotated to the chosen one. These reference frames can be chosen arbitrarily for each final particle rest frame. In the example above, the amplitude for S intermediate state can be referred with respect to the helicity frames defined for R intermediate states, $|\lambda_i\rangle_R$. To this end, the latter must be expressed in terms of the helicity states defined for S intermediate states, $|\lambda_i'\rangle_S$, as

$$\begin{aligned}
|\lambda_i\rangle_R &= \mathcal{R}(\alpha_i,\beta_i,\gamma_i)\,|\lambda_i\rangle_S \\
&= \sum_{\lambda_i'=-s_i}^{s_i} |\lambda_i'\rangle_S \,\langle\lambda_i'|_S\,\mathcal{R}(\alpha_i,\beta_i,\gamma_i)\,|\lambda_i\rangle_S \\
&= \sum_{\lambda_i'=-s_i}^{s_i} D^{s_i}_{\lambda_i',\lambda_i}(\alpha_i,\beta_i,\gamma_i)\,|\lambda_i'\rangle_S\,,
\end{aligned} \tag{1.52}$$

in which $\mathcal{R}(\alpha_i,\beta_i,\gamma_i)$ are the rotations from the helicity frames for S states to those for R states. The amplitude for S intermediate state becomes

$$\begin{aligned}
\mathcal{A}^{A\to S,2\to 1,2,3}_{m_A,\lambda_1,\lambda_2,\lambda_3}(\Omega) &= \langle \boldsymbol{p}_1,\boldsymbol{p}_2,\boldsymbol{p}_3,\lambda_1,\lambda_2,\lambda_3\,|\,T(A\to 1,2,3)\,|\,s_A,m_A\rangle \\
&= \sum_{\lambda_1'=-s_1}^{s_1} D^{*s_1}_{\lambda_1',\lambda_1}(\alpha_1,\beta_1,\gamma_1) \\
&\times \sum_{\lambda_2'=-s_2}^{s_2} D^{*s_2}_{\lambda_2',\lambda_2}(\alpha_2,\beta_2,\gamma_2) \\
&\times \sum_{\lambda_3'=-s_3}^{s_3} D^{*s_3}_{\lambda_3',\lambda_3}(\alpha_3,\beta_3,\gamma_3) \\
&\times \sum_{\lambda_S} \mathcal{H}^{S\to 1,3}_{\lambda_1',\lambda_3'} D^{*s_S}_{\lambda_S,\lambda_1'-\lambda_3'}(\phi_1',\theta_1',0)\mathcal{H}^{A\to S,2}_{\lambda_S,\lambda_2'} D^{*s_A}_{m_A,\lambda_S-\lambda_2'}(\phi_S,\theta_S,0)
\end{aligned} \tag{1.53}$$

Note that the Euler angles describing all the reference frame rotations for each decay chain can be computed from the set of phase space variables Ω describing the multi-body decay, so they do not constitute independent degrees of freedom.

The amplitude associated to a decay with definite values of mother and final particle spins is obtained summing the helicity amplitudes associated to each allowed helicity state of the intermediate resonances. For example, the total amplitude for a three body decay in which sets of intermediate states $\{R_i\}\to 1,2$, $\{S_j\}\to 1,3$ and $\{U_k\}\to 2,3$ are

contributing is

$$\begin{aligned}\mathcal{A}^{A\to 1,2,3}_{m_A,\lambda_1,\lambda_2,\lambda_3}(\Omega) = &\sum_i \mathcal{A}^{A\to R_i,3\to 1,2,3}_{m_A,\lambda_1,\lambda_2,\lambda_3}(\Omega) \\ &+ \sum_j \mathcal{A}^{A\to S_j,2\to 1,2,3}_{m_A,\lambda_1,\lambda_2,\lambda_3}(\Omega) \\ &+ \sum_k \mathcal{A}^{A\to U_k,1\to 1,2,3}_{m_A,\lambda_1,\lambda_2,\lambda_3}(\Omega). \end{aligned} \tag{1.54}$$

1.4.5 Differential decay rate and extraction of the decaying particle polarisation

The differential decay rate for a particle A decaying to a final-state f is described by the probability density $p(\Omega, \boldsymbol{P})$, function of the phase-space variables Ω, and the A particle spin polarisation vector $\boldsymbol{P}$. The final particle polarisations do not enter the decay rate unless measurable, which is not usually the case. The decay probability for definite spin states is the squared modulus of the amplitude of the multi-body decay between the A particle initial state $|s_A, m_A\rangle$ and the final particle state $|\{\boldsymbol{p_i}\}, \{\lambda_i\}\rangle$,

$$p(A \to f) = |\,\langle s_A, m_A|T|\{\boldsymbol{p_i}\}, \{\lambda_i\}\rangle\,|^2 = |\mathcal{A}^{A\to f}_{m_A,\{\lambda_i\}}(\Omega)|^2. \tag{1.55}$$

In practice, it is not possible to measure event-by-event particle polarisations, therefore statistical mixtures of pure quantum spin states must be considered, expressing the probability density in terms of spin density matrices, Eq. (1.12). The above expression, rewritten by inserting suitable identity operators, becomes

$$p(A \to f) = \mathrm{tr}\left[\rho_A T \rho_f T^\dagger\right], \tag{1.56}$$

in which ρ_A and ρ_f are the A and f spin density matrices expressed in their own spin reference frames, respectively, and T now represents the transition operator matrix elements between A and f spin states,

$$T_{m_A,\{\lambda_i\}} = \mathcal{A}^{A\to f}_{m_A,\{\lambda_i\}}(\Omega). \tag{1.57}$$

If final particle polarisations are not measured, the final spin state is a maximally mixed state, $\rho_f = \mathbb{I}/(2s+1)$, in any spin reference frame [16]. By making explicit the sum over spin states, the differential decay rate is written as

$$p(\Omega, \boldsymbol{P}) = \sum_{m,m'=-s_A}^{s_A} \sum_{\{\lambda_i\}=\{-s_i\}}^{\{s_i\}} (\rho_A)_{mm'}\, \mathcal{A}^{A\to f}_{m',\{\lambda_i\}}(\Omega) \mathcal{A}^{*A\to f}_{m,\{\lambda_i\}}(\Omega). \tag{1.58}$$

The differential decay rate of a particle with spin can be therefore exploited to extract its (statistically-averaged) polarisation. The polarisation can be extracted together with the amplitude model of the decay by means of an amplitude analysis over the full decay phase space Ω.

1.4.6 Properties of the polarised decay rate

Let us consider the decay of a particle A, having polarisation vector $\boldsymbol{P}$. The polarisation vector is the only quantity specifying a direction in the A particle system. If $\boldsymbol{P}$ is zero,

nothing specifies a direction in the A system and its decay rate must be isotropic with respect to a reference frame independent of the decay, *e.g.* a given A spin reference frame. In other words, the decay rate specifies the relative angular distribution among daughter particles, but not their orientation relative to an external reference frame. This provide a benchmark test for codes implementing amplitude models: the angular distributions describing the orientation of the decay with respect to an external reference frame must be isotropic irrespective of the amplitude model.

Now let us suppose $\boldsymbol{P} \neq 0$. Under rotations of the polarisation frame, the polarisation vector rotates too, but, for rotational invariance, the decay phase space variables of the differential decay rate must rotate consistently. This implies that the relative orientation of the daughter particles can not depend on the orientation of the decay with respect to an external reference frame. The kinematic distributions describing the relative orientation of daughter particles must be therefore the same for any value of the A polarisation vector, this providing another benchmark test for the amplitude model. Moreover, this fact allows to study the decay amplitude model independently of the polarisation, since the information on the A polarisation only comes from the angular distributions describing the orientation of the decay.

The sensitivity of the decay rate to the particle polarisation depends critically on the amount of parity symmetry violation characterising the decay. If the decay is mediated by a parity conserving interaction, the decay rate does not depend on the polarisation vector. Indeed, parity symmetry requires the decay angular distribution to be symmetric under space coordinates inversion, which requires the decay angular distribution to be equal for $+|\boldsymbol{P}|$ and $-|\boldsymbol{P}|$ polarisation values, for any polarisation vector $\boldsymbol{P}$. In other words, if the decay conserves parity, the resulting angular distribution is not able to discriminate between different polarisation states. Actually, parity violation introduce an asymmetry in the direction specified by $\boldsymbol{P}$.

The particle polarisation vector can be measured from its angular decay distribution only if its decay features parity violation. The situation is different in case the polarisation of the final particles can be accessed (*e.g.* in case they have a weak decay) or if the particle is produced from a weak decay [16]. In the latter case, a complete angular analysis of the weak decay (including other particles produced together with the one under study) allows to determine the particle polarisation, even if it has a parity conserving decay.

As mentioned in Sec. 1.3, the polarisation vector $\boldsymbol{P}$ completely specifies the particle spin state only for spin $1/2$ particles. For generic spin values s, the particle spin state can be described in terms of spherical tensor operators T^L_M, with $0 < L < 2s$ and $-L < M < L$, with L called the rank of the operator [16]. The polarisation vector components constitute the three rank 1 operators. It is possible to demonstrate that from the angular distribution of a parity conserving particle decay, only operators with even rank can be measured, while parity violation (or additional information, as mentioned before) is needed to measure odd rank operators.

Part I

Short-lived particles electromagnetic dipole moment experiment proposal

CHAPTER 2

Heavy baryon electromagnetic dipoles experiment proposal

2.1 Motivation

The measurement of electromagnetic dipole moments is based on the phenomenon of spin precession in electromagnetic fields; in the non-relativistic approximation the polarisation precesses according to [87]

$$\frac{d\mathbf{s}}{d\tau} = \boldsymbol{\mu} \times \mathbf{B}^* + \boldsymbol{\delta} \times \mathbf{E}^* \tag{2.1}$$

in which $\mathbf{E}^*$ and $\mathbf{B}^*$ are the electromagnetic fields in the rest frame of the particle and $\mathbf{s}$, $\boldsymbol{\mu}$ and $\boldsymbol{\delta}$ are the expectation values of the spin, MDM and EDM operators. The measurement of the change in spin direction while travelling in an electromagnetic field allows to access the particle gyromagnetic and gyroelectric factors.

To measure spin precession, an experiment must rely on three main elements: a source of polarised particles, having known polarisation direction and magnitude; a sufficiently intense electromagnetic field to induce a sizeable spin precession angle within the experiment size; a detector able to measure the final polarisation vector. For short-lived particles like charm (beauty) baryons, having a proper lifetime of order 10^{-13} (10^{-12}) s, the conventional electromagnetic fields are too weak to induce significant spin precession before the particle decays. No direct measurement of charm and beauty (heavy, in the following) baryons has been possible until now.

In the following sections the proposal for an experiment measuring heavy baryon electromagnetic dipole moments will be detailed. The possibility of doing CPT symmetry tests using positive and negative charm baryon MDMs will also be discussed. This work has been published as part of Refs. [88, 89].

2.2 Experiment description

The limitations given by the short lifetime of heavy baryons can be overcome by exploiting the phenomenon of particle channeling through a bent crystal [90], where the particle experiences the very large crystal interatomic electric field, of order $10^{11} V/\mathrm{m}$, and by using heavy baryons produced in 7 TeV proton on fixed-target interactions at the Large Hadron Collider (LHC) [91, 92], to amplify the electric field in the baryon rest frame and to dilate the baryon lifetime thanks to Lorentz boost factors up to $\gamma \sim 1000$.

As mentioned in Sec. 2.1, an experiment measuring particle dipole moments from spin precession must rely on three key elements: a source of polarised particles, a suffi-

ciently intense electromagnetic field to induce a sizeable spin precession and a detector able to measure the final polarisation vector.

In proton-nucleon collisions, heavy baryons can be produced with polarisation perpendicular to the production plane defined by the beam and heavy baryon momenta, Sec. 1.3.2, with initial polarisation parallel to the y axis of the coordinate system depicted in Fig. 1.3.

A sizeable spin precession, sensitive to the heavy baryon dipole moments, is achieved exploiting the intense electric field $\mathbf{E}$ between the crystal planes experienced by charged particles when channeled through a bent crystal. In the particle rest frame the electric field transforms into an electromagnetic field

$$\mathbf{E}^* \approx \gamma \mathbf{E}, \qquad \mathbf{B}^* \approx -\gamma \boldsymbol{\beta} \times \mathbf{E}/c, \tag{2.2}$$

which is amplified by the particle Lorentz boost γ with respect to the laboratory frame.

An introduction to the channeling phenomenon is given in Sec. 2.3, while the analytical study of spin precession in the crystal electric field is performed in Sec. 2.4. To induce spin precession for heavy baryons polarised in the y axis direction, the crystal must be bent in the same direction. The coordinate system for the crystal is defined as in Fig. 2.1: the longitudinal crystal direction defines the z axis and the bending direction the y axis, the x axis defining the non-bending direction of the crystal. While for heavy baryons channeled in axial configuration the motion is bound in both bending and non-bending directions, for planar channeling the motion along the x axis is not constrained by the crystal. If the crystal is aligned to the beam (coinciding z axes for the two coordinate frames) the planar channel would constrain the heavy baryon production plane to be the xz crystal plane, and the baryon polarisation to the bending direction y.

In practice the crystal can not be perfectly aligned with the proton beam since channeling of the incoming proton beam must be avoided to prevent the beam to interfere with the detector. For axially bent crystals a tilt in the xz plane by an angle much greater than the Lindhard one, *e.g.* order 100 $\mu\mathrm{rad}$, is sufficient, and fixes the polarisation direction up to variations of order θ_L. For planarly bent crystals, which do not impose acceptance requirements in the x direction, a tilt of order 100 $\mu\mathrm{rad}$ in the yz plane is needed. The tiny discrepancy between heavy baryon polarisation and crystal bending direction would produce a negligible polarisation in the crystal z direction and no polarisation in the non-bending one, so that the initial polarisation is basically still parallel to the y axis in the crystal coordinate frame. Moreover, it is important to note that events in which the heavy baryon is produced in opposite x directions will feature opposite polarisation[1], so that spin precession has to be analysed in bins of the angle θ_x between baryon and beam directions; otherwise, the crystal acceptance must be made asymmetric in the x direction, *e.g.* translating the crystal in the x direction with respect to the proton beam.

In the limit of large boost with Lorentz factor $\gamma \gg 1$ and in absence of baryon EDM, the spin precession is confined to the yz plane, and the precession angle Φ, defined as the angle between the initial and final polarisation vectors, as shown in Fig. 2.1, is [90, 93]

$$\Phi \approx \frac{g-2}{2}\gamma\theta_C. \tag{2.3}$$

The precession angle is proportional to the anomalous MDM, the Lorentz boost and the crystal bending angle $\theta_C = L/R$, in which L is the length (circular arc) of the crystal and

[1] Events in which the baryon is produced in the opposite x direction with respect to the beam are related by a π angle rotation around the beam axis, which reverses the polarisation in the crystal frame Fig. 2.1 or the y axis defined from the production plane Fig. 1.3.

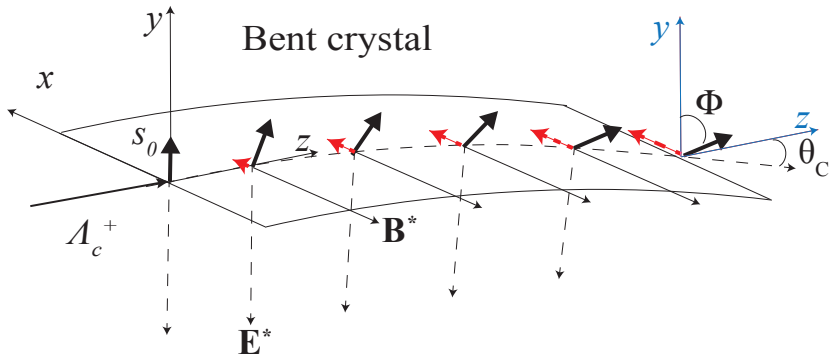

Figure 2.1: from Ref. [88]. Deflection of the heavy baryon trajectory and spin precession in the yz and xy plane induced by the particle MDM and EDM, respectively. The red dashed arrows indicate the (magnified) s_x spin component proportional to the particle EDM. Φ is the MDM precession angle and θ_C is the crystal bending angle.

R its curvature radius. For a precession angle of order one, a curvature $\theta_C \approx 10\,\mathrm{mrad}$ is needed, with crystal parameters of order $L \approx 10\,\mathrm{cm}$ and $R \approx 10\,\mathrm{m}$.

In presence of a non-zero EDM, the spin precession is no longer confined to the yz plane, originating a polarisation component along the non-bending x axis proportional to the particle EDM[2],

$$s_x \approx s_0 \frac{d}{g-2}(1-\cos\Phi), \tag{2.4}$$

represented by the red dashed arrows in Fig. 2.1. A final x component polarisation would constitute a clear experimental signature of a particle EDM.

The possibility to use the highest available proton beams at the LHC energies offers multiple advantages that allow to apply this experimental setup to short-lived heavy baryons: first, the intensity of the electromagnetic fields experienced by the channeled particle, and in turn the amount of spin precession determining the sensitivity to the dipole moments, is proportional to γ, Eqs.(2.2),(2.3); second, the particle lifetime in the laboratory reference system is proportional to γ, increasing the number of heavy baryons able to completely traverse the crystal (*i.e.* undergoing the maximum and analytically known spin precession) before their decay; third, the number of heavy baryons that can enter the channeling condition is proportional to $\gamma^{1/2}$, thanks to the narrower angular spread of heavy baryons with increasing Lorentz boost (proportional to $1/\gamma$), which is partly compensated by the reduction of the channeling acceptance angle Eq. 2.6, proportional to $1/\sqrt{\gamma}$.

The heavy baryon polarisation can be measured from the angular distribution of the particles produced in their decays. While the angular distribution of non-channeled particles allows to determine the initial polarisation along the y axis, that of channeled particles allows to extract the polarisation after precessing in the crystal, which compared to the initial polarisation allows the extraction of the gyromagnetic and gyroelectric factors. The initial polarisation can be also determined from the final one, along with g and d factors, up to discrete ambiguities, discussed in Appendix A.1.

In the simplest case of heavy baryons decaying to two-body final states, the angular

[2]Note that in the limit $g-2 \to 0$ the s_x expression is not singular because it is linear in $g-2$. In fact, expanding the cosine function and substituting Eq. (2.3) one finds $1-\cos\Phi \propto (g-2)^2$.

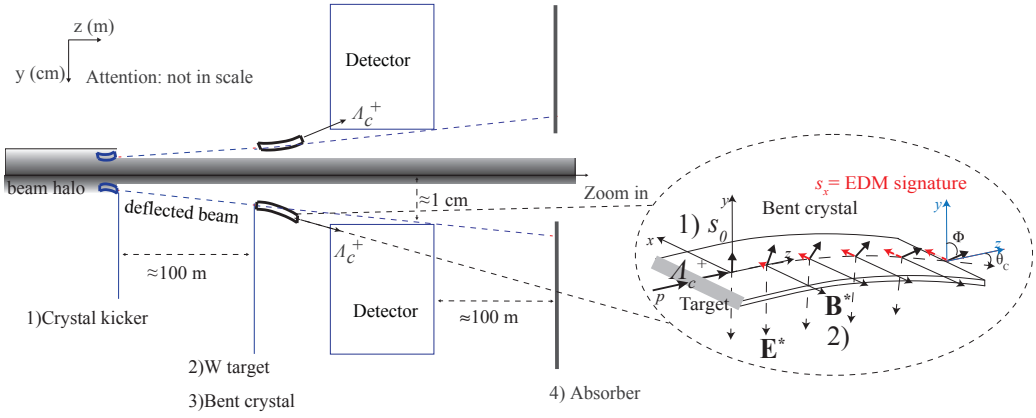

Figure 2.2: from Ref. [89]. Experimental layout for the heavy baryon dipole moments measurement.

distribution of the final state baryon in the heavy baryon rest frame is described by

$$\frac{dN}{d\Omega^*} \propto 1 + \alpha_f \mathbf{s} \cdot \hat{\mathbf{k}}, \tag{2.5}$$

in which α_f is a parity violating coefficient depending on the final state and $\hat{\mathbf{k}}$ the final baryon momentum direction in the heavy baryon rest frame. For heavy baryon decays to more than two particles, the best sensitivity to the polarisation (and therefore to the dipole moments) is achievable by means of an amplitude analysis of the decay over the full decay phase-space, because it allows to exploit all the available decay statistics taking into account the contribution of each intermediate state.

Considering the Λ_c^+ charm baryon, an amplitude analysis of the $\Lambda_c^+ \to pK^-\pi^+$ decay, which is the main decay channel of the Λ_c^+ baryon, has been performed by the E791 experiment at Fermilab on a data sample of 1000 events only [71]. The LHCb experiment has recorded millions of $\Lambda_c^+ \to pK^-\pi^+$ events, allowing to perform detailed studies of the intermediate resonances contributing to the decay. The current status of the full phase space amplitude analysis of the $\Lambda_c^+ \to pK^-\pi^+$ decay, including the extraction of the polarisation vector, being performed on LHCb data from Λ_b^0 semileptonic decays is detailed in the second part of this thesis.

The Λ_c^+ polarisation in proton-nucleus fixed-target collisions can be measured at the 100 GeV energy scale using proton-gas collision data recorded by the LHCb experiment in its fixed-target configuration. The feasibility of the Λ_c^+ polarisation measurement on the LHCb proton-neon fixed-target sample is demonstrated in the third part of this thesis.

The layout of the experiement for heavy baryon dipole moments measurement is depicted in Fig. 2.2. Its core consists of a dense target, *e.g.* a tungsten target, in which proton-nucleon collisions take place, attached to a silicon or germanium bent crystal, to maximise the number of heavy baryons decaying after the crystal. This device is to be placed at a safe distance from the too intense LHC proton beam, while a secondary, less intense proton beam is to be extracted and directed on the target. An extraction scheme using a bent crystal to deflect part of the main LHC beam halo has been proposed [94]

and more detailed studies are ongoing. The target-crystal device must be tilted by a small angle, order $100\ \mu\mathrm{rad}$, to produce polarised heavy baryons and to avoid the channeling of the incoming proton beam. Decays of channeled heavy baryons, which are bent by the crystal at an angle order $10\ \mathrm{mrad}$ from the beam direction, are to be reconstructed by a detector covering the forward angle region close to the beam axis, and featuring excellent tracking and vertexing capabilities, precise momentum measurement and good particle identification performances. Among the existing experiments at the LHC, the LHCb detector is the only one satisfying these requirements. The target-crystal device would be placed in front of the LHCb detector, as close as possible to its vertex locator (see Sec. 4), so that channeled heavy baryons can enter the detector acceptance, $\approx 10\,\mathrm{mrad}$ from the beam axis. The non-interacting protons of the secondary beam and most of the background particles will follow the beampipe without affecting LHCb operations. Sensitivity studies to estimate the achievable precision on heavy baryon dipole moments according to the presented layout are described in Sec. 2.5.

To control systematic uncertainty effects, a second target-crystal device deflecting heavy baryons in the opposite direction should be employed. For example, spin precession effects due to weak nuclear interactions with the crystal lattice are expected to be equal for opposite bending directions, while MDM and EDM induced spin precession effects are opposite for different bendings [95].

The spin precession of particles channeled in bent crystals was firstly observed by the E761 Collaboration [96]. Using a 800 GeV/c proton beam impinging on a Cu target, Σ^+ baryons with 375 GeV/c average momentum were produced and channeled in two bent crystals with opposite bending angles. The MDM of the Σ^+ baryon was measured and proved the viability of this technique for the measurement of the MDM of short-lived particles.

This experiment proposal extends the physics program of a proposed experiment for the measurement of the Λ_c^+ baryon MDM, based on a similar experimental layout [91,92, 97,98], to the measurement of positive and negative heavy baryon magnetic and electric dipole moments.

2.3 Channeling of high energy charged particles

In a crystal the strong electric field experienced by a charged particle in the proximity of the periodic structure of the atoms results in a strong confinement force, which can bound the particle trajectory to follow a crystalline plane or an atomic string, a phenomenon called channeling. In a continuum approximation, which consider the crystal planes and axes as continuous neglecting single-atom effects, a charged particle sees the crystal as a stack of channels, separated by electric potential walls, which become preferential pathways for traversing the crystal. The accuracy of this approximation increases with the particle energy. Channeling can occur if the angle between the particle trajectory and a crystal plane (planar channeling) or a crystal axis (axial channeling) is sufficiently small for the electric potential wall to bound the particle inside the channel. This critical (Lindhard) angle can be expressed as

$$\theta_L = \sqrt{2U_0/(p\beta c)}, \tag{2.6}$$

in which U_0 is the potential-well depth, p the particle momentum and β its velocity [99, 100]. Planar channeling for positive particles has been observed and studied in laboratory up to 6.5 TeV proton energy at the LHC [101]. Channeling of negative particles has been observed in both planar [102] and axial [103] configurations.

Channel Si 110	width d_p(Å)	potential depth U (eV)	maximum electric field U' (GV/ cm)
Planar	1.92	16	5.7
Axial	3.85	114	

Table 2.1: Characteristics of planar and axial Si crystal 110 channel, from Ref. [100].

In a bent crystal, the crystallographic planes and axes are bent too, and channeled particles can follow the crystal curvature, resulting in a net deflection of the incoming direction by an angle equal to that of crystal bending. Charged particle steering without magnets is therefore possible exploiting channeling in bent crystals, which has progressed significantly over the last years. Up to 80% deflection efficiency was reached for positive particles in planar channeling [104], and 90% for negative particles in axial channeling [105], at hundreds of GeV scale. Various applications as circular accelerator halo collimation [106] or beam extraction from an accelerator ring for fixed-target experiments [94] have been studied and proposed also for the LHC.

In the case of axial channeling, negative particles are bound to atomic strings in spiral-like trajectories. Negative particles having a transverse energy (*i.e.* related to the motion orthogonal to the channel) slightly above the potential barrier are not trapped along a single atomic string, but are deflected due to their stochastic scattering with different atomic strings. This phenomenon is called stochastic deflection, and allows negative particles to avoid the fast dechanneling occurring for planar channeling. Moreover, the axial channels for negative particles feature higher potential walls, leading to better channeling efficiency. Axial channeling is therefore promising for negative particles beam deflection. However, reaching a condition of axial alignment for beam steering is relatively more difficult than for planar channeling since the orientation of the crystal with respect to two instead of one rotational axes must be achieved. Note that for positive particles, axial channels are too shallow to be interesting for beam deflection as compared to planar channeling.

Table 2.1 summarises the characteristics of planar and axial silicon (Si) crystal 110 channel, taken from Ref. [100], which will be employed as reference in the following studies.

The planar channel electric potential seen by a positive particle is approximately harmonic, Fig. 2.3, and can be expressed as

$$V(d) = \frac{k}{e}\frac{d^2}{2}, \tag{2.7}$$

in which d is the interplanar distance from the position of the potential minimum and k is a crystal and channel dependent constant representing the curvature of the potential. For a particle moving in a bent crystal, the centrifugal force adds a linear term to the potential, which does not change the curvature but the particle equilibrium position. Therefore, in a bent crystal a channeled particle experiences a net electric field, causing both the particle deflection and spin precession [90]. In Sec. 2.4.1 the spin precession equation are derived for positive planar-channeled particles assuming an harmonic electric potential for the channel.

On the contrary, the planar channel potential seen by a negative particle, Fig. 2.3, or the potential associated to axial channels are far from an harmonic approximation [100]. The validity of the spin precession equations for non-harmonic and axial channel poten-

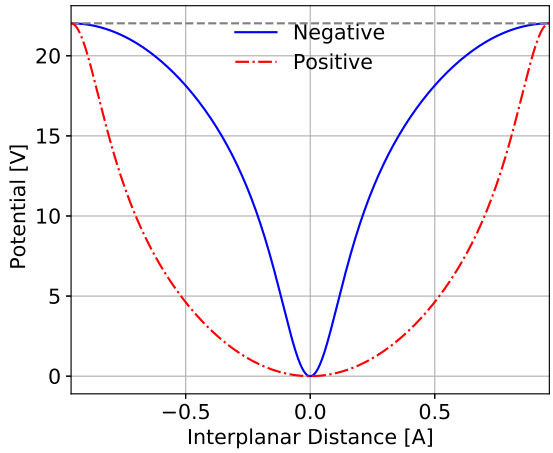

Figure 2.3: from Ref. [89]. Harmonic (red dash-dotted line) and non-harmonic (blue continuous line) electric potential versus interplanar distance for positive and negative particles in a (110) silicon crystal. The electric potential is extracted from GEANT4 simulations. For the sake of comparison the electric potential for negative particles is shifted by half of the interplanar distance.

tials is discussed in Secs. 2.4.3 and 2.4.4, respectively.

Positive particles in channeling condition are repelled by the positive nuclei electric field and their trajectories tend to be far from the lattice sites, experiencing smaller energy losses than particles not in the channeling regime. On the contrary, negative particles are attracted by the same field and can repeatedly oscillate across the nuclei composing the crystal lattice. For this reason negative particles are more likely to undergo nuclear collisions and escape from a channeling bound state. The phenomenon in which a channeled particle leaves the planar or axial channel, as due to interactions with crystal nuclei and electrons, is called dechanneling, and the average length that a channeled particle covers before leaving the potential well is called dechanneling length, L_d. For positive ultra relativistic particles it is well known for crystals having a length along the beam comparable to L_d [100],

$$L_d = \frac{256}{9\pi^2} \frac{p\beta c}{\ln(2m_e c^2\gamma/I) - 1} \frac{a_{\mathrm{TF}} d_p}{Z_i r_e m_e c^2}, \tag{2.8}$$

which scales almost proportionally to the particle momentum-velocity $p\beta$. Here m_e and r_e are the mass and the classical radius of the electron, I is the mean ionisation energy, d_p is the interplanar spacing, a_{TF} is the Thomas-Fermi screening radius, and Z_i and γ are the charge number and boost of the incident particle. The analytical dependence of L_d for negative particles is not known.

The channeling efficiency is defined as the fraction of particles channeled when entering the crystal, *i.e.* within the Lindhard angle, that conserve the channeling condition until they exit from the crystal. Under harmonic potential approximation, the potential depth for positive particles in a bent crystal as a function of the crystal bending radius R

is reduced,

$$U_0(R) = U_0(R \to \infty)\left(1 - \frac{R_c}{R}\right)^2, \tag{2.9}$$

in which R_c is the critical radius for channeling, the minimum bending radius for which channeling can occur, corresponding to the crystal curvature for which the centrifugal force exceeds the electric one,

$$R_c = \frac{p\beta}{U'}, \tag{2.10}$$

in which U' is the maximum channel electric field.

The acceptance Lindhard angle Eq. (2.6) is thus also reduced

$$\theta_L(R) = \theta_L(R \to \infty)\left(1 - \frac{R_c}{R}\right), \tag{2.11}$$

and the dechanneling length Eq. (2.8) is shortened by a factor [100]

$$L_d(R) = L_d(R = \infty)\left(1 - \frac{R_c}{R}\right)^2. \tag{2.12}$$

The channeling efficiency as a function of R can be therefore written as

$$\varepsilon_{\mathrm{CH}}(R) = \frac{\theta_L(R)}{\alpha}\exp\left(-\frac{L}{L_d(R)}\right), \tag{2.13}$$

in which α is the angular divergence of the incoming particles and L is the crystal length. The channeling efficiency is thus factored in two terms, the first represents the efficiency for a particle to enter the channeling regime, the second expresses the efficiency reduction due to dechanneling effects. The first term is valid for the usual case in which the particle angular divergence is much greater than the Lindhard angle and assuming the particle angular distribution to be approximately uniform.

The deflection efficiency of the channeling process in bent crystals for negative particles, for which analytical formulas are not available, can be studied by means of Monte Carlo simulations [89].

2.4 Spin precession equations

The time evolution of the spin-polarisation vector for a particle with charge q in an electromagnetic field, as a function of the proper time τ, is given by the Thomas-Bargmann-Michel-Telegdi (T-BMT) covariant equation in the quasi-classical particle motion approx-

imation[3] [107],

$$\begin{aligned}\frac{da^\mu}{d\tau} &= \frac{g\mu_B}{\hbar}\left[F^{\mu\nu}a_\nu + \left(a_\alpha F^{\alpha\beta}u_\beta\right)\frac{u^\mu}{c^2}\right] \\ &- (a_\alpha \dot{u}^\alpha)\frac{u^\mu}{c^2} \\ &- \frac{d\mu_B}{\hbar}\left[F^{*\mu\nu}a_\nu + \left(a_\alpha F^{*\alpha\beta}u_\beta\right)\frac{u^\mu}{c^2}\right], \end{aligned} \tag{2.14}$$

in which $F^{\mu\nu}$ is the electromagnetic field strength tensor, $a^\mu = (a^0, \mathbf{a})$ is the spin 4-pseudovector, and $p^\mu = mu^\mu = (E/c, \mathbf{p})$ is the momentum 4-vector. For homogeneous fields the velocity derivative is given by the Lorentz force,

$$\dot{u}^\mu \equiv \frac{du^\mu}{d\tau} = \frac{q}{mc}F^{\mu\nu}u_\nu. \tag{2.15}$$

In a frame in which the particle has velocity $\boldsymbol{\beta} = \mathbf{p}/m\gamma$, *e.g.* the laboratory frame, a^μ is given by [16, 87]

$$\mathbf{a} = \mathbf{s} + \frac{\gamma^2}{\gamma+1}(\boldsymbol{\beta}\cdot\mathbf{s})\boldsymbol{\beta}\,, \;\; a^0 = \boldsymbol{\beta}\cdot\mathbf{a} = \gamma(\boldsymbol{\beta}\cdot\mathbf{s}), \tag{2.16}$$

in which the components of the momentum 4-vector are $p^0 = \gamma mc^2$ and $\mathbf{p} = \gamma m\boldsymbol{\beta}c$. Substituting in Eq.(2.14), the spin precession equation become [16, 87, 108],

$$\begin{aligned}\frac{d\mathbf{s}}{dt} = \mathbf{s}\times\boldsymbol{\Omega} &= \begin{cases} \dfrac{ds_x}{dt} = s_y\Omega_z - s_z\Omega_y \\ \dfrac{ds_y}{dt} = s_z\Omega_x - s_x\Omega_z \\ \dfrac{ds_z}{dt} = s_x\Omega_y - s_y\Omega_x \end{cases}, \\ \boldsymbol{\Omega} &= \boldsymbol{\Omega}_{\rm MDM} + \boldsymbol{\Omega}_{\rm EDM} + \boldsymbol{\Omega}_{\rm TH}, \end{aligned} \tag{2.17}$$

in which t is the time in the laboratory frame, and the precession angular velocity vector $\boldsymbol{\Omega}$ has been split into three terms, corresponding to the MDM, EDM and Thomas precession contributions,

$$\begin{aligned}\boldsymbol{\Omega}_{\rm MDM} &= \frac{g\mu_B}{\hbar}\left(\mathbf{B} - \frac{\gamma}{\gamma+1}(\boldsymbol{\beta}\cdot\mathbf{B})\boldsymbol{\beta} - \boldsymbol{\beta}\times\mathbf{E}\right), \\ \boldsymbol{\Omega}_{\rm EDM} &= \frac{d\mu_B}{\hbar}\left(\mathbf{E} - \frac{\gamma}{\gamma+1}(\boldsymbol{\beta}\cdot\mathbf{E})\boldsymbol{\beta} + \boldsymbol{\beta}\times\mathbf{B}\right), \\ \boldsymbol{\Omega}_{\rm TH} &= \frac{\gamma^2}{\gamma+1}\boldsymbol{\beta}\times\frac{d\boldsymbol{\beta}}{dt} \\ &= \frac{q}{mc}\left[\left(\frac{1}{\gamma}-1\right)\mathbf{B} + \frac{\gamma}{\gamma+1}(\boldsymbol{\beta}\cdot\mathbf{B})\boldsymbol{\beta}\right. \\ &- \left.\left(\frac{1}{\gamma+1}-1\right)\boldsymbol{\beta}\times\mathbf{E}\right]. \end{aligned} \tag{2.18}$$

[3] Quantum mechanical effects are negligible for relativistic particles, since their associated Compton and De Broglie wavelengths are much smaller than the other length scales involved (they are order 10^{-17} m for a particle energy of 100 GeV).

in which the electromagnetic fields $\mathbf{E}$ and $\mathbf{B}$ are expressed in the laboratory frame.

Thomas precession, caused by the rotation of the instantaneous inertial frame produced by the Lorentz force, does not contribute for a neutral particle ($q = 0$); in that case the classical spin precession equation is obtained

$$d\mathbf{s}/d\tau = \boldsymbol{\mu} \times \mathbf{B}^* + \boldsymbol{\delta} \times \mathbf{E}^*, \tag{2.19}$$

in which $\mathbf{E}^*$ and $\mathbf{B}^*$ are the electromagnetic fields in the rest frame of the particle [87]; τ is the time in the particle rest frame. Eqs. (2.17) and (2.18) can be generalised to account for field gradient effects as described in Ref. [109, 110].

2.4.1 Spin precession of planar-channeled positive baryons

For the case of positive baryons channeled in a bent crystal $\mathbf{B} = 0$ and $q = +1$, so Eq. (2.18) simplifies to

$$\begin{aligned} \boldsymbol{\Omega} &= \frac{2\mu'}{\hbar}(\mathbf{E} \times \boldsymbol{\beta}) + \frac{d\mu_B}{\hbar}\mathbf{E} + \frac{1}{\gamma+1}\frac{2\mu_B}{\hbar}(\mathbf{E} \times \boldsymbol{\beta}) \\ &- \frac{d\mu_B}{\hbar}\frac{\gamma}{\gamma+1}(\boldsymbol{\beta} \cdot \mathbf{E})\boldsymbol{\beta}, \end{aligned} \tag{2.20}$$

in which

$$\mu' = \frac{g-2}{2}\frac{e\hbar}{2mc}, \tag{2.21}$$

is the anomalous magnetic moment for a spin-1/2 particle. The term proportional to $1/(\gamma+1)$ can be neglected for ultra relativistic heavy baryons, having $\gamma \gg 1$, since being composite particles, the heavy baryon $g-2$ is expected to be of order 1. Similarly, $\gamma/(\gamma+1)$ can be approximated to 1.

The trajectory of a particle channeled in a bent crystal is described using the coordinate system defined in Fig. 2.1. It is defined such that the origin of the coordinate system coincides with the crystal center of curvature. Radial coordinates are then defined in order to separate the longitudinal motion of the channeled particle at constant radius from the transverse motion given by oscillations in the channel potential, as depicted in Fig. 2.4 [111]

$$\begin{aligned} x(t) &= \text{ const.}, \\ y(t) &= \rho(t)\cos(\Omega t), \\ z(t) &= \rho(t)\sin(\Omega t), \end{aligned} \tag{2.22}$$

in which Ω is the revolution frequency for the particle traversing the bent crystal, *i.e.* rotating around the curvature center. In ultra-relativistic regime it is well approximated by $\Omega \approx c/R$, R being the crystal curvature radius. This way, a down-bending crystal, *i.e.* with y coordinate opposite to the bending direction, is described.

The electric potential felt by the channeled baryon can be approximated as an harmonic potential, Sec. 2.3,

$$V(\rho) = \frac{k}{e}\frac{[\rho(t) - \rho_0]^2}{2}, \tag{2.23}$$

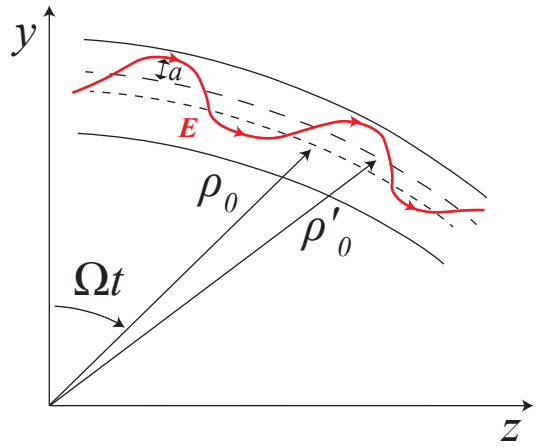

Figure 2.4: from Ref. [88]. Radial coordinates definition: ρ_0 is the radius corresponding to the minimum of the harmonic electric potential; ρ'_0 represents the radial equilibrium position of the electric and centrifugal potential. The red curve represents the particle trajectory inside the crystal in presence of the radial electric field $\mathbf{E}$, a is the oscillation amplitude and Ω the revolution frequency.

and the corresponding electric field is

$$\begin{aligned} E_x &= 0, \\ E_y &= -\frac{dV}{d\rho}\cos(\Omega t), \\ E_z &= -\frac{dV}{d\rho}\sin(\Omega t). \end{aligned} \tag{2.24}$$

The radius of the trajectory as a function of time follows an harmonic motion,

$$\rho(t) = \rho'_0 + a\cos(\Omega_k t + \delta), \tag{2.25}$$

in which a, Ω_k and δ are the oscillation amplitude, frequency and phase, respectively. The radial equilibrium position ρ'_0 differs from the electric potential minimum position ρ_0, thanks to the centrifugal potential. The oscillation frequency depends on the potential curvature k and the particle energy W as

$$\Omega_k = \sqrt{kc^2/eW}, \tag{2.26}$$

while a and δ depend on the baryon incoming angle and position with respect to the planar channels.

Substituting the radial coordinates and applying the ultra-relativistic approximation

to Eq. (2.20), the precession vector $\mathbf{\Omega}$ is

$$\begin{aligned}
\Omega_x &\approx \frac{2\mu'}{\hbar}(E_y\beta_z - E_z\beta_y) = \frac{2\mu'}{\hbar}\left(-\frac{dV}{d\rho}\frac{\rho\Omega}{c}\right), \\
\Omega_y &\approx \frac{d\mu_B}{\hbar}\left[E_y - (\boldsymbol{\beta}\cdot\mathbf{E})\,\beta_y\right] \\
&= -\frac{d\mu_B}{\hbar}\frac{dV}{d\rho}\cos(\Omega t) \\
&+ \frac{d\mu_B}{\hbar}\frac{dV}{d\rho}\frac{\dot{\rho}}{c^2}\left[-\rho\Omega\sin(\Omega t) + \dot{\rho}\cos(\Omega t)\right], \\
\Omega_z &\approx \frac{d\mu_B}{\hbar}\left[E_z - (\boldsymbol{\beta}\cdot\mathbf{E})\,\beta_z\right] \\
&= -\frac{d\mu_B}{\hbar}\frac{dV}{d\rho}\sin(\Omega t) \\
&+ \frac{d\mu_B}{\hbar}\frac{dV}{d\rho}\frac{\dot{\rho}}{c^2}\left[\rho\Omega\cos(\Omega t) + \dot{\rho}\sin(\Omega t)\right].
\end{aligned} \tag{2.27}$$

In absence of EDM, *i.e.* $d = 0$, the precession vector is along the x axis, and the spin precession inside the bent crystal is confined to the yz plane. Eq. (2.17) becomes

$$\frac{ds_x}{dt} = 0 \qquad \frac{ds_y}{dt} = s_z(t)\Omega_x \qquad \frac{ds_z}{dt} = s_y(t)\Omega_x, \tag{2.28}$$

leading to the differential equations

$$\frac{d^2 s_{y(z)}}{dt^2} = -\Omega_x^2 s_{y(z)}(t) \pm s_{z(y)}(t)\frac{d\Omega_x}{dt} \tag{2.29}$$

for y and z spin components. Solving the equations applying the $\mathbf{s}_0 = (0, s_0, 0)$ initial condition, the spin time evolution

$$\mathbf{s}(t) = \begin{cases} s_x(t) = 0 \\ s_y(t) = s_0\cos\left(\int_0^t \Omega_x dt'\right) \\ s_z(t) = s_0\sin\left(\int_0^t \Omega_x dt'\right) \end{cases}, \tag{2.30}$$

The integral can be expressed as follows, using Eqs. (2.23), (2.25), (2.27),

$$\begin{aligned}
\int_0^t \Omega_x dt' &= -\frac{2\mu'\Omega}{\hbar c}\int_0^t \rho\frac{dV}{d\rho}dt' \\
&= -\frac{2\mu'\Omega}{\hbar c}\int_0^t \left[\rho_0' + a\cos(\Omega_k t + \delta)\right]\frac{k}{e}\left[\rho_0' - \rho_0 + a\cos(\Omega_k t + \delta)\right]dt' \\
&\approx \left[\frac{2\mu'}{\hbar}E(\rho_0')t - \frac{2\mu'}{\hbar}\frac{ka}{e\Omega_k}\sin(\Omega_k t + \delta)\right] \\
&= \omega t - \beta\sin(\Omega_k t + \delta),
\end{aligned} \tag{2.31}$$

in which $\rho_0' = c/\Omega$ and $a \ll \rho$ have been used. The term ωt represents a constant spin

precession of frequency

$$\omega = \frac{2\mu'}{\hbar} E(\rho'_0), \tag{2.32}$$

which is the effect of the non-zero electric field $E(\rho'_0)$ felt by the particle in its equilibrium position. The value of the spin precession frequency can be obtained requiring the electric force in the particle equilibrium position ρ'_0 to be identical to the centripetal force,

$$f_c = \frac{m\gamma c^2}{\rho'_0} = eE(\rho'_0). \tag{2.33}$$

The spin precession angle introduced in Eq. (2.3) is therefore $\Phi = \omega\bar{t}$, with $\bar{t} \approx L/c$ the time needed to traverse the crystal, L being the crystal length. Eq. 2.3 is obtained substituting Eqs.(2.32), (2.33) in the Φ definition, originally derived in [93].

The second term proportional to

$$\beta = \frac{2\mu' ka}{\hbar e \Omega_k} \tag{2.34}$$

represents an oscillating spin precession contribution with zero mean value due to the particle oscillations around its equilibrium position.

To understand the impact of the oscillating (and experimentally uncontrollable) contribution, it is useful to estimate the typical values for the physical quantities involved for the experimental layout under consideration. Taking $R \sim 10\,\mathrm{m}$ as a typical value for the crystal curvature, the revolution frequency is $\Omega \approx c/R \sim 10^7\,\mathrm{Hz}$, the oscillation amplitude is $a \sim 10^{-10}\,\mathrm{m}$, and the channel potential curvature is $k \approx 3.5 \times 10^{17}\,\mathrm{eV/cm^2}$ for a Si 110 channel[4], estimated from Table 2.1 values, yielding $\Omega_k \approx 1.8 \times 10^{13}\,\mathrm{Hz}$ for $1\,\mathrm{TeV}$ particles. A typical value for the spin precession frequency can be derived from Eqs. (2.32),(2.33), obtaining $\omega \sim 10^{10}\,\mathrm{Hz}$. Therefore, a hierarchy of frequencies $\Omega \sim 10^7\,\mathrm{Hz} \ll \omega \sim 10^{10}\,\mathrm{Hz} \ll \Omega_k \sim 10^{13}\,\mathrm{Hz}$ arise.

Taking $L \sim 10\,\mathrm{cm}$ as a typical crystal length, the constant spin precession term is at the order of $\omega L/c \approx 3\,\mathrm{rad}$. The β parameter, representing the amplitude of the oscillating contribution can be estimated remembering that for a baryon $2\mu' \sim \mu_B = \frac{e\hbar}{2mc}$ and choosing for instance the mass of the Λ_c^+ baryon $m = m(\Lambda_c^+) \approx 2.3\,\mathrm{GeV}$, resulting in $\beta \sim 3 \times 10^{-4}\,\mathrm{rad}$. This term can be therefore neglected.

Finally, the spin time evolution is [111],

$$\mathbf{s}(t) = \begin{cases} s_x(t) = 0 \\ s_y(t) = s_0 \cos(\omega t) \\ s_z(t) = s_0 \sin(\omega t) \end{cases} . \tag{2.35}$$

In presence of a non-zero EDM the spin precession is no longer confined to the yz plane, since all the $\mathbf{\Omega}$ vector components become non-zero. Given that EDMs of fundamental particles are still unobserved, it reasonable to expect any EDM effect to be tiny compared to the MDM effects, *i.e.* $d \ll (g-2)$. In other words one expects $\Omega_y, \Omega_z \ll \Omega_x$, and spin precession equations can still be obtained analytically. In this approximation and looking at Eq. (2.27) the s_y and s_z spin components evolve as in the zero EDM case ($d = 0$), with the precession determined only by the MDM, while the EDM generates an

[4] According to the harmonic approximation Eq. (2.23), the curvature of the potential k depend on the channel depth U_0 and the interplanar separation a as $k = 8U_0/a^2$.

s_x spin component otherwise not present,

$$\begin{aligned}\frac{ds_x}{dt} &= s_y\Omega_z - s_z\Omega_y \\ &= \frac{d\mu_B}{\hbar}\frac{dV}{d\rho}s_0\Big\{\sin\left[(\omega-\Omega)t\right] \\ &+ \frac{\dot\rho\rho\Omega}{c^2}\cos\left[(\omega-\Omega)t\right] - \frac{\dot\rho^2}{c^2}\sin\left[(\omega-\Omega)t\right]\Big\}. \end{aligned} \tag{2.36}$$

In Eq. (2.36) one can approximate $\omega - \Omega \approx \omega$ and neglect terms of order $\dot\rho/c$, since

$$\dot\rho = -a\Omega_k\sin(\Omega_k t+\delta) \sim a\Omega_k \sim 10^3\,\mathrm{m/s} \ll c, \tag{2.37}$$

so that it reduces to

$$\frac{ds_x}{dt} = \frac{d\mu_B}{\hbar}\left(-\frac{dV}{d\rho}\right)s_0\sin(\omega t), \tag{2.38}$$

Writing the electric field as done in Eq. 2.31,

$$E(\rho) = -dV/d\rho = -\frac{k}{e}(\rho(t)-\rho_0) = E(\rho_0') - \frac{k}{e}a\cos(\Omega_k t+\delta), \tag{2.39}$$

Eq. (2.38) can be split in two analytically integrable parts

$$s_x(t) = \frac{d\mu_B}{\hbar}s_0E(\rho_0')\int_0^t\sin(\omega t')dt' - \frac{d\mu_B}{\hbar}\frac{ka}{e}s_0\int_0^t\cos(\Omega_k t'+\delta)\sin(\omega t')dt'. \tag{2.40}$$

Substituting Eqs. (2.21),(2.32), the first integral is

$$\frac{d\mu_B}{\hbar}\frac{E(\rho_0')}{\omega}\left[1-\cos(\omega t)\right] = \frac{d}{g-2}\left[1-\cos(\omega t)\right], \tag{2.41}$$

which, in terms of the precession angle Φ, is the anticipated Eq. (2.4). The second can be decomposed into two terms proportional to $\sin(\Omega_k t')\sin(\omega t')$ and $\cos(\Omega_k t')\sin(\omega t')$, whose integrals are trigonometric functions multiplied by the factor

$$\sim \frac{d\mu_B}{\hbar}\frac{ka}{e\Omega_k} \sim \frac{d}{g-2}\beta, \tag{2.42}$$

in which the Ω_k at the denominator comes from the integration itself. The quantity β, defined in Eq. (2.34), was already seen to be order 2×10^{-4} making this contribution negligible.

The time evolution of the spin-polarisation vector in presence of a non-negligible EDM is therefore

$$\mathbf{s}(t) \;=\; \begin{cases} s_x(t) \approx s_0\dfrac{d}{g-2}\big[1-\cos(\omega t)\big] \\ s_y(t) \approx s_0\cos(\omega t) \\ s_z(t) \approx s_0\sin(\omega t)\end{cases} . \tag{2.43}$$

Summarizing, the baryon spin, initially directed along the y axis as required by the strong production, precesses in the yz (bending) plane due to the interaction of the baryon MDM; in presence of a non-zero EDM a spin component in the x direction is produced.

A comparison between spin precession analytical calculations and numerical integration of the T-BMT classical equations of motion in Monte Carlo simulation has been successfully performed [89].

2.4.2 Electric field gradients

The equations describing the particle trajectory and its spin precession in an electromagnetic field, including first-order electromagnetic field gradients, as well as a particle EDM contributions, are derived in [110]. In absence of magnetic fields the spin precession vector $\mathbf{\Omega} = \mathbf{\Omega}_{\rm MDM} + \mathbf{\Omega}_{\rm EDM} + \mathbf{\Omega}_{\rm TH}$ is

$$\begin{aligned}
\mathbf{\Omega}_{\rm MDM} &= \frac{g\mu_B}{\hbar}\left[\mathbf{E}\times\boldsymbol{\beta}\right] \\
&+ \frac{g\mu_B}{2mc}\frac{\gamma(\boldsymbol{\beta}\times\nabla)}{\gamma+1}\left[\mathbf{s}\cdot(\mathbf{E}\times\boldsymbol{\beta})\right], \\
\mathbf{\Omega}_{\rm EDM} &= \frac{d\mu_B}{\hbar}\left[\mathbf{E}-\frac{\gamma(\boldsymbol{\beta}\cdot\mathbf{E})\boldsymbol{\beta}}{\gamma+1}\right] \\
&+ \frac{d\mu_B}{2mc}\frac{\gamma(\boldsymbol{\beta}\times\nabla)}{\gamma+1}\left[\mathbf{s}\cdot\left(\mathbf{E}-\frac{\gamma\boldsymbol{\beta}(\boldsymbol{\beta}\cdot\mathbf{E})}{\gamma+1}\right)\right],
\end{aligned} \tag{2.44}$$

with unchanged Thomas precession component as in Eq. (2.18). Assuming the harmonic potential approximation Eq. (2.23), the typical magnitude of the electric field gradient is

$$\frac{d|\mathbf{E}|}{d\rho} = \frac{k}{e}, \tag{2.45}$$

and employing the values used in the previous Sec. 2.4.1, the ratio of the field gradient terms to the homogeneous field ones is estimated to be

$$\frac{\hbar\, d|\mathbf{E}|/d\rho}{2mc|\mathbf{E}|} = \frac{\hbar k\rho_0'}{2m^2\gamma c^3} \sim 2.3\times10^{-3}\,\frac{1}{\gamma}, \tag{2.46}$$

which is negligibly small in the ultra-relativistic regime considered.

When including electric field gradient effects, in absence of magnetic fields, the particle trajectory equation becomes

$$\begin{aligned}
mc\frac{d(\gamma\boldsymbol{\beta})}{dt} &= q\mathbf{E} \\
&+ \gamma^2\frac{g\mu_B}{2}\left[\nabla+\boldsymbol{\beta}\times(\boldsymbol{\beta}\times\nabla)+\frac{\boldsymbol{\beta}}{c}\frac{\partial}{\partial t}\right] \\
&\quad [\mathbf{s}\cdot(\mathbf{E}\times\boldsymbol{\beta})] \\
&+ \gamma^2\frac{d\mu_B}{2}\left[\nabla+\boldsymbol{\beta}\times(\boldsymbol{\beta}\times\nabla)+\frac{\boldsymbol{\beta}}{c}\frac{\partial}{\partial t}\right] \\
&\quad \left[\mathbf{s}\cdot\left(\mathbf{E}-\frac{\gamma\boldsymbol{\beta}(\boldsymbol{\beta}\cdot\mathbf{E})}{\gamma+1}\right)\right],
\end{aligned} \tag{2.47}$$

in which the first term is the Lorentz force and the following two terms are the MDM and EDM contributions. In the experimental setup under consideration the initial spin vector is orthogonal to $\mathbf{E}\times\boldsymbol{\beta}$, making the MDM contribution negligible. The typical

magnitude of the ratio between the EDM electric field gradient term and the Lorentz force contribution, computed similarly as for Eq. (2.46), is $\sim d\gamma \times 10^{-3}$, which can be close to 1 for $\gamma \sim 1000$ only if $d \sim 1$, that is for similar EDM and MDM magnitudes. However, we assume the EDM magnitude to be tiny with respect to the MDM one, as already assumed in the derivation of the spin equation of motion. In case of a very large EDM, this term would make the spin precession frequency dependent on the spin direction.

2.4.3 Spin precession for planar-channeled negative baryons

The spin precession time evolution derived for planar-channeled positive baryons in Sec. 2.4.1 can not be straightforwardly applied to planar-channeled negative baryons. Indeed, those equations were derived under the assumption of an harmonic electric potential which is unsuitable for crystal channels as seen by negative particles, Fig. 2.3. Nonetheless, a simple argument allows to extend the validity of the mentioned spin precession equations to the general case of a non-harmonic potential.

The derivation of the spin time evolution in Sec. 2.4.1 did not use the assumption of an harmonic potential until Eq. (2.30). The integral expressing the amount of spin precession can be approximated as

$$\int_0^t \rho \frac{dV}{d\rho} dt' \approx \rho_0' \int_0^t \frac{dV}{d\rho} dt', \tag{2.48}$$

since the radial coordinate ρ is fixed by the crystal channel up to $\delta\rho/\rho = \mathcal{O}(\text{Å}/m) = 10^{-10}$. Over a complete oscillation in the channel potential it is showed that the effect of this term is equivalent to that of the electric field in the particle equilibrium radial position ρ_0',

$$\int_0^t \frac{dV}{d\rho} dt' = -E(\rho_0')t, \tag{2.49}$$

which is determined solely by the centripetal force f_c, Eq. (2.33). This statement follows by computing

$$\int_0^t \frac{dV}{d\rho} dt' - [-E(\rho_0')t] = \int_0^t \left(\frac{dV}{d\rho} + \frac{f_c}{e} \right) dt' \tag{2.50}$$

for a complete particle oscillation. By changing the integration variable to $d\rho$ and $dt' = d\rho/\dot{\rho}$, then $\dot{\rho}$ is determined by the non-relativistic energy conservation for the radial motion of channeled particles [100]

$$W_r = \frac{1}{2} M \dot{\rho}^2 + eV(\rho) + f_c \rho, \tag{2.51}$$

as

$$\dot{\rho} = \sqrt{\frac{2}{m}} \sqrt{(W_r - f_c\rho - eV(\rho))}, \tag{2.52}$$

in which $M = m\gamma$ and W_r is the total radial energy, assumed to be constant during a particle oscillation. The relation holds because the longitudinal motion is ultra-relativistic and independent from the radial one, which is non-relativistic since the potential depth is $\mathcal{O}(100\,\text{eV}) \ll m$. The integration boundaries $\rho_{1,2}$ are chosen to be the particle oscilla-

tion limits, in which

$$\frac{1}{2}M\dot{\rho}^2 = 0 \leftrightarrow eV(\rho_{1,2}) + f_c\rho_{1,2} = W_r \ . \tag{2.53}$$

Finally, the integral can be trivially computed as

$$\begin{aligned}
&\frac{1}{e}\sqrt{\frac{m}{2}}\int_{\rho_1}^{\rho_2}\frac{e\frac{dV}{d\rho}+f_c}{\sqrt{W_r - f_c\rho - eV(\rho)}}d\rho \\
&= -\frac{1}{e}\sqrt{\frac{m}{2}}\left(\sqrt{W_r - f_c\rho_2 - eV(\rho_2)}\right. \\
&\left.-\sqrt{W_r - f_c\rho_1 - eV(\rho_1)}\right) \\
&= 0.
\end{aligned} \tag{2.54}$$

The derivation of spin precession equations for non-zero EDM hold as well, since the approximations $\dot{\rho} \ll c$ and $\beta \ll 1$ applied to obtain Eq. (2.43) are still valid also for non-harmonic potentials.

Therefore, spin precession effects due to the particle oscillation in the channel cancel out at each particle oscillation, so that the net spin precession depends uniquely on the electric field in the equilibrium position. The spin evolution equations describing MDM and EDM effects, Eq. (2.43), hold as for an harmonic planar channel potential, and in particular for the potential seen by negative particles. These equations have been successfully cross-checked against Monte Carlo simulation also for negative planarly-channeled baryons [89].

2.4.4 Axial channeling case

The phenomenon of axial channeling has been observed both for positive and negative particles, see Sec. 2.3, but it has not been considered for spin precession to date. Here the possibility to induce spin precession in axial-channeled particles for potential applications in MDM and EDM measurements of charged baryons is discussed.

The same layout of Fig. 2.1 is considered, in which the crystal is now bent along a crystallographic axis instead of a plane. Polar coordinates are introduced for the bending plane as in Eq. (2.22) and the electric field described by the axial channel potential $V(x,\rho)$ is

$$\mathbf{E} \ = \ \begin{cases} E_x = -\dfrac{dV}{dx} \\ E_y = -\dfrac{dV}{d\rho}\cos(\Omega t) \\ E_z = -\dfrac{dV}{d\rho}\sin(\Omega t) \ . \end{cases} \tag{2.55}$$

In analogy with planar-channeled particles described in Sec. 2.4.1, the longitudinal velocity is ultra-relativistic, while the velocity components orthogonal to the channel are non-relativistic; their contribution to the spin precession described in Eq. (2.18) is negligible. Accordingly, the particle velocity inside the bent crystal can be simplified as

$$\beta_x = 0, \quad \beta_y = -\sin(\Omega t) \approx 0, \quad \beta_z = \cos(\Omega t) \approx 1, \tag{2.56}$$

to a very good approximation for a typical crystal bending angle $\theta_C \sim 10$ mrad[5].

The spin evolves according to the spin precession Eq. (2.17) with precession vector $\mathbf{\Omega}$ following from Eqs. (2.18), (2.55), (2.56),

$$\mathbf{\Omega} = \begin{cases} \Omega_x = -\dfrac{2\mu'}{\hbar}\dfrac{dV}{d\rho} - \dfrac{d\mu_B}{\hbar}\dfrac{dV}{dx} \\ \Omega_y = \dfrac{2\mu'}{\hbar}\dfrac{dV}{dx} - \dfrac{d\mu_B}{\hbar}\dfrac{dV}{d\rho} \\ \Omega_z = 0\,. \end{cases} \tag{2.57}$$

The main difference with respect to the planar channeling case is the presence of the E_x electric field component, which in principle entangles the MDM and EDM induced spin rotation. Nonetheless, in the following it is shown that the contribution of the dV/dx terms can be neglected and the spin precession evolution derived for planar-channeled charged baryons applies also to axial-channeled particles.

During one oscillation in the channel potential, the particle spin can be assumed to be constant since the typical spin precession frequency $\omega = 2\mu' E(\rho_0')/\hbar \sim 10^{10}$ Hz is three orders of magnitude lower than the oscillation frequency of the particle trapped in the channel, $\Omega_k \sim 10^{13}$ Hz[6]. In the $d \ll g-2$ assumption, the two MDM-induced dominant components $\Omega_x \propto dV/d\rho$ and $\Omega_y \propto dV/dx$, describing spin precession in the yz and xz planes, respectively, can be considered to act independently of each other; namely, the spin rotation in the yz plane is not influenced by the spin rotation in the xz plane and vice versa. In this case Eq. (2.49) can be applied to both contributions: while the centripetal force induces a net spin precession in the yz plane identical to that of planarly-channeled particles, the effect of dV/dx mediates to zero over each particle oscillation, since no centripetal force acts in the x direction, *i.e.* $E_x(\rho_0') = 0$.

The limit of the assumptions is checked estimating the typical amount of spin precession accumulated during an incomplete particle oscillation, which may lead to an imperfect cancellation of the dV/dx contribution. From Eq. (2.57), this amount is at the order of

$$\Delta \approx \frac{2|\mu'|}{\hbar}\int_{\text{half}} |\mathbf{E}|dt \approx \frac{2|\mu'|}{\hbar}\frac{|\mathbf{E}|}{2\Omega_k}, \tag{2.58}$$

in which the integration is carried on one half of an oscillation. The typical electric field magnitude of the axial channel during half oscillation is estimated as the ratio between the potential depth U_0 and half of the channel width $d_p/2$ for a 110 axis aligned Si crystal, Table 2.1, yielding $|\mathbf{E}| \approx 6 \times 10^{11}\,\mathrm{eV/m}$. An estimate of the oscillation frequency Eq. (2.26), is obtained assuming the potential curvature associated to an harmonic potential $k = 8U_0/a^2 \approx 6.1 \times 10^{17}\,\mathrm{eV/cm^2}$ for $W = 1$ TeV particles, finding $\Omega_k \approx 2.3 \times 10^{13}$ Hz. Note that this frequency does not change significantly from that associated to planar channeling. Finally it is taken $2\mu' \sim \mu_B = \frac{e\hbar}{2mc}$ with the Λ_c^+ baryon mass, and the quantity Δ is found to be of order

$$\Delta \approx 1.7 \times 10^{-3}\,\mathrm{rad}. \tag{2.59}$$

Neglecting EDM effects ($d = 0$), Eqs. (2.17), (2.57) show that dV/dx modifies the s_x spin component via $ds_x/dt = -s_z\Omega_y$. Since the s_z spin component is not constant during a complete oscillation, the dV/dx contribution is not exactly zero and can be

[5]These are equivalent to the approximations $\dot{\rho} \ll c$ and $\Omega \ll \omega$ applied in the derivation of Eq. (2.43).

[6]Note that while ω depends only on the centripetal force, which is the same in case of planar and axial channeling for identical crystal curvatures, Ω_k it is expected to be even higher for negative particle axial channels since these feature more intense electric fields, see Sec. 2.3.

conservatively estimated as

$$\delta s_x \approx \frac{2\mu'}{\hbar}\int s_z(t)\frac{dV(t)}{dx}dt \lessapprox \Delta\frac{2\mu'}{\hbar}\int_{\rm half}\frac{dV(t)}{dx}dt$$
$$\lessapprox \Delta^2 \approx 2.9\times10^{-6}\,{\rm rad}. \tag{2.60}$$

in which $s_z(t) = \overline{s}_z + \delta s_z(t)$ changes by an amount of order Δ. The integrated effect along the whole crystal is conservatively estimated by multiplying δs_x by the number of particle oscillations,

$$\Delta s_x \approx \delta s_x \frac{L\Omega_k}{c} \approx 2.2\times10^{-2}\,{\rm rad}, \tag{2.61}$$

in which a crystal length of $L = 10\,{\rm cm}$ is taken. Such a component does not significantly affect the main MDM spin precession in the yz plane, so that Eq. (2.35) hold as for planarly-channeled particles. Therefore, axial channeling is suitable to measure the MDM of negative particles, and the separate measurement of particle and antiparticle MDMs, exploiting both planar and axial channeling spin precession, would allow CPT symmetry tests.

The amount of s_x spin component induced by MDM spin precession may fake a possible EDM effect: however, the conservatively estimated Δs_x has to be considered as an upper limit. For example, the effect produced for each particle oscillation may not sum coherently over all the crystal length, as assumed in the estimation. More detailed studies of the dynamics of axially-channeled particles will be needed to properly quantify Δs_x and enable EDM measurements with axial channeling spin precession.

2.5 Sensitivity study

In this section, the achievable precision on the dipole moments of heavy baryons is studied considering the experiment layout described in Sec. 2.2. Numerical values will be computed for the most abundant Λ_c^+ charm baryon.

The rate of heavy baryons B produced with 7 TeV protons colliding on a fixed target can be estimated as

$$N_B = \frac{\rm PoT}{A}\sigma(pp\to BX)N_T, \tag{2.62}$$

in which ${\rm PoT} = Ft$ is the number of protons directed to the target, equal to the product of the proton flux F times the data-taking time t, A is the beam transverse area, N_T is the number of target nucleons, and $\sigma(pp\to BX)$ is the cross-section for B production in pp interactions at $\sqrt{s} = 114.6\,{\rm GeV}$ center-of-mass energy. The number of target nucleons is

$$N_T = \frac{N_A\rho_T A T A_N}{A_T}, \tag{2.63}$$

in which N_A is the Avogadro number, ρ_T (T) is the target density (thickness) and A_T (A_N) is the atomic mass (atomic mass number). The rate of heavy baryons channeled in the bent crystal and reconstructed in the LHCb detector is estimated as

$$N_B^{\rm reco} = N_B\mathcal{B}(B\to f)\varepsilon_{\rm CH}(B)\varepsilon_{\rm DF}(B)\varepsilon_{\rm det}(B\to f), \tag{2.64}$$

in which $\mathcal{B}(B\to f)$ is the branching ratio for the baryon decay to the final state f and the decay reconstruction efficiency has been factored into channeling, decay flight and detector efficiencies. The numerical values employed for the sensitivity study are sum-

Definition	Quantity	Value	Unit
Avogadro number	N_A	6.022×10^{23}	atoms/mol
Target density (W)	ρ_T	19.25	g/cm^3
Target thickness	T	0.5	cm
Atomic mass (W)	A_T	183.84	g/mol
Atomic mass number (W)	A_N	183.84	
pp cross-section to Λ_c^+	$\sigma(pp \to \Lambda_c^+ X)$	10.8	µb
Branching fraction [24]	$\mathcal{B}\,(\Lambda_c^+ \to \Delta^{++}K^-)$	1.08%	
Lorentz boost	γ	437	
Crystal length	L	10	cm
Crystal radius	R	10	m
Channeling efficiency	$\varepsilon_{\rm CH}\,(\Lambda_c^+)$	5.5×10^{-4}	
Decay flight efficiency	$\varepsilon_{\rm DF}(\Lambda_c^+)$	2.2%	
Detector efficiency	$\varepsilon_{\rm det}(\Lambda_c^+ \to pK^-\pi^+)$	5.4%	
Λ_c^+ mass [24]	m	2286.46	MeV
Λ_c^+ lifetime [24]	τ	2.00×10^{-13}	s
Λ_c^+ polarisation	s_0	0.6	
Asymmetry parameter	$\alpha_{\Delta^{++}K^-}$	-0.67	
MDM anomaly	$(g-2)/2$	0.3	

Table 2.2: Definitions and estimated values of the relevant quantities for the Λ_c^+ charm baryon EDM and MDM sensitivity study, for a tungsten (W) target.

marized in Table 2.2.

The Λ_c^+ cross section can be estimated from the total charm production cross section per nucleon measured by the LHCb experiment in proton-helium collisions at $\sqrt{s} = 86.6\,\text{GeV}$ [112][7],

$$\sigma_{c\bar{c}} = (144 \pm 12.1_{\text{stat.}} \pm 3.5_{\text{syst.}})\ \mu\text{b}, \tag{2.65}$$

rescaled to $\sqrt{s} = 114.6\,\text{GeV}$ assuming a linear dependence on $\sqrt{s}$. By applying the Λ_c^+ average fragmentation function from LEP measurements [113], $\sigma_{\Lambda_c^+}/\sigma_{c\bar{c}} = 5.7 \pm 0.6 \pm 0.3\%$, the Λ_c^+ cross section is $\sigma_{pp\to\Lambda_c^+} \approx 10.8\,\mu\text{b}$.

The channeling efficiency of the crystal is estimated as in Eq. (2.13), using the Si 110 planar channel characteristics in Table 2.1. The typical angular divergence is $\alpha \approx 1/\gamma \approx 2.3\,\text{mrad}$ for 1 TeV Λ_c^+ baryons, the critical radius Eq. (2.10) is $R_c = 1.75\,\text{m}$, the Lindhard angle Eq. (2.6) for a straight crystal is $\theta_L = 5.66\,\mu\text{rad}$ and the straight crystal dechanneling length Eq. (2.8) is $L_d = 11.3\,\text{cm}$ using $I = 176$ eV, $a_{TF} = 0.194$Å in silicon and $e_r = 2.818\times10^{-15}\,\text{m}$ [100]. The channeling efficiency is found to be $\varepsilon_{\rm CH}(\Lambda_c^+) = 5.5\times10^{-4}$.

The fraction of Λ_c^+ baryons decaying after the crystal, *i.e.* experiencing spin precession through all the crystal length, is

$$\varepsilon_{\rm DF}(B) = \exp\left(-\frac{L}{c\tau\gamma}\right), \tag{2.66}$$

in which τ is the heavy baryon lifetime. The requirement that the baryon should have

[7] The $c\bar{c}$ cross-section reported in Ref. [112] is twice the correct one. An erratum is in preparation.

decayed after the crystal selects effectively the baryons with higher energy. For 1 TeV Λ_c^+ baryons the decay flight efficiency is $\varepsilon_{\rm DF}(\Lambda_c^+) \approx 2.2\%$, raising up to $\varepsilon_{\rm DF}(\Lambda_c^+) \approx 19\%$ for $\gamma = 1000$. Therefore, a precise assessment of this efficiency would require the knowledge of the heavy baryon energy spectrum.

The detector efficiency $\varepsilon_{\rm det}$ groups different detector-related reconstruction efficiencies. The geometrical acceptance for $\Lambda_c^+ \to pK^-\pi^+$ decaying into the LHCb detector is estimated at the order of $\varepsilon_{\rm geo} \approx 25\%$ according to simulation studies [88]. The LHCb software-based trigger for the upgraded detector [114] is expected to have an efficiency for charm hadrons comparable to the current high level trigger [115], $\varepsilon_{\rm trigger} \approx 80\%$. A specific trigger scheme for the fixed-target experiment can be adopted to enhance the trigger efficiency for Λ_c^+ decays close to 100%, based, for example, on the energy loss in an instrumented silicon crystal as exploited in the E761 experiment [96]. The tracking efficiency is estimated to be 70% per track, leading to an efficiency $\varepsilon_{\rm track} \approx 34\%$ for a Λ_c^+ decay with three charged particles. The detector reconstruction efficiency is therefore $\varepsilon_{\rm det} = \varepsilon_{\rm geo}\varepsilon_{\rm trigger}\varepsilon_{\rm track} \approx 5.4 \times 10^{-2}$.

The final polarisation of Λ_c^+ baryons can be easily measured from the angular distribution of Λ_c^+ decays to quasi-two body final states like pK^{*0}, $\Delta^{++}\pi^-$, or $\Lambda(1520)\pi^+$, which is described by Eq. (2.5). This way, the polarisation along a given axis $\hat{\boldsymbol{\imath}}$ can be extracted by means of a fit to the $\cos\theta_i = \hat{\boldsymbol{\imath}} \cdot \hat{\boldsymbol{k}}$ distribution,

$$\frac{dN}{d\cos\theta_i} = \frac{1}{2}(1 + A_i \cos\theta_i), \tag{2.67}$$

in which $A_i = \alpha_f s_x$. The asymmetry parameters a_f for the mentioned final states can be computed from the $\Lambda_c^+ \to pK^-\pi^+$ amplitude analysis performed by the E791 experiment [71] as described in Ref. [88]. In the following the $\Lambda_c^+ \to \Delta^{++}K^-$ decay will be considered, for which $\alpha_{\Delta^{++}K^-} = -0.67 \pm 0.30$.

For the sensitivity study $s_0 = 0.6$ and $(g-2)/2 = 0.3$ are assumed for the Λ_c^+ baryon, as inspired by the experimental results and the available theoretical predictions, respectively, reported in Secs. 2.1, 2.2. The d and $g-2$ values can be obtained inverting Eqs. (2.3), (2.4), as

$$\begin{aligned} d &\approx \frac{(g-2)A_x}{\alpha s_0 \left(\cos\Phi - 1\right)}, \\ g-2 &\approx \frac{2}{\gamma\theta_C} \arccos\left(\frac{A_y}{\alpha s_0}\right) \\ &\approx \frac{2}{\gamma\theta_C} \arcsin\left(\frac{A_z}{\alpha s_0}\right), \end{aligned} \tag{2.68}$$

From linear fit properties, the statistical uncertainty on the fitted A_i values is

$$\sigma_{A_i} = \sqrt{\frac{1 - A_i^2}{N^2}} \approx \frac{1}{\sqrt{N}}, \tag{2.69}$$

in the $A_x \ll 1$ limit. Thus, the main contribution to the statistical uncertainty on d and g

can be estimated as

$$\begin{aligned}\sigma_d &\approx \frac{g-2}{\alpha s_0 \left(\cos\Phi - 1\right)} \frac{1}{\sqrt{N^{\rm reco}_{\Lambda_c^+}}},\\ \sigma_g &\approx \frac{2}{\alpha s_0 \gamma \theta_C} \frac{1}{\sqrt{N^{\rm reco}_{\Lambda_c^+}}}.\end{aligned} \tag{2.70}$$

Negligibly small uncertainties on θ_C, γ and the initial Λ_c^+ polarisation s_0 are assumed, the latter to be measured with large samples of non-channeled Λ_c^+ decays.

According to Ref. [94], the proton flux which can be directed on the target-crystal device can be up to $F = 10^7 p/\,\mathrm{s}$. Assuming a data-taking time compatible with a dedicated run of the LHCb experiment of one month, one can obtain $\approx 2.6 \times 10^{13}$ PoT. From these collisions, ≈ 12 channeled Λ_c^+ baryons can be recorded, enough for a proof-of-principle test of the experimental layout but not for a dipole moment measurement.

Nonetheless, such a proton flux may be compatible with a longer data-taking run concurrent with the LHCb proton-proton collision program. Assuming a two-year effective data-taking with the same proton flux, $\approx 6.2 \times 10^{14}$ PoT can be obtained, corresponding to ≈ 290 channeled Λ_c^+ baryons, leading to precisions on the gyromagnetic and gyroelectric factors of order

$$\sigma_g \approx 4\%, \qquad\qquad \sigma_d \approx 8\%. \tag{2.71}$$

The precision on the Λ_c^+ baryon EDM would be at $\sigma_\delta \approx 1.8 \times 10^{-16} e\,\mathrm{cm}$ level. Better precisions could be reached with a future dedicated experiment for fixed-target physics, allowing for higher proton flux and better reconstruction efficiency.

A more precise sensitivity study should take into account the energy spectrum and the angular distribution of the produced baryons, which would also allow to optimise the crystal length and curvature according to the best precision on the dipole moments. Moreover, a detailed amplitude model of the $\Lambda_c^+ \to pK^-\pi^+$ decay would allow to achieve the best precision on the Λ_c^+ polarisation and to employ all the $\Lambda_c^+ \to pK^-\pi^+$ decays. A better precision is therefore expected with respect to the presented estimates.

Compared to charm baryons, beauty baryons feature lower production cross-sections, lower branching fractions (because they have more final states available), lower reconstruction efficiencies (because of the cascade decays leading to more final state particles) but higher lifetimes. Sensitivity studies based on the $\overline{\Xi}_b^+$ baryon, which is the lightest charged beauty baryon stable under strong interaction, show that the achievable precision on beauty baryon dipole moments is two orders of magnitude worse than for charm baryons [89].

2.6 Conclusions

A proposal to measure the dipole moments of heavy baryons using bent crystals at the LHC has been presented. Previous proposals regarding the measurement of charm baryon magnetic dipole moments have been extended to the even more interesting case of EDM measurements, which are powerful probes for new physics, deriving the spin precession equations for planarly-channeled positive baryons in bent crystals for non-zero EDM. The same equations have been shown to be valid also for negative baryons channeled in both planar and axial configuration, opening the possibility to perform

CPT tests by comparing baryon and antibaryon MDMs. Sensitivity studies have been performed considering a realistic experimental layout, in which protons extracted from the main LHC beam are directed onto a target-bent crystal device placed in front of the LHCb detector, which is used to reconstruct the heavy baryon decays. A dedicated run of one month would allow a proof-of-principle of the measurement, while an extended data-taking concurrent with the proton-proton collision program would be able to measure Λ_c^+ baryon gyromagnetic factor at $\sigma_g \approx 4\%$ precision, which would allow to effectively discriminate among different charm baryon models. The attainable Λ_c^+ baryon EDM limit would be at the $10^{-16} e\,\mathrm{cm}$ level, already able to challenge the current charm EDM indirect limits. The expected number of beauty baryons is too low for an interesting measurement of their dipole moments in the proposed setup, however, beauty baryons can be interesting in light of a possible dedicated fixed-target experiment able to run at higher proton flux intensities.

CHAPTER 3

τ lepton electromagnetic dipole moments proposal

3.1 Motivation

The measurement of the τ lepton electromagnetic dipole moments is extremely interesting since, for a third generation elementary particle, both electric and magnetic DMs are probes for physics beyond the SM. For instance, the anomalous MDM of the electron has provided an extremely accurate test of quantum electrodynamics, while that of the muon is contrasting with SM predictions with a statistical significance of about 3.6 standard deviations [22]. Moreover, new physics effects can be naively expected to be enhanced with increasing particle masses: the electroweak corrections to dipole moments are proportional to m_τ^2/Λ^2, in which m_τ is the τ mass and Λ a new physics energy scale, leading to an $m_\tau^2/m_e^2 \sim 10^7$ and $m_\tau^2/m_\mu^2 \sim 3 \times 10^2$ relative enhancement of new physics effects compared to the electron and muon, respectively [116,117]. In the SM, the τ anomalous MDM is expected to be $a = (g-2)/2 \approx 10^{-3}$ [116], along with a practically negligible EDM.

Indirect estimates of the τ MDM have been extracted from the comparison between precise measurements of $\tau^+\tau^-$ pair production cross sections in e^+e^- annihilation and theoretical predictions. As of today, a is experimentally known at few percent level [24, 118], more than one order of magnitude above the SM prediction. Similarly, τ EDM indirect limits have been derived from the quadratic dependence of $\tau^+\tau^-$ cross sections on the CP-violating EDM form factor [117], leading to indirect limits at $10^{-16}\ e\,\mathrm{cm}$ level [119].

The direct measurement of the τ lepton electromagnetic dipole moments has never been performed because of the τ short lifetime $\approx 3 \times 10^{-13}\,\mathrm{s}$, posing similar problems to the measurement of heavy baryons dipole moments. Indeed, the τ mass and lifetime are similar to charm baryons typical ones, and, contrarily to the lighter leptons, the τ decays to hadronic final-states with large branching fractions. However, there are two critical problems to be overcome in order to apply the experimental setup devised for heavy baryons dipole moments measurement.

One problem is that the direct production of $\tau^+\tau^-$ pairs in proton-nucleon collisions is an electromagnetic process, which is expected to be much suppressed with respect to the strong interaction mediated charm baryon production cross-section Eq. (2.65). Much larger samples of τ leptons can be therefore obtained from decays of charm mesons, mostly from the $D_s^+ \to \tau^+\nu_\tau$ decay. However, the almost complete polarisation along the τ momentum produced in the weak decay mediates to zero in the laboratory reference frame, since a spin-zero meson decay is isotropic. An additional complication with respect to the heavy baryon case is that, for conservation of the lepton flavour number, at least one undetectable neutrino is produced in the τ decay. Therefore it is not possi-

ble to completely reconstruct the decay angular distribution from detectable final state particles.

In the following, it is shown how the experimental setup proposed for the measurement of heavy baryons electromagnetic dipole moments can be adapted to select τ^+ leptons with non-zero polarisation, along with a novel method to extract the τ^+ polarisation from partially reconstructed hadronic decays. Spin precession equations and sensitivity studies for the measurement of τ^+ dipole moments are also presented. This work has been published in Physical Review Letters, Ref. [120].

3.2 Kinematic selection of τ^+ polarisation

The spin-polarisation vector of the τ^+ in its rest frame can be determined from the squared decay amplitude of the $D_s^+ \to \tau^+\nu_\tau$ decay. Summing over the neutrino spin states and considering that the ν_τ is massless and unobserved [121],

$$|\overline{\mathcal{M}}|^2 = \frac{g^4}{8m_W^4}|V_{cs}|^2 f_{D_s}^2 m_\tau^2 \left(p\cdot k - m_\tau a\cdot k\right), \tag{3.1}$$

in which $g = e/\sin\theta_W$, with θ_W the electroweak mixing angle, m_W the W boson mass, V_{cs} the Cabibbo-Kobayashi-Maskawa matrix element, f_{D_s} the D_s^+ decay constant, p (k) the 4-momentum of the τ^+ (ν_τ), and a^μ the τ^+ spin 4-pseudovector vector. In the τ^+ rest frame, $a^\mu = (0, \boldsymbol{s})$. Evaluating Eq. (3.1) in the τ^+ rest frame, and neglecting constant terms one obtains

$$p\cdot k - m_\tau a\cdot k = \omega\left(1 + \boldsymbol{s}\cdot\hat{\mathbf{q}}'\right), \tag{3.2}$$

in which $\omega = (m_{D_s}^2 - m_\tau^2)/2$ and $\hat{\mathbf{q}}'$ is the unit vector along the D_s^+ momentum in the τ^+ rest frame. Therefore the τ^+ spin-polarisation vector is directed along the D_s^+ direction as seen from its rest frame. Expressed in terms of laboratory frame momenta, Eq. (3.2) becomes

$$\boldsymbol{s} = \hat{\mathbf{q}}' = \frac{1}{\omega}\left(m_\tau\mathbf{q} - q_0\mathbf{p} + \frac{\mathbf{q}\cdot\mathbf{p}}{p_0 + m_\tau}\mathbf{p}\right). \tag{3.3}$$

When evaluated in the D_s^+ rest frame, Eq. (3.2) leads to $\mathbf{s} = -\hat{\mathbf{p}}^\star$, *i.e.* that the τ^+ has negative helicity in the D_s^+ rest frame, as expected from the structure of charged weak current interactions and angular momentum conservation.

The decay of a spin-zero meson is isotropic for rotational invariance, implying that to obtain a non-zero τ^+ mean polarisation in the laboratory frame kinematic requirements must be applied. This is not trivial since undetectable neutrinos characterise both production and decay of the τ^+ lepton. The problem is solved exploiting the narrow angular acceptance of the channeling condition for ultra-relativistic particles: a longitudinal negative polarisation (along the crystal z axis, with the crystal coordinate frame defined as in Fig. 2.1), $s_z \approx \beta^\star/\beta \approx -0.10$, is induced by the larger acceptance for forward emitted τ^+ with respect to the backward direction, since the first have larger Lorentz boost and narrower angular spread. Here β ($\beta^\star$) indicates the velocity of the D_s^+ (τ^+) in the laboratory (D_s^+ rest) frame. The s_z polarisation can be enhanced by applying kinematic selection criteria to further increase the population of forward emitted τ^+ leptons, *e.g.* selecting τ^+ decays with large momentum of the detectable final particle system.

A large transverse (along the crystal y axis) $s_y \geq 50\%$ polarisation can be obtained by considering $D_s^+ \to \tau^+\nu_\tau$ decays in which the D_s^+ meson decays after channeling through a first bent crystal and τ^+ leptons are channeled through a second bent crystal, tilted with respect to the first one. This way the angle between D_s^+ and τ^+ momenta

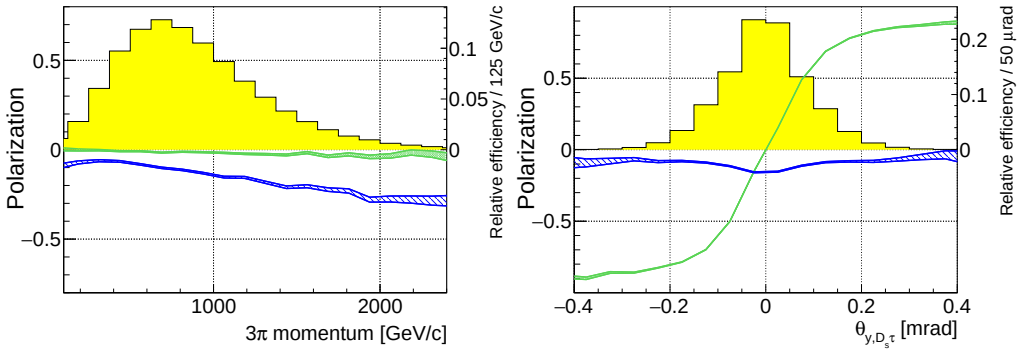

Figure 3.1: from Ref. [120]. Spin-polarisation along the (blue) z and (green) y axes as a function of (left) the momentum of the 3π system and (right) the $\theta_{y,D_s\tau}$ angle. The coloured bands represent one-standard deviation regions arising from the limited simulation statistics. The yellow histograms show the spectra of the signal (channeled) τ^+ leptons, normalized to unity. The polarisation along x, not shown, is consistent with zero.

is constrained, but at the price of a much lower efficiency mainly due to the double channeling requirements. This two crystal scheme was also proposed in Ref. [122].

Considering the laboratory and crystal reference frames defined for the heavy baryon experiment case, Fig. 2.1, with the crystal tilted by an angle $\theta_y \approx 100\,\mu\text{rad}$ in the bending plane yz with respect to the proton beam, the projections of the polarisation vector are

$$\begin{aligned} s_{0,x} &\approx \frac{m_\tau\,|\mathbf{q}|}{\omega}\theta_{x,D_s\tau}, \\ s_{0,y} &\approx \frac{m_\tau\,|\mathbf{q}|}{\omega}\theta_{y,D_s\tau}, \\ s_{0,z} &\approx s_{0,\parallel} = \frac{1}{\omega}\left(|\mathbf{q}|\,p_0 - q_0\,|\mathbf{p}|\right), \end{aligned} \tag{3.4}$$

in which $s_{0,\parallel}$ is the spin projection along the τ^+ direction (longitudinal polarisation, $\mathbf{s}\cdot\hat{\mathbf{p}}$), $\theta_{D_s\tau}$ is the angle between the D_s^+ meson and the τ^+ lepton in the laboratory frame, and $\theta_{y,D_s\tau}$ ($\theta_{x,D_s\tau}$) its projection along the crystal y (x) axis. All angles are small, $\mathcal{O}(\,\text{mrad})$, due to the highly boosted D_s^+ mesons produced by the multi-TeV protons and the low Q-value of the $D_s^+ \to \tau^+\nu_\tau$ decay. Rotational invariance in the τ^+ production and the fact that $\theta_{x,D_s\tau}$ is unconstrained in planar channeling implies that s_x averages to zero, whereas s_z and s_y depend on momenta and $\theta_{y,D_s\tau}$, respectively.

The τ^+ polarisation is studied by exploiting large samples of simulated $D_s^+ \to \tau^+\nu_\tau$, $\tau^+ \to \pi^+\pi^-\pi^+\bar{\nu}_\tau$ events from 7 TeV proton collisions on protons at rest, generated using PYTHIA [123], EVTGEN [124], and a fast simulation that generates phase-space kinematics of the D_s^+ and τ^+ decays. The τ^+ planar channeling has been simulated using a parametrization based on the current theoretical description described in Sec. 2.3. Here, a $L = 8\,\text{cm}$ length, $\theta_C = 16\,\text{mrad}$ bent germanium crystal tilted by $\theta_y = 0.1\,\text{mrad}$, placed $L_{\text{tar}} = 8\,\text{cm}$ downstream of a $T = 1\,\text{cm}$ thick tungsten target, has been taken, following from the sensitivity study described later in Sec. 3.5. Fig. 3.1, shows the dependence of the selected τ^+ polarisation as a function of (left) the momentum of the 3π system, highly correlated with the τ^+ momentum itself, and (right) the $\theta_{y,D_s\tau}$ angle.

The initial τ^+ polarisation can be accurately determined by reconstructing unchan-

neled τ^+ decays with kinematic properties similar to the signal or using simulated decays calibrated with data samples, provided that an accurate description of the experimental setup is available.

3.3 Spin precession equations

The spin-polarisation precession induced by the interaction of the MDM and EDM of a relativistic, positive particle planarly channeled in a bent crystal was derived in Sec. 2.4.1 under the hypothesis that for a composite particle the anomalous MDM is order 1. This is not the case for the τ^+ lepton, for which $a \approx 10^{-3}$, and the term

$$\frac{1}{\gamma+1}\frac{2\mu_B}{\hbar}\left(\mathbf{E}\times\boldsymbol{\beta}\right) \tag{3.5}$$

in Eq. (2.20) can be no longer neglected even for $\gamma \approx 1000$, since the other MDM contribution is proportional to a. This term contributes to the spin precession in the yz bending plane independently of the anomalous MDM of the particle. In absence of a τ^+ EDM, the precession angle becomes

$$\Phi \approx \left(\frac{g-2}{2}+\frac{1}{\gamma+1}\right)\gamma\theta_C, \tag{3.6}$$

with unchanged precession equation Eq. (2.35) for transverse initial polarisation. For longitudinal initial polarisation the spin precession equation is

$$\mathbf{s}(t) \;=\; \begin{cases} s_x(t) = 0 \\ s_y(t) = -s_0\sin(\omega t) \\ s_z(t) = s_0\cos(\omega t) \end{cases} . \tag{3.7}$$

For non-zero EDM, the assumption $d \ll g-2$ may be still valid, leading to analogous equations as for heavy baryons. Nonetheless, a more refined analytical calculation has been performed for the case in which MDM and EDM effects have comparable magnitudes, for both transverse and longitudinal initial polarisation [120].

The spin rotation for longitudinal initial polarisation, $\boldsymbol{s}_0 = (0,0,s_{0,z})$, is

$$\begin{aligned}
\frac{s_x}{s_{0,z}} &\approx \frac{d'}{a'_d}\left[-c\sin\Phi+\frac{a'}{a'_d}s\left(1-\cos\Phi\right)\right] \approx -\frac{d'}{a'_d}\sin\Phi, \\
\frac{s_y}{s_{0,z}} &\approx \frac{a'}{a'_d}\left[\sin\Phi+\frac{{d'}^2}{a'_d a'}sc\left(1-\cos\Phi\right)\right] \approx \frac{a'}{a'_d}\sin\Phi, \\
\frac{s_z}{s_{0,z}} &\approx \frac{{a'}^2}{{a'_d}^2}\left[\left(1+\frac{{d'}^2}{{a'}^2}c^2\right)\cos\Phi+\frac{{d'}^2}{{a'}^2}s^2\right] \approx \cos\Phi,
\end{aligned} \tag{3.8}$$

in which

$$a' = \frac{g-2}{2}+\frac{1}{1+\gamma}, \tag{3.9}$$

$d' = d/2$, $a'_d = \sqrt{{a'}^2+{d'}^2}$, and $\Phi = \gamma\theta_C a'_d$ is the precession angle. The coefficients s and c are given by $\sin(\Omega t)$ and $\cos(\Omega t)$, respectively, in which $\Omega t \approx c/R \times L/c = \theta_C \sim 10^{-2}\,\mathrm{rad}$ is the average rotation angle of the particle trajectory when traversing the bent crystal

with revolution frequency Ω in a time interval t (see definitions in Sec. 2.4.1). For each component, the first expression holds at precision $\mathcal{O}(10^{-5})$, whereas the second approximation applies at $\mathcal{O}(10^{-2})$. Similarly, the spin motion for transverse initial polarisation, $\boldsymbol{s}_0 = (0, s_{0,y}, 0)$, is given by

$$\begin{aligned}
\frac{s_x}{s_{0,y}} &\approx \frac{d'}{a'_d}\left[\frac{a'}{a'_d}c\,(1-\cos\Phi) + s\sin\Phi\right] \approx \frac{d'a'}{{a'_d}^2}\,(1-\cos\Phi)\,,\\
\frac{s_y}{s_{0,y}} &\approx \frac{{a'}^2}{{a'_d}^2}\left[\frac{{d'}^2}{{a'}^2}c^2 + \left(1+\frac{{d'}^2}{{a'}^2}s^2\right)\cos\Phi\right] \approx \frac{{d'}^2}{{a'_d}^2} + \frac{{a'}^2}{{a'_d}^2}\cos\Phi,\\
\frac{s_z}{s_{0,y}} &\approx \frac{a'}{a'_d}\left[-\sin\Phi + \frac{{d'}^2}{a'_d a'}sc\,(1-\cos\Phi)\right] \approx -\frac{a'}{a'_d}\sin\Phi,
\end{aligned} \tag{3.10}$$

which, in the limit $g-2 \gg 1/\gamma, d$, reduces to the expression obtained for heavy baryons, Eq. (2.43).

3.4 Polarisation extraction from partially reconstructed decays

A novel analysis technique based on multivariate classifiers using reconstructed kinematic variables of the τ^+ decays is employed to determine the rotation of the τ^+ spin-polarisation vector. In the following, the $\tau^+ \to \pi^+\pi^-\pi^+\bar{\nu}_\tau$ is considered because of its favourable features compared to other τ^+ final states: one single undetectable neutrino, a measurable decay vertex defined by the three hadron tracks and a large branching fraction of $(9.31 \pm 0.05)\%$ [24].

The optimal polarisation extraction technique for τ leptons exploited for LEP experiments [125], cannot be directly applied in this case because the τ^+ energy is not known. Indeed, at the e^+e^- LEP collider $\tau^+\tau^-$ pairs were produced from Z^0 decays, the τ^+ energy being $E_\tau = \sqrt{s}/2 \approx m(Z^0)/2$ from energy conservation, while in proton-nucleus collisions the centre-of-mass energy of the parton-parton collision is unknown. Therefore, the angles between the 3π system and the crystal axes in the τ^+ rest frame are not precisely determined, and it is not possible to easily relate the τ^+ polarisation with the decay angular distribution. A novel technique is explored to extract the τ^+ polarisation, in which the theoretical decay distribution is replaced by multivariate classifiers taking into account the uncertainties related to the imperfect reconstruction of the decay, without need of an explicit parametrisation of partial reconstruction effects.

For each crystal axis, a classifier discriminating τ^+ full polarisation between positive and negative axis direction is built. It is trained on simulated $\tau^+ \to \pi^+\pi^-\pi^+\bar{\nu}_\tau$ decays of channeled τ^+ passing the selection requirements described in Sec. 3.2, in which full ± 1 τ^+ polarisation is set in turn along the crystal axes. The discrimination is based on the variables describing the $\tau^+ \to \pi^+\pi^-\pi^+\bar{\nu}_\tau$ decay distribution, referred hereafter with the symbol $\boldsymbol{\zeta}$: the angle between the 3π system and the polarisation direction in the τ^+ rest frame, two- and three-pion invariant masses and the angles describing the 3π decay plane orientation in the 3π helicity frame reached from the τ^+ rest frame[1]. For the determination of an approximate τ^+ rest frame, the τ^+ momentum magnitude is estimated taking the mean expected value in bins of the 3π momentum magnitude and angle formed with the τ^+ decay direction. In absence of the undetectable τ^+ production

[1] It is the coordinate frame in which the z axis coincides with the 3π momentum expressed in the τ^+ rest frame.

vertex, the τ^+ momentum direction is assumed to be that connecting the D_s^+ production vertex and the τ^+ decay vertex, following the curvature of the crystal channeling plane. The vertex positions are smeared according to Gaussian distributions to mimic experimental resolutions, assumed to be 13 μm and 70 μm for D_s^+ production vertices in the longitudinal and transverse directions with respect to the beam, respectively, 100 μm and 1 mm for τ^+ decay vertices. These values have been taken from the LHCb VELO detector performances [126], in which primary pp collision vertices resolutions have been chosen for the D_s^+ production vertices, while VELO decay vertices resolutions have been multiplied by a factor 5 to mimic the larger uncertainties in the reconstruction of very boosted τ^+ decays.

The polarisation component s_i is extracted by fitting the classifier distribution $\mathcal{W}_i(\eta)$, in which $\eta \equiv \eta(\boldsymbol{\zeta})$ is the classifier response, with templates representing the response distributions $\mathcal{W}_i^{\pm}(\eta)$ for $s_i = \pm 1$ polarisations,

$$\begin{aligned}\mathcal{W}_i(\eta) &= \frac{1+s_i}{2}\mathcal{W}_i^+(\eta) + \frac{1-s_i}{2}\mathcal{W}_i^-(\eta) \\ &= \frac{\mathcal{W}_i^+(\eta)+\mathcal{W}_i^-(\eta)}{2} + s_i\frac{\mathcal{W}_i^+(\eta)-\mathcal{W}_i^-(\eta)}{2}.\end{aligned} \tag{3.11}$$

The statistical separation between templates, measuring the ability of the classifier to discriminate between opposite polarisations, also represents the squared average event Fisher information [125] or sensitivity to the polarisation (at $s_i = 0$) from maximum-likelihood fits,

$$S_i^2 = \frac{1}{N\sigma_i^2} = \left\langle \left(\frac{\mathcal{W}_i^+(\eta) - \mathcal{W}_i^-(\eta)}{\mathcal{W}_i^+(\eta) + \mathcal{W}_i^-(\eta)} \right)^2 \right\rangle, \tag{3.12}$$

in which σ_i is the statistical uncertainty on s_i.

The polarisation vector is obtained fitting independently each polarisation component from the three classifier responses. The method is tested on simulated channeled τ^+ decays passing the selection requirements, with τ^+ polarisation as produced by the $D_s^+ \to \tau^+\nu_\tau$ decay, and compared against the analytical result, retrieving compatible polarisation values. The template fits for the case of longitudinal polarisation generated with a single bent crystal, for Multilayer Perceptron Networks classifiers are shown in Fig. 3.2. Negligible differences are seen using either Multilayer Perceptron Networks or Boosted Decision Trees [127] classifiers. The precision loss on the polarisation components due to partial reconstruction can be estimated from the average event information associated to the template fits, Eq. (3.12), compared to the ideal value of 0.58 reached in case the complete kinematics of the τ^+ decay is reconstructed [125]. The average event information values are $S_x \approx S_y \approx 0.42$ and $S_z \approx 0.23$, corresponding to an increase of statistical uncertainies of a factor ≈ 1.4 for x, y polarisation components and a factor ≈ 2.5 for the s_z component.

Studies with variants of the τ^+ rest frame reconstruction algorithm, including the one proposed in Ref. [128], show that the angle between the 3π system and the z axis in the τ^+ rest frame is very sensitive to the estimation of the τ^+ momentum, this leading to significantly different distribution between true and reconstructed values. On the contrary, the angles between the 3π system and the x, y axes in the τ^+ rest frame are basically independent on the τ^+ momentum. This behaviour is a consequence of the large τ^+ Lorentz boost in the z direction, and it explains the lower precision on the s_z polarisation component observed.

Summarising, it has been shown that this method is able to measure the τ^+ polarisa-

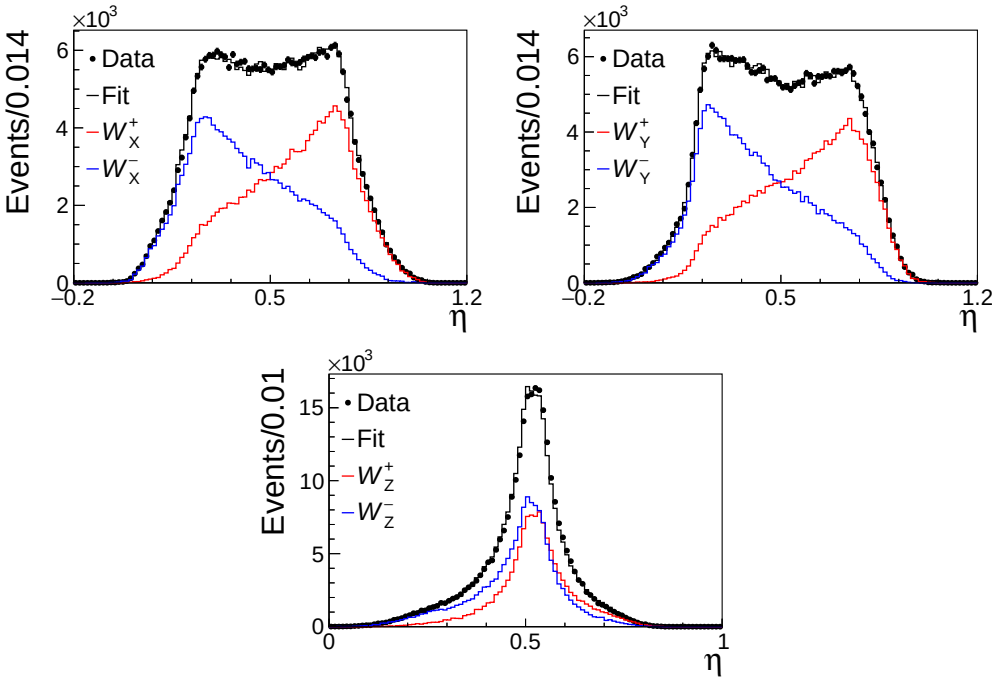

Figure 3.2: Template fit to Multilayer Perceptron Networks responses on simulated events for (top left) x, (top right) y and (bottom) z components, for longitudinal polarisation generated by a single bent crystal.

tion from measurable quantities of its decay distribution, without the need of an explicit parametrisation of the detector response and partial reconstruction effects, since differences in the reconstructed τ^+ decay distributions between polarisation states are learned by the classifiers from simulated decays. Therefore, a sufficiently accurate simulation (as compared to the expected τ^+ dipole moments uncertainties) of the experimental setup and of the $\tau^+ \to \pi^+\pi^-\pi^+\bar{\nu}_\tau$ decay is needed to apply this technique.

3.5 Sensitivity study

The vast majority of τ^+ leptons produced in proton-nucleon interactions at $\approx 115\,\text{GeV}$ centre-of-mass energy comes from $D_s^+ \to \tau^+\nu_\tau$ decays. The corresponding cross section is estimated to be $\sigma[pp \to D_s^+(\to \tau^+\nu_\tau)X] \approx 0.98\,\mu\text{b}$ using the following inputs: the total charm production cross section measured by LHCb in proton-helium collisions at $\sqrt{s} = 86.6\,\text{GeV}$ [112], Eq. (2.65), rescaled to $\sqrt{s} = 114.6\,\text{GeV}$ assuming a linear dependence on $\sqrt{s}$, the fragmentation fraction $f(c \to D_s^+) = (9.25 \pm 0.82)\%$ [113], and the branching fraction $\mathcal{B}(D_s^+ \to \tau^+\nu_\tau) = (5.55 \pm 0.24)\%$ [24].

The rate of τ^+ leptons produced with 7 TeV protons on a fixed target can be estimated as done for heavy baryons, Eqs. (2.62), (2.63),

$$N_{\tau^+} = \frac{\text{PoT}}{A}\sigma[pp \to D_s^+(\to \tau^+\nu_\tau)X]N_T, \tag{3.13}$$

while those reconstructed by the experimental setup can be expressed as in Eq. (2.64),

$$N_{\tau^+}^{\text{reco}} = N_{\tau^+}\mathcal{B}(\tau^+ \to \pi^+\pi^-\pi^+\bar{\nu}_\tau)\varepsilon_{\text{CH}}(\tau^+)\varepsilon_{\text{DF}}(D_s^+, \tau^+)\varepsilon_{\text{det}}. \tag{3.14}$$

Here, $\varepsilon_{\text{DF}}(D_s^+, \tau^+)$ includes both D_s^+ and τ^+ decay flight requirements, *i.e.* that the τ^+ lepton is produced before the crystal and decays after channeling through the whole crystal length.

The largely dominant contribution to the statistical uncertainty on a and d can be estimated from Eqs. (3.8) and (3.10). For small Φ (as $\gamma\theta_C \sim 10$ and $a'_d \sim 10^{-3}$) and longitudinal initial polarisation,

$$\sigma_a \approx \frac{1}{S_y s_{0,z}\gamma\theta_C}\frac{1}{\sqrt{N_{\tau^+}^{\text{reco}}}}, \quad \sigma_d \approx \frac{2}{S_x s_{0,z}\gamma\theta_C}\frac{1}{\sqrt{N_{\tau^+}^{\text{reco}}}}, \tag{3.15}$$

in which S_i is the average event information obtained in Sec. 3.4. Negligibly small uncertainties on θ_C, γ and s_0, are assumed. Analogously, for transverse initial polarisation,

$$\sigma_a \approx \frac{1}{S_z s_{0,y}\gamma\theta_C}\frac{1}{\sqrt{N_{\tau^+}^{\text{reco}}}}, \quad \sigma_d \approx \frac{2}{S_x s_{0,y}(\gamma\theta_C)^2 a'}\frac{1}{\sqrt{N_{\tau^+}^{\text{reco}}}}. \tag{3.16}$$

For given γ, $N_{\tau^+}^{\text{reco}}$, initial polarisation and average event information along the three axes, the sensitivities are similar except for d from transverse polarisation, which has a relative ~ 10 suppression factor, which comes from the quadratic dependence on Φ in Eq. (3.10).

An optimization of the single bent crystal configuration (initial longitudinal polarisation) has been performed to minimise the statistical uncertainty on the τ^+ dipole moments, using the simulation described in Sec. 3.2. The optimal crystal values have been found to be $\theta_C = 16\,\text{mrad}$ and $L = 8\ \text{cm}$ for a germanium crystal; moreover minimal uncertainties are found for channeled events satisfying $p_{3\pi} > 800\,\text{GeV}/c$ (more details in

Definition	Quantity	Value	Unit
Target thickness	T	2.5	cm
pp cross-section to $D_s^+(\to \tau^+\nu_\tau)$	$\sigma[pp \to D_s^+(\to \tau^+\nu_\tau)X]$	0.98	µb
Branching fraction [24]	$\mathcal{B}\,(\tau^+ \to \pi^+\pi^-\pi^+\bar{\nu}_\tau)$	9.31%	
τ mass [24]	m	1776.86	MeV
Crystal length	L	8	cm
Crystal curvature	θ_C	16	mrad
3π momentum cut	$p_{3\pi}$	> 800	GeV/c
Average Lorentz boost	γ	775	
Initial z polarisation	$s_{0,z}$	-0.178	
Combined channeling and decay flight efficiency	$\varepsilon_{\rm CH}(\tau^+)\varepsilon_{\rm DF}(D_s^+,\tau^+)$	7.68×10^{-6}	
Detector efficiency	$\varepsilon_{\rm det}$	40%	

Table 3.1: Values employed for the τ^+ lepton EDM and MDM sensitivity study.

Ref. [120]).

For germanium crystal with optimal parameters, a longitudinal polarisation $s_{0,z} = -0.178$, a combined channeling and decay flight efficiency $\varepsilon_{\rm CH}(\tau^+)\varepsilon_{\rm DF}(D_s^+,\tau^+) = 7.68\times 10^{-6}$ and average Lorentz boost $\gamma = 775$ are obtained. Germanium crystals provide enhanced channeling efficiency over silicon ones, featuring higher potential walls thanks to the higher Z nucleus charge, while keeping identical polarimeter characteristics. A reconstruction efficiency of 40% is assumed for a detector dedicated to fixed-target events.

Using the quantities summarised in Table 3.1, Eqs. (3.13), (3.14) and assuming a dataset of 10^{17} PoT, about 8.1×10^5 fully channeled $\tau^+ \to \pi^+\pi^-\pi^+\bar{\nu}_\tau$ decays can be reconstructed. From Eqs. (3.15), (3.16), a statistical uncertainty on the anomalous τ^+ MDM of 1.2×10^{-3} can be obtained, sufficient to test SM predictions. A precision on the gyroelectric factor of $\sigma_d = 2.4\times 10^{-3}$, corresponding to a τ^+ EDM at $\sigma_\delta \approx 6.5\times 10^{-18} e\,\text{cm}$ is achievable.

More refined estimates have been obtained in Ref. [120], in which a and d sensitivities are assessed from a large number of pseudo-experiments generated and fit using a probability density function based on the spin precession equation of motion and angular distributions proportional to $1 + S_i s_i \hat{k}_i$, in which $\hat{\mathbf{k}}$ is the τ^+ direction in the D_s^+ helicity frame. This method provides uncertainties about a factor two larger than those obtained analytically.

3.6 Conclusions

A novel method for the direct measurement of the τ^+ electromagnetic dipole moments has been presented with interesting perspective for a stringent test of the SM and search of new physics. The experimental setup for the proposed measurement of heavy baryons dipole moments using bent crystals can be applied also for τ^+ leptons produced from charm meson decays, in which a non-zero polarisation is produced by the kinematic selection required by the channeling condition. Spin precession equations have been derived for the case of small ($\approx 10^{-3}$) anomalous MDM. A novel technique based on multivariate classifiers has been tested to measure the τ^+ polarisation from measured

distributions of the partially reconstructed $\tau^+ \to \pi^+\pi^-\pi^+\bar{\nu}_\tau$ decay. A sensitivity study is performed considering a single bent crystal setup with a detector dedicated to fixed-target collisions. The SM prediction for the τ^+ anomalous MDM is shown to be experimentally testable with a statistics of order 10^{17} protons on target; at the same time a search for the τ^+ EDM reaching $10^{-17} e\,\mathrm{cm}$ level can be performed.

Part II

Amplitude analysis of the $\Lambda_c^+ \to pK^-\pi^+$ decay at LHCb

CHAPTER 4

The LHCb experiment

4.1 CERN and the Large Hadron Collider

The CERN (Conseil Européen pour la Recherche Nucléaire) is the European Council for Nuclear Research, founded in 1952. The laboratory extends across the border between Switzerland and France in the Geneva area, located between the Léman lake and the Jura massif.

The jewel in the crown of the CERN facilities is undoubtedly the Large Hadron Collider (LHC) particle accelerator [129], which is the most powerful particle accelerator to date. It is built inside a 26.7 km circular tunnel at a depth of about 100 m underground and provided proton-proton collisions at a centre of mass energy $\sqrt{s}$ of 7 TeV from 2010 to 2011, 8 TeV during 2012 and up to 13 TeV during Run 2 (2015-2018). For Run 3 operations, which will start in 2021 after the ongoing Long Shutdown 2 phase, the LHC is expected to reach its design pp collision energy of 14 TeV. LHC is also able to operate with heavy ions, notably proton-lead and lead-lead collisions. The LHC is able to accelerate particles up to the TeV energy scale thanks to its superconducting radio-frequency cavities, generating electric potentials up to 2 MV each. A system of dipole superconducting magnets provides the necessary ≈ 8 T magnetic field to maintain particles into circular trajectory, while quadrupole and octupole magnets focus the particle bunches to minimise beam losses. Superconducting magnets operate at 1.9 K temperature, which is achieved thanks to a huge cooling system based on superfluid helium.

The CERN accelerator complex, Fig. 4.1, is composed by a chain of accelerators of increasing dimension allowing to gradually boost the energy of protons or heavy ions up to the LHC operational energy. The proton acceleration chain starts with the extraction of protons as nuclei of hydrogen atoms. These are accelerated to 50 keV energy and lead to the LINAC2 linear accelerator in which they reach 50 MeV energy. Then, protons reach 1.4 GeV energy in the Proton Synchrotron Booster and 26 GeV in the Proton Synchrotron from which they are injected into the Super Proton Synchrotron (SPS), which accelerates protons up to 450 GeV energy. Finally, protons are transferred to the LHC, where protons are accelerated in opposite directions into separate beampipes and forced to collide in four interaction points (IP) where the seven current LHC experiments are located: ATLAS and LHCf (IP1), ALICE (IP2), CMS and TOTEM (IP5), LHCb and MoEDAL (IP8). Protons running in the LHC are organised in bunches up to 1.15×10^{11} protons, with a maximum of 2808 circulating bunches in the ring. The bunch crossing rate is 40 MHz, corresponding to an interval of 25 ns between two consecutive collisions. A key parameter of an accelerator is the instantaneous luminosity $\mathcal{L}(t)$, representing the number of collisions provided as a function of time. The luminosity increases not only with the intensity of the colliding beams but also reducing the region in which proton bunches interact. The LHC features a nominal peak instantaneous luminosity of $10^{34} cm^{-2} s^{-1}$.

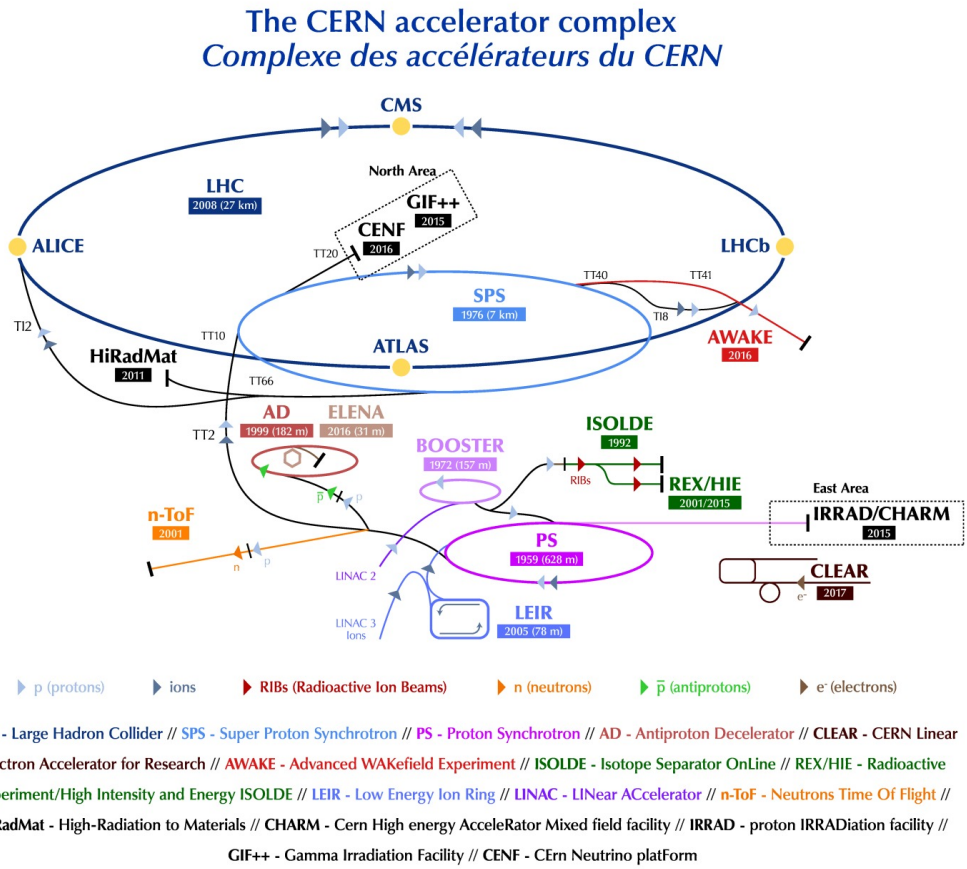

Figure 4.1: from `cdsweb.cern.ch`. The CERN accelerator complex.

4.2 Overview of the LHCb experiment

The LHCb experiment is the flavour physics experiment on the Large Hadron Collider (LHC) at CERN [130]. Its main purpose is the indirect search of beyond the SM physics effects by making very precise measurements on heavy hadron decays, especially by studying rare processes and CP-violating signatures. However, the LHCb experiment has significantly contributed also to other particle physics studies, thanks to its particular geometry: heavy baryon spectroscopy, with the discovery of new quark bound states; searches for possible new light particles; studies of heavy ion (proton-lead and lead-lead) collisions. Moreover, LHCb is the only experiment at the LHC able to collect proton-gas fixed-target collisions thanks to its internal gas target SMOG.

The LHCb detector has been specifically designed for flavour physics at the LHC accelerator. Its peculiar structure is much more similar to a fixed-target experiment design than to the "barrel plus endcaps" design which characterises the other large detectors at the LHC. This geometry was chosen following the peaked angular distributions at low polar angles of $b\bar{b}$ quark pairs, Fig. 4.3, which are mainly produced from the fusion of two (or more) gluons radiated by the proton quark constituents. Beauty particles are therefore very likely to be produced in the same forward (or backward) direction at very small angles with respect to the beam axis. A large number of beauty particles are produced thanks to the high $b\bar{b}$ cross-section at TeV energy scale. For example, at $\sqrt{s} = 7\,\mathrm{TeV}$ pp center of mass energy the cross-section to produce beauty hadrons inside the LHCb acceptance is [131]

$$\sigma(pp \to H_b X) = (75.3 \pm 5.4_{stat} \pm 13.0_{syst})\ \mu\mathrm{b} \tag{4.1}$$

much larger than at B-factory experiments using e^+e^- collisions, which exploit the electromagnetic production process. Moreover, LHCb has access to many more beauty hadron states than B-factories, like unprecedented samples of beauty baryons.

The LHCb detector is designed as a single-arm forward spectrometer with an approximate angular acceptance from $10\,\mathrm{mrad}$ to $300\,\mathrm{mrad}$ in the magnet bending plane and to 250 mrad in the non-bending plane, which corresponds to a pseudorapidity[1] range of $2 < \eta < 5$. Fig. 4.2 presents the layout of the LHCb detector and of its subdetectors. The tracking system, described in Sec. 4.2.1 is composed by: the Vertex Locator (VELO), which is able to measure the heavy hadron decay vertices displaced from the pp collision point; the TT and T1,T2,T3 stations, tracking charged particles before and after the magnet, respectively, to provide momentum and charge measurements. The particle identification information is obtained from different systems for different particles, Sec. 4.2.2: two ring-imaging Čerenkov (RICH) detectors provide particle identification mainly for charged hadrons, the calorimeters identify electrons and neutral photons, the Muon system identifies muon tracks. The trigger system deployed for Run 2 to effectively select only the interesting pp collision events is presented in Sec. 4.2.3. The SMOG system to collect proton-gas fixed-target collisions is described in Sec. 4.2.4.

The LHCb experiment in Run 2 operated at a nominal average luminosity of 4×10^{32} $cm^{-2}s^{-1}$, much smaller than the luminosity delivered to ATLAS and CMS detectors, in order to have a smaller number of interactions, about one pp collision per bunch crossing. This choice is needed for a good track reconstruction; for instance, multiple pp interactions in the same event may be mistaken for heavy hadron decay vertices. The luminosity at the LHCb interaction point is levelled during LHC fills by changing the

[1] Pseudorapidity is defined as $\eta = -\ln(\tan(\theta/2))$, θ being the angle measured with respect to the beam axis.

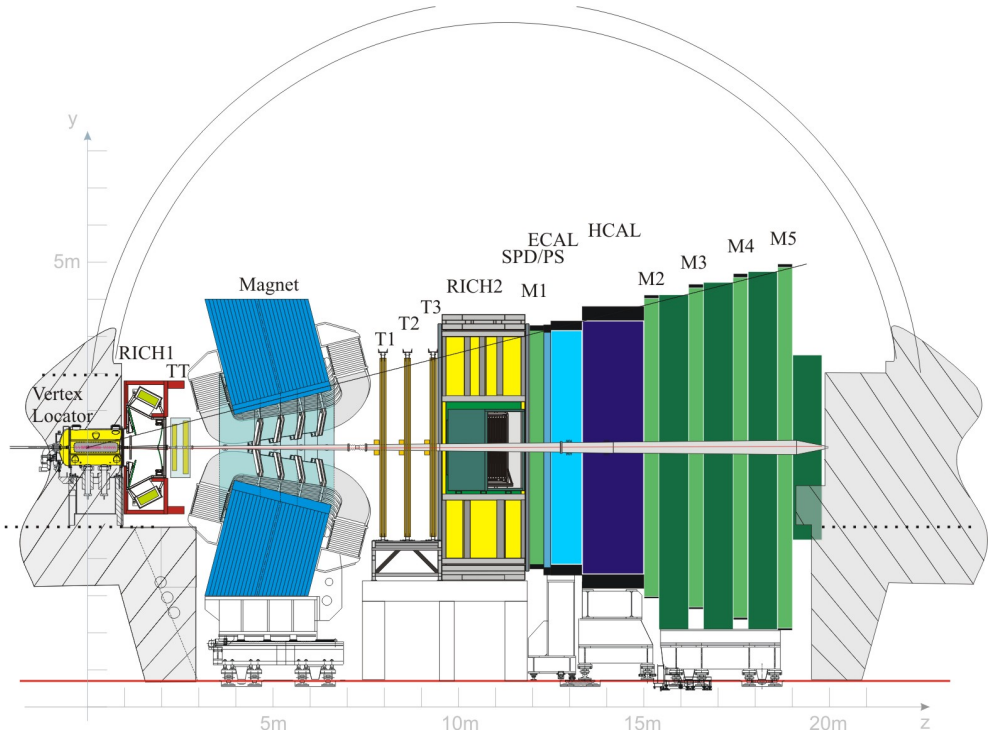

Figure 4.2: from `cdsweb.cern.ch`. Lateral view of the LHCb detector.

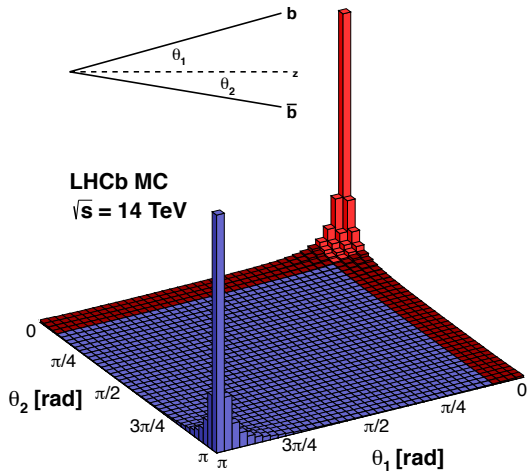

Figure 4.3: from `lhcb.web.cern.ch`. Simulated $b\bar{b}$ angular distribution at $\sqrt{s} = 14\,\mathrm{TeV}$. The red region corresponds to the LHCb detector acceptance.

transversal distance between the two beams, to keep a stable instantaneous luminosity, within a $\pm 5\%$ range. This allows to reduce effects of the luminosity decay due to proton beam losses, like systematic uncertainties due to different detector occupancies, and to keep the same trigger configuration during a fill.

4.2.1 Tracking system

Starting from the pp interaction point, the Vertex Locator (VELO) [132] is the first subdetector, which provides precise measurement of the track coordinates close to the interaction point, allowing the LHCb experiment to reconstruct displaced decay vertices of charm and beauty hadron decays.

The VELO system consists of 21 silicon stations placed along the beam direction, each one composed by one left and one right module. Each module consist of two sensors: a radial (R-sensor) and an angular one (Φ-sensor). The azimuthal coverage is about 182° for each sensor, giving a small overlap between the right and left modules in order to simplify the relative alignment and to guarantee a full azimuthal acceptance. In addition to the 42 VELO stations, 4 Pile-Up (PU) veto modules containing only an R-sensor are installed in the opposite direction with respect to the rest of the LHCb detector, and used as a pile-up veto counter for the Level-0 trigger. The inter-strip pitch of the silicon sensors varies from approximately 40 to 100 $\mu\mathrm{m}$. The VELO single hit resolution ranges between 4 and 20 $\mu\mathrm{m}$, depending on the inter-strip pitch and on the track angle. The two modules are closed only when the proton beam is in stable condition, because the closed VELO approaches the proton beam down to 8 mm distance. Otherwise, *e.g.* during injection phase, the modules are mechanically opened to avoid destructive interactions with the beam. The VELO system configuration and a schematic view of the sensors are shown in Fig. 4.4.

The VELO system is able to measure tracks in the full LHCb angular acceptance and

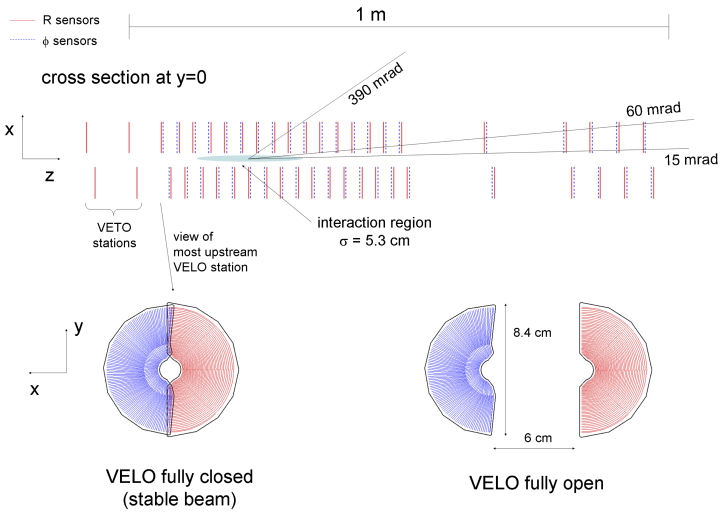

Figure 4.4: from Ref. [130]. (top) VELO detector layout and VELO sensors in (bottom left) closed and (bottom right) open configuration.

partially in the backward hemisphere to improve the primary vertex resolution. The error on the primary vertex position mainly depends on the number of tracks produced in a pp collision, Fig. 4.5. For a typical event, the resolution in the beam direction is 71 μm and 13 μm in the perpendicular direction [126]. The resolution on the track impact parameter (IP), essential quantity to identify decay vertices displaced from the primary vertex, is at tens of μm level, inversely proportial to the track transverse momentum, Figure 4.6.

Besides the VELO detector, the tracking system consists of a silicon Inner Tracker (IT) [133] and a gas-based Outer Tracker (OT) [134]. It provides efficient reconstruction and precise momentum measurement of charged tracks, track directions for ring reconstruction in the RICH detectors and information for the higher level trigger.

The tracking detectors are arranged in four stations. The Tracker Turicensis (TT) is lo-

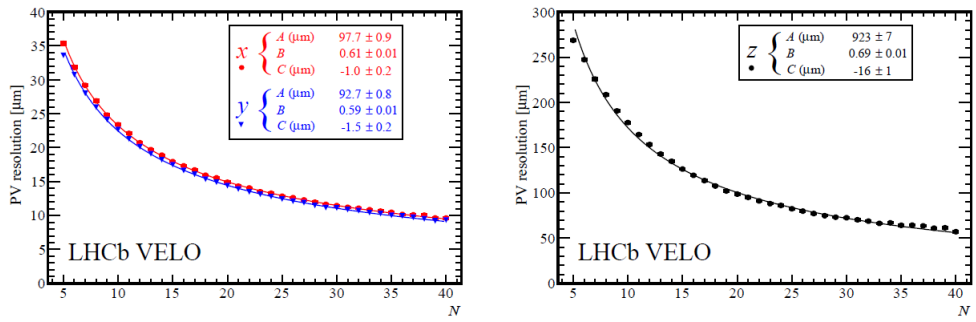

Figure 4.5: from Ref. [126]. Primary vertex (left) x,y and (right) z coordinate resolutions measured by the VELO detector as a function of the number of tracks in the pp event.

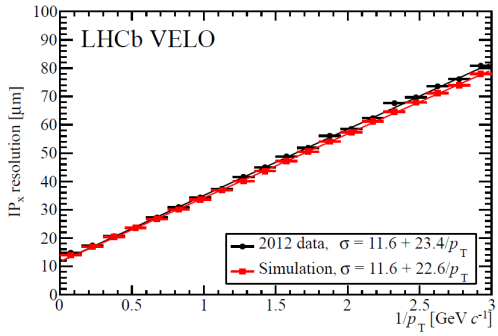

Figure 4.6: from Ref. [126]. Impact parameter x coordinate resolution measured by the VELO detector as a function of the inverse of the track transverse momentum.

cated before the magnet, after RICH1 detector. Due to its reduced dimensions it contains only IT modules. Three stations (T1, T2, T3) are located after the magnet, before RICH2 detector, and they are composed by an IT module located in an elliptical shaped region around the beam pipe and an OT one which covers most of the acceptance. Indeed, in the region covered by the IT the particle flux is about 20 times bigger than the flux in the OT region, so IT employs a different technology to achieve a finer granularity and a better radiation hardiness.

The IT system employs silicon microstrips detectors with a strip pitch of 183 μm for the TT and 198 μm for other stations. To improve track reconstruction, these detectors are composed by four layers with vertical strips in the first and in the last layer, whereas the other two layers are rotated by stereo angles of $\pm 5°$, to provide tracking information in the vertical direction, Fig. 4.7. Hit resolutions have been measured to be 59 and 50 μm for the TT and other IT modules, respectively. The OT system is composed by an array of straw tubes modules each one consisting of two panels and two sidewalls forming a stable, gas-tight box containing up to 256 straw tubes. Each tube has an inner diameter of 4.9 mm, filled with a mixture of argon (70%) and carbon dioxide (28.5%) and oxygen (1.5%), which guarantees fast drift time and a sufficient drift-coordinate hit resolution of about 200 μm. Like the silicon tracker, also OT modules are composed by four layers arranged in a similar geometry.

The momentum of charged tracks is measured from the curvature induced by the dipole magnetic field between TT and T1, T2, T3 tracking stations. The field is generated by a dipole warm magnet [135], composed by two trapezoidal coils bent at $45°$ on the two transverse sides and placed mirror-symmetrically, Fig. 4.8. It has a bending power (given by the integrated magnetic field) of 4 Tm. A very good momentum resolution of charged particles is reached by the LHCb tracking system, with a relative uncertainty of 0.5% at low momentum up to 1.0% for $p = 200\,\text{GeV}/c$ [115], Fig. 4.9.

4.2.2 Particle identification system

Charged hadron identification in LHCb is performed by means of an high performance Ring-Imaging Čerenkov system composed by two detectors aiming at different momentum ranges [136]. They reconstruct Čerenkov light emitted by charged particles traversing a medium faster than the speed of light in the medium. The angle of Čerenkov radiation emission with respect to the particle momentum θ_C is related to the particle

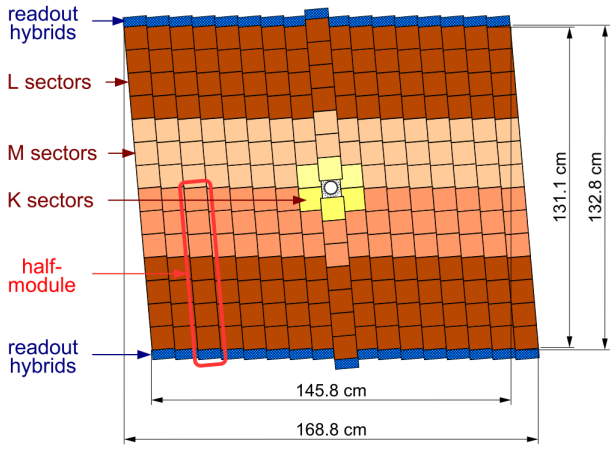

Figure 4.7: from Ref. [130]. Layout of the third TT detection layer. Different readout sectors are indicated by different shadings.

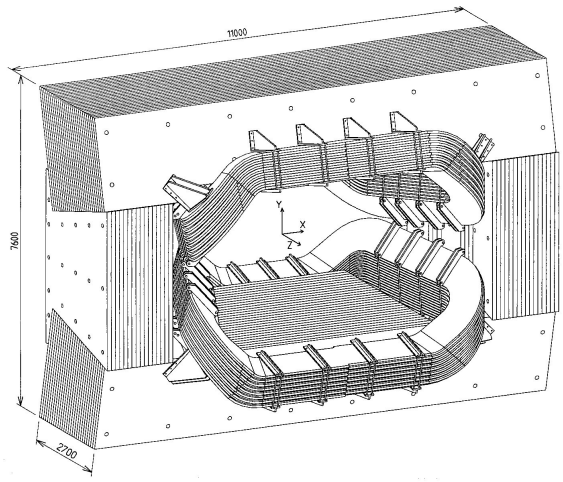

Figure 4.8: from `lhcb.web.cern.ch`. The LHCb magnet.

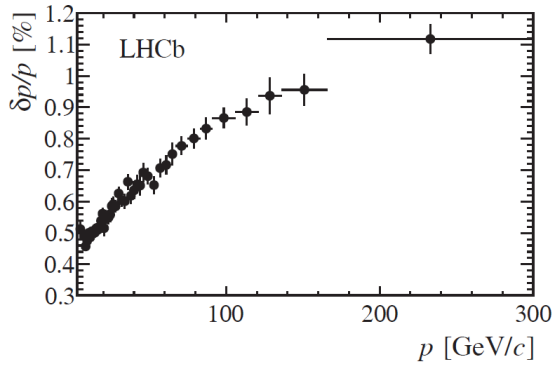

Figure 4.9: from Ref. [115]. Relative uncertainty on charged tracks momentum.

velocity as

$$cos(\theta_C) = \frac{1}{n\beta}, \tag{4.2}$$

in which n is the medium refractive index. Combining this information with the momentum measured by the tracking system, the particle mass can be obtained.

RICH1 is located upstream of the magnet and it identifies low momentum particles $2 < p < 60\,\mathrm{GeV}/c$. It employs C_4F_{10} gas radiators and has a polar angle acceptance from 25 to 300 mrad. RICH2, located downstream of the magnet and the tracking stations, has a smaller angular acceptance (from 15 to 120 mrad in the horizontal plane and from 15 to 100 mrad in the vertical plane) and it covers the high momentum range, $15 < p < 100\,\mathrm{GeV}/c$, by means of a CF_4 radiator. RICH1 and RICH2 layouts are shown in Fig. 4.10. Čerenkov light is focused onto the photon detector planes using tilted spherical mirrors and secondary plane mirrors, in order to reflect the image out of the spectrometer acceptance. The baseline photon detectors are multianode photomultiplier tubes (MaPMT).

The reconstructed Čerenkov angles for single tracks are reported in (left) Fig.4.11, showing well resolved bands for muons, pions, kaons and protons over most of the covered momentum range. The ability of kaon identification using delta log-likelihood differences for the two hypothesis is shown in (right) Fig.4.11.

The LHCb calorimeter system [137] has been devised for the identification of high transverse energy hadrons, electrons and photons candidates. It measures their energy and position providing essential information for the Level-0 trigger candidate selection. Its structure consists of a single-layer pre-shower detector (PSD) made by 14 mm thick lead plates and 10 mm square scintillators, followed by an electromagnetic calorimeter (ECAL) and an hadronic calorimeter (HCAL). A scintillator pad detector (SPD) is located before the PSD.

The ECAL is made up of 70 layers consisting of 2 mm thick lead plates and 4 mm thick polystyrene-based scintillator plates. It has the important function of detecting photons with adequate granularity and energy resolution for prompt photons and π^0 reconstruction. For $p_{\mathrm{T}} < 2\,\mathrm{GeV}/c$ neutral pions are mainly reconstructed combining two separate clusters in the ECAL (resolved π^0), while for greater transverse momenta the two photons are measured as a single cluster (merged π^0).

The HCAL consists of 16 mm thin iron plates spaced with 4 mm thick scintillating

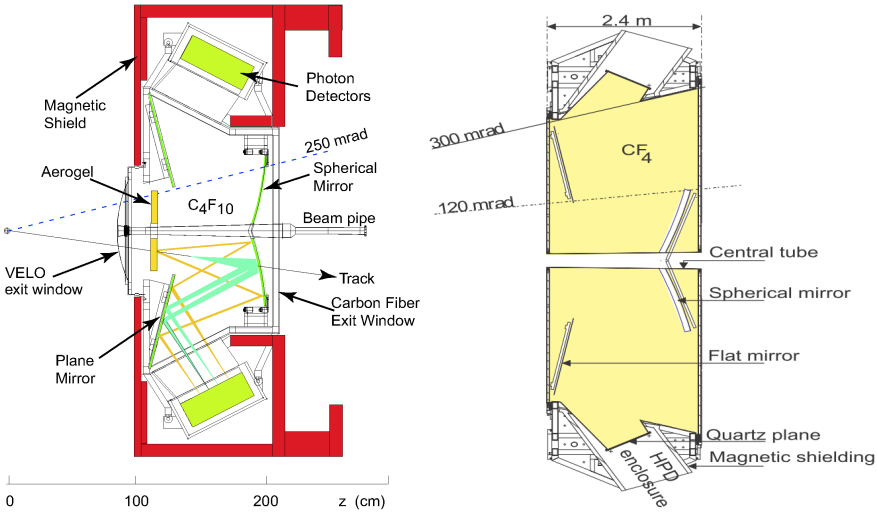

Figure 4.10: from Ref. [130]. (left) RICH 1 and (right) RICH 2 schemes.

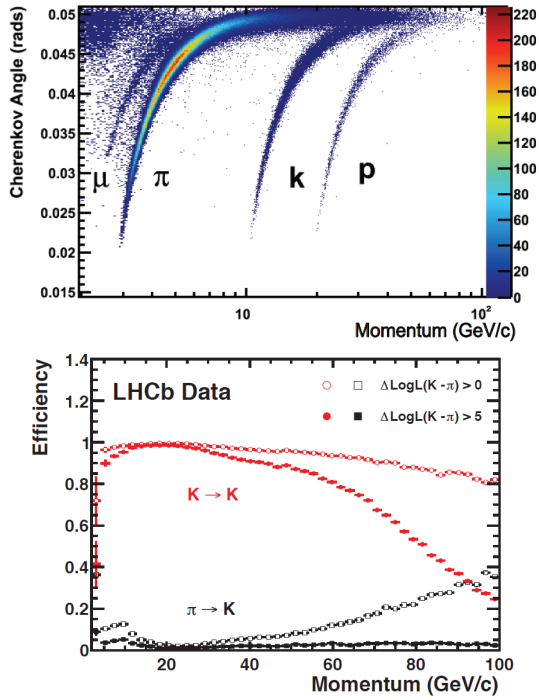

Figure 4.11: from Ref. [115]. (left) Reconstructed Čerenkov angle for isolated tracks, as a function of track momentum in the C_4F_{10} radiator. (right) Kaon identification efficiency and pion misidentification rate measured as a function of track momentum.

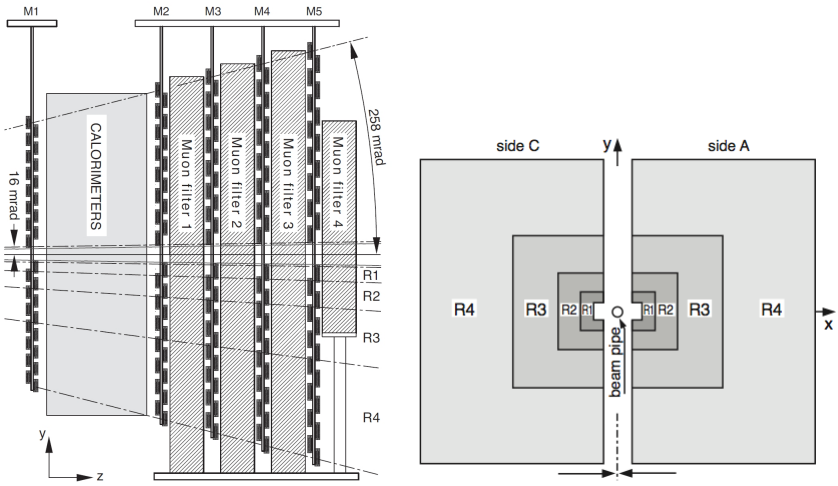

Figure 4.12: from Refs. [130], [139]. (left) Side view of the Muon System and (right) Station layout with the four regions R1-R4.

tiles arranged parallel to the beam pipe.

The energy resolution has been measured to be

$$\frac{\sigma_E}{E} \simeq \frac{9\%}{\sqrt{E[\,\mathrm{GeV}]}} \oplus 0.8\%, \qquad \frac{\sigma_E}{E} \simeq \frac{69\%}{\sqrt{E[\,\mathrm{GeV}]}} \oplus 10\%, \tag{4.3}$$

for the ECAL and the HCAL, respectively. The good resolution of the ECAL allow to effectively distinguish electrons from charged hadrons, while the HCAL information is employed for the Level-0 trigger to select purely hadronic events.

The muon system [138] consists of five tracking stations placed along the beam axis, the first one (M1) lies in front of the calorimeters and the other four, interleaved with three 80 cm thick iron filters to stop all other charged particles, lie after the calorimeters, (left) Fig. 4.12. The muon stations are equipped with Multi Wire Proportional Chambers (MWPCs) except for the inner region of M1, where Gas Electron Multiplier (GEM) chambers are employed for their better ageing properties, as they have to stand a greater particle flux.

The inner and outer angular acceptances of the muon system are 20 (16) mrad and 306 (258) mrad in the bending (non-bending) plane, similar to the tracking system acceptances. This corresponds to a geometrical acceptance of about 20% of the full solid angle for muons coming from b quark decays. Each station is subdivided in four regions R1-R4 whose linear dimensions and logical pad size scale in the ratio 1:2:4:8 with the beam distance, (right) Fig. 4.12. The detector granularity varies such that its contribution to the muon p_{T} resolution compensates the multiple-scattering contribution. This latter contribution increases as the muons energy decrease, therefore the detector resolution must increase with the distance from the beam axis because high-momentum tracks tend to be closer to the beam.

The muon system has been designed to achieve a 95% trigger efficiency for events producing a muon, the trigger algorithm requiring a five-fold coincidence in a time lapse smaller than the pp collision period (25 ns). The lower momentum threshold for efficient

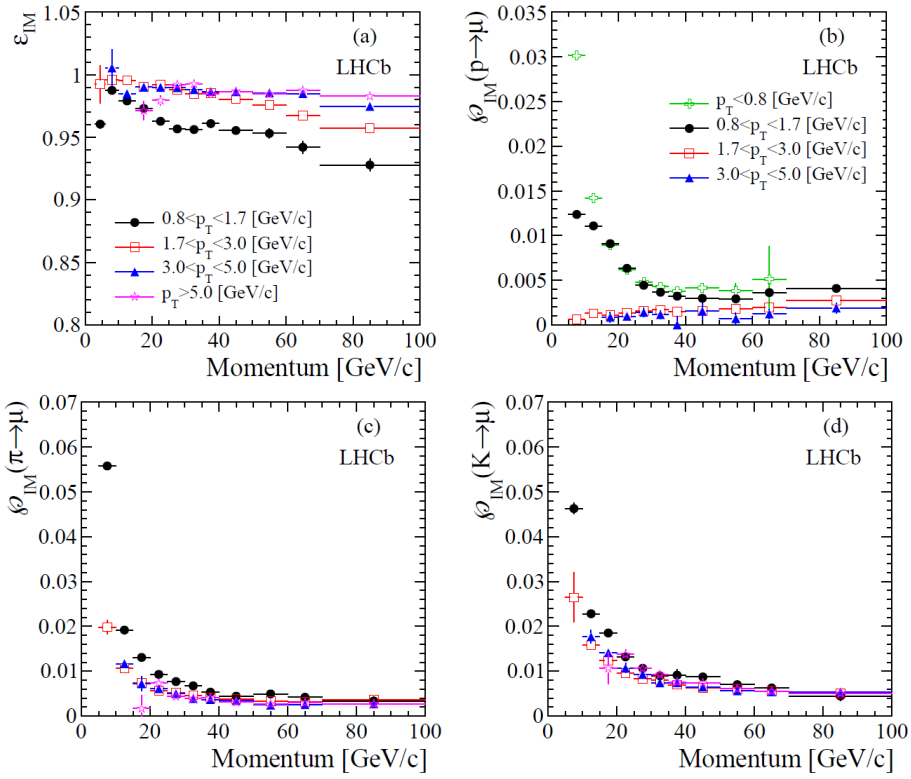

Figure 4.13: from Ref. [139]. (top left) Muon trigger efficiency ε_{IM} and (others) charged hadron-to-muon misidentification rates $\mathcal{P}(h \to \mu)$.

muon triggering is about 6 GeV/c. Muon trigger efficiency and charged hadron-to-muon misidentification rates are reported in Fig. 4.13.

4.2.3 Trigger system in Run 2

The amount of raw data collected by the LHCb detector in 40 MHz pp collisions is too big to be stored, moreover, only few pp interactions produce interesting events. The LHCb trigger system for Run 2 [140], which improved the original Run 1 version [141], has been developed to reduce the event rate to be recorded down to about 12.5 kHz, which is small enough to allow to store the selected events for the offline analysis. The trigger system consist of two main selections: the Level-0 trigger (L0) and the High Level Trigger (HLT). The trigger scheme is summarised in Fig. 4.14.

L0 is hardware-implemented and reduces the event rate at 1 MHz, at which the detector can be read out. L0 selects candidates combining information from calorimeter and muon system, selecting events featuring high transverse momentum and/or energy, at few GeV level. HLT is software-based and reduces the event rate at 12.5 kHz using a full event reconstruction based on particle identification, track and vertex reconstruction and impact parameter measurements. It consists of two different levels HLT1 and HLT2 acting sequentially, HLT1 being designed to be faster than HLT2 to cope with the L0 output event rate. The HLT1 performs an inclusive selection of events based on one-

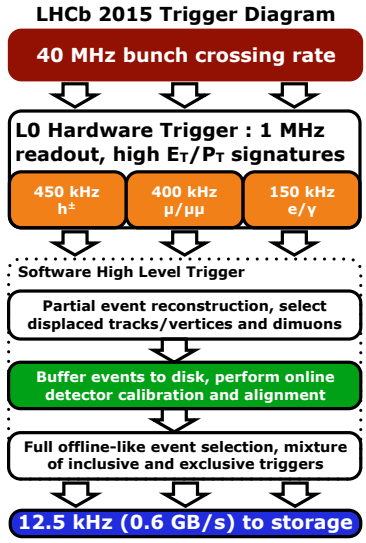

Figure 4.14: The LHCb trigger diagram for Run 2.

or two-track signatures, on the presence of muon tracks displaced from the PVs, or on dimuon combinations in the event. Events selected by the HLT1 trigger are buffered to disk storage, so they can be further processed during inter-fill periods, and the detector can be calibrated and aligned before running the HLT2 stage. Once the detector is aligned and calibrated, events are passed to HLT2, in which a full reconstruction is performed, which allows for a wide range of inclusive and exclusive final states to trigger the event.

4.2.4 SMOG system

The system for measuring overlap with gas (SMOG) device, has been originally designed to perform precise luminosity measurements [142] thanks to "beam-gas imaging" luminosity calibration; indeed it allowes LHCb to operate as a fixed-target experiment, extending its initial physics reach. The SMOG system, Fig. 4.15, injects noble gases in the beam pipe section crossing the VELO detector, with pressures of order 10^{-7} mbar, two orders of magnitude higher than the typical pressure of the LHC vacuum. SMOG gives the unique opportunity to study nucleus-nucleus and proton-nucleus collisions on various targets. Thanks to the very high boost of the proton-nucleus system, the LHCb acceptance covers the backward rapidity hemisphere in the center-of-mass system of the reaction y^*, in the range $-2.5 < y^* < 0$.

4.3 LHCb data samples

The pp collision data samples recorded by the LHCb experiment are summarised in Fig. 4.16, in which the integrated luminosity and the circulating proton beams energy is reported for each year of data taking. LHCb has recorded a total of $\approx 9\,\text{fb}^{-1}$, of which $\approx 6\,\text{fb}^{-1}$ at $\sqrt{s} = 13\,\text{TeV}$ during Run 2, and $\approx 3\,\text{fb}^{-1}$ at $\sqrt{s} = 7 - 8\,\text{TeV}$ during Run 1.

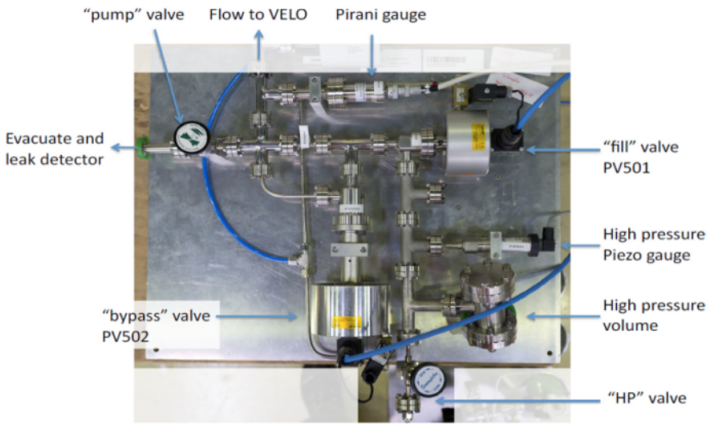

Figure 4.15: from Ref. [143]. The SMOG gas feed system.

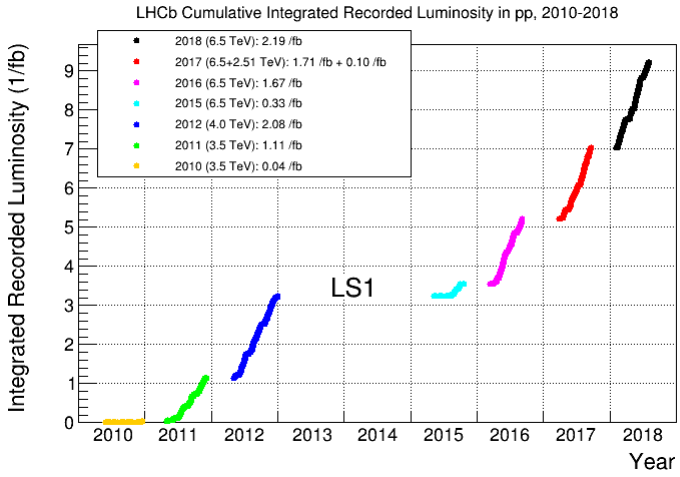

Figure 4.16: from `lhcb.web.cern.ch`. Integrated luminosity recorded by the LHCb experiment in *pp* collisions. The legend reports the year of data taking and the energy of the circulating proton beams .

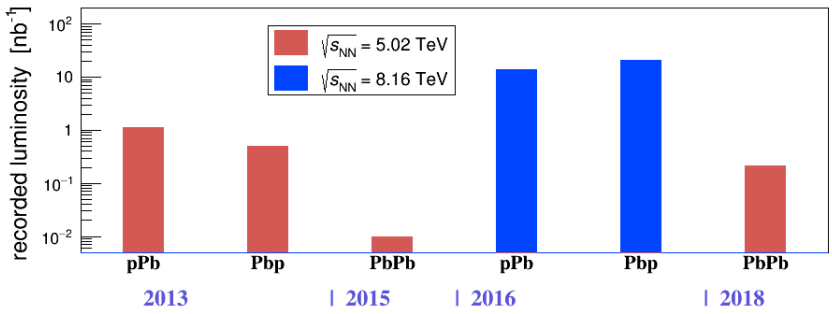

Figure 4.17: from `lhcb.web.cern.ch`. Heavy ion pPb and PbPb collision samples recorded by the LHCb experiment.

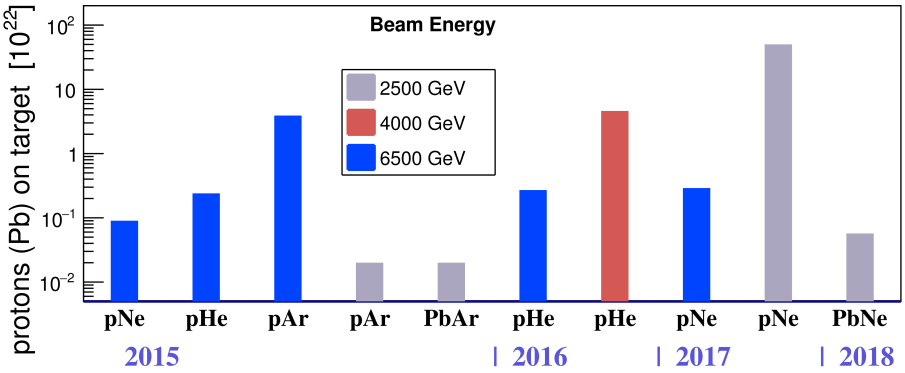

Figure 4.18: from `lhcb.web.cern.ch`. SMOG proton-gas fixed-target samples recorded by the LHCb experiment.

LHCb has also recorded heavy ion samples in pPb and PbPb collision mode, summarised in Fig. 4.17, and proton-gas fixed-target SMOG events, Fig. 4.18. Since the density of the gas is known only at 10% level, the exact luminosity of the SMOG fixed-target data samples can be measured independently from proton-electron elastic collisions [144]. To date, the luminosity measurement has been performed only for the proton-helium data samples collected in 2016.

4.4 LHCb upgrade

At the time of writing this thesis, the LHCb experiment is undergoing a major upgrade, which will make LHCb able to run at a luminosity of $2 \times 10^{33}\ cm^{-2}s^{-1}$, five times the nominal Run 2 value, with a target integrated luminosity of 50 fb^{-1} to be recorded during Run 3 and 4. The LHCb spectrometre used in Run 1 and 2 is not suitable for such a rate of pp collisions, in particular due to perfomance degradation with increasing detector occupancy, limits of the trigger system and insufficient radiation hardness of the tracking detectors. The major features of the upgraded LHCb experiment concern trigger and tracking systems.

The new trigger strategy will be software-based only, with no hardware selection anymore [114]. All the subdetectors will be read out at the 30 MHz rate of pp inelastic collisions, and raw data processed by a dedicated computing farm. A two-level software trigger will select the interesting events to be stored and will perform real-time detector calibration and alignment. The complete reconstruction performed by the second software level will produce data ready for offline analysis. This trigger scheme will allow to increase significantly the efficiency for a broad range of LHCb physics channels.

New detectors will replace the tracking system [145], all featuring better tracking performances and increased radiation hardness: the new vertex locator will consist of $55 \times 55\,\mu\mathrm{m}$ pixel sensors, able to move down to 5 mm from the beam; the tracking stations before the magnet will be replaced by the upstream tracker (UT), consisting of silicon microstrips with finer segmentation than before; the tracking stations after the magnet will be replaced by a scintillating fibre tracker (SciFi), featuring spatial resolutions of $\approx 70\,\mu\mathrm{m}$.

Particle identification detectors will also undergo updates [146]. The RICH1 detector will have a modified optics and mechanics to reduce occupancy, with new multianode photomultipliers with finer granularity. The calorimeter system has been adapted to withstand the higher particle fluxes, lowring the photomultiplier tubes gain. SPD and PS detectors, as well as the first muon station will be removed. New read-out electronics have been developed for all subdetectors, to enable their read-out at 30 MHz frequency.

The SMOG internal gas target will also be upgraded to SMOG2 [143]. The main element of SMOG2 is a storage cell for the injected gas, to be installed at the upstream edge of the VELO, coaxial with the LHC beam. Its main advantage is the possibility to reach effective areal gas densities (and thus luminosities) higher by one order of magnitude with respect to SMOG by injecting gas at the same flow rate. Moreover, SMOG2 will allow to inject gas species other than noble gases, a more precise determination of the gas density (and luminosity), and a better defined interaction region. In principle, SMOG2 could also run in parallel with pp collision runs, if fixed-target collisions are proved to not interfere with pp data taking.

4.4.1 Future plans

Besides the ongoing upgrade, the LHCb collaboration is considering the future detector upgrades to take place during Long Shutdown 3 (upgrade Ib) and 4 (upgrade II) [147], with the goal of fully exploiting the LHC potential for flavour physics, aiming at 300 fb^{-1} of pp collisions to be recorded during Run 5 and 6. A number of projects are under consideration to improve detector granularity and radiation hardness, improve coverage for low p_{T} tracks and the inclusion of timing information in tracking (4D tracking), which would enable to effectively distinguish different collision vertices. The current and foreseen LHCb upgrades within LHC schedule are summarised in Table 4.1, along with the recorded and planned integrated luminosities in pp collisions.

4.5 LHCb analysis software

All LHCb analysis software is developed under `Gaudi` [148] framework, an experiment independent open project providing interfaces and services for building HEP experiment frameworks for event data processing applications. Dedicated packages take care of the different steps necessary to obtain completely reconstructed candidates from raw data as well as accurate event simulations describing both particle physics and detector response.

LHC phase	Years	LHCb upgrades	Recorded/Planned $\int \mathcal{L}dt$
Run 1	2010-2012		3 fb^{-1}
Long Shutdown 1	2013-2014		
Run 2	2015-2018		6 fb^{-1}
Long Shutdown 2	2019-2020	Upgrade I	
Run 3	2021-2023		
Long Shutdown 3	2024-2025	Upgrade Ib	
Run 4	2026-2029		50 fb^{-1}
Long Shutdown 4	2030	Upgrade II	
Run 5	2031-2033		
Long Shutdown 5	2034		
Run 6	2035-2037		300 fb^{-1}

Table 4.1: The LHC schedule, with the planned LHCb experiment upgrades. Integrated luminosities refer to pp collisions.

4.5.1 Offline data reconstruction

Data selected by both L0 and HLT trigger levels, consisting of digitised data coming from the different subdetectors, are stored for the offline analysis. Candidates reconstruction is performed by `Brunel` [149] package: it takes care of track identification starting from measured hits in each detector, reconstructs particles momentum and energy as well as primary and secondary vertexes (derived from the intersection of two or more tracks) and performs the particle identification (PID) process combining data from RICH, ECAL, HCAL and muon system to compute efficient PID variables.

Next, data go through the *stripping* process, in which candidates are divided into categories called *streams* grouping decays with common features. For each stream several loose selection criteria called *stripping lines* are defined. Each stripping line is a set of standard requirements for restricting the search for a particular decay channel to a subset of the whole data. The stripping procedure as well as the complete decay chain reconstruction is performed by `DaVinci` [150] package.

4.5.2 Monte Carlo simulation

Simulated events generated with the Monte Carlo (MC) method are extensively used in particle physics analyses. MC dataset production process is carried out by `Gauss` [151] package, interfaced with specific packages for handling generation and simulation phases. Generation of the physical process including the proton-proton interaction described by the known theoretical models and the subsequent hadronisation process is performed by PYTHIA [123] package, simulation of the mother B particle decay of interest is done by EVTGEN [124] package, in which final-state radiation is generated using PHOTOS [152] package. Heavy baryon events produced in heavy nuclei collisions are obtained combining heavy baryon decays generated from proton-proton collisions with minimum bias heavy nuclei collisions generated with the EPOS [153] package. The simulation phase consisting in describing the interaction among particles and detectors, taking into account all the geometric and material details of each subdetector, is made by `Geant4` [154] package. Output produced by `Gauss` package is further elaborated by `Boole` [155]

package, the LHCb digitisation application, simulating the detector response, the read-out electronics behaviour and also the Level-0 trigger level. Its output, digitised data reproducing real data coming from the real detector, are then reconstructed exactly in the same way as real data.

CHAPTER 5

Amplitude analysis of the $\Lambda_c^+ \to pK^-\pi^+$ decay at LHCb

5.1 Motivation

The weak interaction, charged-current mediated, Cabibbo favoured $\Lambda_c^+ \to pK^-\pi^+$ decay is the most abundant decay mode of the Λ_c^+ baryon, with a known branching fraction of $(6.35 \pm 0.33)\%$ [24], making it the most suited channel to study the Λ_c^+ baryon properties, like polarisation and electromagnetic dipole moments. Indeed, two-body decays like $\Lambda_c^+ \to pK_S^0$ or $\Lambda_c^+ \to \Lambda\pi^+$, which are characterised by simple angular distributions, feature lower branching fractions $\lessapprox 1\%$ and a reduced detector reconstruction efficiency for the presence of strange particles with lifetimes of order 10^{-10} s. The latter is very relevant for fixed-target experiments performed with protons at the TeV energy, where the large Lorentz boost increases the typical strange particle mean flight distances up to tens of meters.

Nonetheless, the $\Lambda_c^+ \to pK^-\pi^+$ decay structure is poorly known to date, since the only amplitude analysis of $\Lambda_c^+ \to pK^-\pi^+$ decays was performed by the E791 experiment at Fermilab on a data sample of ≈ 1000 candidates only [71]. Moreover, the amplitude model employed in the E791 amplitude analysis is not correct, since the rotation of the final proton spin for different decay chains to a reference helicity frame, as in Eq. (1.52), is missing.

A precise amplitude analysis of the $\Lambda_c^+ \to pK^-\pi^+$ decay, including the extraction of the Λ_c^+ polarisation, is of fundamental interest beyond the determination of its intermediate resonance structure. A method to extract the Λ_c^+ baryon polarisation is essential for the proposed search of charm baryon electric and magnetic dipole moments using bent crystals at LHC(b), Chapter 2. As discussed in Sec. 1.3.2, Λ_c^+ polarisation measurements are closely related to the c-quark polarisation, allowing to study both new physics contributions and the non-perturbative QCD regime hadronisation process [64]. For example, the inclusion of a $\Lambda_c^+ \to pK^-\pi^+$ amplitude model in $\Lambda_b^0 \to \Lambda_c^+ l^- \bar{\nu}_l$ angular analyses increases the sensitivity to possible beyond the SM physics contributions [82]. Methods to perform angular analyses of semileptonic $b \to cl\nu$ processes even at hadron collider experiments like LHCb have been proposed [156].

The amplitude analysis of the $\Lambda_c^+ \to pK^-\pi^+$ decay allows to study parity violation, *e.g.* by measuring the unknown effective decay asymmetry parameters α relating the Λ_c^+ polarisation to the quasi two-body decay distribution of spin 1/2 intermediate resonances,

$$\frac{dN}{d\cos\theta_R} \propto 1 + \alpha\cos\theta_R, \tag{5.1}$$

in which $\cos\theta_R = \boldsymbol{P}\cdot\hat{\boldsymbol{p}}(R)$ is the cosine of the angle between the polarisation vector and the direction of the intermediate resonance in the Λ_c^+ rest frame. A linear dependence

on $\cos\theta_R$ arise from the interference of parity conserving and parity violating amplitudes [16]. The α parameters can be extracted from the resonance contribution to the amplitude fit by integrating over all the decay angles except $\cos\theta_R$. Knowledge of the decay structure is also useful for performing localised CP-volation searches in the decay phase space. These can be carried out in a model-dependent way by comparing amplitude model fits to baryon and antibaryon decays, or in a model-independent way by tailoring the partition of the phase space according to the known intermediate resonances to localise and optimise the sensitivity to CP-violation [83].

The LHCb experiment has recorded millions of $\Lambda_c^+ \to pK^-\pi^+$ candidates, both from semileptonic $\Lambda_b^0 \to \Lambda_c^+\mu^- X$ decays and from prompt pp collisions, allowing to perform very detailed studies of its decay structure and to measure the Λ_c^+ polarisation in both weak and strong interaction production processes. In this part of the thesis, the status of the $\Lambda_c^+ \to pK^-\pi^+$ amplitude analysis from semileptonic production at LHCb is presented. In Sec. 5.2 the $\Lambda_c^+ \to pK^-\pi^+$ amplitude model is built following the helicity formalism detailed in Sec. 1.4; the selection of $\Lambda_c^+ \to pK^-\pi^+$ candidates from LHCb data samples, including combinatorial and physical background rejection, is presented in Sec. 5.3. The amplitude fits are detailed in Sec. 5.4: in particular two-dimensional Dalitz plot fits are shown in Sec. 5.4.4 and full phase space five-dimensional fits in Sec. 5.4.5. The conclusions of the amplitude analysis are summarised in Sec. 5.5.

5.2 The $\Lambda_c^+ \to pK^-\pi^+$ amplitude model

5.2.1 Λ_c^+ baryon polarisation frame

Charm baryons originated in Λ_b^0 semileptonic decays can be polarised thanks to the structure of the charged current weak force mediating semileptonic decays. Since parity is maximally violated in such transitions, the baryon polarisation is expected to be mostly parallel to the Λ_c^+ momentum as seen from the Λ_b^0 rest frame. Therefore, the "ideal" polarisation frame would be the helicity frame of the Λ_c^+ baryon reached from the Λ_b^0 rest frame. However, the presence of an undetectable neutrino in the Λ_b^0 decay prevents a precise reconstruction of the Λ_b^0 rest frame, making the mentioned polarisation frame hardly accessible.

In this analysis the helicity frame of the Λ_c^+ baryon reached from the laboratory frame is employed, which is well defined since the Λ_c^+ decay is fully reconstructed. However, this choice leads to a dilution of the original polarisation since the actual quantisation axis will be uncontrollably rotated event-by-event from the "ideal" one, because of the unknown orientation of the Λ_b^0 decay in the laboratory frame.

The muon momentum is used to define the orthogonal polarisation axes, by choosing the x-axis as the component of the muon momentum orthogonal to the Λ_c^+ momentum.

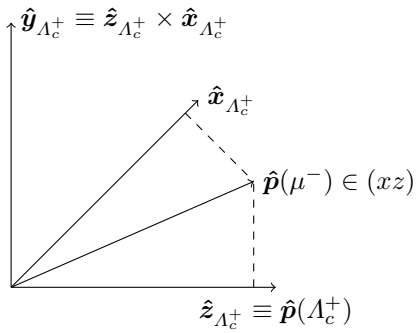

Figure 5.1: Definition of the Λ_c^+ polarisation frame.

The three polarisation frame axes are thus defined as follows, Fig. 5.1,

$$\begin{aligned}
\hat{\boldsymbol{z}}_{\Lambda_c^+} &= \hat{\boldsymbol{p}}(\Lambda_c^+) \\
\hat{\boldsymbol{x}}_{\Lambda_c^+} &= \frac{\boldsymbol{p}(\mu^-) - [\boldsymbol{p}(\mu^-) \cdot \hat{\boldsymbol{p}}(\Lambda_c^+)]\,\hat{\boldsymbol{p}}(\Lambda_c^+)}{\left|\boldsymbol{p}(\mu^-) - \left[\boldsymbol{p}(\mu^-) \cdot \hat{\boldsymbol{p}}(\Lambda_c^+)\right]\hat{\boldsymbol{p}}(\Lambda_c^+)\right|} \\
&= \frac{\boldsymbol{p}(\Lambda_c^+) \times \boldsymbol{p}(\mu^-)}{\left|\boldsymbol{p}(\Lambda_c^+) \times \boldsymbol{p}(\mu^-)\right|} \times \hat{\boldsymbol{p}}(\Lambda_c^+) \\
\hat{\boldsymbol{y}}_{\Lambda_c^+} &= \hat{\boldsymbol{z}}_{\Lambda_c^+} \times \hat{\boldsymbol{x}}_{\Lambda_c^+} \\
&= \frac{\boldsymbol{p}(\Lambda_c^+) \times \boldsymbol{p}(\mu^-)}{\left|\boldsymbol{p}(\Lambda_c^+) \times \boldsymbol{p}(\mu^-)\right|},
\end{aligned} \tag{5.2}$$

in which the Λ_c^+ and muon momenta are expressed in the laboratory frame.

5.2.2 Three-body decay phase space

A particle three-body decay is described by 5 degrees of freedom, resulting from 12 four momentum components constrained by 3 mass requirements and 4 energy-momentum conservation relations, which confines the daughters momenta to a plane in the rest frame of the mother particle. For an unpolarised baryon, there is no preferred direction in space and the decay is isotropic for rotational invariance. In this case, the decay plane orientation is irrelevant and the decay is described by two variables only, which are usually chosen to be two of the three available two-body invariant masses (Dalitz variables) since the phase space density is uniform over them. For the $\Lambda_c^+ \to pK^-\pi^+$ decay, $m^2_{pK^-}$ and $m^2_{K^-\pi^+}$ are selected. For non-zero polarisation the decay is no more isotropic and the decay spatial orientation must be specified by the three Euler angles describing the rotation from the Λ_c^+ polarisation frame to the decay plane reference frame.

The decay plane (DP) reference frame is chosen in such a way that the proton momentum defines the z axis, while the component of the kaon momentum orthogonal to

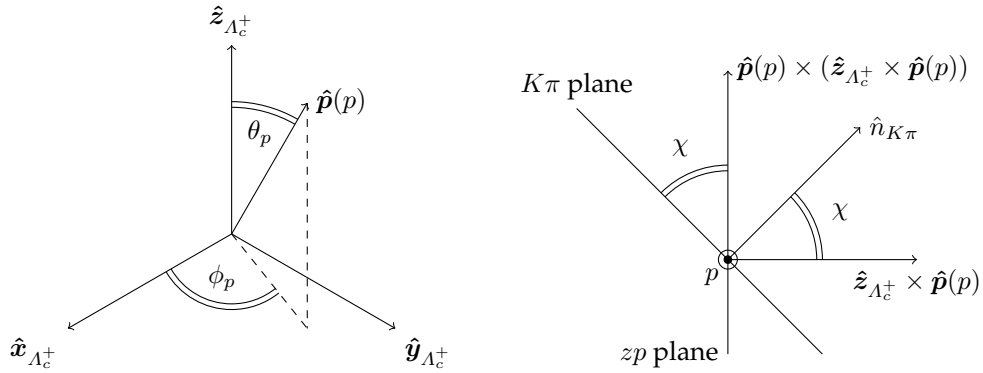

Figure 5.2: Definition of the Euler angles describing the rotation from the Λ_c^+ polarisation frame to the decay plane reference frame: (left) proton polar and azimuthal angles and (right) χ angle.

the proton momentum defines the x axis,

$$\begin{aligned}
\hat{\boldsymbol{z}}_{\mathrm{DP}} &= \hat{\boldsymbol{p}}(p) \\
\hat{\boldsymbol{x}}_{\mathrm{DP}} &= \frac{\boldsymbol{p}(K^-) - [\boldsymbol{p}(K^-) \cdot \hat{\boldsymbol{p}}(p)]\,\hat{\boldsymbol{p}}(p)}{|\boldsymbol{p}(K^-) - [\boldsymbol{p}(K^-) \cdot \hat{\boldsymbol{p}}(p)]\,\hat{\boldsymbol{p}}(p)|} \\
&= \frac{\boldsymbol{p}(p) \times \boldsymbol{p}(K^-)}{|\boldsymbol{p}(p) \times \boldsymbol{p}(K^-)|} \times \hat{\boldsymbol{p}}(p) \\
\hat{\boldsymbol{y}}_{\mathrm{DP}} &= \hat{\boldsymbol{z}}_{\mathrm{DP}} \times \hat{\boldsymbol{x}}_{\mathrm{DP}} \\
&= \frac{\boldsymbol{p}(p) \times \boldsymbol{p}(K^-)}{|\boldsymbol{p}(p) \times \boldsymbol{p}(K^-)|}
\end{aligned} \tag{5.3}$$

in which the momenta are expressed in the Λ_c^+ rest frame. With this definition the α Euler angle is the azimuthal angle of the proton in the Λ_c^+ polarisation frame, ϕ_p, the β angle is the polar angle of the proton, θ_p, and the γ angle is the signed angle formed by the proton and the Λ_c^+ quantisation axis $\hat{\boldsymbol{z}}_{\Lambda_c^+}$ and the plane formed by the kaon and the pion, named χ, Fig. 5.2. In formulae, following from Eq. (1.27),

$$\begin{aligned}
\phi_p &= \mathrm{atan2}(\hat{\boldsymbol{p}}(p) \cdot \hat{\boldsymbol{y}}_{\Lambda_c^+}, \hat{\boldsymbol{p}}(p) \cdot \hat{\boldsymbol{x}}_{\Lambda_c^+}) \\
\theta_p &= \arccos\left(\hat{\boldsymbol{p}}(p) \cdot \hat{\boldsymbol{z}}_{\Lambda_c^+}\right) \\
\chi &= \mathrm{atan2}(\hat{\boldsymbol{z}}_{\Lambda_c^+} \cdot (\hat{\boldsymbol{p}}(p) \times \hat{\boldsymbol{p}}(K^-)), -\hat{\boldsymbol{z}}_{\Lambda_c^+} \cdot \left[(\hat{\boldsymbol{p}}(p) \times \hat{\boldsymbol{p}}(K^-)) \times \hat{\boldsymbol{p}}(p)\right])
\end{aligned} \tag{5.4}$$

The five phase space variables are therefore chosen to be

$$\Omega = (m^2_{pK^-}, m^2_{K^-\pi^+}, \cos\theta_p, \phi_p, \chi), \tag{5.5}$$

so that the phase space density is uniform over the five variables. Their allowed range is $\cos\theta_p \in [-1, 1]$ and $\phi_p, \chi \in [-\pi, \pi]$. while the mass distributions are constrained to a rounded-triangle shape in the $(m^2_{pK^-}, m^2_{K^-\pi^+})$ plane (Dalitz plot, see Fig. 5.16).

5.2.3 Amplitude model for the $\Lambda_c^+ \to pK^-\pi^+$ decay

The amplitude model for the $\Lambda_c^+ \to pK^-\pi^+$ decay is built exploiting the helicity formalism described in Sec. 1.4.4. Intermediate states can contribute to the decay for all the three possible two-particle systems, so that amplitudes for $\Lambda_c^+ \to \Lambda^*(\to pK^-)\pi^+$, $\Lambda_c^+ \to \Delta^{++*}(\to p\pi^+)K^-$ and $\Lambda_c^+ \to K^*(\to K^-\pi^+)p$ decay chains must be considered.

Let's first consider the decay chain $\Lambda_c^+ \to \Lambda^*(\to pK^-)\pi^+$. The weak decay $\Lambda_c^+ \to \Lambda^*\pi^+$ is described by Eq.(1.43),

$$\mathcal{A}^{\Lambda_c^+\to\Lambda^*\pi^+}_{m_{\Lambda_c^+},\lambda_{\Lambda^*}}(\theta_{\Lambda^*},\phi_{\Lambda^*}) = \mathcal{H}^{\Lambda_c^+\to\Lambda^*\pi^+}_{\lambda_{\Lambda^*},0} D^{*1/2}_{m_{\Lambda_c^+},\lambda_{\Lambda^*}}(\phi_{\Lambda^*},\theta_{\Lambda^*},0), \tag{5.6}$$

in which $m_{\Lambda_c^+}$ is the Λ_c^+ spin projection along the Λ_c^+ quantisation axis, λ_{Λ^*} the Λ^* helicity and $\theta_{\Lambda^*}, \phi_{\Lambda^*}$ the polar and azimuthal angles of the Λ^* momentum in the Λ_c^+ frame. Angular momentum conservation relations Eq. (1.45) imply there are 2 allowed helicity couplings, $\lambda_{\Lambda^*} = \pm 1/2$, to fit for each resonance whatever J_{Λ^*} is. The two couplings are independent of each other because of parity violation in the weak $\Lambda_c^+ \to \Lambda^*\pi^+$ decay.

The strong decay $\Lambda^* \to pK^-$ is described by

$$\mathcal{A}^{\Lambda^*\to pK^-}_{\lambda_{\Lambda^*},\lambda_p^{\Lambda^*}}(\theta_p^{\Lambda^*},\phi_p^{\Lambda^*}) = \mathcal{H}^{\Lambda^*\to pK^-}_{\lambda_p^{\Lambda^*},0} D^{*J_{\Lambda^*}}_{\lambda_{\Lambda^*},\lambda_p^{\Lambda^*}}(\phi_p^{\Lambda^*},\theta_p^{\Lambda^*},0)\mathcal{R}(m^2_{pK^-}), \tag{5.7}$$

in which $\mathcal{R}(m^2_{pK^-})$ is the lineshape of the Λ^* resonance. Since strong decays conserve parity the two helicity couplings corresponding to $\lambda_p^{\Lambda^*} = \pm 1/2$ are related by Eq. (1.46),

$$\mathcal{H}^{\Lambda^*\to pK^-}_{-\lambda_p^{\Lambda^*},0} = -P_{\Lambda^*}(-1)^{J_{\Lambda^*}-1/2}\mathcal{H}^{\Lambda^*\to pK^-}_{\lambda_p^{\Lambda^*},0}, \tag{5.8}$$

in which P_{Λ^*} is the parity of the Λ^* resonance and the proton and kaon parities $P_p = 1$, $P_K = -1$ have been inserted. In the fit model these couplings can not be determined independently of $\mathcal{H}^{\Lambda_c^+\to\Lambda^*\pi^+}_{\lambda_{\Lambda^*},0}$ couplings, so that they are absorbed into the latter setting them as $\mathcal{H}^{\Lambda^*\to pK^-}_{+1/2,0} = 1$ and $\mathcal{H}^{\Lambda^*\to pK^-}_{-1/2,0} = -P_{\Lambda^*}(-1)^{J_{\Lambda^*}-1/2}$, with zero imaginary parts. The angles $\phi_p^{\Lambda^*}$ and $\theta_p^{\Lambda^*}$ are the azimuthal and polar angles of the proton momentum in the Λ^* helicity frame, while the proton helicity $\lambda_p^{\Lambda^*}$ is defined in the proton helicity frame reached from the Λ^* resonance.

Considering now the decay chain $\Lambda_c^+ \to \Delta^{++*}(\to p\pi^+)K^-$, the weak decay $\Lambda_c^+ \to \Delta^{++*}K^-$ is described by

$$\mathcal{A}^{\Lambda_c^+\to\Delta^{++*}K^-}_{m_{\Lambda_c^+},\lambda_{\Delta^{++*}}}(\theta_{\Delta^{++*}},\phi_{\Delta^{++*}}) = \mathcal{H}^{\Lambda_c^+\to\Delta^{++*}K^-}_{\lambda_{\Delta^{++*}},0} D^{*1/2}_{\mu,\lambda_{\Delta^{++*}}}(\phi_{\Delta^{++*}},\theta_{\Delta^{++*}},0), \tag{5.9}$$

with two helicity couplings corresponding to $\lambda_{\Delta^{++*}} = \pm 1/2$ to fit for each resonance, as for the Λ^* decay chain. The strong decay $\Delta^{++*} \to p\pi^+$ amplitude is written as

$$\mathcal{A}^{\Delta^{++*}\to p\pi^+}_{\lambda_{\Delta^{++*}},\lambda_p^{\Delta^{++*}}}(\theta_p^{\Delta^{++*}},\phi_p^{\Delta^{++*}}) = \mathcal{H}^{\Delta^{++*}\to p\pi^+}_{\lambda_p^{\Delta^{++*}},0} D^{*J_{\Delta^{++*}}}_{\lambda_{\Delta^{++*}},\lambda_p^{\Delta^{++*}}}(\phi_p^{\Delta^{++*}},\theta_p^{\Delta^{++*}},0)\mathcal{R}(m^2_{p\pi^+}), \tag{5.10}$$

in which $\phi_p^{\Delta^{++*}}$ and $\theta_p^{\Delta^{++*}}$ are defined in the Δ^{++*} helicity frame, and $\lambda_p^{\Delta^{++*}}$ in the proton helicity frame reached from the Δ^{++*} resonance. In the fit model the strong decay helicity couplings are absorbed into $\mathcal{H}^{\Lambda_c^+\to\Delta^{++*}K^-}_{\lambda_{\Delta^{++*}},0}$ setting them to $\mathcal{H}^{\Delta^{++*}\to p\pi^+}_{+1/2,0} = 1$ and

$\mathcal{H}^{\Delta^{+++}\to p\pi^+}_{-1/2,0} = -P_{\Delta^{+++}}(-1)^{J_{\Delta^{+++}}-1/2}$.

For the third decay chain $\Lambda_c^+ \to K^*(\to K^-\pi^+)p$, the weak decay $\Lambda_c^+ \to K^*p$ is described by

$$\mathcal{A}^{\Lambda_c^+\to K^*(\to K^-\pi^+)p}_{m_{\Lambda_c^+},\lambda_{K^*},\lambda_p^{\Lambda_c^+}}(\theta_{K^*},\phi_{K^*}) = \mathcal{H}^{\Lambda_c^+\to K^*p}_{\lambda_{K^*},\lambda_p^{\Lambda_c^+}} D^{*1/2}_{\mu,\lambda_{K^*}-\lambda_p^{\Lambda_c^+}}(\phi_{K^*},\theta_{K^*},0), \tag{5.11}$$

in which $\lambda_p^{\Lambda_c^+}$ is defined in the proton helicity frame reached from the Λ_c^+ baryon. For spin zero K^* resonances angular momentum conservation allows two complex couplings corresponding to $\lambda_p^{\Lambda_c^+} = \pm 1/2$, for higher spin resonances four couplings are allowed, corresponding to $\{\lambda_{K^*} = 0,1;\ \lambda_p^{\Lambda_c^+} = 1/2\}$ and $\{\lambda_{K^*} = -1,0;\ \lambda_p^{\Lambda_c^+} = -1/2\}$. The strong decay $K^* \to K^-\pi^+$ contribution is

$$\mathcal{A}^{K^*\to K^-\pi^+}_{\lambda_{K^*}} = \mathcal{H}^{K^*\to K^-\pi^+}_{0,0} D^{*J_{K^*}}_{\lambda_{K^*},0}(\phi_K,\theta_K,0)\mathcal{R}(m^2_{K^-\pi^+}), \tag{5.12}$$

in which ϕ_K and θ_K are the kaon azimuthal and polar angles in the K^* helicity frame. In the fit model the coupling $\mathcal{H}^{K^*\to K^-\pi^+}_{0,0}$ is set equal to 1 and absorbed in $\mathcal{H}^{\Lambda_c^+\to K^*p}_{\lambda_{K^*},\lambda_p^{\Lambda_c^+}}$.

Before summing the amplitudes, the different proton helicity frames defined for each decay chain must be rotated to a reference proton spin frame. The reference proton spin frame is taken to be the canonical frame reached from the Λ_c^+ polarisation frame, the one obtained by a pure boost from the Λ_c^+ to the proton rest frames. The other proton helicity frames are rotated to the reference one by means of the Euler rotation Eq. (1.52). The Euler angles are determined applying Eq. (1.27) to the coordinate axes describing each proton helicity frame obtained by sequentially applying the helicity transformations to the Λ_c^+ polarisation frame, by sequentially applying the helicity rotations to the latter system. After application of the proton spin rotation, as in Eq. (1.53), the helicity amplitudes for the three kind of intermediate states become, denoting with m_p the proton spin projection in its canonical reference frame,

$$\begin{aligned}
\mathcal{A}^{\Lambda_c^+\to\Lambda^*(\to pK^-)\pi^+}_{m_{\Lambda_c^+},\lambda_{\Lambda^*},m_p}(\Omega) = &\sum_{\lambda_p^{\Lambda^*}=\pm 1/2} D^{*1/2}_{\lambda_p^{\Lambda^*},m_p}(\alpha_{\Lambda^*},\beta_{\Lambda^*},\gamma_{\Lambda^*}) \\
&\times D^{*1/2}_{m_{\Lambda_c^+},\lambda_{\Lambda^*}}(\phi_{\Lambda^*},\theta_{\Lambda^*},0) D^{*J_{\Lambda^*}}_{\lambda_{\Lambda^*},\lambda_p^{\Lambda^*}}(\phi_p^{\Lambda^*},\theta_p^{\Lambda^*},0) \\
&\times \mathcal{H}^{\Lambda_c^+\to\Lambda^*\pi^+}_{\lambda_{\Lambda^*},0}\mathcal{H}^{\Lambda^*\to pK^-}_{\lambda_p^{\Lambda^*},0}\mathcal{R}(m^2_{pK^-}), \\
\mathcal{A}^{\Lambda_c^+\to\Delta^{+++}(\to p\pi^+)K^-}_{m_{\Lambda_c^+},\lambda_{\Delta^{+++}},m_p}(\Omega) = &\sum_{\lambda_p^{\Delta^{+++}}=\pm 1/2} D^{*1/2}_{\lambda_p^{\Delta^{+++}},m_p}(\alpha_{\Delta^{+++}},\beta_{\Delta^{+++}},\gamma_{\Delta^{+++}}) \\
&\times D^{*1/2}_{m_{\Lambda_c^+},\lambda_{\Delta^{+++}}}(\phi_{\Delta^{+++}},\theta_{\Delta^{+++}},0) D^{*J_{\Delta^{+++}}}_{\lambda_{\Delta^{+++}},\lambda_p^{\Delta^{+++}}}(\phi_p^{\Delta^{+++}},\theta_p^{\Delta^{+++}},0) \\
&\times \mathcal{H}^{\Lambda_c^+\to\Delta^{+++}K^-}_{\lambda_{\Delta^{+++}},0}\mathcal{H}^{\Delta^{+++}\to p\pi^+}_{\lambda_p^{\Delta^{+++}},0}\mathcal{R}(m^2_{p\pi^+}),
\end{aligned}$$

$$\begin{aligned}\mathcal{A}^{\Lambda_c^+\to K^*(K^-\pi^+)p}_{m_{\Lambda_c^+},\lambda_{K^*},m_p}(\Omega) = &\sum_{\lambda_p^{\Lambda_c^+}=\pm 1/2} D^{*1/2}_{\lambda_p^{\Lambda_c^+},m_p}(\alpha_{K^*},\beta_{K^*},\gamma_{K^*}) \\ &\times D^{*1/2}_{m_{\Lambda_c^+},\lambda_{K^*}-\lambda_p^{\Lambda_c^+}}(\phi_{K^*},\theta_{K^*},0) D^{*J_{K^*}}_{\lambda_{K^*},0}(\phi_K,\theta_K,0) \\ &\times \mathcal{H}^{\Lambda_c^+\to K^* p}_{\lambda_{K^*},\lambda_p^{\Lambda_c^+}} \mathcal{H}^{K^*\to K^-\pi^+}_{0,0} \mathcal{R}(m^2_{K^-\pi^+}). \end{aligned} \tag{5.13}$$

The complete amplitude for the $\Lambda_c^+ \to pK^-\pi^+$ decay is obtained summing the amplitudes for all the intermediate resonances and their allowed helicity states, like in Eq. (1.54),

$$\begin{aligned}\mathcal{A}_{m_{\Lambda_c^+},m_p}(\Omega) = &\sum_{i=1}^{N_{\Lambda^*}} \sum_{\lambda_{\Lambda_i^*}} \mathcal{A}^{\Lambda_c^+\to \Lambda_i^*(\to pK^-)\pi^+}_{m_{\Lambda_c^+},\lambda_{\Lambda_i^*},m_p}(\Omega) \\ &+ \sum_{j=1}^{N_{\Delta^{++*}}} \sum_{\lambda_{\Delta_j^{++*}}} \mathcal{A}^{\Lambda_c^+\to \Delta_j^{++*}(\to p\pi^+)K^-}_{m_{\Lambda_c^+},\lambda_{\Delta_j^{++*}},m_p}(\Omega) \\ &+ \sum_{k=1}^{N_{K^*}} \sum_{\lambda_{K_k^*}} \mathcal{A}^{\Lambda_c^+\to K_k^*(K^-\pi^+)p}_{m_{\Lambda_c^+},\lambda_{K_k^*},m_p}(\Omega). \end{aligned} \tag{5.14}$$

The differential decay rate for Λ_c^+ baryons in a generic state of polarisation to be measured from the amplitude fit, is represented by Eq. (1.56). The most general spin $1/2$ density matrix is

$$\rho^{\Lambda_c^+} = \frac{1}{2}\left(\mathbb{I} + \boldsymbol{P}\cdot\boldsymbol{\sigma}\right) = \frac{1}{2}\begin{pmatrix} 1+P_z & P_x - iP_y \\ P_x + iP_y & 1-P_z \end{pmatrix}, \tag{5.15}$$

in which P_x, P_y, P_z are the polarisation components in the chosen coordinate system and $\boldsymbol{\sigma}$ the three Pauli matrices. The density matrix representing the $pK^-\pi^+$ polarisation is that of a maximally mixed state (in any proton spin basis)

$$\rho^{pK^-\pi^+} = \frac{\mathbb{I}}{2}, \tag{5.16}$$

since the proton polarisation can not be measured.

The transition operator matrix elements in the chosen Λ_c^+ and proton spin bases are the helicity amplitudes $\mathcal{A}_{m_{\Lambda_c^+},m_p}(\Omega)$, Eq. (5.14)

$$T = \begin{pmatrix} \mathcal{A}_{1/2,1/2}(\Omega) & \mathcal{A}_{1/2,-1/2}(\Omega) \\ \mathcal{A}_{-1/2,1/2}(\Omega) & \mathcal{A}_{-1/2,-1/2}(\Omega) \end{pmatrix}, \tag{5.17}$$

and the differential rate Eq. (1.56) turns out to be proportional to

$$\begin{aligned} p(\Omega, \vec{P}) \propto \sum_{m_p=\pm 1/2} \Big[&(1+P_z)|\mathcal{A}_{1/2,m_p}(\Omega)|^2 + (1-P_z)|\mathcal{A}_{-1/2,m_p}(\Omega)|^2 \\ &+ (P_x - iP_y)\mathcal{A}^*_{1/2,m_p}(\Omega)\mathcal{A}_{-1/2,m_p}(\Omega) \\ &+ (P_x + iP_y)\mathcal{A}_{1/2,m_p}(\Omega)\mathcal{A}^*_{-1/2,m_p}(\Omega) \Big]. \end{aligned} \tag{5.18}$$

5.2.4 Polarisation effects on the phase space distributions

Following the discussion in Sec. 1.4.6, the presence of a Λ_c^+ polarisation can only influence the three angular distributions $\cos\theta_p, \phi_p, \chi$ describing the orientation of the decay plane. These effects can be easily seen using the Dalitz plot decomposition proposed in Ref. [157], which factorises the decay amplitude separating invariant mass and orientation angles dependence. For the $\Lambda_c^+ \to pK^-\pi^+$ decay the decomposition is written as

$$\mathcal{A}_{m_{\Lambda_c^+}, m_p}(\Omega) = \sum_{\nu_{\Lambda_c^+}} D^{*1/2}_{m_{\Lambda_c^+}, \nu_{\Lambda_c^+}}(\phi_p, \theta_p, \chi) O^{\nu_{\Lambda_c^+}}_{m_p}(m^2_{pK^-}, m^2_{K^-\pi^+}), \tag{5.19}$$

in which the Wigner D matrix describes the rotation of the Λ_c^+ spin states from its polarisation frame to the decay plane coordinate system defined in Sec. 5.2.2, while the rest of the amplitude $O^{\nu_{\Lambda_c^+}}_{m_p}(m^2_{pK^-}, m^2_{K^-\pi^+})$ describes the Λ_c^+ decay amplitude in terms of Λ_c^+ spin projections expressed in the decay plane coordinate system. This way of writing the $\Lambda_c^+ \to pK^-\pi^+$ amplitude model is equivalent to that described in Sec. 5.2.3. In that case, the relation between Λ_c^+ and resonant states is done starting directly from the Λ_c^+ polarisation frame, and the intermediate state helicity angles θ_R, ϕ_R depend on all the five phase space variables.

The decay rate following from the decomposition Eq. (5.19) in terms of the Λ_c^+ density matrix is (omitting Λ_c^+ subscripts)

$$\begin{aligned} p(\Omega, \vec{P}) \propto &\sum_{m,m'} \rho_{m,m'} \sum_{\nu,\nu'} D^{*1/2}_{m,\nu}(\phi_p, \theta_p, \chi) D^{1/2}_{m',\nu'}(\phi_p, \theta_p, \chi) \\ &\times \sum_{m_p} O^{\nu}_{m_p}(m^2_{pK^-}, m^2_{K^-\pi^+}) O^{*\nu'}_{m_p}(m^2_{pK^-}, m^2_{K^-\pi^+}). \end{aligned} \tag{5.20}$$

The properties of the decay rate described in Sec. 1.4.6 following from rotational invariance are apparent from the properties of the D rotation matrices. For unpolarised baryons, $\rho_{m,m'} = \delta_{m,m'}/2$, isotropy follows from the orthogonality of the rotation operators

$$\sum_m D^{*1/2}_{m,\nu}(\phi_p, \theta_p, \chi) D^{1/2}_{m,\nu'}(\phi_p, \theta_p, \chi) \propto \delta_{\nu,\nu'}, \tag{5.21}$$

while the independence of invariant mass distributions from the polarisation vector follows from the orthogonality relation

$$\int_{-\pi}^{\pi} d\phi_p \int_{-\pi}^{\pi} d\chi \int_0^{\pi} d\cos\theta_p D^{*1/2}_{m,\nu}(\phi_p, \theta_p, \chi) D^{1/2}_{m',\nu'}(\phi_p, \theta_p, \chi) \propto \delta_{m,m'}\delta_{\nu,\nu'}. \tag{5.22}$$

The effects of the polarisation vector on the decay distribution have a simple dependence on the decay plane orientation angles, which can be shown from the decay rate decom-

position Eq. (5.20) after some algebraic operations, integrating over the invariant mass variables. A z-components polarisation introduces a $P_z \cos\theta_p$ dependence, while the orthogonal components affect the azimuthal proton angle distribution adding a $P_x \cos\phi_p$ or $P_y \sin\phi_p$ dependence. Basically, this simple angular dependence describes the projection of the Λ_c^+ polarisation vector on the decay plane coordinate system. Note that the structure of the Λ_c^+ decay amplitude, described by the $O^{\nu_{\Lambda_c^+}}_{m_p}(m^2_{pK^-}, m^2_{K^-\pi^+})$ terms, determines the coefficients multiplying the polarisation-dependent angular terms, influencing the decay sensitivity to the polarisation components.

5.3 Data and simulation samples

The data samples considered in this analysis consist of pp collisions recorded by the LHCb experiment in 2015 and 2016, corresponding to integrated luminosities of 0.33 and 1.67 fb^{-1}, respectively. The $\Lambda_c^+ \to pK^-\pi^+$ signal candidates are selected from semileptonic Λ_b^0 decays by using a filtering set of criteria, called `B2DMuNuX_Lc` stripping line,whose selection criteria are listed in Table 5.1. Candidates are also required to have activated the following trigger lines of the LHCb trigger system, described in Sec. 4.2.3: `L0Muon`, `Hlt1TrackMuon` and one of the topological `Hlt2TopoMuNBodyDecision`, $N = 2, 3, 4$, trigger lines. The `L0Muon` hardware trigger line requires the event to contain a muon with sufficiently high $p_{\rm T}$; the `Hlt1TrackMuon` trigger is devised for selecting heavy hadrons decaying to at least one muon by exploiting the muon $p_{\rm T}$ and χ^2 impact parameter with respect to the primary vertex; the `Hlt2TopoMuNBodyDecision` triggers exploit the event topological information in a Boosted Decision Tree to trigger inclusively on heavy hadron decays to N particles including one muon. The five $\Lambda_c^+ \to pK^-\pi^+$ phase-space variables are computed applying the kinematic fitter *DecayTreeFitter* [158], performing a refitting of the entire decay chain fixing the reconstructed Λ_c^+ invariant mass to the PDG value [24].

Two simulation samples are used in the analysis. The first reproduces semileptonic $\Lambda_b^0 \to \Lambda_c^+ \ell^- \bar{\nu}_\ell$ decays, $l = \mu^-, \tau^-$, with the $\Lambda_c^+ \to pK^-\pi^+$ decay simulated with a simple decay model including the three resonances $\Lambda^*(1520), \Delta^{++*}(1232), K^*(892)$ and a flat phase space component, which compose the E791 amplitude model [71]. This sample consists of 10^7 generated events, of which $\approx 130'000$ passing stripping and trigger requirements, and will be referred to as "full simulation". A second simulation sample with higher statistics is generated using the faster-simulation option *ReDecay* [159], which reduces by 10 times the CPU consumption by re-using each complete simulated event by generating 100 signal decays which are added to the same non-signal part of the event. This sample reproduces $\Lambda_c^+ \to pK^-\pi^+$ flat phase space decays from semileptonic $\Lambda_b^0 \to \Lambda_c^+ \mu^- \bar{\nu}_\mu$ events and consists of 1.6 millions events after stripping and trigger requirements. Distributions for different physical quantities, including the $\Lambda_c^+ \to pK^-\pi^+$ phase space variables, have been compared between the two simulation samples, to check the assumptions behind the *ReDecay* method are suitable for the analysis purposes. The validation plots are reported in Appendix A.2, in which only the flat phase space $\Lambda_c^+ \to pK^-\pi^+$ events are selected for comparison. Simulated events which are not reconstructed as signal $\Lambda_c^+ \to pK^-\pi^+$ decays are removed from the simulation samples (truth-matching).

Particle	Quantity	Requirement
μ	min p_T	1 GeV
	min p	6 GeV
	track ghost probability	< 0.35
	track χ^2/ndf	< 3
	min primary vertex IP χ^2	9
	min PID_μ	0
hadron	min p_T	250 MeV
	track ghost probability	< 0.35
	track χ^2/ndf	< 3
	min primary vertex IP χ^2	4
K	min p	2 GeV
	min PID_K	-2
π	min p	2 GeV
	max PID_K	10
p	min p	8 GeV
	min PID_p	0
	min $\mathrm{PID}_p - \mathrm{PID}_K$	0
Λ_c^+	$m(pK\pi)$ interval	$m(\Lambda_c^+)_{\mathrm{PDG}} \pm 80\,\mathrm{MeV}$
	DOCA χ^2 limit between daughter tracks	20
	max vertex χ^2/ndf	6.0
	min χ^2 distance from primary vertex	25
	min $cos(\mathrm{DIRA})$	0.99
Λ_b^0	$m(\Lambda_c^+\mu)$ interval	2.2-8.0 GeV
	DOCA χ^2 limit between daughter tracks	10
	max vertex χ^2/ndf	9.0
	min $cos(\mathrm{DIRA})$	0.999
	Λ_c^+ vertex z position - Λ_b^0 vertex z position	$> -2\,\mathrm{mm}$

Table 5.1: `B2DMuNuX_Lc` stripping line selection criteria. Ghost probability refers to the probability of the track to be a fake one; track χ^2/ndf is computed from the track fit done at event reconstruction stage; PID_h is the delta log-likelihood between h and pion identities obtained from particle identification systems; DOCA is the distance of closest approach between a pair of tracks; DIRA is the angle between the momentum of the particle and the direction of flight from the primary vertex to the decay vertex.

Quantity	Requirement
Λ_c^+ vertex z position - Λ_b^0 vertex z position	< 6 mm
$\log(\mathrm{FD}\chi^2)(\Lambda_b^0)$	> 6.5
$\mathrm{ProbNN}(p \to p)$	> 0.95
$\mathrm{ProbNN}(p \to K^-)$	> 0.7

Table 5.2: Selection requirements for $\Lambda_c^+ \to pK^-\pi^+$ candidates from Λ_b^0 semileptonic decays. See text for quantity definitions.

5.3.1 Selection and invariant mass fit

A tight selection is developed to reduce the combinatorial background contamination to a level small enough to neglect its contribution to the amplitude fit. A cut-based selection has been studied on 2015 year data, its requirements reported in Table 5.2. The selection requires $\Lambda_c^+ \to pK^-\pi^+$ candidates to have: a limited displacement between Λ_c^+ and Λ_b^0 vertex z positions; a Λ_b^0 vertex separated from the primary vertex, measured by the logarithm of the flight distance χ^2, $\log(\mathrm{FD}\chi^2)(\Lambda_b^0)$; good particle identification responses for proton and kaon hadrons, measured from the neural-network based $\mathrm{ProbNN}(h \to h')$ variables representing the probability for the hadron h to be identified as h'. The separation between signal and background distributions for the employed variables, obtained applying the *sPlot* statistical technique [160] to the 2015 data sample, is displayed in Fig. 5.3. The requirement on the proton identification $\mathrm{ProbNN}(p \to p)$ is by far the most effective.

To evaluate the amount of combinatorial background passing the selection requirements, its contribution is separated from $\Lambda_c^+ \to pK^-\pi^+$ candidates by means of a fit to the $pK^-\pi^+$ invariant mass distribution. The $\Lambda_c^+ \to pK^-\pi^+$ candidates are modelled using two Crystal-Ball PDFs with asymmetric power-law tails, while the combinatorial background is parametrised by an exponential PDF $\propto e^{cx}$. The Crystal Ball PDF is a four-parameter function made of a Gaussian connected with a power-law tail in such a way to have continuous derivative,

$$CB(x|\overline{x},\sigma,\alpha,n) = N \begin{cases} \exp\left(\frac{(x-\overline{x})^2}{2\sigma^2}\right) & \text{for } \alpha > 0, \frac{(x-\overline{x})}{\sigma} > -\alpha \\ & \text{for } \alpha < 0, \frac{(x-\overline{x})}{\sigma} < -\alpha \\ A\left(B - \frac{(x-\overline{x})}{\sigma}\right)^{-n} & \text{for } \alpha > 0, \frac{(x-\overline{x})}{\sigma} < -\alpha \\ & \text{for } \alpha < 0, \frac{(x-\overline{x})}{\sigma} > -\alpha \end{cases}, \tag{5.23}$$

in which $A = \left(\frac{n}{|\alpha|}\right)^n \exp\left(-\frac{|\alpha^2|}{2}\right)$, $B = \frac{n}{|\alpha|} - |\alpha|$ and N is the normalisation factor.

The fit to the $pK^-\pi^+$ invariant mass distribution for 2016 data selected candidates is shown in Fig. 5.4, results reported in Table 5.3. The selection retains 1.28 millions of $\Lambda_c^+ \to pK^-\pi^+$ candidates, reducing the combinatorial background contribution in the signal region chosen as $|m(pK^-\pi^+) - m(\Lambda_c^+)_{\mathrm{PDG}}| < 15\,\mathrm{MeV}$ to 1.7% of the candidates. Only candidates from this signal region will be employed for the amplitude fits.

The $\Lambda_c^+ \to pK^-\pi^+$ phase space one-dimensional projections of 2016 data selected candidates are reported in Fig. 5.5. The residual background distributions are estimated from the signal sidebands defined as $|m(pK^-\pi^+) - m(\Lambda_c^+)_{\mathrm{PDG}}| > 40\,\mathrm{MeV}$.

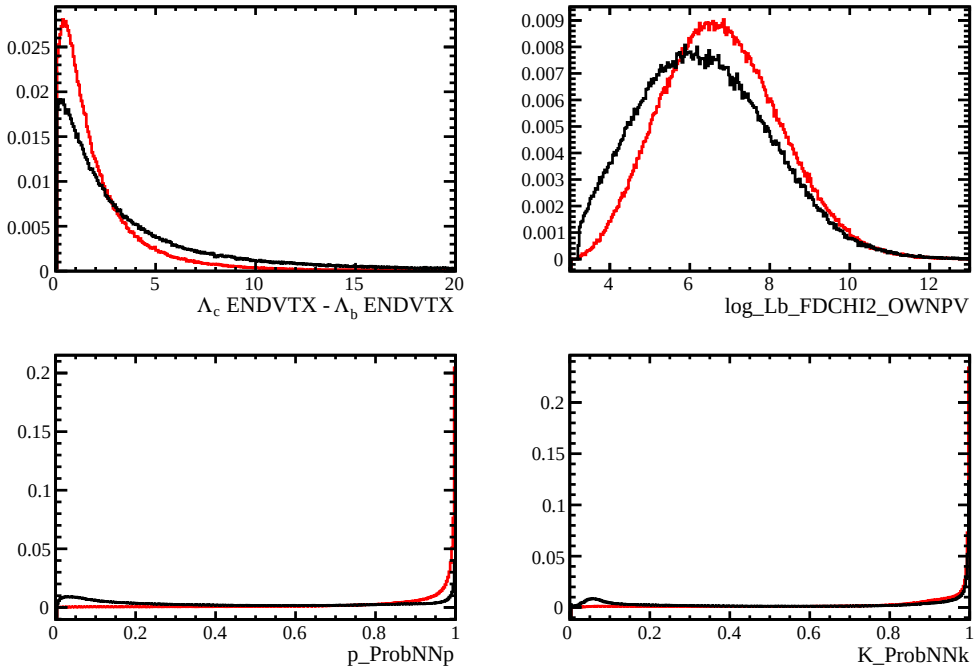

Figure 5.3: Separation between signal (red) and background (black) s-Weighted normalised distributions of the selection variables for 2015 data.

Parameter	Central value ± Uncertainty
Signal events	1281200 ± 1450
Background events	117150 ± 1950
CB $\overline{x}$ $\left[\mathrm{GeV}/c^2\right]$	2.2868 ± 0.00000280
CB1 σ $\left[\mathrm{MeV}/c^2\right]$	4.9518 ± 0.00388
CB2 σ $\left[\mathrm{MeV}/c^2\right]$	8.2588 ± 0.0340
CB1 α	2.3119 ± 0.00212
CB2 α	-4.7914 ± 7.51
CB1 n	1.0774 ± 0.00364
CB2 n	15.166 ± 29.6
CB1 fraction	0.67358 ± 0.000798
Exp c $\left[(\mathrm{GeV}/c^2)^{-1}\right]$	-3.3642 ± 0.217

Table 5.3: Results of the fit to the $pK^-\pi^+$ invariant mass of 2016 data selected candidates.

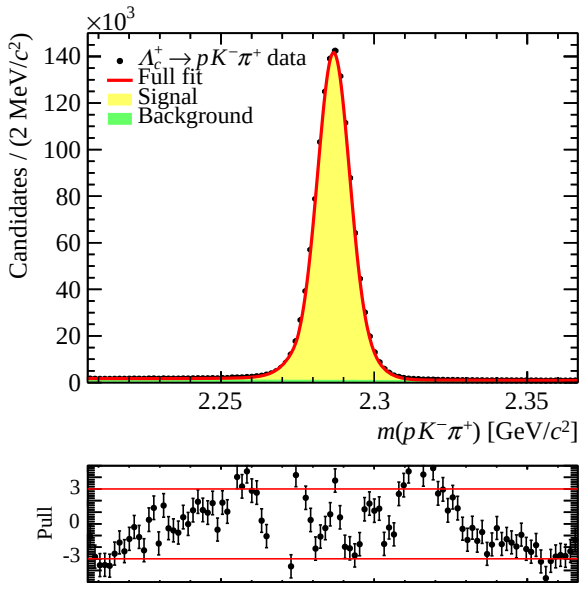

Figure 5.4: Fit to the $pK^-\pi^+$ invariant mass of 2016 data selected candidates. The distribution of the residuals is reported as a check of the fit quality. Note that due to the very high number of events $> 10^6$ a perfect agreement between data and the effective fit model is almost impossible, since the fit becomes sensitive to fine details of the invariant mass distribution.

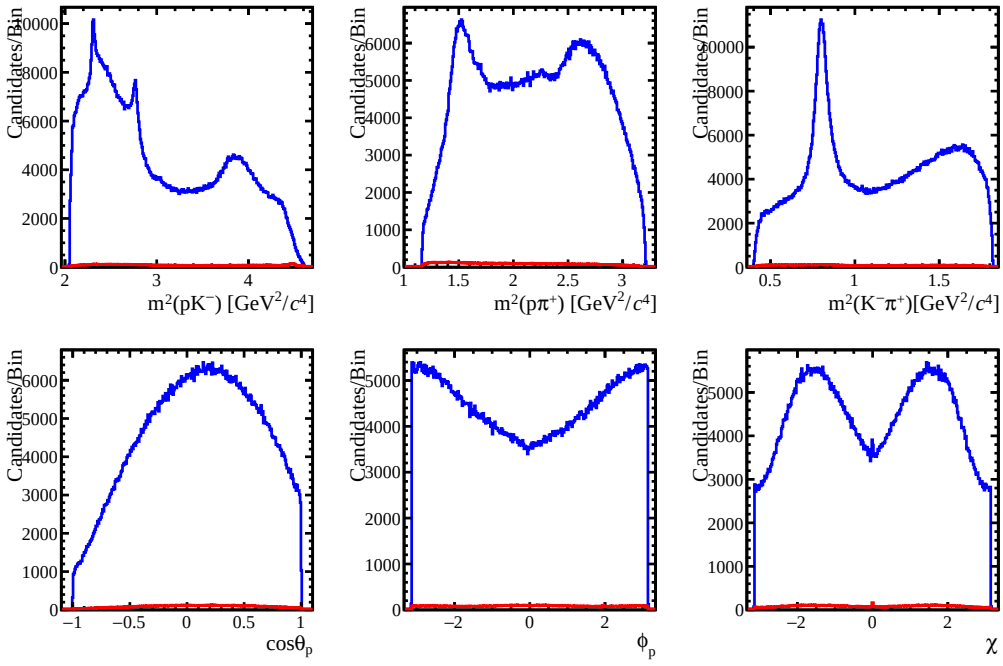

Figure 5.5: (blue) $\Lambda_c^+ \to pK^-\pi^+$ phase space one-dimensional projections of 2016 data selected candidates. (red) background contribution estimated from the signal sidebands.

5.3.2 Physical backgrounds

Three-body hadronic decays of charm hadrons can constitute potential physical backgrounds to the $\Lambda_c^+ \to pK^-\pi^+$ decays if some of the final-state hadrons are wrongly identified. The Cabibbo-favoured $D^+ \to K^+\pi^-\pi^+$ and $D_s^+ \to K^+K^-\pi^+$ may enter the signal region due to a proton mis-identification, while Cabibbo-suppressed $\Lambda_c^+ \to pK^-K^+$ and $\Lambda_c^+ \to p\pi^-\pi^+$ may fake signal candidates due to a wrong kaon or pion assignment. Moreover, four-body decays of charm mesons in which one hadron is not reconstructed may contribute as well to the Λ_c^+ signal region. The presence of these physical backgrounds is searched for by reconstructing the invariant mass of the three daughter particle with different mass hypothesis plotted versus the $pK^-\pi^+$ invariant mass. Fig. 5.6 shows the invariant mass distributions for candidates passing stripping and trigger requirements only. Contributions from $D^+ \to K^+\pi^-\pi^+$ and $D_s^+ \to K^+K^-\pi^+$ decays due to single mis-identifications are visible as horizontal lines corresponding to D^+ and D_s^+ invariant masses, while $\Lambda_c^+ \to pK^-K^+$ and $\Lambda_c^+ \to p\pi^-\pi^+$ decays do not contribute because outside the range covered by $\Lambda_c^+ \to pK^-\pi^+$ candidates (the horizontal band corresponding to the Λ_c^+ mass is empty). No broader structures at $K^+\pi^-\pi^+$ and $K^+K^-\pi^+$ invariant masses lower than D^+ and D_s^+ masses, indicating partially reconstructed decays, are visible. After application of the selection requirements no evidence of residual physical backgrounds is visible, Fig. 5.7. In fact, charm meson decays are effectively rejected by the tight proton PID requirement.

A complementary study, which is more sensitive to partially reconstructed backgrounds, is performed by plotting the momentum asymmetries of the Λ_c^+ daughters versus the $pK^-\pi^+$ invariant mass. The three momentum asymmetries β_h for $h = p, K^-, \pi^+$ hadrons versus the other two hadrons in the decay h_1, h_2 is defined as

$$\beta_h = \frac{p(h_1) + p(h_2) - p(h)}{p(h_1) + p(h_2) + p(h)}. \tag{5.24}$$

Along with the Λ_c^+ invariant mass under the nominal $\Lambda_c^+ \to pK^-\pi^+$ mass assignment, it fully parametrises alternative mass hypotheses in which the assignment of the h hadron is changed. The $\beta_h - m(pK^-\pi^+)$ plane therefore provides an additional check. Fig. 5.8 shows the momentum asymmetry distributions for the three hadrons, for candidates passing stripping and trigger requirements only: sharp bands are visible only for β_p, these corresponding to the already observed $D^+ \to K^+\pi^-\pi^+$ and $D_s^+ \to K^+K^-\pi^+$ backgrounds. No broader structures highlighting partially reconstructed decays are present. After application of the full selection no evidence of residual physical backgrounds is visible, Fig. 5.9. Therefore, no selection cuts against physical backgrounds are applied.

5.3.3 Comparison between real and simulated data

Simulated data are used in this analysis to describe the efficiency of the detector as a function of the $\Lambda_c^+ \to pK^-\pi^+$ decay phase space variables. To properly subtract the detector efficiency reconstruction effects it is therefore crucial for the simulation to reproduce real data as accurately as possible.

The variables used to select $\Lambda_c^+ \to pK^-\pi^+$ candidates, listed in Table 5.2, have been chosen not only for their ability to separate signal from combinatorial background, but also because their distributions are well reproduced in simulation. Fig. 5.10 reports the comparison between s-Weighted $\Lambda_c^+ \to pK^-\pi^+$ real data and simulated ReDecay sample distributions for the selection variables. The agreement is quite good, even if not

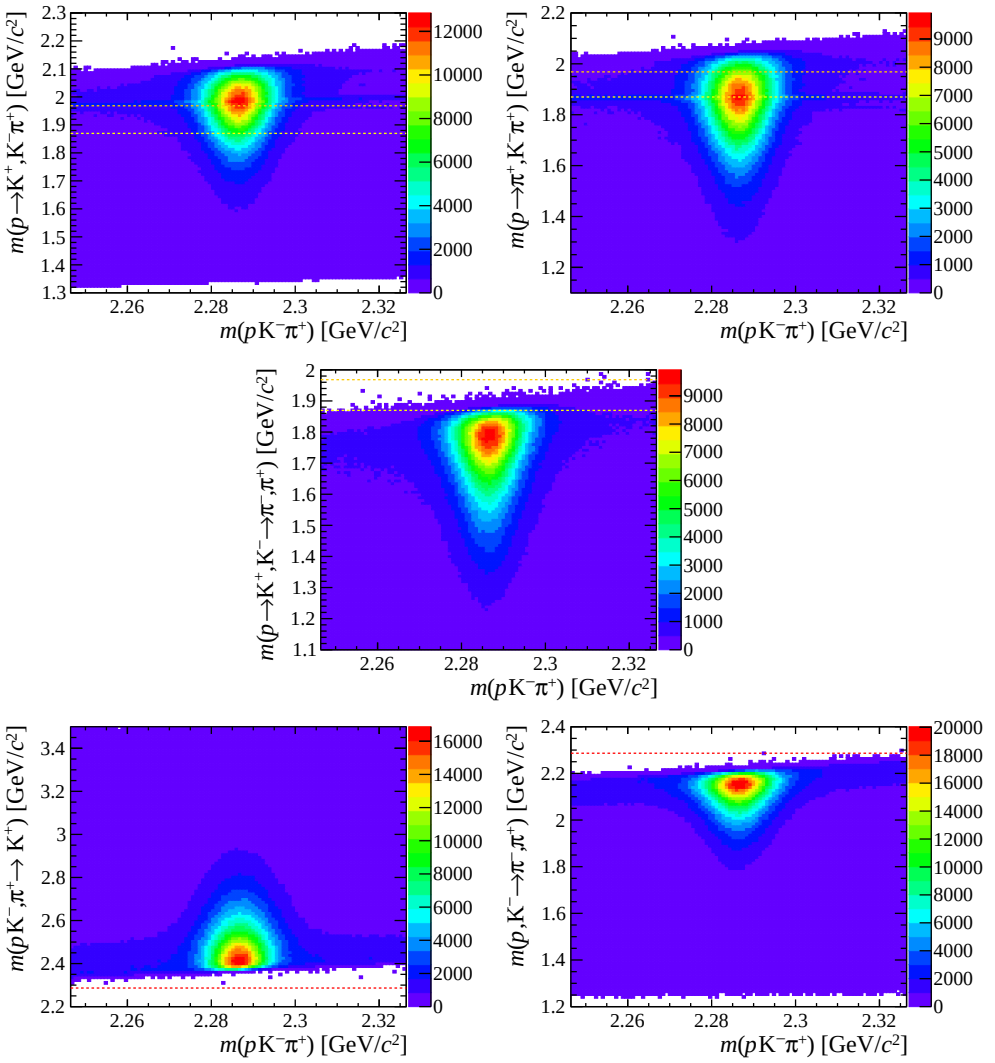

Figure 5.6: Invariant mass distributions for $pK^-\pi^+$ mass hypothesis versus (Top, Center) $D^+_{(s)} \to h^+h^-h^+$ and (Bottom) $\Lambda_c^+ \to ph^-h^+$ alternative mass hypothesis for candidates passing stripping and trigger requirements. Horizontal dashed lines correspond to the (yellow) D^+, (orange) D_s^+ and (red) Λ_c^+ PDG masses [24].

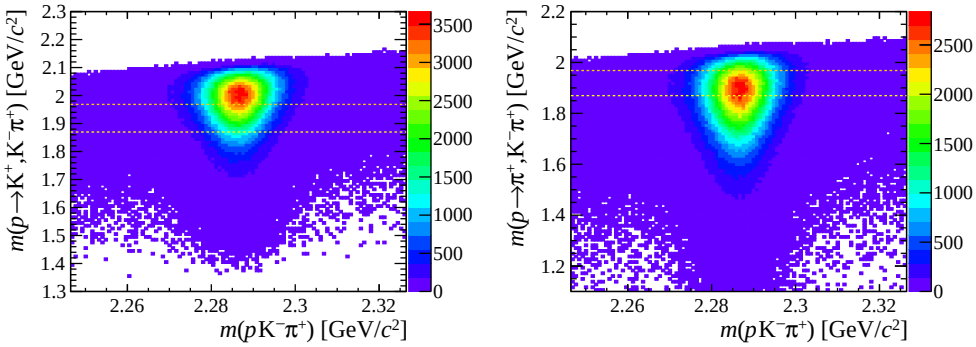

Figure 5.7: Invariant mass distributions for $pK^-\pi^+$ mass hypothesis versus $D^+_{(s)} \to h^+h^-h^+$ alternative mass hypothesis for candidates passing the full selection process. Horizontal dashed lines correspond to the (yellow) D^+, (orange) D^+_s and (red) Λ^+_c PDG masses [24]

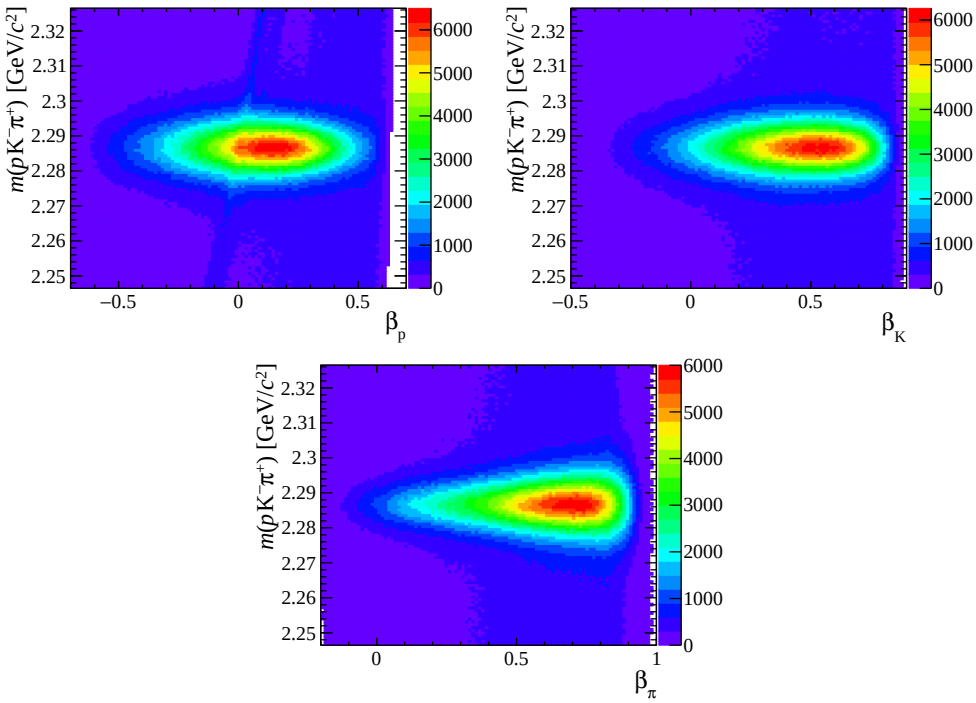

Figure 5.8: Invariant mass distributions for $pK^-\pi^+$ mass hypothesis versus hadron momentum asymmetries for candidates selected with stripping and trigger requirements only.

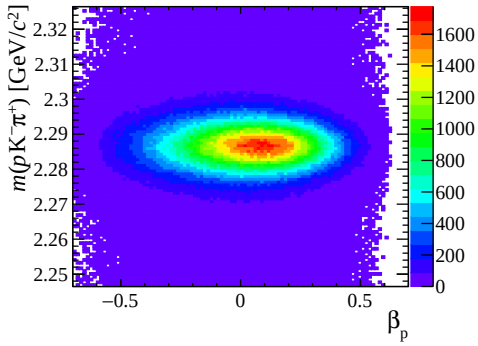

Figure 5.9: Invariant mass distributions for $pK^-\pi^+$ mass hypothesis versus proton momentum asymmetry for candidates passing the full selection process.

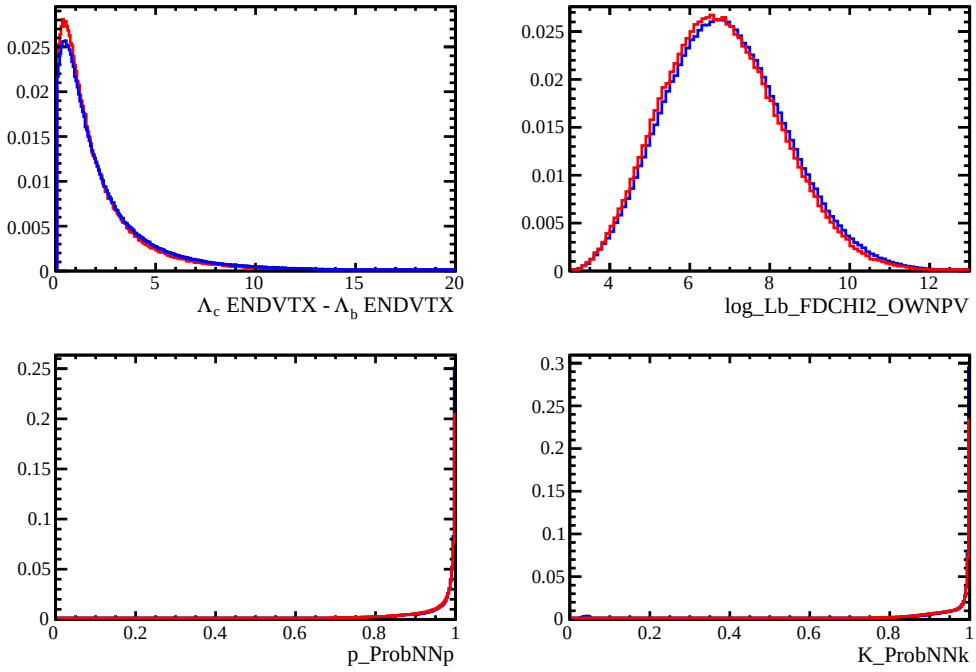

Figure 5.10: Selection variable normalised distributions for s-Weighted $\Lambda_c^+ \to pK^-\pi^+$ data candidates (red) and simulated ReDecay sample (blue).

perfect, but it is important to stress that a perfect agreement between real and simulated data is difficult to achieve since the real $\Lambda_c^+ \to pK^-\pi^+$ decay structure is unknown, its determination being the target of this analysis.

5.4 Amplitude fit

The amplitude model free parameters, collectively indicated as ω, are determined from a maximum likelihood (ML) fit to the data sample $\{\Omega_i\}$ by minimising the negative logarithmic likelihood (NLL)

$$-\log \mathcal{L}(\omega) = -\sum_{i=1}^{N} \log p_{tot}(\Omega_i|\omega), \tag{5.25}$$

in which $p_{tot}(\Omega_i|\omega)$ represents the total fitting PDF,

$$p_{tot}(\Omega_i|\omega) = \frac{p(\Omega_i|\omega)\epsilon(\Omega_i)}{I(\omega)}\frac{n_{sig}}{N} + p_{bkg}(\Omega_i)\frac{n_{bkg}}{N}, \tag{5.26}$$

describing the conditional probability of having the experimental points Ω_i given the parameters ω. This PDF includes the $\Lambda_c^+ \to pK^-\pi^+$ decay rate Eq. (5.18) now indicated as $p(\Omega_i|\omega)$, the efficiency variation over the phase space $\epsilon(\Omega)$ and the background contribution, which, in this approach, is included in the amplitude model with a parametric PDF $p_{bkg}(\Omega)$ rather than statistically subtracted (see Ref. [75] for a comparison of the two methods). The number of signal and background events, n_{sig} and n_{bkg}, can be determined from the fit to the Λ_c^+ invariant mass, Fig. 5.4. $I(\omega)$ is the normalisation of the signal part of the total PDF,

$$I(\omega) = \int p(\Omega|\omega)\epsilon(\Omega)d\Omega, \tag{5.27}$$

which can be computed numerically without explicitly knowing the efficiency function $\epsilon(\Omega)$, by using simulated flat phase space events reconstructed through the detector. Indeed, the integration variables can be changed from the decay phase space $d\Omega$ to the phase space as seen from the detector viewpoint $d\Omega' = \epsilon(\Omega)d\Omega$, so that

$$I(\omega) = \int p(\Omega|\omega)d\Omega' = \frac{\sum_i p(\Omega_i^{\rm MC}|\omega)}{N^{\rm MC}}, \tag{5.28}$$

in which $\{\Omega_i^{\rm MC}\}$, $i = \{1, ..., N^{\rm MC}\}$ are the simulated phase space points.

Exploiting the logarithm properties, the log-likelihood Eq. (5.25) can be rewritten as

$$\begin{aligned} -\log \mathcal{L}(\omega) = &-\sum_{i=1}^{N} \log\left[p(\Omega_i|\omega) + \frac{p_{bkg}(\Omega_i)I(\omega)}{\epsilon(\Omega_i)}\frac{n_{bkg}}{n_{sig}}\right] \\ &+ N\log I(\omega) + \text{constant}, \end{aligned} \tag{5.29}$$

showing that in presence of a background contribution, both the efficiency and background functions over the decay phase space $\epsilon(\Omega)$ and $p_{bkg}(\Omega)$ need to be parametrised. However, their contribution to the parameter estimation is proportional to the ratio n_{bkg}/n_{sig}, which for a good background rejection is small, and any systematic uncer-

tainty associated to the choice of the parametrisation is suppressed by this ratio. The tight selection presented in Section 5.3.1 reduces the ratio to $n_{bkg}/n_{sig} = 1.7\%$, small enough to neglect the background contribution (see Fig. 5.5). In this case the NLL becomes

$$-\log\mathcal{L}(\omega) = -\sum_{i=1}^{N}\log p(\Omega_i|\omega) + N\log I(\omega) + \text{constant}, \tag{5.30}$$

and no efficiency parametrisation is needed since its effect is folded in the computation of the amplitude model normalisation, Eq. (5.28).

The central value of the parameters ω are estimated by finding the stationary points ω_0 of the NLL, corresponding to

$$\frac{\partial\log\mathcal{L}(\omega)}{\partial\omega} = \sum_{i=1}^{N}\frac{\partial p_{tot}(\Omega_i|\omega)}{\partial\omega}\frac{1}{p_{tot}(\Omega_i|\omega)} = 0. \tag{5.31}$$

For generic likelihoods, the 1σ statistical standard deviation of the fit parameters ω is given by the multi-dimensional contour defined by

$$\log\mathcal{L}(\omega_0) - \log\mathcal{L}(\omega) = \frac{1}{2}, \tag{5.32}$$

which, in practice, is very arduous to compute for a large number of parameters. In many practical cases the likelihood function is approximately Gaussian, and the NLL parabolic in ω. In this case, the second derivative of the NLL is related to the variance of the Gaussian likelihood function as

$$\begin{aligned}-\frac{\partial^2\log\mathcal{L}(\omega)}{\partial\omega^2}\bigg|_{\omega_0} &= \frac{1}{\sigma^2} \\ &= \sum_{i=1}^{N}\frac{\partial^2 p_{tot}(\Omega_i|\omega)}{\partial\omega^2}\frac{1}{p_{tot}(\Omega_i|\omega)} - \left(\frac{\partial p_{tot}(\Omega_i|\omega)}{\partial\omega}\right)^2\frac{1}{p_{tot}(\Omega_i|\omega)^2},\end{aligned} \tag{5.33}$$

and can be used to estimate the 1σ standard deviation interval associated to each fit parameter. Note that while Eq. (5.32) defines a possibly asymmetric multi-dimensional 1σ contour, Eq. (5.33) returns by construction symmetric 1σ intervals for each parameter independently.

For performing the $\Lambda_c^+ \to pK^-\pi^+$ amplitude analysis the TensorFlowAnalysis package [161] is chosen. TensorFlowAnalysis is a collection of useful functions to perform amplitude fits, developed within the LHCb Collaboration, based on top of the machine-learning framework TensorFlow [162]. An already implemented amplitude model for $\Lambda_c^+ \to pK^-\pi^+$ decays has been generalised from Dalitz plot to full phase space 5-dimensional fit, including the extraction of the Λ_c^+ polarisation vector and the inclusion of detector efficiency effects. The main advantages of the TensorFlowAnalysis package with respect to other amplitude fit frameworks are those following from Tensorflow features.

Tensorflow is based on the computer algebra paradigm, in which users do not run directly calculations, but specify the computational graph describing what has to be computed. For example, the definition of the amplitude model can be more flexible since the explicit data flow behind its definition needs not to be specified, but it is handled automatically by Tensorflow. Tensorflow is able to handle tensor data, optimise auto-

matically the computational graph, and compile for different architectures. This is very important for the present analysis, since the amplitude model is complicated due to the presence of sequential decays, involving many rotations, and a large number of resonant states, which would be prohibitive to implement using basic, hard-coded functions.

One drawback is that Tensorflow built-in minimisation functions are not suitable for physics, since they do not deal with the errors associated to fit parameters. For this reason the TensorFlowAnalysis package exploits the MINUIT package for ML fits [163]. In MINUIT, the NLL minimisation algorithm MIGRAD is employed, along with the HESSE method for computing 1σ standard deviations by means of Eq. (5.33). MINUIT also provides the MINOS method for error computation, which returns asymmetric 1σ standard deviation intervals representing 1-dimensional projections of the contour Eq. (5.32) for each fit parameter. The MINOS method is not used by default since it is very demanding in terms of computational resources; tests on simplified amplitude models showed that MINOS errors are not significantly different from HESSE ones.

The free parameters ω include the real and imaginary parts of the complex helicity couplings, resonance parameters like masses and widths and the three Λ_c^+ polarisation components. Since the normalisation of the model is fixed, Eq. (5.27), one of the helicity couplings must be fixed to a constant value, so that the value of the other couplings is expressed relative to the reference one. In this analysis the $K^*(892)$ helicity coupling $\mathcal{H}^{\Lambda_c^+\to K^* p}_{0,-1/2}$ has been chosen as the reference coupling, fixed to one, with zero imaginary part.

The fit quality can be assessed in different ways. The simplest method is to compare 1- or 2- dimensional phase space distributions between data and model. Graphically it is achieved by comparing data with model histograms, the latter obtained by weighing the flat phase space simulated events according to amplitude model values, in order to include the detector efficiency effect as for the amplitude model normalisation. This is the most straightforward method to spot manifest discrepancies and their location in the decay phase space, but its sensitivity is limited by the use of projections. A χ^2-based test is more sensitive to differences between data and model phase space multidimensional distributions. A generalised version of the χ^2 test for weighted histograms [164] is computed by dividing the decay phase space in bins with roughly the same amount of data points, by using the adaptive binning technique implemented in the ROOT package [165]. A p-value for the two distributions to be statistically compatible can be drawn knowing the number of degrees of freedom. The distributions of the residuals for each bin give information on the location of the discrepancies in the phase space.

5.4.1 Preliminary amplitude fit test to simulation events

As a first preliminary test, the amplitude fit framework has been tested on simulated events at generation-level, without including detector reconstruction effects. The chosen amplitude fit reproduces the full simulation sample decay model, which includes the three resonances $\Lambda^*(1520), \Delta^{++*}(1232), K^*(892)$ and a flat phase-space component. In the simulation, the Λ_c^+ baryon is generated with zero polarisation, with uniform decay orientation angles, while the amplitude model allows for a generic polarisation vector. Moreover, the amplitude model allows for interference between resonances, while the simulated sample has been generated without interference effects. The amplitude model contains 18 parameters to be determined from the fit, of which 12 real couplings, the $\Lambda^*(1520)$ mass and width, the flat phase-space component fraction and 3 polarisation components. Masses and widths of the $K^*(892)$ and $\Delta^{++*}(1232)$ resonances are fixed to the PDG values [24] Note that it is not possible to perfectly match the implementation of

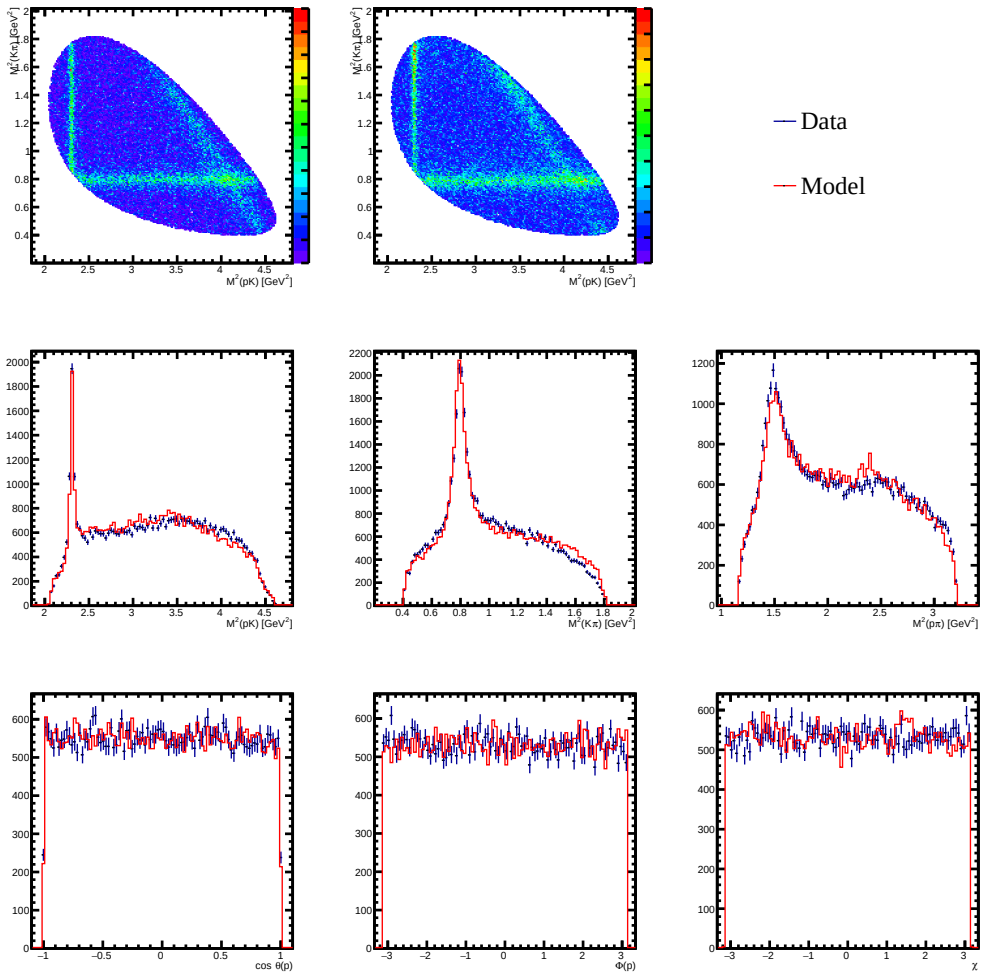

Figure 5.11: Test fit done on 50'000 generation-level simulation events.

the decay model between the amplitude model and that used for the simulation: small discrepancies in phase space distributions between simulation and amplitude model are thus expected.

The test fit done on 50'000 simulation events is reported in Fig. 5.11. Apart some discrepancies in the mass distributions, which can be due to the mismatch between generation and fit amplitude models, the polarisation vector is found to be compatible with the generation null value,

$$P_x = -0.001 \pm 0.021 \qquad P_y = 0.001 \pm 0.021 \qquad P_z = 0.054 \pm 0.026.$$

To study the ability of the amplitude model to measure non-zero polarisation, toy simulation samples are generated sampling the amplitude model resulting from the previous fit to the generation-level simulation sample, but imposing full polarisation in

turn on the three components. The test fits performed on 50'000 toy simulated events show that the polarisation vector is correctly measured for all the three components: for $P_z = 1$, Figure 5.12,

$$P_x = -0.037 \pm 0.020 \qquad P_y = -0.029 \pm 0.020 \qquad P_z = 0.984 \pm 0.025;$$

for $P_x = 1$, Figure 5.13,

$$P_x = 0.991 \pm 0.022 \qquad P_y = -0.017 \pm 0.020 \qquad P_z = -0.013 \pm 0.023;$$

for $P_y = 1$, Figure 5.14,

$$P_x = -0.029 \pm 0.021 \qquad P_y = 1.000 \pm 0.039 \qquad P_z = -0.019 \pm 0.023.$$

The effect of the polarisation is clearly visible in the phase space angular distributions. A longitudinal polarisation produce a linear dependence in $\cos\theta_p$, while the orthogonal components affect the azimuthal proton angle distribution adding a $\cos\phi_p$ or $\sin\phi_p$ dependence for P_x or P_y polarisation, respectively, as expected from the discussion in Sec. 5.2.4.

Next, the amplitude model is tested on simulated $\Lambda_c^+ \to pK^-\pi^+$ events reconstructed by the LHCb detector. The detector efficiency is included by using the high-statistics ReDecay simulation of flat phase space $\Lambda_c^+ \to pK^-\pi^+$ decays to compute the normalisation of the amplitude model, Eq. (5.28). A test fit is done on 30'000 reconstructed simulation events, basically all events passing the selection requirements, reported in Fig. 5.15. The efficacy of the method is visible in the phase space angular distributions: the evident distortions due to the detector reconstruction are well reproduced by the fit model within statistical uncertainties, and the measured polarisation is correctly compatible with zero,

$$P_x = 0.009 \pm 0.023 \qquad P_y = 0.033 \pm 0.024 \qquad P_z = -0.009 \pm 0.034.$$

5.4.2 Model building

The $\Lambda_c^+ \to pK^-\pi^+$ amplitude model is built by adding helicity amplitudes corresponding to the various intermediate states, Eq. (5.14). The intermediate resonances must be carefully chosen in order to describe the decay phase-space distributions. Following the discussion in Sec. 1.4.6, the determination of the resonance structure of the $\Lambda_c^+ \to pK^-\pi^+$ decay can be factorised from the Λ_c^+ polarisation determination, and the first can be studied by means of 2-dimensional Dalitz plot fits.

The knowledge about Λ^*, Δ^{++*} and K^* resonances according to the PDG [24] is summarised in Table 5.4. The contribution of $\Sigma^* \to pK^-$ resonances is possible but suppressed since it involves a $\Delta I = 1$ strong isospin difference, while Λ^* resonances have zero isospin [24]. Moreover, their contribution would be difficult to separate from that of Λ^* resonances, so they are neglected as done in [75].

The efficiency-uncorrected Dalitz plot for 2016 $\Lambda_c^+ \to pK^-\pi^+$ selected candidates is shown in Fig. 5.16. In first approximation, $\Lambda^* \to pK^-$ resonances are visible as vertical bands, $K^* \to K^-\pi^+$ as horizontal bands and $\Delta^{++*} \to p\pi^+$ as diagonal bands, in which the different intensity patterns can be given by the spin of the resonance, by interference patterns or non-uniform detector efficiency. Regarding the Λ^* pattern, there are two clear narrow bands corresponding to the $\Lambda^*(1520)$ and $\Lambda^*(1670)$ resonances, plus broader bands in between and below the $\Lambda^*(1520)$ mass, possible signs of $\Lambda^*(1405)$

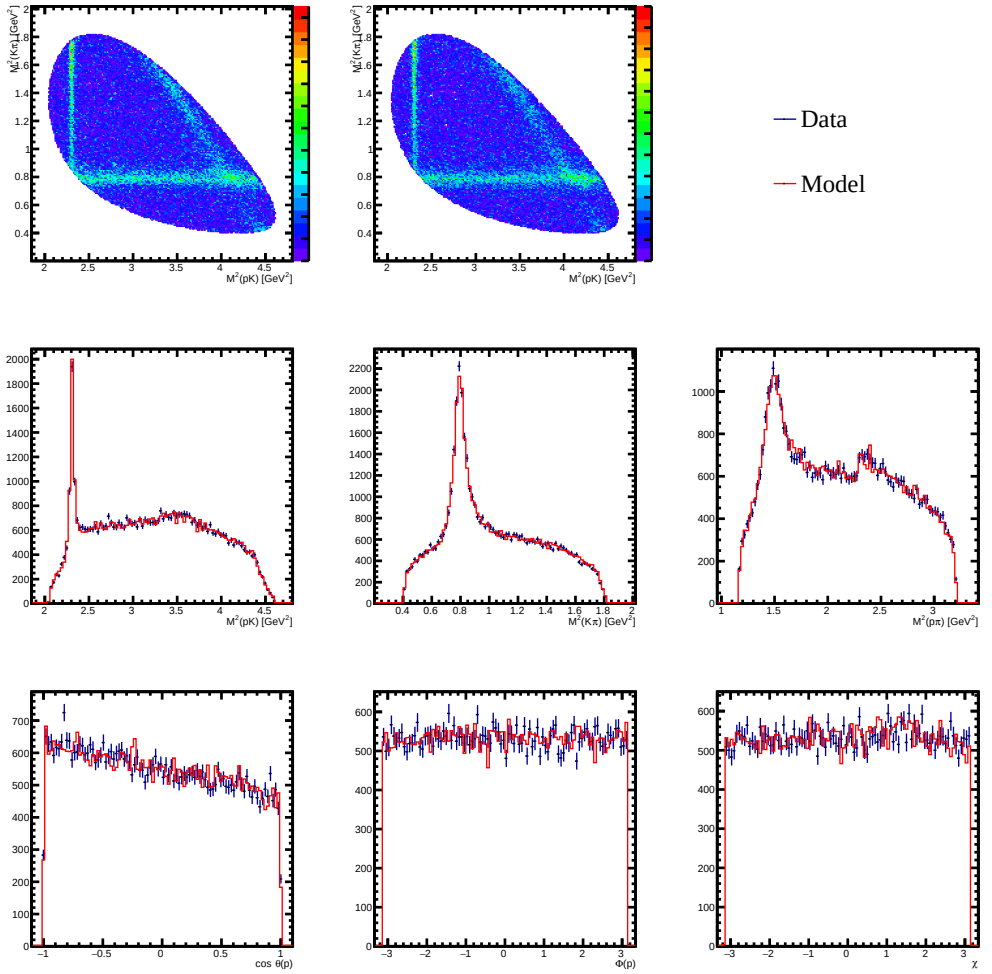

Figure 5.12: Test fit done on 50′000 toy simulation events generated with $P_z = 1$.

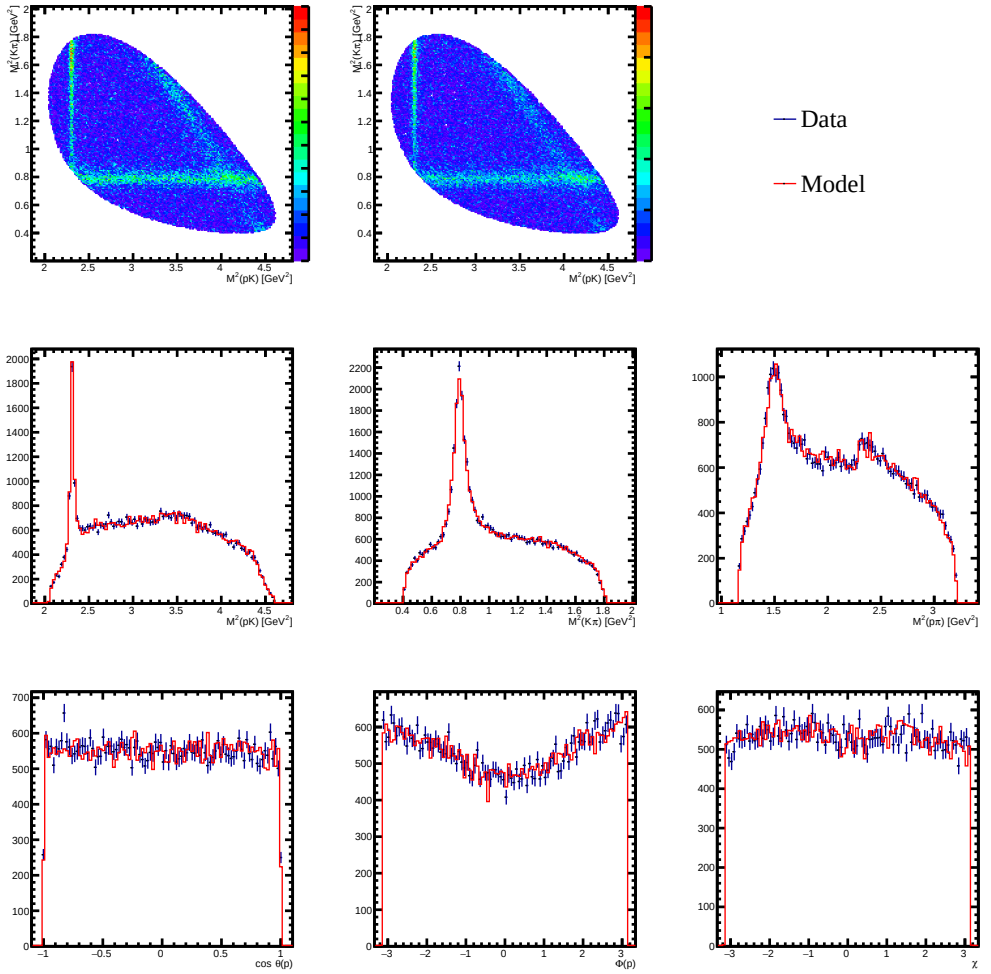

Figure 5.13: Test fit done on 50'000 toy simulation events generated with $P_x = 1$.

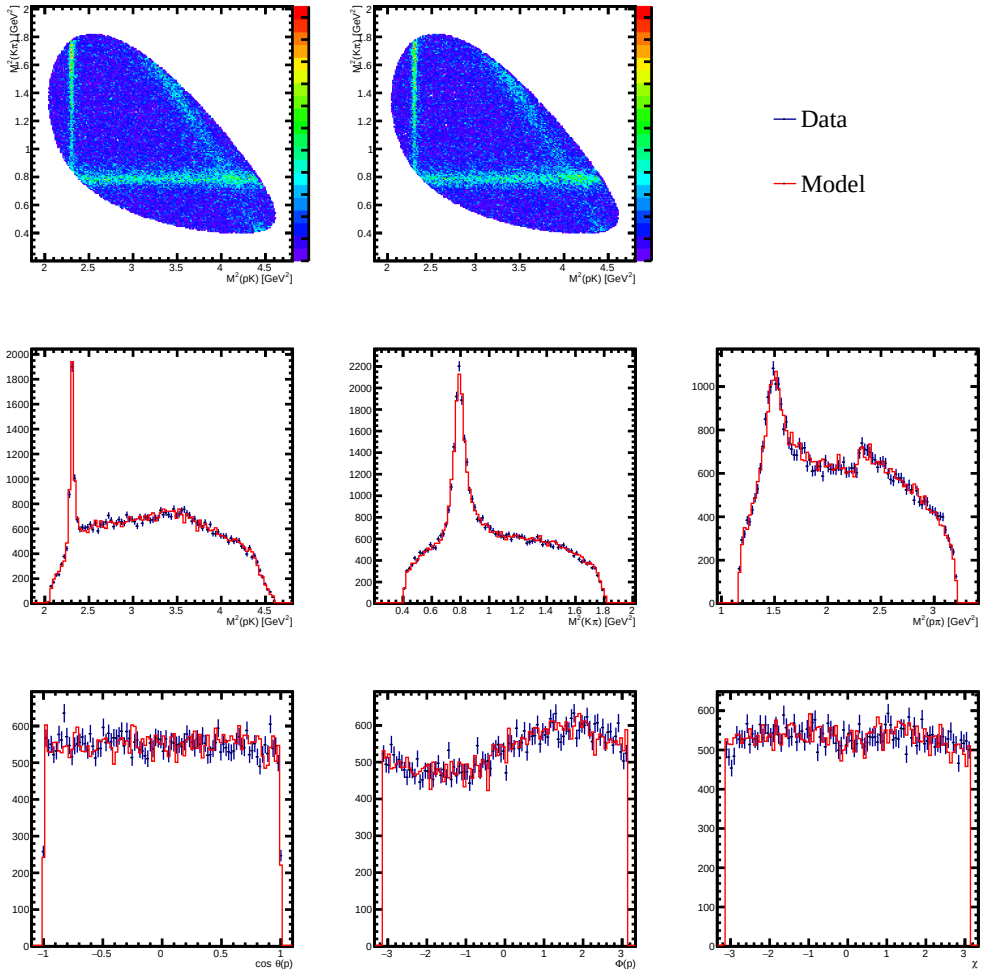

Figure 5.14: Test fit done on 50'000 toy simulation events generated with $P_y = 1$.

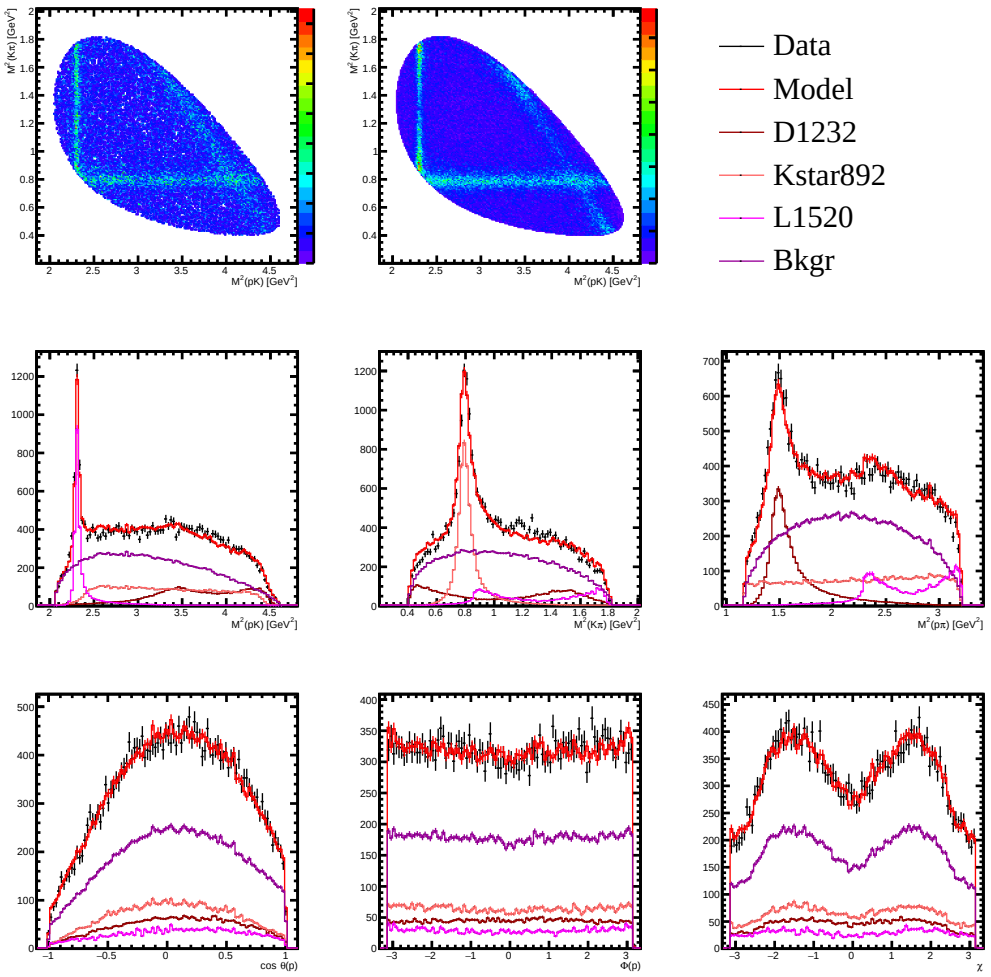

Figure 5.15: Test amplitude fit done on 30′000 reconstructed simulation events. "Bkgr" indicates the flat phase space component.

Resonance	J^P	BW mass (MeV)	BW width (MeV)	Existence
$\Lambda^*(1405)$	$1/2^-$	$1405.1^{+1.3}_{-1.0}$	50.5 ± 2.0	certain
$\Lambda^*(1520)$	$3/2^-$	1519.5 ± 1.0	15.6 ± 1.0	certain
$\Lambda^*(1600)$	$1/2^+$	$1560 - 1700$	$50 - 250$	very likely
$\Lambda^*(1670)$	$1/2^-$	$1660 - 1680$	$25 - 50$	certain
$\Lambda^*(1690)$	$3/2^-$	$1685 - 1695$	$50 - 70$	certain
$\Lambda^*(1710)$	$1/2^+$	1713 ± 13	180 ± 40	poor
$\Lambda^*(1800)$	$1/2^-$	$1720 - 1850$	$200 - 400$	very likely
$\Lambda^*(1810)$	$1/2^+$	$1750 - 1850$	$50 - 250$	very likely
$\Lambda^*(1820)$	$5/2^+$	$1815 - 1825$	$70 - 90$	certain
$\Lambda^*(1830)$	$5/2^-$	$1810 - 1830$	$60 - 110$	certain
$\Lambda^*(1890)$	$3/2^+$	$1850 - 1910$	$60 - 200$	certain
$\Lambda^*(2000)$		≈ 2000		poor
$\Lambda^*(2020)$	$7/2^+$	≈ 2020		poor
$\Lambda^*(2050)$	$3/2^-$	2056 ± 22	493 ± 60	poor
$\Lambda^*(2100)$	$7/2^-$	$2090 - 2110$	$100 - 250$	certain
$\Lambda^*(2110)$	$5/2^+$	$2090 - 2140$	$150 - 250$	very likely
$\Delta^{++*}(1232)$	$3/2^+$	$1230 - 1234$	$114 - 120$	certain
$\Delta^{++*}(1600)$	$3/2^+$	$1500 - 1640$	$200 - 300$	certain
$\Delta^{++*}(1620)$	$1/2^-$	$1590 - 1630$	$110 - 150$	certain
$\Delta^{++*}(1700)$	$3/2^-$	$1690 - 1730$	$220 - 380$	certain
$K_0^*(700)$	0^+	824 ± 30	478 ± 50	certain
$K^*(892)$	1^-	891.76 ± 0.25	47.3 ± 0.5	certain
$K^*(1410)$	1^-	1421 ± 9	236 ± 18	certain
$K_0^*(1430)$	0^+	1425 ± 50	270 ± 80	certain

Table 5.4: List of Λ^*, Δ^{++*} and K^* resonances possibly contributing to the $\Lambda_c^+ \to pK^-\pi^+$ phase space according to the PDG [24]. Here, J^P is the spin-parity assignment, BW mass and widths represent the approximate values assuming relativistic Breit-Wigner lineshape and the last column reports the degree of experimental evidence for the resonance existence.

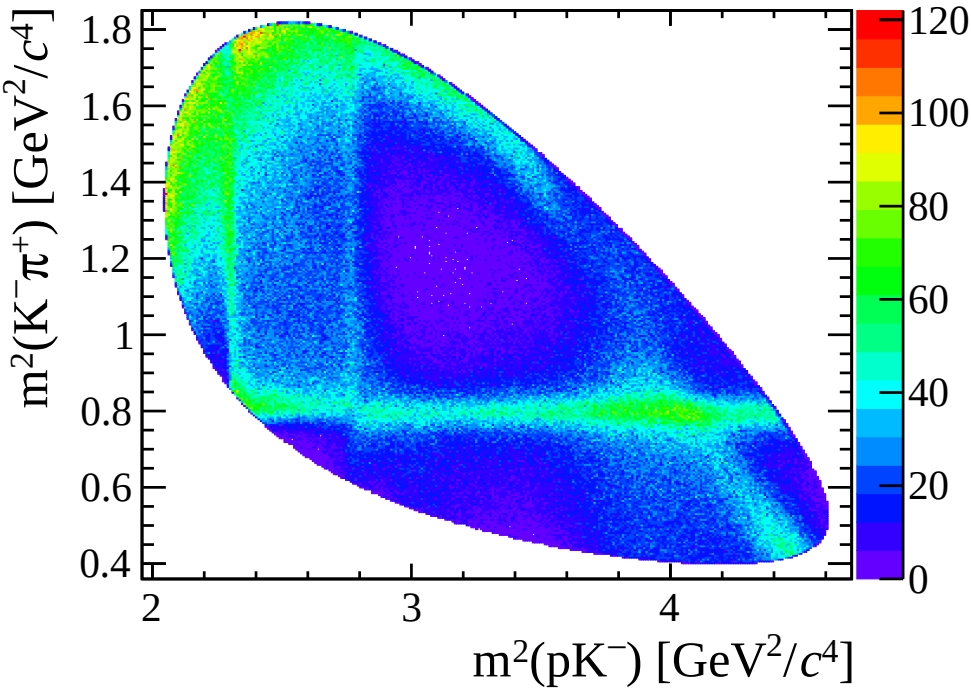

Figure 5.16: Efficiency-uncorrected Dalitz plot for 2016 $\Lambda_c^+ \to pK^-\pi^+$ candidates.

Resonance	J^P	BW mass (MeV)	BW width (MeV)
$\Lambda^*(1405)$	$1/2^-$	1405.1	50.5
$\Lambda^*(1520)$	$3/2^-$	$1515 - 1523$	$10 - 20$
$\Lambda^*(1600)$	$1/2^+$	1600	150
$\Lambda^*(1670)$	$1/2^-$	1670	25
$\Lambda^*(1690)$	$3/2^-$	1690	60
$\Lambda^*(2000)$	$1/2^-$	$1900 - 2100$	$20 - 400$
$\Delta^{+++*}(1232)$	$3/2^+$	1232	120
$\Delta^{+++*}(1620)$	$1/2^-$	1620	130
Non-resonant	0^+		
$K^*(892)$	1^-	891.76	47.3
$K^*(1410)$	1^-	1421	236
$K_0^*(1430)$	0^+	1425	270

Table 5.5: List of the intermediate resonances included in the reduced $\Lambda_c^+ \to pK^-\pi^+$ amplitude model, with J^P the spin-parity assignment, and the Breit-Wigner parameters which, in the amplitude fit, are floated within the reported range, or fixed to the given value if no interval is quoted.

(whose pole mass is below the pK^- mass threshold) and $\Lambda^*(1600)$ resonances. The only other vertical band is an excess of events in the region $m^2_{pK^-} \in 3.8 - 4.0\,\mathrm{GeV}^2$, better visible in the $m^2_{pK^-}$ projection Fig. 5.5, which can be a sign of additional Λ^* resonances for which there is no clear evidence according to the PDG [24]. Regarding the K^* resonances there is only the clear band of the $K^*(892)$; higher mass $K^*(1410)$ and $K_0^*(1430)$ resonances, having pole masses outside the allowed phase-space, may contribute thanks to the lower mass tail of their broad distribution, possibly explaining the presence of a large number of events at high $m^2_{K^-\pi^+}$ invariant mass. Even if a spin-zero non-resonant component cannot be excluded by eye, the center of the Dalitz plot is almost empty of events. Finally, the diagonal band of the $\Delta^{+++*}(1232)$ is apparent, plus an unclear band at higher $m^2_{p\pi^+}$ mass compatible with another Δ^{+++*} resonance; according to the 1-dimensional $m^2_{p\pi^+}$ projection the excess is mostly compatible with a $\Delta^{+++*}(1620)$ resonance.

Following the qualitative inspection of the Dalitz plot, two amplitude models are set, with the same resonance content but with a different number of free parameters. The possible Λ^* resonances contribution in the region $m^2_{pK^-} \in 3.8 - 4.0\,\mathrm{GeV}^2$ is considered by introducing a spin $1/2$ $\Lambda^*(2000)$ resonance component. In the "reduced" model, defined in Table 5.5, most of the Breit-Wigner masses and widths are fixed to the central values reported by the PDG [24]; for the very narrow $\Lambda^*(1520)$ resonance its mass and width are left floating around the central values to take into account experimental resolution effects, while for the $\Lambda^*(2000)$ resonance its mass and width are floated in wide ranges. In the "extended model", defined in Table 5.6, the mass and widths of resonances which have not been experimentally well determined, according to the PDG, are left as floating parameters in the fit. The "reduced model" consist of 60 free parameters: 54 real couplings, 2 masses, 2 widths and 2 LASS lineshape parameters (see next Sec. 5.4.3). The extended model feature 71 free parameters, having 5 and 6 more floating masses and widths, respectively.

Resonance	J^P	BW mass (MeV)	BW width (MeV)
$\Lambda^*(1405)$	$1/2^-$	1405.1	50.5
$\Lambda^*(1520)$	$3/2^-$	$1515 - 1523$	$10 - 20$
$\Lambda^*(1600)$	$1/2^+$	$1550 - 1700$	$50 - 300$
$\Lambda^*(1670)$	$1/2^-$	1670	$25 - 50$
$\Lambda^*(1690)$	$3/2^-$	1690	60
$\Lambda^*(2000)$	$1/2^-$	$1900 - 2100$	$20 - 400$
$\Delta^{+++*}(1232)$	$3/2^+$	$1200 - 1300$	$110 - 150$
$\Delta^{+++*}(1620)$	$1/2^-$	$1590 - 1630$	$110 - 150$
Non-resonant	0^+		
$K^*(892)$	1^-	891.76	47.3
$K^*(1410)$	1^-	1421	236
$K_0^*(1430)$	0^+	$1375 - 1475$	$190 - 350$

Table 5.6: List of the intermediate resonances included in the extended $\Lambda_c^+ \to pK^-\pi^+$ amplitude model, with J^P the spin-parity assignment, and the Breit-Wigner parameters which, in the amplitude fit, are floated within the reported range, or fixed to the given value if no interval is quoted.

5.4.3 Resonance lineshapes

By default resonances are parametrised with relativistic Breit-Wigner lineshapes, which are well-suited for relatively narrow resonances far from other nearby resonances and the threshold of additional decay channels. To reproduce the typical suppression of transitions involving non-zero orbital angular momentum, the Breit-Wigner parametrisation is multiplied by angular barrier terms involving Blatt-Weisskopf form factors [166, 167]

$$\mathcal{R}_{\rm BW}(m^2) = \left[\frac{q(m)}{q_0}\right]^{L_{\Lambda_c^+}} \left[\frac{p(m)}{p_0}\right]^{L_R} \frac{F_{\Lambda_c^+}(m, L_{\Lambda_c^+}) F_R(m, L_R)}{m_0^2 - m^2 - im_0\Gamma(m)}, \tag{5.34}$$

in which the mass-dependent width

$$\Gamma(m) = \Gamma_0 \left[\frac{p(m)}{p_0}\right]^{2L_R+1} \frac{m_0}{m} F_R^2(m, L_R), \tag{5.35}$$

is introduced. The definition of the different quantities entering the above expressions are the following: m is the invariant mass of the resonance, m_0 and Γ_0 are its Breit-Wigner mass and width, $p(m)$ is the momentum of one of the decay products in the resonance two-body decay, $p_0 \equiv p(m_0)$, $q(m)$ is the momentum of one of the decay products in the Λ_c^+ two-body decay $\Lambda_c^+ \to Rh$, $q_0 = q(m_0)$, $L_{\Lambda_c^+}$ and L_R are the orbital angular momenta associated to the Λ_c^+ and R decays, respectively. The Blatt-Weisskopf form factors [166, 167] for the resonance, $F_R(m, L_R)$, and for the Λ_c^+, $F_{\Lambda_c^+}(m, L_{\Lambda_c^+})$, are

parametrised as

$$F_{R,\Lambda_c^+}(m,L) = \begin{cases} 1 & L=0 \\ \sqrt{\frac{1+z_0^2}{1+z^2(m)}} & L=1 \\ \sqrt{\frac{9+3z_0^2+z_0^4}{9+3z^2(m)+z^4(m)}} & L=2 \\ \sqrt{\frac{225+45z_0^2+6z_0^4+z_0^6}{225+45z^2(m)+6z^4(m)+z^6(m)}} & L=3 \end{cases}, \tag{5.36}$$

in which the definitions of the terms $z(m)$ and z_0 depend on whether the form factor for the resonance R or for the Λ_c^+ is being considered. For R these terms are given by $z(m) = p(m)d$ and $z_0 = p_0 d$, in which $p(m)$ is the momentum of one of the decay products in the resonance two-body decay, $p_0 \equiv p(m_0)$, and d is a radial[1] parameter taken to be $1.5\,\text{GeV}^{-1}$. For the Λ_c^+ baryon the respective functions are $z(m) = q(m)d$ and $z_0 = q_0 d$, in which $q(m)$ is the momentum of one of the decay products in the Λ_c^+ two-body decay $\Lambda_c^+ \to Rh$, $q_0 = q(m_0)$, and $d = 5.0\,\text{GeV}^{-1}$. Previous studies showed the amplitude analysis is very weakly sensitive to the d values [84].

The mass-dependent width and the form factors depend on the orbital angular momenta of the two-body decays. For the Λ_c^+ weak decay, the orbital angular momentum is not constrained, so the minimum possible one is taken. For half-integer spin Λ^*, Δ^{*++} resonances it is $L_{\Lambda_c^+} = J_R - 1/2$, J_R being the resonance spin, it is $L_{\Lambda_c^+} = 0$ for spin zero K^* resonances and $L_{\Lambda_c^+} = J_R - 1$ for higher spin K^* resonances. For the strong decay of Λ^*, Δ^{*++} resonance, the orbital angular momentum L_R is determined by the conservation of angular momentum, which requires $L_R = J_R \pm 1/2$, and the parity of the resonance[2], $P_R = -(-1)^{L_R}$, which chooses one of the L_R values. For K^* resonances, decaying into two mesons, the orbital angular momentum is $L_R = J_R$.

Some of the resonances employed in the amplitude model can not be parametrised by relativistic Breit-Wigner lineshapes. The $K_0^*(1430)$ resonance strongly interferes with the non-resonant S-wave component and they are collectively parametrised by the LASS lineshape [168],

$$\mathcal{R}_{\text{LASS}}(m^2) = \frac{m}{q\cot\delta_B - iq} + e^{2i\delta_B}\frac{m_0\Gamma_0\frac{m_0}{q_0}}{m_0^2 - m^2 - im_0\Gamma_0\frac{q}{m}\frac{m_0}{q_0}} \tag{5.37}$$

in which

$$\cot\delta_B = \frac{1}{aq} + \frac{1}{2}rq, \tag{5.38}$$

with a and r being parameters named the scattering length and the effective range, respectively, while other quantities are defined as for Eq. 5.34. Since a and r are decay-dependent they are left as floating parameters in the amplitude fit.

The $\Lambda^*(1405)$ resonance has its pole mass below the threshold of pK^- production, and it contributes to the $\Lambda_c^+ \to pK^-\pi^+$ decay due to its higher mass tail. Its effect can be described by the Breit-Wigner lineshape Eq. 5.34 with one modification: in the computation of the momenta the pole mass is replaced by an effective one m_0^{eff} inside

[1] The angular barrier factors arise from the non-relativistic quantisation of a particle in a radial potential, and d represents, loosely speaking, the radius of the resonance.

[2] The additional minus sign is given by the negative parity of the final state meson.

the kinematically allowed range, by means of the ad-hoc formula [169]

$$m_0^{\text{eff}} = m^{\min} + \frac{1}{2}\left(m^{\max} - m^{\min}\right)\left[1 + \tanh\left(\frac{m_0 - \frac{m^{\min}+m^{\max}}{2}}{m^{\max} - m^{\min}}\right)\right] \tag{5.39}$$

in which $m^{\min}$ and $m^{\max}$ are the minimum and maximum allowed masses. The Flatté lineshape [170] has not been used for the moment, since it would add two additional parameters to the fit model.

5.4.4 Dalitz plot 2-dimensional fits

Two-dimensional Dalitz plot fits have been performed integrating over the decay orientation angles $\cos\theta_p, \phi_p, \chi$, therefore not sensitive to the Λ_c^+ polarisation, but only to the decay amplitude model. The Dalitz plot fits are carried out on 100'000 $\Lambda_c^+ \to pK^-\pi^+$ data candidates selected from the data sample collected in 2016, a number of events determined by the available statistics of the ReDecay simulation sample, which amounts to $\approx$ 450'000 events passing the selection process. A sufficiently large simulation sample is needed to precisely compute the model normalisation and subtract the detector efficiency effects. The fit is performed with initial values of the floating parameters thrown randomly in their allowed range, and the best result according to the minimum NLL is selected among 10 different fits. Fit fractions for each resonance R are obtained by computing the integral over the Dalitz plot of the amplitude model in which only the R contribution is left,

$$\int d\Omega \sum_{m_{\Lambda_c^+}, m_p} \left| \sum_{\lambda_R} \mathcal{A}^{\Lambda_c^+ \to Rh}_{m_{\Lambda_c^+}, \lambda_R, m_p}(\Omega) \right|^2 . \tag{5.40}$$

The departure of the sum of the fit fractions from one indicates the presence of interference effects.

The amplitude fit result for the reduced model described in Table 5.5 is shown in Fig. 5.17, the fit parameters values returned by MINUIT are reported in Table 5.7. The amplitude fit result for the extended model described in Table 5.6 is shown in Fig. 5.19, the fit parameters values which were fixed in the reduced model are reported in Table 5.8. The fit fractions associated to the two models are reported in Table 5.9, the associated statistical uncertainties are missing since their computation has still to be implemented[3].

The best amplitude fit with the reduced model shows no significant discrepancies in the 1-dimensional projections. The residuals between data and fit model distributions are reported in Fig. 5.18: a negative tension is apparent in the center of the Dalitz plot, where the model seems to overestimate the data, while a positive tension is visible at the edge where the $\Lambda^*(1520)$ and $K^*(892)$ resonances meet. The associated χ^2/ndf is 1436.37/939=1.53, with a NLL for of -20379.3. The best amplitude fit with the extended model features no significant discrepancies in the 1-dimensional projections as well. The residuals between data and fit model distributions are reported in Fig. 5.20, displaying the same tensions as for the reduced model, Fig. 5.18. The associated χ^2/ndf is 1418.05/928=1.53, practically equal to that of the reduced model, with a NLL of -20421.4. All the resonances included in the amplitude models have non-negligible fit fractions, apart from the $\Lambda^*(1690)$ resonance, whose fit fraction is $\leq 1\%$.

[3] Its evaluation will be important when systematic uncertainties associated to fit fractions will be properly estimated.

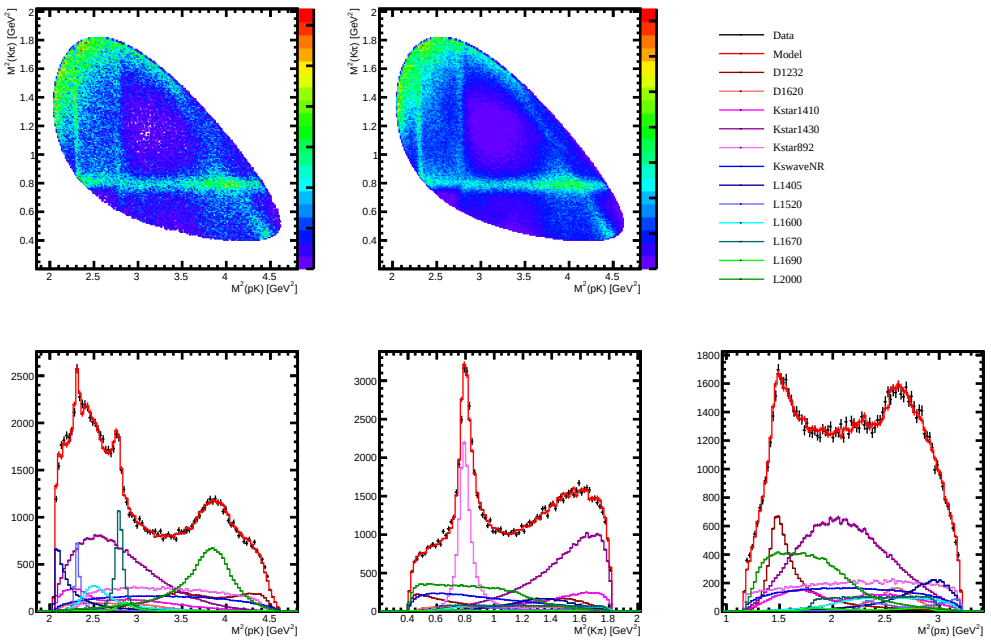

Figure 5.17: Dalitz plot amplitude fit results for the reduced model on 100'000 $\Lambda_c^+ \to pK^-\pi^+$ candidates.

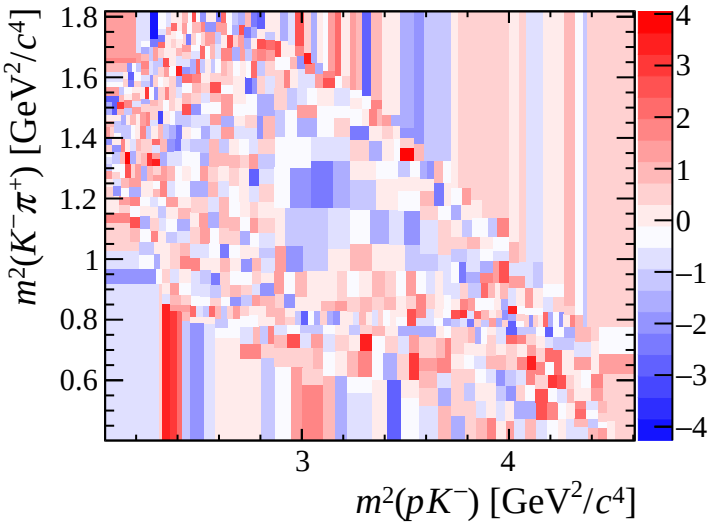

Figure 5.18: Dalitz plot amplitude fit residuals between data and model, for the reduced model on 100'000 $\Lambda_c^+ \to pK^-\pi^+$ candidates. The associated χ^2/ndf is 1436.37/939=1.53.

Parameter	Central value ± Uncertainty	Parameter	Central value ± Uncertainty
a_LASS	0.974626 ± 0.055703	r_LASS	19.133840 ± 1.157610
ML1520	1.520529 ± 0.000634	GL1520	0.014623 ± 0.002538
ML2000	1.972995 ± 0.001762	GL2000	0.138392 ± 0.002990
ArKswave_1	-6.482974 ± 0.586021	AiKswave_1	14.720211 ± 0.678673
ArKswave_2	5.381012 ± 0.767511	AiKswave_2	3.656190 ± 0.630537
ArKst892_2	-0.420210 ± 0.071521	AiKst892_2	-0.328464 ± 0.078473
ArKst892_3	-0.502029 ± 0.069484	AiKst892_3	1.530955 ± 0.049805
ArKst892_4	-0.084397 ± 0.043801	AiKst892_4	-0.198552 ± 0.052774
ArKst1410_1	-2.824465 ± 0.400512	AiKst1410_1	4.468027 ± 0.574243
ArKst1410_2	-2.815474 ± 0.475799	AiKst1410_2	-0.071873 ± 0.661246
ArKst1410_3	-1.313387 ± 0.751539	AiKst1410_3	4.934985 ± 0.494556
ArKst1410_4	6.720931 ± 0.353235	AiKst1410_4	3.368807 ± 0.367342
ArKst1430_1	2.278030 ± 0.504737	AiKst1430_1	-15.098954 ± 0.403538
ArKst1430_2	-10.237877 ± 0.410889	AiKst1430_2	-3.424862 ± 0.354024
ArL1405_1	-2.052190 ± 0.090731	AiL1405_1	-1.683788 ± 0.152498
ArL1405_2	-1.171505 ± 0.168473	AiL1405_2	-0.230015 ± 0.150507
ArL1520_1	0.508186 ± 0.095989	AiL1520_1	-0.163491 ± 0.027476
ArL1520_2	-0.130801 ± 0.032993	AiL1520_2	0.187029 ± 0.038424
ArL1600_1	0.211495 ± 0.119396	AiL1600_1	-1.093854 ± 0.109560
ArL1600_2	-1.463896 ± 0.128385	AiL1600_2	-1.229667 ± 0.125308
ArL1670_1	0.670561 ± 0.028507	AiL1670_1	0.281996 ± 0.049339
ArL1670_2	0.381101 ± 0.027047	AiL1670_2	-0.036219 ± 0.040471
ArL1690_1	0.427019 ± 0.048743	AiL1690_1	0.136084 ± 0.071195
ArL1690_2	-0.096511 ± 0.081779	AiL1690_2	-0.684386 ± 0.058000
ArL2000_1	2.899369 ± 0.123978	AiL2000_1	-1.951281 ± 0.162981
ArL2000_2	-3.439083 ± 0.156026	AiL2000_2	-1.444882 ± 0.147557
ArD1232_1	1.625160 ± 0.089338	AiD1232_1	1.180555 ± 0.119759
ArD1232_2	2.690759 ± 0.086101	AiD1232_2	-0.841648 ± 0.094539
ArD1620_1	-0.415376 ± 0.089799	AiD1620_1	1.591540 ± 0.085674
ArD1620_2	0.282203 ± 0.082533	AiD1620_2	-0.397312 ± 0.083178

Table 5.7: Fit parameters returned by MINUIT for the Dalitz plot amplitude fit with reduced model on 100'000 $\Lambda_c^+ \to pK^-\pi^+$ candidates. Uncertainties are the 1σ standard deviations returned by HESSE. Fit parameters are defined in Appendix A.3.

Parameter	Central value ± Uncertainty	PDG values (GeV)
MKst1430	1.475000 ± 0.007415	1.425 ± 0.050
GKst1430	0.350000 ± 0.008271	0.270 ± 0.080
ML1520	1.519833 ± 0.000489	1.5195 ± 0.0010
GL1520	0.013496 ± 0.001198	0.0156 ± 0.0010
ML1600	1.617676 ± 0.008456	$1.560 - 1.700$
GL1600	0.123779 ± 0.019487	$0.050 - 0.250$
GL1670	0.037830 ± 0.003100	$0.025 - 0.050$
ML2000	1.973700 ± 0.002141	≈ 2
GL2000	0.130829 ± 0.006173	
MD1232	1.234520 ± 0.002144	$1.230 - 1.234$
GD1232	0.119093 ± 0.006507	$0.114 - 0.120$
MD1620	1.630000 ± 0.000902	$1590 - 1630$
GD1620	0.150000 ± 0.002814	$0.110 - 0.150$

Table 5.8: Resonance masses and widths returned by MINUIT for the Dalitz plot amplitude fit with extended model on 100'000 $\Lambda_c^+ \to pK^-\pi^+$ candidates. Uncertainties are the 1σ standard deviations returned by HESSE. Fit parameters are defined in Appendix A.3. Results are compared to the PDG values reported in Table 5.4.

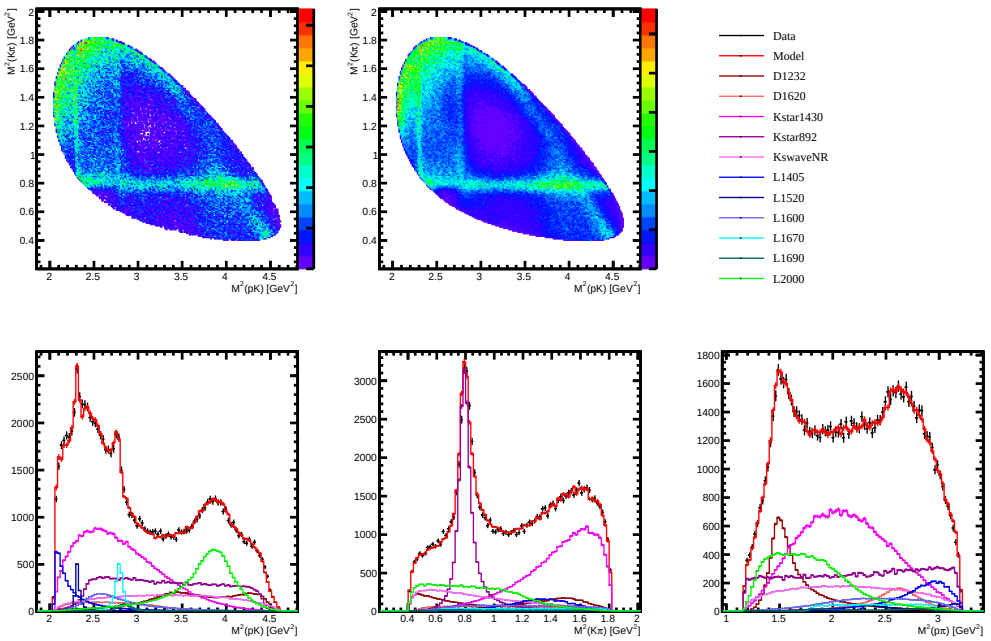

Figure 5.19: Dalitz plot amplitude fit results for the extended model on 100'000 $\Lambda_c^+ \to pK^-\pi^+$ candidates.

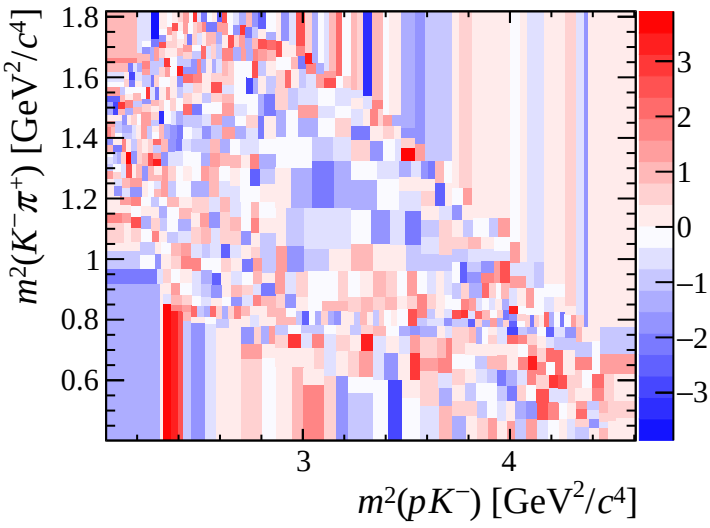

Figure 5.20: Dalitz plot amplitude fit residuals between data and model, for the extended model on 100'000 $\Lambda_c^+ \to pK^-\pi^+$ candidates. The associated χ^2/ndf is 1418.05/928=1.53.

Resonance	FF reduced	FF extended	FF reduced alternative sample
Non resonant	0.109282	0.182511	0.109799
$K^*(892)$	0.151852	0.143938	0.178592
$K^*(1410)$	0.076787	0.097761	0.179808
$K^*(1430)$	0.287793	0.415955	0.205860
$\Lambda^*(1405)$	0.054438	0.052562	0.062724
$\Lambda^*(1520)$	0.022108	0.017247	0.015797
$\Lambda^*(1600)$	0.046379	0.024183	0.030307
$\Lambda^*(1670)$	0.048842	0.054381	0.033665
$\Lambda^*(1690)$	0.009556	0.004960	0.016908
$\Lambda^*(2000)$	0.162436	0.156100	0.180881
$\Delta^{*++}(1232)$	0.093962	0.098731	0.091483
$\Delta^{*++}(1620)$	0.035749	0.055507	0.042587
Sum	1.099183	1.303839	1.148411

Table 5.9: Fit fractions for the Dalitz plot amplitude fit with reduced and extended model on 100'000 $\Lambda_c^+ \to pK^-\pi^+$ candidates, and for the reduced model on the alternative sample of 100'000 $\Lambda_c^+ \to pK^-\pi^+$ candidates. The computation of statistical uncertainties has to be implemented.

Even if reduced and extended models feature basically the same fit quality, some of the resonance fit fractions are different between the two, notably for non resonant, $K^*(1430)$ and $\Lambda^*(1600)$ contributions. Also the sum of fit fractions is significantly different, showing large interference effects for the extended model. The resonance masses and widths returned by the fit are reported in Table 5.8: while most are well within their allowed range, the $K^*(1430)$ and $\Delta^{*++}(1620)$ mass and width are found at the maximum values.

As a cross-check, the fit for the reduced model is repeated on a different sample of 100'000 $\Lambda_c^+ \to pK^-\pi^+$ data candidates, in the following called alternative sample. Its results are displayed in Fig. 5.21 and the associated fit fractions reported in Table 5.9.

The best amplitude fit with the reduced model on the alternative sample shows no discrepancies in the 1-dimensional projections. The residuals between data and fit model distributions are reported in Fig. 5.22, displaying a similar pattern as in Fig. 5.18. The associated χ^2/ndf is 1393.59/928=1.48, slightly better than the previous reduced model fit, with a lower NLL of -20824.0 as well.

The fit fractions retrieved by the fit on the alternative sample show differences with respect to those obtained fitting the nominal sample, especially for overlapping resonances. In particular it is difficult to isolate contributions from $K^*(1410)$ and $K^*(1430)$, since they enter the decay phase space only via their low mass tails. Moreover, the amplitude fit does not seem to significantly depend on the resonance parameters which are left floating in the extended model. Therefore, at present the amplitude fit is not able to discriminate well between neighbouring resonance contributions. A better discrimination could be achieved by increasing the fitted number of events or by fitting the full five-dimensional phase space.

The fit fraction of the $\Lambda^*(2000)$ resonance included in the fit models is greater than 15% for all the presented fits, despite no clear evidence for such kind of states has been reported to date. To quantify the statistical significance of the observed contribution, the

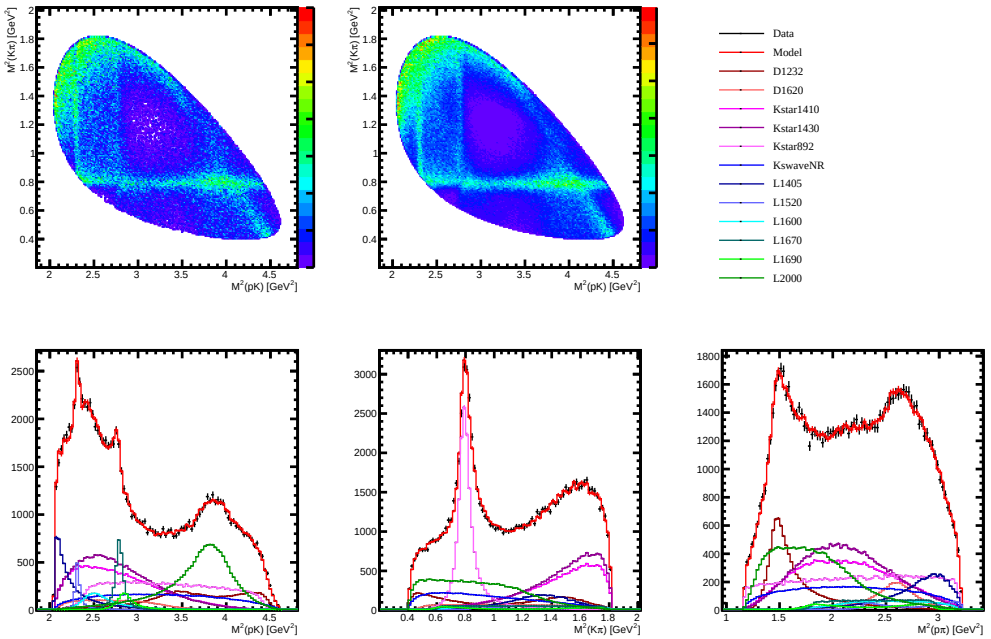

Figure 5.21: Dalitz plot amplitude fit results for the reduced model on the alternative sample of 100′000 $\Lambda_c^+ \to pK^-\pi^+$ candidates.

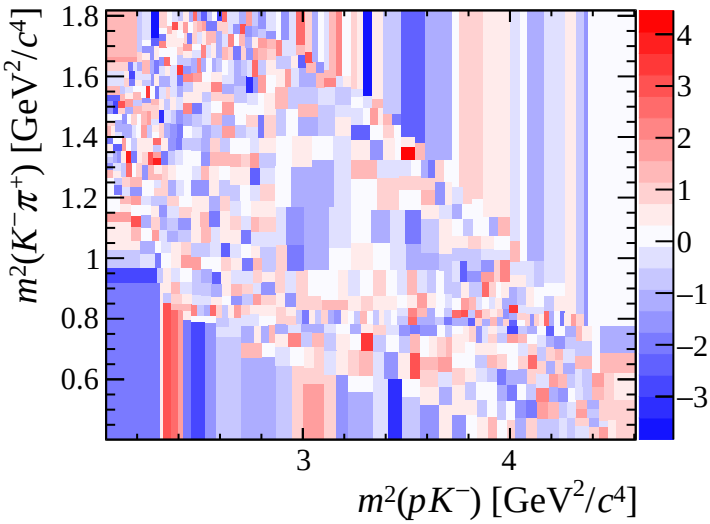

Figure 5.22: Dalitz plot amplitude fit residuals between data and model, for the reduced model on on the alternative sample of 100′000 $\Lambda_c^+ \to pK^-\pi^+$ candidates. The associated χ^2/ndf is 1393.59/939=1.48.

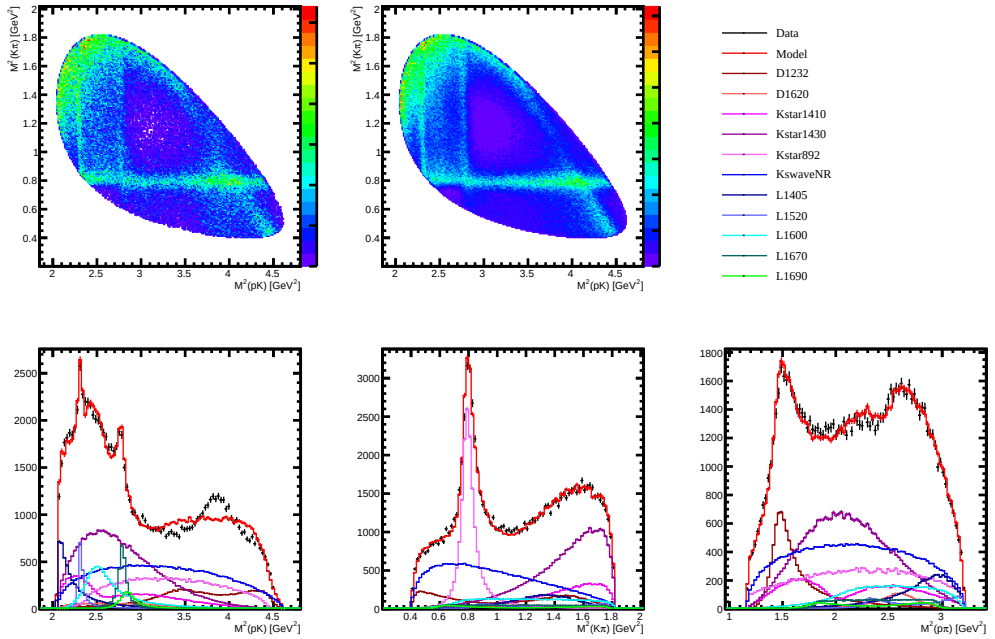

Figure 5.23: Dalitz plot amplitude fit results for the reduced model without $\Lambda^*(2000)$ resonance on 100'000 $\Lambda_c^+ \to pK^-\pi^+$ candidates.

amplitude fit is repeated removing the $\Lambda^*(2000)$ resonance from the reduced model. The result of the fit is reported in Fig. 5.23: clearly it is not possible to obtain a good fit of the $m^2_{pK^-}$ invariant mass in the 2 GeV region without the $\Lambda^*(2000)$ state. The NLL associated to the best fit is -19833.7, the difference with respect to the reduced model being $\Delta LL = 545.6$. According to the Wilks' theorem [171], the quantity $2\Delta LL$ approaches the χ^2 distribution in the limit of infinite statistics, with a number of degrees-of-freedom equal to the difference of free parameters between the two models. In this case, there are six parameters associated to the $\Lambda^*(2000)$ resonance (mass, width and four real couplings), leading to a χ^2/ndf of 1090/6, corresponding to a statistical significance of 32.5σ. The amplitude fits establish with overwhelming statistical significance the presence of Λ^* resonances contribution in the region $m^2_{pK^-} \in 3.8 - 4.0\,\mathrm{GeV}^2$; this contribution can be parametrised by a spin 1/2 state with a mass around 1.97 GeV and a width around 140 MeV.

5.4.5 Full phase space 5-dimensional fits

The full phase space fits are performed in analogy with the Dalitz plot fit, on 100'000 $\Lambda_c^+ \to pK^-\pi^+$ data candidates selected from the data sample collected in 2016, using the reduced model, Table 5.5. The result is shown in Fig. 5.24 and the associated fit fractions in Table 5.10.

Discrepancies in the one-dimensional phase space distributions are visible for the best full phase space amplitude fit: the invariant mass distributions do not match those of the Dalitz plot amplitude fits and there is a different trend between data and ampli-

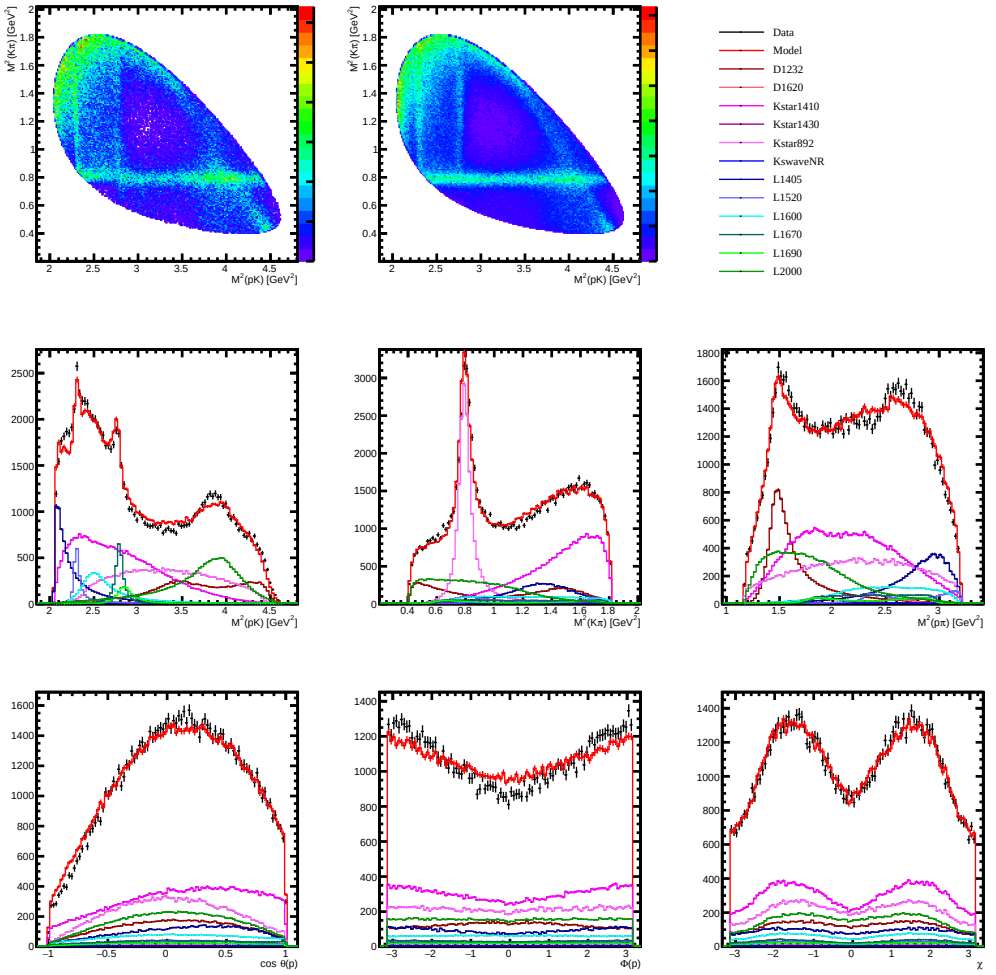

Figure 5.24: Phase space amplitude fit results for the reduced model on 100'000 $\Lambda_c^+ \to pK^-\pi^+$ candidates.

Resonance	Fit fraction
Non resonant	0.003625
$K^*(892)$	0.201816
$K^*(1410)$	0.283104
$K^*(1430)$	0.003664
$\Lambda^*(1405)$	0.087003
$\Lambda^*(1520)$	0.024638
$\Lambda^*(1600)$	0.057809
$\Lambda^*(1670)$	0.029792
$\Lambda^*(1690)$	0.017905
$\Lambda^*(2000)$	0.146268
$\Delta^{*++}(1232)$	0.115455
$\Delta^{*++}(1620)$	0.007105
Sum	0.978184

Table 5.10: Fit fractions for the phase space amplitude fit with reduced model on 100'000 $\Lambda_c^+ \to pK^-\pi^+$ candidates.

tude model in the ϕ_p distribution. The $\cos\theta_p$ and χ distributions are in good agreement. The fitted polarisation components are

$$P_x = 0.224 \pm 0.007 \qquad P_y = 0.015 \pm 0.007 \qquad P_z = -0.120 \pm 0.007.$$

To understand why the fit is unable to match the invariant mass distributions of data and amplitude model, contrarily to the good agreement reached in Dalitz plot fits, the phase space amplitude fit is also performed by fixing the decay amplitude model according to the Dalitz plot fit results presented in Table 5.7 and fitting only for the three polarisation components. The best result is shown in Fig. 5.25, which displays enhanced discrepancies in the mass distributions and a weird step distribution for the amplitude model ϕ_p distribution. The observed problems point towards issues in the way the 5-dimensional amplitude model is implemented in TensorFlowAnalysis, which however were not visible in the test fits done on simulated events, Sec. 5.4.1. In the following section extensive tests of the amplitude model trying to isolate the source of the problem are presented.

5.4.6 Extensive amplitude fit tests

The first test performed is to check if the model is isotropic in the decay orientation angles for zero polarisation. As explained in Sec. 1.4.6 this property follows from rotational invariance and must be satisfied irrespective of the decay model. The test has been performed generating 100'000 events from the reduced amplitude model Dalitz plot fit, Table 5.7, with no polarisation, showing the phase space distributions reported in Fig. 5.26. Consistently with the results of Fig. 5.25, while $\cos\theta_p$ and χ distributions are uniform, the ϕ_p distribution has a clearly unphysical step. The step is located at $\phi_p = 0$, suggesting the model is in some way different for positive and negative ϕ_p. However, it is important to note that the distributions associated to the single resonances fractions are uniform for all the intermediate states, indicating that the problem is related to interference effects only. This is consistent with the tests performed on simulated events, Sec. 5.4.1, since the

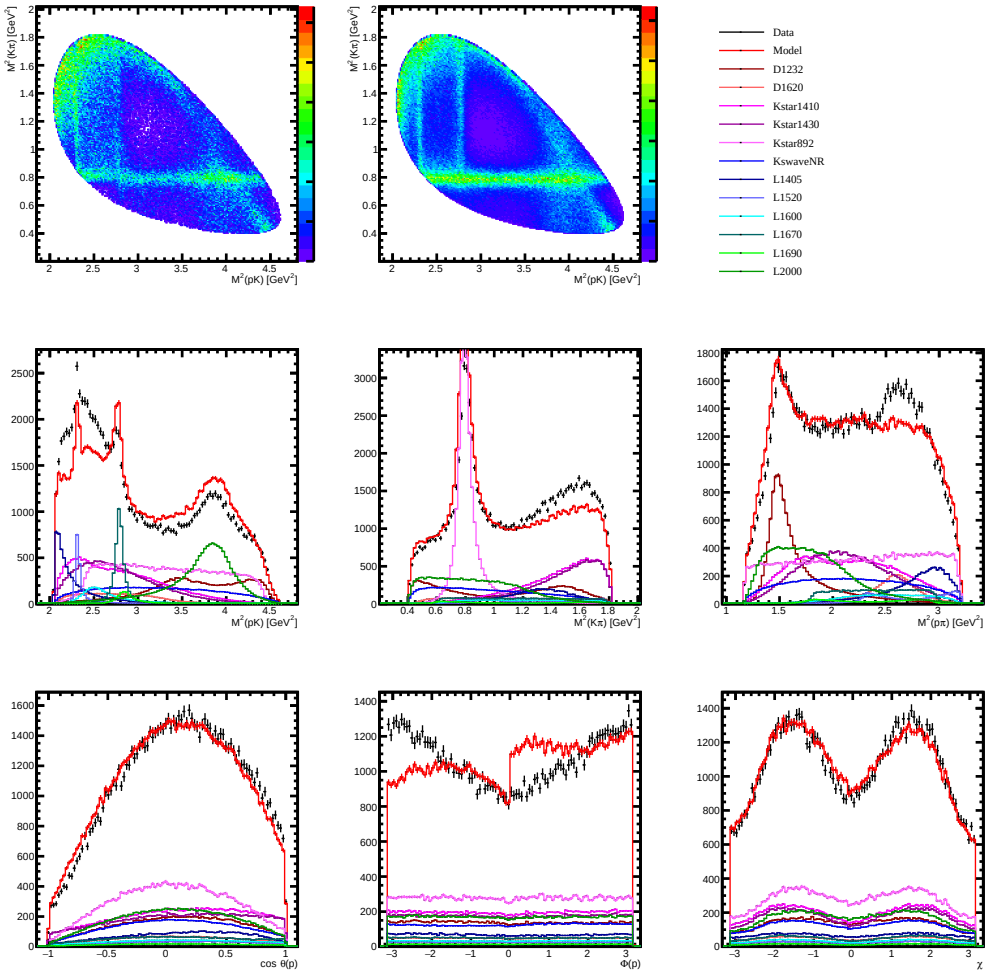

Figure 5.25: Phase space amplitude fit results for fixed reduced model and floating polarisation vector on 100'000 $\Lambda_c^+ \to pK^-\pi^+$ candidates.

model used to produce the simulation sample did not include interference effects.

The test is repeated changing the resonance content of the amplitude model. It is found that anisotropies in ϕ_p distributions arise only when resonances belonging to different decay channels interfere: they have been observed in the interference of one Λ^* and one Δ^{*++}, one K^* and one Δ^{*++} and one Λ^* and one K^* resonances. On the other hand, no anisotropies are seen when resonances belonging to the same decay channel interfere. Fig. 5.27 presents the test performed generating 10^6 events from the reduced amplitude model Dalitz plot fit at zero polarisation in which only Λ^* resonances are kept.

A second test is performed generating 100'000 events from the same model but with full polarisation on the different components, Figs. 5.28-5.31. For rotational invariance the invariant mass distributions must be constant for varying polarisation; indeed the invariant mass distributions are basically the same for zero and full polarisations. Regarding the angular distributions associated to the single resonance fraction, these follow the simple patterns for full polarisation seen in Figs. 5.12-5.14: linear in $\cos\theta_p$ for P_z and a $\cos\phi_p$ or $\sin\phi_p$ dependence for P_x or P_y polarisation, respectively. The angular distributions of the total model are more complicated, still featuring the step at $\phi_p = 0$.

A third test is set performing a full phase space amplitude fit using the reduced model to a sample consisting of 80'000 events, featuring invariant mass distributions generated according to the Dalitz plot fit of Table 5.7 and uniformly generated angular distributions corresponding to zero polarisation. No detector efficiency effects are included here. The result is reported in Fig. 5.32: the fit is able to select an amplitude model with uniform angular distributions at the price of creating discrepancies in the invariant masses. Interestingly, the extracted polarisation is close to zero as it should be,

$$P_x = -0.005 \pm 0.007 \qquad P_y = -0.033 \pm 0.008 \qquad P_z = -0.014 \pm 0.003,$$

with a bias of ≈ 0.03 in P_y, even if uncertainties are oddly different for different components.

The last test is performed as the third one, but including efficiency effects. The generated sample is built in the same way but throwing events from the ReDecay simulated sample. The result is reported in Fig. 5.33 and it is in line with that of Fig. 5.32. The extracted polarisation is less compatible with to zero than before,

$$P_x = -0.059 \pm 0.005 \qquad P_y = -0.014 \pm 0.005 \qquad P_z = 0.066 \pm 0.005,$$

with a bias up to 0.066, but this time uncertainties are similar for all the polarisation components.

From the latter two tests, it is possible to conclude that the departure of the amplitude model angular distributions from isotropy for zero polarisation is heavily model-dependent; so the strange step-like ϕ_p distribution is a feature of the particular model employed and exists models whose angular distributions are uniform. This has been cross-checked by repeating the first test, Fig. 5.26, with different models, showing that the interference pattern changes with the generation model.

Summarising, the amplitude model shows an unphysical, model-dependent behaviour in interference effects, which prevents the full phase space amplitude fit to reproduce the observed distributions. At the time of writing this thesis, the cause of this problem is still under investigation.

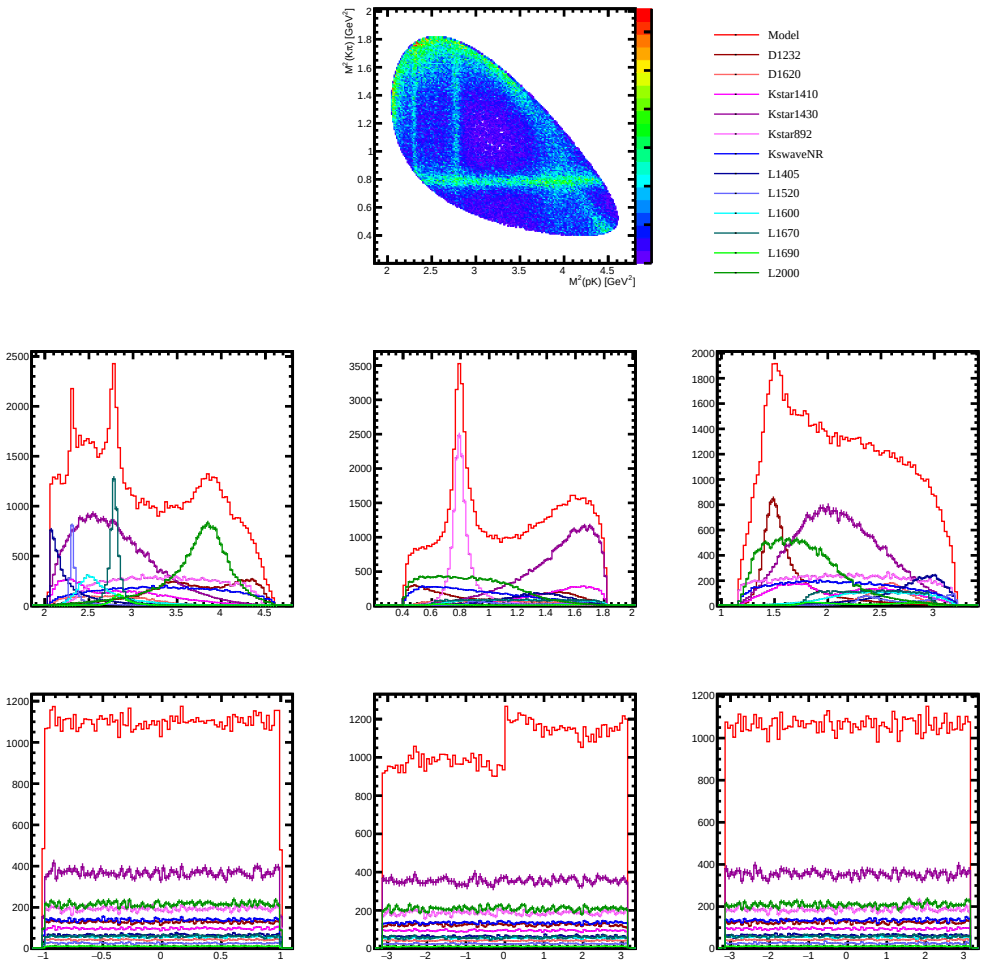

Figure 5.26: Phase space distributions generated from the amplitude model obtained from the Dalitz plot fit to the reduced model with zero polarisation, for 100’000 events.

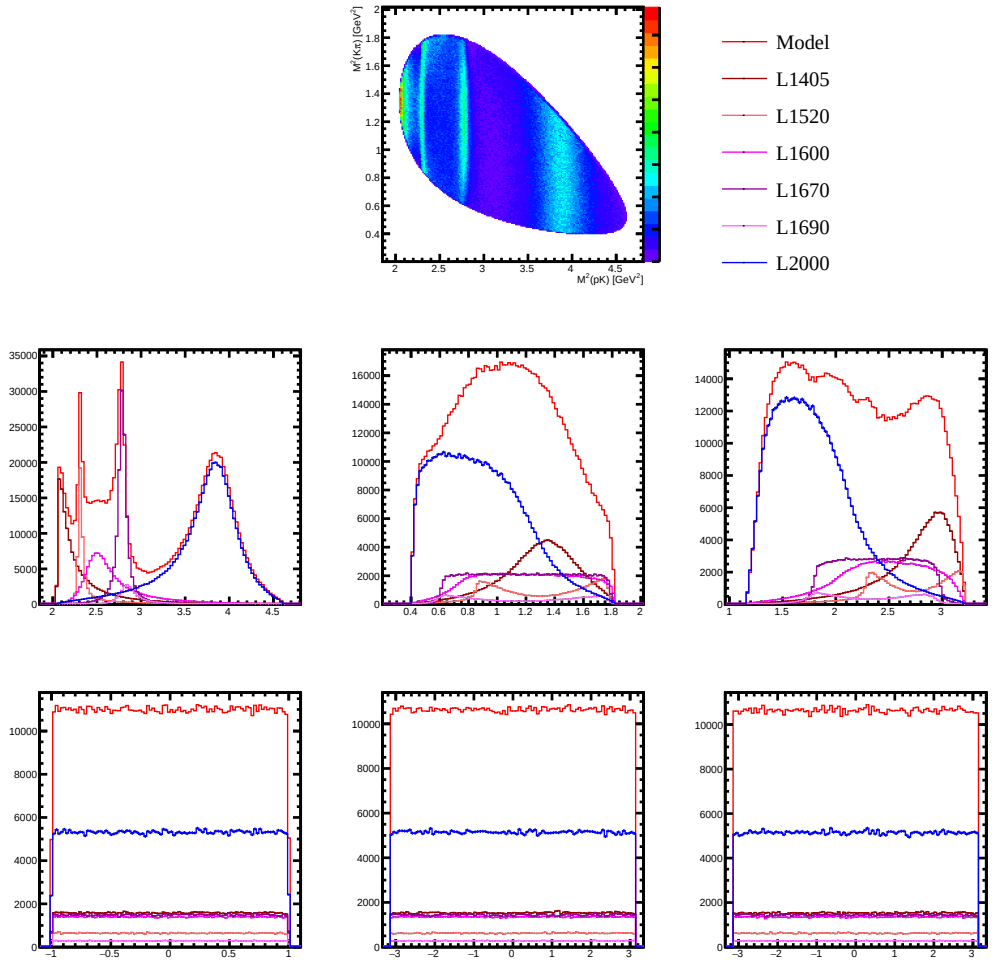

Figure 5.27: Phase space distributions generated from the amplitude model obtained from the Dalitz plot fit to the reduced model with zero polarisation in which only Λ^* resonances are kept, for 10^6 events.

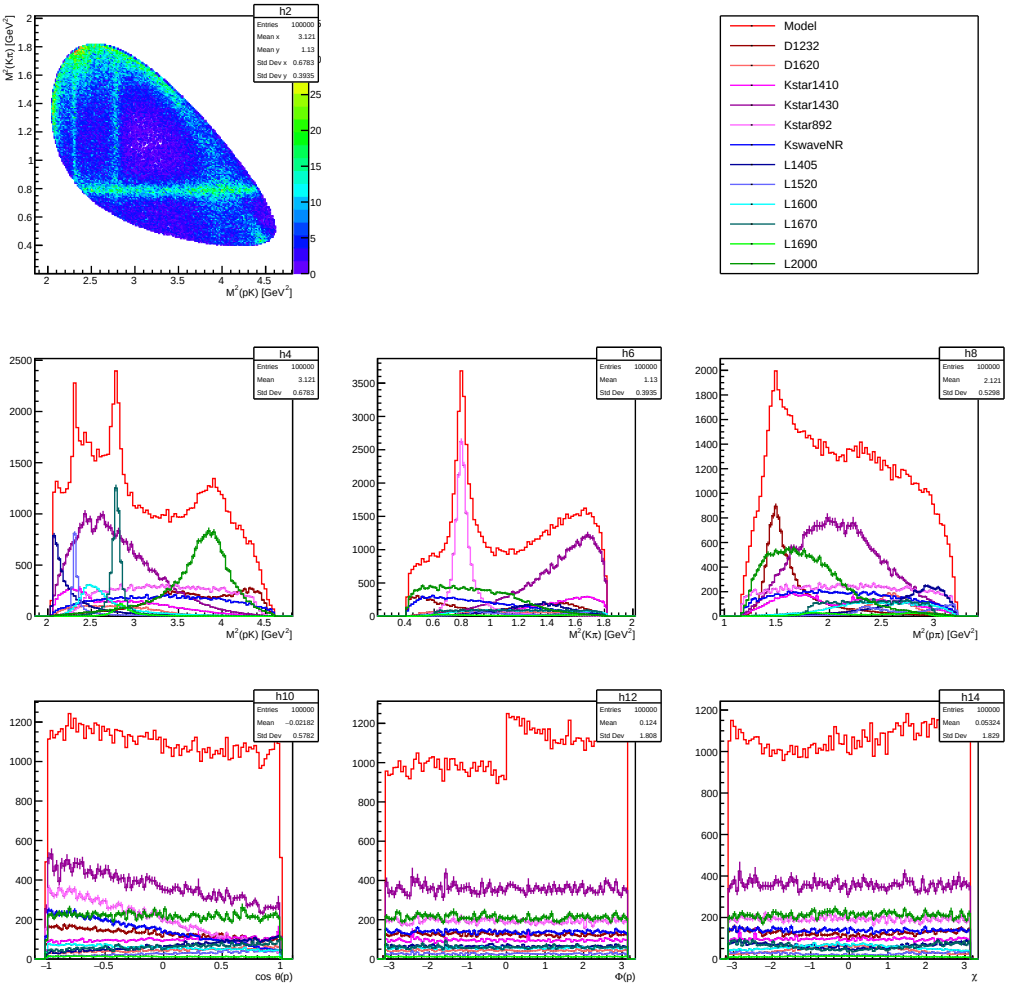

Figure 5.28: Phase space distributions generated from the amplitude model obtained from the Dalitz plot fit to the reduced model with full polarisation $P_z = 1$, for 100′000 events.

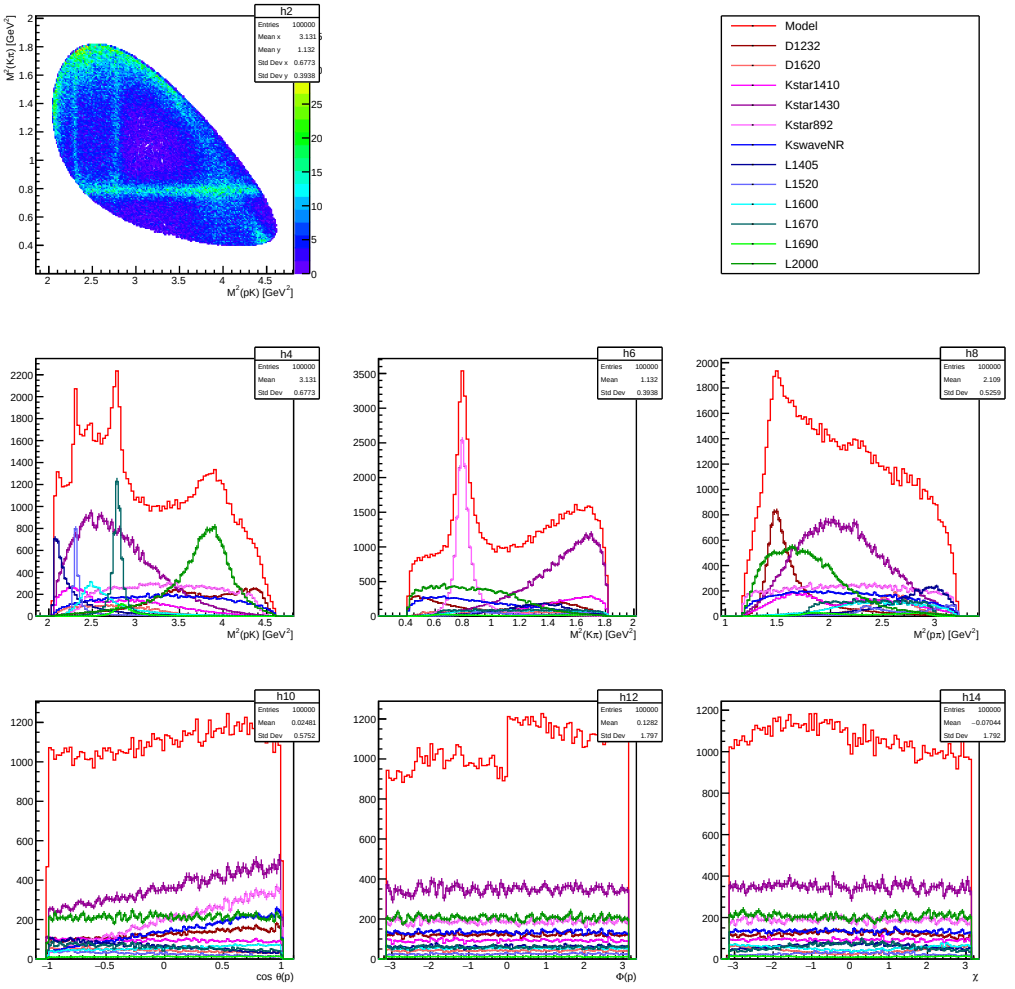

Figure 5.29: Phase space distributions generated from the amplitude model obtained from the Dalitz plot fit to the reduced model with full polarisation $P_z = -1$, for 100'000 events.

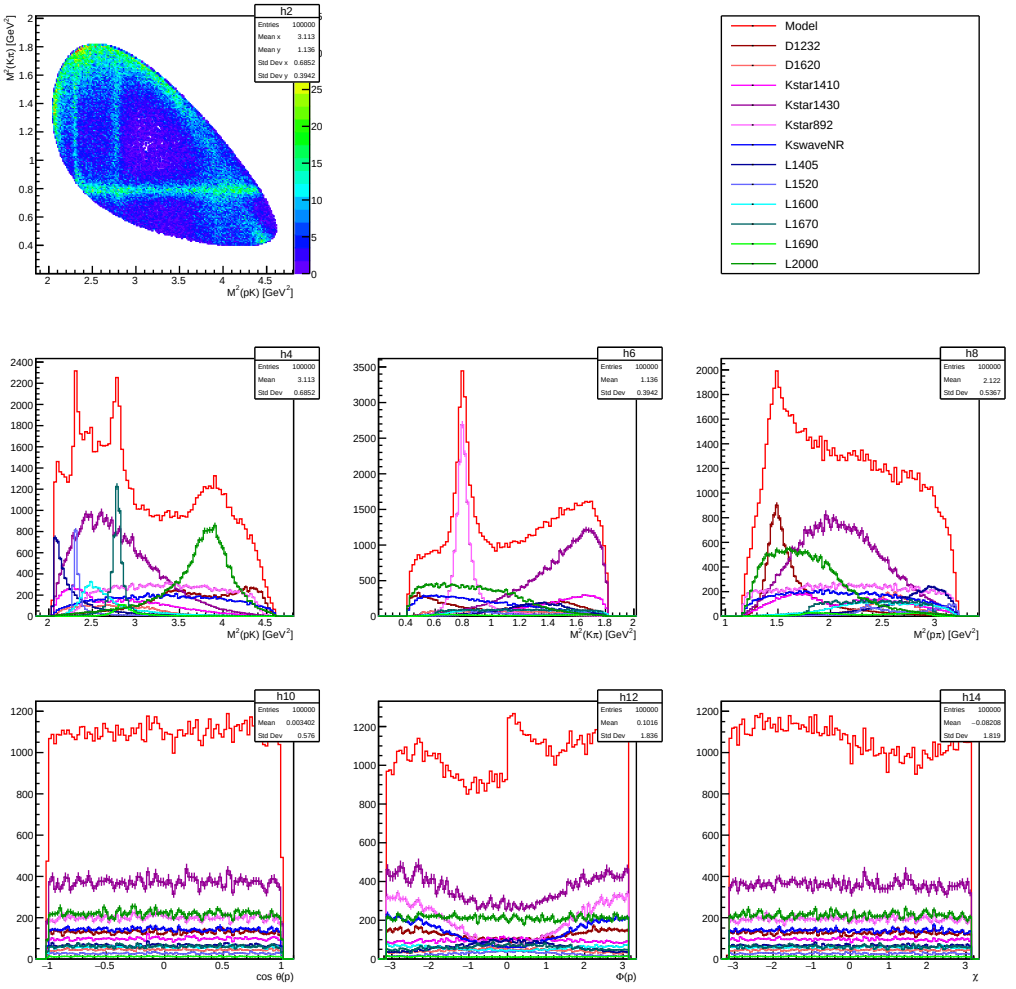

Figure 5.30: Phase space distributions generated from the amplitude model obtained from the Dalitz plot fit to the reduced model with full polarisation $P_x = 1$, for 100'000 events.

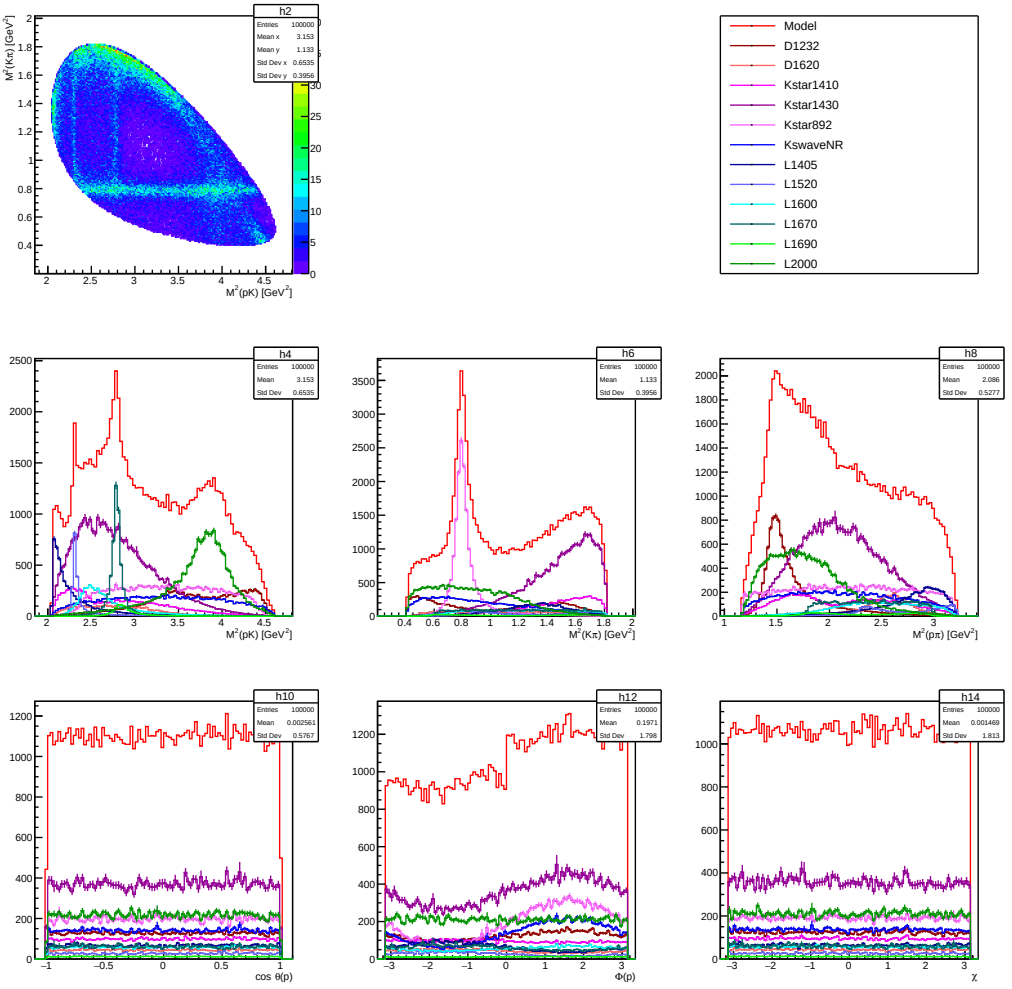

Figure 5.31: Phase space distributions generated from the amplitude model obtained from the Dalitz plot fit to the reduced model with full polarisation $P_y = 1$, for 100'000 events.

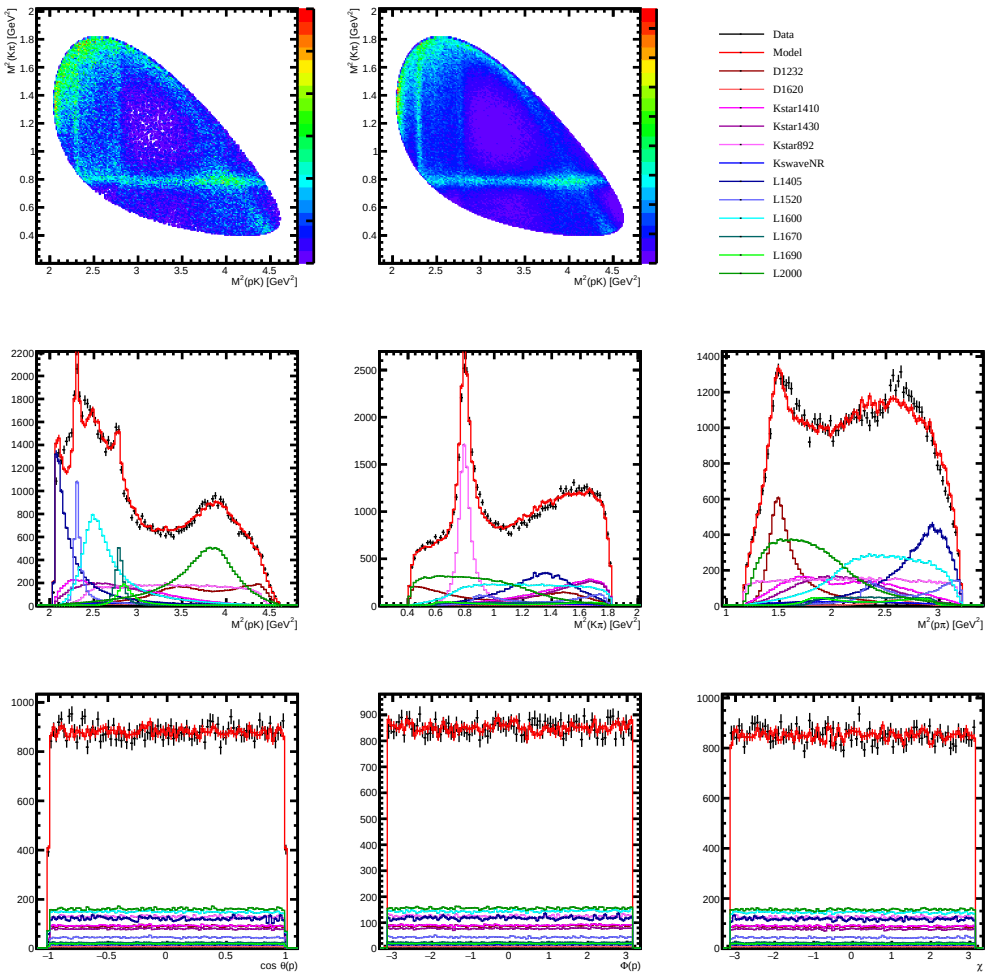

Figure 5.32: Fit to a generated sample with uniform angular distributions of 80'000 events, without detector efficiency effects. See text for details.

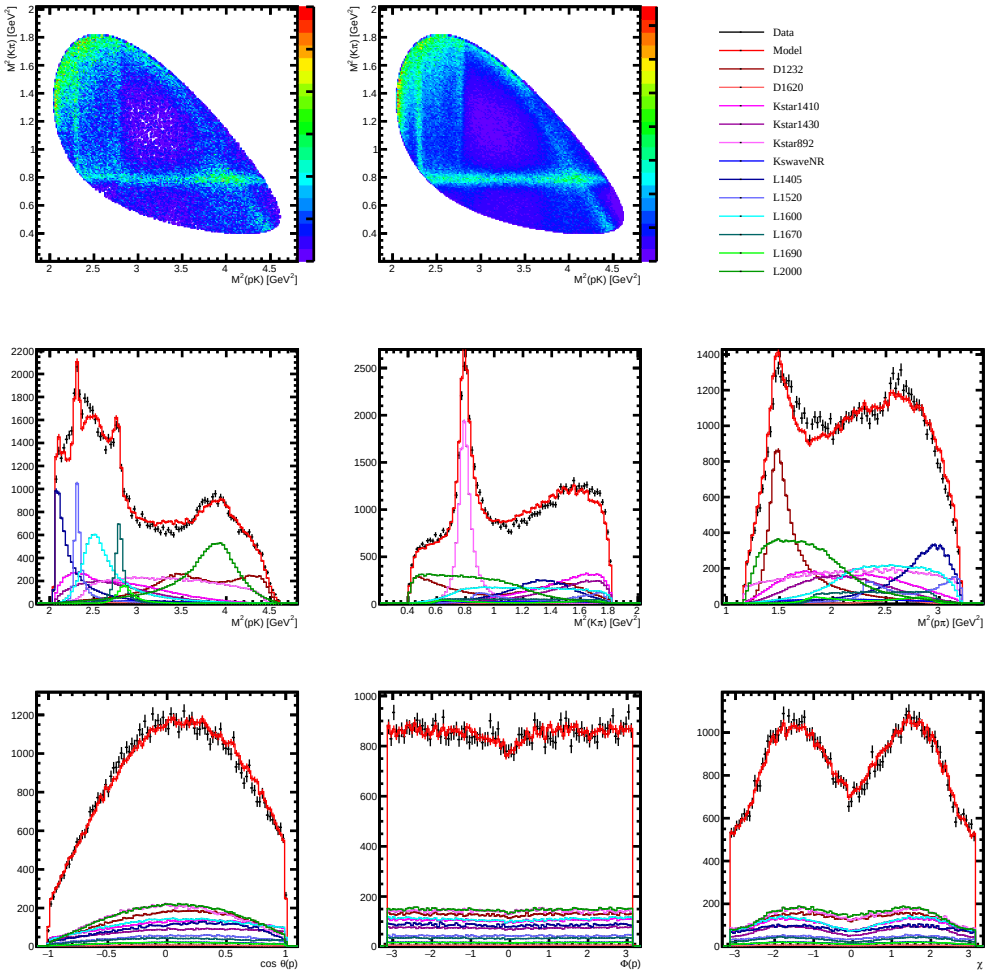

Figure 5.33: Fit to generated sample with uniform angular distributions of 80'000 events, including detector efficiency effects. See text for details.

5.4.7 Sensitivity to polarisation

The precision of the proposed experiment for the Λ_c^+ baryon dipole moments measurement depends in a critical way on the sensitivity of the $\Lambda_c^+ \to pK^-\pi^+$ decay distributions to the Λ_c^+ polarisation. In Sec. 2.5, the sensitivity to the polarisation has been estimated from the information available on the quasi two-body decay $\Lambda_c^+ \to \Delta^{++}K^-$. In the following, the sensitivity to the polarisation of the reduced amplitude model derived in Sec. 5.4.4 is studied. Since this model is not the final amplitude fit, given the problems affecting the full phase space amplitude fit, the presented results have to be considered preliminary; the aim of this study is to show how the sensitivity to the polarisation can be extracted from an amplitude model.

The amplitude model defined by the polarised decay rate Eq. (5.18) is considered for the case of P_z polarisation only: for rotational invariance, the sensitivity to the polarisation will be the same for any component, as far as detector efficiency effects are not included. For instance, the study for the τ^+ polarisation extraction presented in Sec. 3.4 showed a different sensitivity for different polarisation components because reconstruction effects were included in the definition of the templates Eq. (3.11). The decay rate Eq. (5.18) for $P_x = P_y = 0$ can be written, following the notation of Ref. [125], as

$$p(\Omega, P_z) = f(\Omega) + P_z\, g(\Omega), \tag{5.41}$$

with

$$\begin{aligned} f(\Omega) &\propto \sum_{m_p=\pm 1/2} \left[|\mathcal{A}_{1/2,m_p}(\Omega)|^2 + |\mathcal{A}_{-1/2,m_p}(\Omega)|^2\right] \\ &= p(\Omega, P_z = 0) \\ g(\Omega) &\propto \sum_{m_p=\pm 1/2} \left[|\mathcal{A}_{1/2,m_p}(\Omega)|^2 - |\mathcal{A}_{-1/2,m_p}(\Omega)|^2\right] \\ &\propto p(\Omega, P_z = 1) - p(\Omega, P_z = -1), \end{aligned} \tag{5.42}$$

normalised in such a way that

$$\int p(\Omega, P_z) d\Omega = \int f(\Omega) d\Omega = 1, \tag{5.43}$$

with the g function integrating to zero over the phase space,

$$\int g(\Omega) d\Omega = 0. \tag{5.44}$$

Given the NLL Eq. (5.25) with p_{tot} the decay rate Eq. (5.41), the P_z uncertainty for $P_z = 0$ follows from Eq. (5.33) as

$$\begin{aligned} \frac{1}{\sigma^2} &= -\frac{\partial^2 \log \mathcal{L}(\omega)}{\partial P_z^2}\bigg|_{P_z=0} \\ &= \sum_i^N \frac{g^2}{f^2}(\Omega_i), \end{aligned} \tag{5.45}$$

in which the fit parameters ω are fixed to the values obtained for the reduced model

Dalitz plot fit, Table 5.7.

The sensitivity to the polarisation is measured by the squared average event Fisher information

$$S^2 = \frac{1}{N\sigma^2} = \left\langle \frac{g^2}{f^2}(\Omega) \right\rangle = \int \frac{g^2}{f}(\Omega) d\Omega, \tag{5.46}$$

which, for the amplitude model under study, is found to be $S = 0.38$. This value is compared to the case of the two-body decay distribution Eq. (2.5), for which the Fisher information depends on the decay asymmetry parameter α_f as

$$S = \frac{|\alpha_f|}{\sqrt{3}}. \tag{5.47}$$

An effective α parameter for the amplitude model can be obtained inverting Eq. (5.47), obtaining $\alpha = 0.65$.

This preliminary result suggests that the sensitivity of the amplitude model to the polarisation is similar to that assumed for the quasi two-body decay $\Lambda_c^+ \to \Delta^{++} K^-$ in Table 2.2, $|\alpha_{\Delta^{++}K^-}| = 0.67$; however, the use of the amplitude model allows to exploit the full statistics of $\Lambda_c^+ \to pK^-\pi^+$ decays. Therefore, in the sensitivity study for the Λ_c^+ dipole moments, Sec. 2.5, the number of useful Λ_c^+ decays $N^{\rm reco}_{\Lambda_c^+}$ can be increased by a factor $\mathcal{B}(\Lambda_c^+ \to pK^-\pi^+)/\mathcal{B}(\Lambda_c^+ \to \Delta^{++}K^-) \approx 5.8$, according to the PDG values [24].

To evaluate the sensitivity to the polarisation as a function of the Dalitz plot, the squared Fisher information is computed as a function of $m^2_{pK^-}$ and $m^2_{K^-\pi^+}$ invariant masses,

$$S^2(m^2_{pK^-}, m^2_{K^-\pi^+}) = \int \frac{g^2}{f}(\Omega) d\cos\theta_p d\phi_p d\chi, \tag{5.48}$$

and shown in Fig. 5.34.

The sensitivity to the polarisation of each contribution of the amplitude model is obtained computing S when only one resonance is kept in the amplitude model; however, this way the information about the interference pattern is lost. The S values and the associated decay asymmetry α parameters are reported in Table 5.11. When final values will be available, these α parameters will supersede those derived from the E791 experiment amplitude analysis [88].

5.5 Conclusions and future plans

The amplitude analysis of $\Lambda_c^+ \to pK^-\pi^+$ decays from Λ_b^0 semileptonic production recorded by the LHCb experiment is well under way. The amplitude model for a full phase space fit of $\Lambda_c^+ \to pK^-\pi^+$ decays, allowing the extraction of the polarisation vector, has been developed following the helicity formalism, within the TensorFlowAnalysis package. A very pure selection of $\Lambda_c^+ \to pK^-\pi^+$ candidates has been developed, which allow to neglect background contributions in the amplitude fit. This way the code is able to account for detector efficiency effects exploiting simulated $\Lambda_c^+ \to pK^-\pi^+$ events reconstructed by the LHCb detector without the need of explicit parametrisation.

The decay model is built according to the current knowledge of resonances contributing to pK^-, $p\pi^+$ and $K^-\pi^+$ decay channels. Two models with identical resonance content but different number of fit parameters have been considered. The 2-dimensional Dalitz plot amplitude fits well describe the invariant mass decay distributions. An unex-

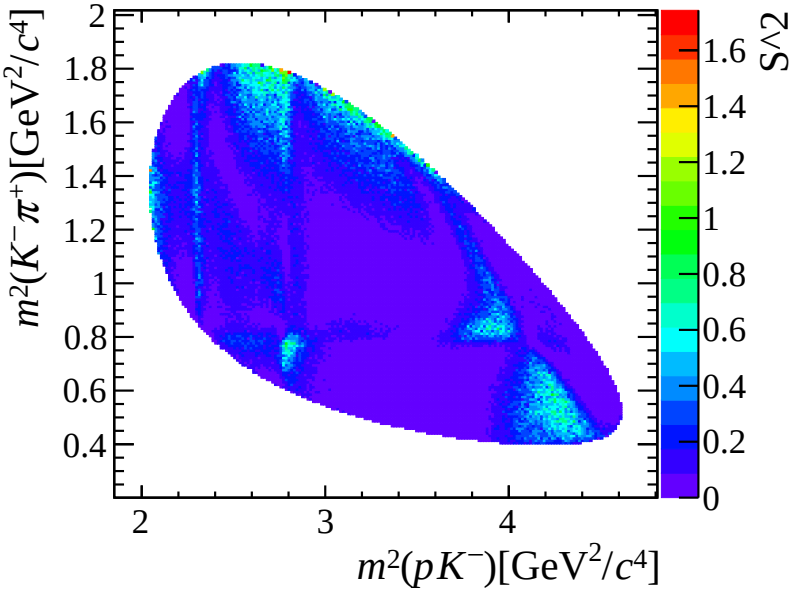

Figure 5.34: Squared Fisher information associated to P_z polarisation over the Dalitz plot.

Resonance	S	α
Non resonant	0.42	0.72
$K^*(892)$	0.46	0.80
$K^*(1410)$	0.31	0.53
$K^*(1430)$	0.19	0.33
$\Lambda^*(1405)$	0.38	0.66
$\Lambda^*(1520)$	0.40	0.69
$\Lambda^*(1600)$	0.28	0.49
$\Lambda^*(1670)$	0.33	0.57
$\Lambda^*(1690)$	0.24	0.41
$\Lambda^*(2000)$	0.04	0.07
$\Delta^{*++}(1232)$	0.19	0.33
$\Delta^{*++}(1620)$	0.48	0.84

Table 5.11: Fisher information and decay asymmetry parameters associated to each contribution of the amplitude model.

Resonance	Fit fraction
Non resonant	0.418255
$K^*(892)$	0.091210
$K^*(1410)$	0.118811
$K^*(1430)$	0.290045
$\Lambda^*(1405)$	0.059900
$\Lambda^*(1520)$	0.014751
$\Lambda^*(1600)$	0.052037
$\Lambda^*(1670)$	0.012482
$\Lambda^*(1690)$	0.014049
$\Lambda^*(2000)$	0.157156
$\Delta^{*++}(1232)$	0.086709
$\Delta^{*++}(1620)$	0.066167
Sum	1.381570

Table 5.12: Fit fractions for the phase space amplitude fit for the reduced model on 100'000 $\Lambda_c^+ \to pK^-\pi^+$ candidates, performed with a preliminary amplitude model based on the prescriptions of Refs. [157, 172].

pected contribution from Λ^* resonances is observed with statistical significance of 32.5σ, which can be parametrised by a spin $1/2$ state with mass around 1.97 GeV and width around 140 MeV. Fit fractions for overlapping resonances are not well determined with the employed statistics.

Full phase space 5-dimensional amplitude fits are performed, but a problem related to the implementation of the amplitude model prevents the fits to find a good description of the phase space distributions. A thorough set of tests has shown that the issue is uniquely related to an unphysical, model-dependent interference pattern, which only arise when resonances belonging to different decay chains interfere. The cause of this problem was still not clear at the time of writing this thesis. During the review stage, a possible issue related to unphysical phases introduced between different decay chains has been identified [172]. Preliminary work in this direction suggests that a precise matching of the phases associated to spin states is able to solve the discrepancy seen in the ϕ_p distribution: Fig. 5.35 shows a phase space amplitude fit for the reduced amplitude model, the analogue of Fig. 5.24, performed with a preliminary amplitude model based on the prescriptions of Refs. [157, 172]; the associated fit fractions are reported in Table 5.12. This amplitude fit must be considered as work in progress, since a proper test of its implementation has not been performed yet.

A preliminary study to quantify the sensitivity to the polarisation of the amplitude model has been performed, suggesting that it is similar to that assumed for the quasi two-body decay $\Lambda_c^+ \to \Delta^{++}K^-$ in the sensitivity study for the proposed experiment for charm baryon dipole moments measurement. This would allow an increase of the useful Λ_c^+ decays for the dipole moments measurement of a factor six. Interestingly, the sensitivity to the polarisation is basically unchanged when computed with the new, preliminary amplitude model of Fig. 5.35, suggesting it is a model-independent feature of the $\Lambda_c^+ \to pK^-\pi^+$ decay.

Besides understanding the problem affecting full phase space amplitude fits, the next step of the analysis will be to increase the fitted data sample to allow a better determination of the amplitude model. The bottleneck is currently given by the size of the

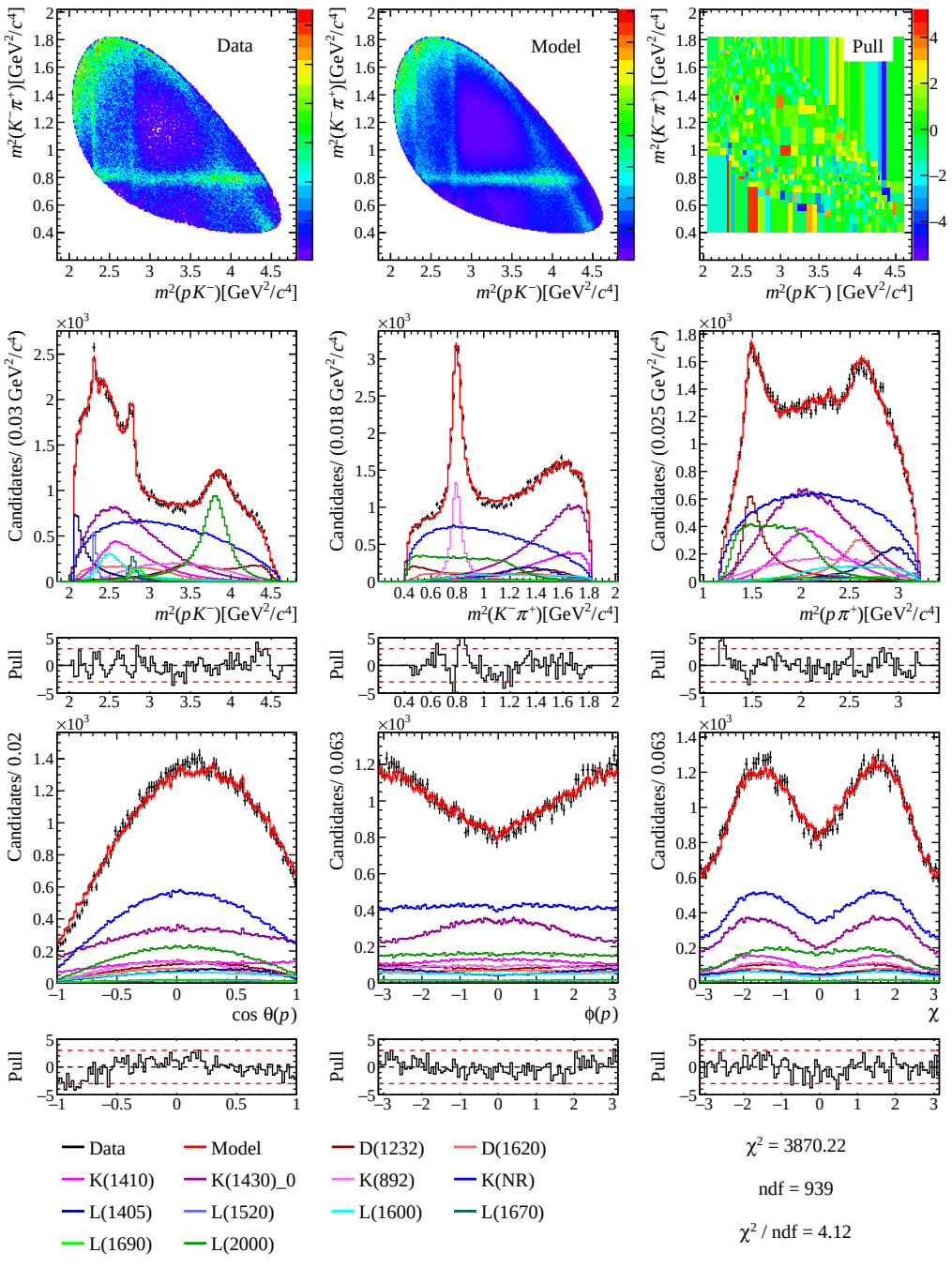

Figure 5.35: A phase space amplitude fit for the reduced model on 100′000 $\Lambda_c^+ \to pK^-\pi^+$ candidates, performed with a preliminary amplitude model based on the prescriptions of Refs. [157, 172]. This amplitude fit is the analogue of Fig. 5.24 and must be considered as work in progress.

simulation sample. After a reasonably good amplitude model is found, systematic uncertainties can be evaluated. A particular attention would be required for the systematic uncertainty associated to the choice of the amplitude model.

Part III

Λ_c^+ polarisation measurement in p-Ne collisions at $\sqrt{s} = 68.6\,\mathrm{GeV}$ at LHCb

CHAPTER 6

Λ_c^+ polarisation measurement in proton-neon collisions at $\sqrt{s} = 68.6\,\text{GeV}$ at LHCb

6.1 Motivation

The measurement of Λ_c^+ baryon polarisation is an interesting probe for low-energy QCD models trying to explain its structure [173]. According to heavy quark effective theory, most of the c-quark polarisation is expected to be retained by the charm baryon, this giving information on the c-quark polarisation and its production mechanisms, see Sec. 1.3.2.

Due to the smaller production cross-sections of charm baryons with respect to light and strange ones, only two Λ_c^+ polarisation measurements have been performed to date, both in proton-nucleus fixed-target configurations. The measurements using 230 GeV π^- collisions on Cu target by the NA32 experiment at CERN-SPS [70] and 500 GeV π^- on a Pt-diamond target by the E791 experiment [71], reported a trend of increasing negative Λ_c^+ baryon polarisation with p_{T}

The $\Lambda_c^+ \to pK^-\pi^+$ events from collisions of 2.5 TeV protons on gaseous neon recorded by the LHCb experiment in its fixed-target (SMOG) configuration can probe the Λ_c^+ polarisation at the unprecedented center-of-mass energy $\sqrt{s} = 68.6\,\text{GeV}$. A significant Λ_c^+ polarisation in fixed-target collisions of LHC protons is crucial for the proposed search of charm baryon electromagnetic dipole moments using bent crystals at LHC(b), Chapter 2, being the sensitivity to dipole moments directly proportional to the Λ_c^+ polarisation, Eq. (2.70).

In this part of the thesis, the status of the the Λ_c^+ polarisation measurement in proton-neon collisions at $\sqrt{s} = 68.6\,\text{GeV}$ recorded by LHCb is presented. In Sec. 6.2 the studies performed to select $\Lambda_c^+ \to pK^-\pi^+$ candidates from the LHCb SMOG proton-neon data sample are presented, including the rejection of combinatorial background and of pp collision events. The effectiveness of the polarisation extraction and the evaluation of the associated systematic uncertainty, using the $\Lambda_c^+ \to pK^-\pi^+$ amplitude model obtained from pp collisions in Chapter 5, is reported in Sec. 6.3. The conclusions are summarised in Sec. 6.4.

6.2 Data and simulation samples

The Λ_c^+ polarisation in proton-gas fixed-target collisions is studied using the proton-neon data sample recorded by the LHCb experiment in 2017, in which 2.5 TeV protons collided on neon atoms injected in the Vertex Locator tank by the SMOG system, yielding fixed-target collisions at centre-of-mass energy of $68.6\,\text{GeV}$. This sample has been

Particle	Quantity	Cut
hadron	min p_{T}	200 MeV
	min p	3 GeV
	track χ^2/ndf	< 5
	min primary vertex IP χ^2	2
p	min PID_p	5
	min $\mathrm{PID}_p - \mathrm{PID}_K$	5
K	min PID_K	5
π	max PID_K	5
$\{p, K, \pi\}$	greater hadron p_{T}	> 1 GeV
	greater two hadron p_{T}	> 400 MeV
	greater hadron primary vertex IP χ^2	> 9
	greater two hadron primary vertex IP χ^2	> 4
Λ_c^+	$m(pK\pi)$ interval	$m(\Lambda_c^+)_{\mathrm{PDG}} \pm 500$ MeV
	DOCA χ^2 limit between daughter tracks	2.0

Table 6.1: `HeavyIonOpenCharmLc2PKpiLine` selection criteria. See Table 5.1 for quantity definitions.

obtained from a total of 4.5×10^{23} protons on target, corresponding to an integrated luminosity of $\approx 200\,\mathrm{nb}^{-1}$. Contrarily to previous proton-gas data samples, recorded during dedicated accelerator operations with no proton-proton collision program, proton-neon collisions were recorded simultaneously with proton-proton collisions at $\sqrt{s} = 5\,\mathrm{TeV}$. This allowed for an unprecedented luminosity of the recorded sample, but at the price of an higher background rate of overlapping proton-proton collisions.

SMOG data samples are indeed collected only when fully-filled Beam 1 bunches cross empty Beam 2 bunches at the Interaction Point (IP), so that no proton-proton collisions are expected. However, due to imperfections in the beam operations, some protons of the Beam 2 can leak from filled bunches to empty ones, called ghost charges, causing unwanted proton-proton collision events. These events can be separated from true fixed-target collisions thanks to the different topology of the latter, as explained in Sec. 6.2.1.

The $\Lambda_c^+ \to pK^-\pi^+$ candidates are selected from the proton-neon 2017 sample applying the `HeavyIonOpenCharmLc2PKpiLine` stripping selection, whose criteria are listed in Table 6.1. Two software trigger selection lines are available: `Hlt1SMOGpKPi` and `Hlt2SMOGLc2KPPi`, with selection criteria listed in Tables 6.2 and 6.3, respectively. No specific hardware trigger selection is applied.

A simulation sample reproducing $\Lambda_c^+ \to pK^-\pi^+$ fixed-target collisions with a flat phase space decay model has been produced. To reproduce the typical features of a proton-nucleus collision, the charm baryon decay generated using PYTHIA [123] package is superimposed on minimum bias proton-neon events generated with the EPOS generator for heavy ion collisions [153]. The sample consists of one million generated events, of which 4188 passing the stripping requirements, whose reconstructed $m(pK^-\pi^+)$ is displayed in Fig. 6.1. Only 1046 events (25% of the total), composing the peak at the known Λ_c^+ mass, are correctly reconstructed as signal events, while the remainder consist of badly reconstructed events. The main cause of unsuccessful reconstruction is due to background tracks coming from other primary vertexes (37%), from the same primary vertex (20%) or from fake tracks (14%); a consequence of the harsh environment charac-

Particle	Quantity	Cut
hadron	min p_T	600 MeV
	min p	4 GeV
	max track χ^2/ndf	2
$\{p, K, \pi\}$	greater hadron p_T	$> 900\,\text{MeV}$
	DOCA limit between daughter tracks	0.2 mm
Λ_c^+	$m(pK\pi)$ interval	$m(\Lambda_c^+)_\text{PDG} \pm 150\,\text{MeV}$
	max vertex χ^2/ndf	10

Table 6.2: `Hlt1SMOGpKPi` trigger selection criteria.

Particle	Quantity	Cut
hadron	min p_T	200 MeV
$\{p, K, \pi\}$	greater hadron p_T	$> 1\,\text{GeV}$
	greater two hadron p_T	$> 400\,\text{MeV}$
Λ_c^+	$m(pK\pi)$ interval	$[2211, 2543]$ MeV
	max vertex χ^2/ndf	25

Table 6.3: `Hlt2SMOGLc2KPPi` trigger selection criteria.

terising the proton-neon data-taking.

6.2.1 Global selection of fixed-target events

A global selection of fixed-target events to reject proton-proton collision events due to ghost charge collisions can be set exploiting the different characteristic topology of fixed-target events with respect to pp collision events. The topology can be controlled by the following quantities: the z coordinate of the primary vertex z_{PV}, the number of hits registered in the VELO pile-up veto counter `nPUHits` and the number of reconstructed backward tracks (opposite to the rest of the LHCb detector) `nBackTracks`. Fixed-target events feature forward, high momentum and high pseudorapidity tracks only, `nBackTracks` ≈ 0, and a wide z_{PV} distribution following the gas density in the beampipe. If the primary vertex is inside the VELO detector, no hits are expected in the pile-up counter described in Sec. 4.2.1, `nPUHits` ≈ 0; events in which the primary vertex is upstream the VELO, featuring significant activity in the pile-up counter, can also be considered as signal events. Proton-proton collision events are instead symmetric in forward and backward directions, characterised by significant backward activity and a z_{PV} distribution centred around the interaction point $z = 0$. Note that the VELO pile-up counters are located between $z = -315$ and $z = -220$ mm. The z_{PV}-`nPUHits` distribution of stripped $\Lambda_c^+ \to pK^-\pi^+$ candidates, highlighting the three types of decay topologies present in the SMOG dataset, is displayed in Fig. 6.2

A conservative global selection is applied to effectively remove pp collisions, summarised in Table 6.4. In the region $-100 < z_{PV} < 100$ mm in which most of the pp collision events take place no activity in the backward part of the VELO detector, `nPUHits` $= 0$ and `nBackTracks` $= 0$. Some backward activity, `nPUHits` < 5 and `nBackTracks` < 5, is allowed for events in $-200 < z_{PV} < -100$ and $100 < z_{PV} < 200$ mm. Further studies can be carried out to improve the signal efficiency, possibly including signal

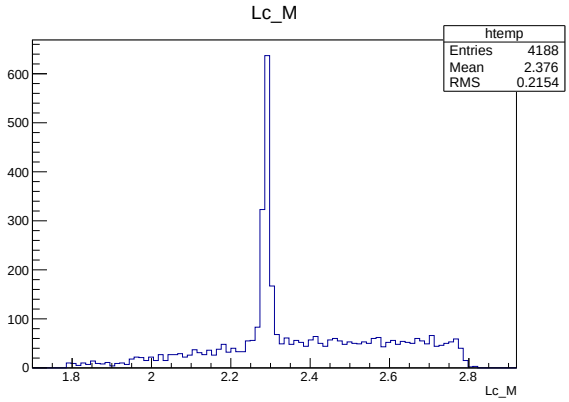

Figure 6.1: The $pK^-\pi^+$ invariant mass distribution of $\Lambda_c^+ \to pK^-\pi^+$ simulated events passing stripping requirements.

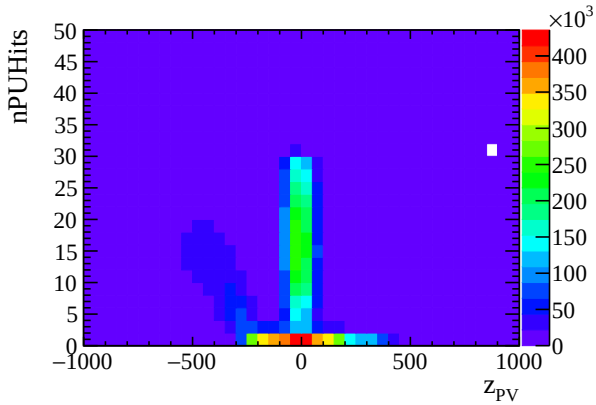

Figure 6.2: The z_{PV}-nPUHits distribution of stripped $\Lambda_c^+ \to pK^-\pi^+$ candidates. SMOG events occurring inside the VELO detector correspond to the bottom horizontal band at nPUHits≈ 0 extending inside the VELO coverage; upstream SMOG events correspond to the diagonal band extending in the backward direction with increasing pile-up counter activity; pp collision events correspond to the vertical band mostly confined to the $-100 < z_{PV} < 100$ mm region.

z_{PV} region (mm)	nPUHits	nBackTracks
$-200 < z_{PV} < -100$	< 5	< 5
$-100 < z_{PV} < 100$	$= 0$	$= 0$
$100 < z_{PV} < 200$	< 5	< 5

Table 6.4: Global selection cuts applied to remove pp collisions events.

Quantity	Cut
$\text{PID}_p(p)$	> 15
$\text{PID}_K(K)$	> 15
$\text{PID}_K(\pi)$	< -30
Λ_c^+ decay vertex χ^2/ndf	< 6
Λ_c^+ PV impact parameter χ^2/ndf	< 2
DIRA angle	< 0.015
Λ_c^+ lifetime	> 0.5 ps

Table 6.5: Requirements of the cut-based selection for $\Lambda_c^+ \to pK^-\pi^+$ fixed-target candidates. See Table 5.1 for quantity definitions.

Parameter	Central value $\pm$ Uncertainty
Signal events	172.07 $\pm$ 16.1
Background events	242.05 $\pm$ 18.1
Gauss $\overline{x}$ $\left[\text{GeV}/c^2\right]$	2.2889 $\pm$ 0.000669
Gauss σ $\left[\text{MeV}/c^2\right]$	6.6869 $\pm$ 0.668
Exp c $\left[(\text{GeV}/c^2)^{-1}\right]$	-0.081944 $\pm$ 1.40

Table 6.6: Results of the invariant mass fit of $\Lambda_c^+ \to pK^-\pi^+$ candidates after the cut-based selection described in Table 6.5.

events occurring upstream the VELO detector.

6.2.2 Selection and invariant mass fit

A simple cut-based selection, aiming at high signal purity, is studied on $\Lambda_c^+ \to pK^-\pi^+$ candidates selected by the stripping line and triggered on signal by both the trigger lines described in Sec. 6.2, its requirements listed in Table 6.5. The selection requires $\Lambda_c^+ \to pK^-\pi^+$ candidates to have: good hadron identification responses, measured from the delta log-likelihood PID_h between h and pion hypotheses; good Λ_c^+ decay vertex; Λ_c^+ impact parameter compatible with the primary vertex; Λ_c^+ momentum compatible with flight direction and a sufficiently long lifetime to remove prompt background.

Signal and background contributions are separated from $\Lambda_c^+ \to pK^-\pi^+$ candidates by means of a fit to the $pK^-\pi^+$ invariant mass distribution, in which a Gaussian and an exponential are employed as signal and background models, respectively. The fit to the $pK^-\pi^+$ invariant mass distribution for fixed-target $\Lambda_c^+ \to pK^-\pi^+$ selected candidates is shown in Fig. 6.3, results reported in Table 6.6. A signal yield of 172 ± 16 is found, with a peak resolution of ≈ 6.7 MeV. The background yield 242 ± 18 corresponds to a background fraction of $\approx 21\%$ in the signal region chosen as $|m(pK^-\pi^+) - m(\Lambda_c^+)_{\text{PDG}}| < 15\,\text{MeV}$. The significance figure-of-merit $S/\sqrt{S+B}$, computed using signal and background yields in the signal region, is 11.7.

Besides the cut-based selection, a more refined selection based on a multivariate classifier is explored. The basic idea is to exploit the sample of $D^+ \to K^-\pi^+\pi^+$ fixed-target candidates, having a much larger statistics than the $\Lambda_c^+ \to pK^-\pi^+$ one, to train a Boosted Decision Tree (BDT) discriminating between signal and background events. The $D^+ \to K^-\pi^+\pi^+$ has indeed a three-body topology similar to $\Lambda_c^+ \to pK^-\pi^+$ de-

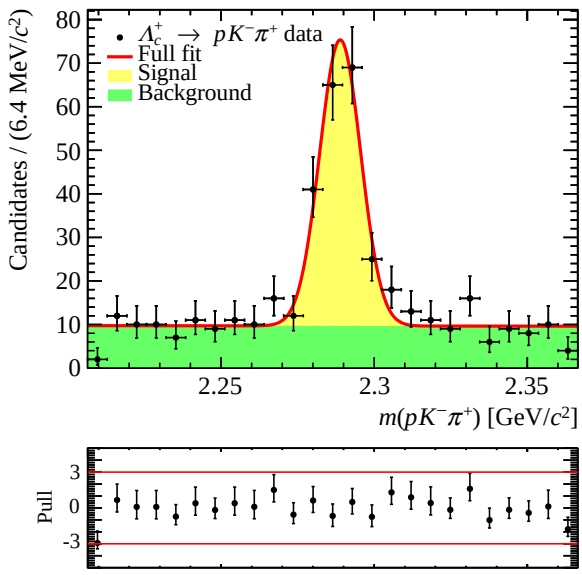

Figure 6.3: Invariant mass distribution of $\Lambda_c^+ \to pK^-\pi^+$ candidates after the cut-based selection described in Table 6.5.

Quantity	Cut
$\mathrm{PID}_K(K)$	> 0
$\mathrm{PID}_K(\pi)$	< -70
D^+ decay vertex χ^2/ndf	< 6
D^+ PV impact parameter χ^2/ndf	< 4
DIRA angle	< 0.03
D^+ lifetime	> 0.3 ps

Table 6.7: Loose selection requirements for the $D^+ \to K^-\pi^+\pi^+$ training sample.

cays, but the D_s^+ meson mean lifetime $\tau(D^+) = 1.04\,\mathrm{ps}$ is about five times larger than the Λ_c^+ baryon one $\tau(\Lambda_c^+) = 0.2\,\mathrm{ps}$. The classifier response on $D^+ \to K^-\pi^+\pi^+$ and $\Lambda_c^+ \to pK^-\pi^+$ candidates is therefore expected to be similar but not equal. Training on a simulated $\Lambda_c^+ \to pK^-\pi^+$ sample larger than the one available at present is planned to reach a better agreement with $\Lambda_c^+ \to pK^-\pi^+$ candidates. In this study trigger requirements are not applied since they have a signal efficiency of $1/3$ only. The training sample is obtained from $D^+ \to K^-\pi^+\pi^+$ candidates selected from their dedicated stripping line satisfying the fixed-target global selection described in Sec. 6.2.1. The purity of the sample is increased applying the loose requirements listed in Table 6.7. Signal and background yields from the $K^-\pi^+\pi^+$ invariant mass fit, employing the same model as for Fig. 6.3, are $S = 7652 \pm 155$ and $B = 46347 \pm 250$. The invariant mass fit is shown in Fig.6.4, results reported in Table 6.8. This way the sample is pure enough to apply the *sPlot* statistical technique [160] to derive signal and background distributions.

The classifier is trained using topological information on half of the $D^+ \to K^-\pi^+\pi^+$ sample; since the final hadrons are different for D^+ and Λ_c^+ decays, particle identifica-

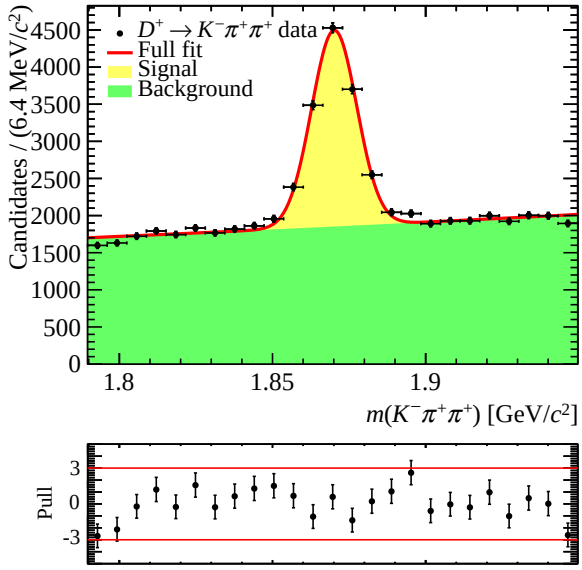

Figure 6.4: Invariant mass distribution of $D^+ \to K^-\pi^+\pi^+$ candidates passing the loose requirements described in Table 6.7.

Parameter	Central value ± Uncertainty
Signal events	7652.4 ± 155
Background events	46347 ± 250
Gauss $\overline{x}$ $\left[\text{GeV}/c^2\right]$	1.8701 ± 0.000156
Gauss σ $\left[\text{MeV}/c^2\right]$	7.3893 ± 0.160
Exp c $\left[(\text{GeV}/c^2)^{-1}\right]$	1.0611 ± 0.101

Table 6.8: Results of the invariant mass fit of $D^+ \to K^-\pi^+\pi^+$ candidates passing the loose requirements described in Table 6.7.

Quantity	Statistical separation (%)
D^+ lifetime	45.49
D^+ decay vertex χ^2/ndf	41.52
DIRA angle	35.74
faster π^+ PV impact parameter $\log\chi^2/\mathrm{ndf}$	35.61
slower π^+ PV impact parameter $\log\chi^2/\mathrm{ndf}$	28.93
K^- PV impact parameter $\log\chi^2/\mathrm{ndf}$	14.48
Primary vertex χ^2/ndf	11.79
D^+ PV impact parameter χ^2/ndf	6.371

Table 6.9: Topological variables used for the BDT training, ranked according to their statistical separation evaluated on the $D^+ \to K^-\pi^+\pi^+$ training sample.

Quantity	Cut
$\mathrm{PID}_p(p)$	> 5
$\mathrm{PID}_K(K)$	> 5
D^+ decay vertex χ^2/ndf	< 6
D^+ PV impact parameter χ^2/ndf	< 4
DIRA angle	< 0.03
D^+ lifetime	> 0.3 ps

Table 6.10: Loose selection requirements for the $\Lambda_c^+ \to pK^-\pi^+$ sample, equal to those applied to the $D^+ \to K^-\pi^+\pi^+$ training sample, Table 6.7, apart from particle identification requirements.

tion requirements are to be studied separately. The topological variables with the best statistical separation[1] between signal and background distributions, Table 6.9, are fed to the BDT.

The optimisation of the cut on the BDT response is performed by finding the maximum of the significance figure-of-merit, computed using signal and background efficiencies derived from the second half of the $D^+ \to K^-\pi^+\pi^+$ sample starting from initial

[1]The difference between signal and background PDFs for a training variable x, $s(x)$ and $b(x)$, representing its discrimination power, can be measured by the statistical separation defined as

$$\langle S^2 \rangle = \frac{1}{2}\int \left(\frac{s(x)-b(x)}{s(x)+b(x)}\right)^2 dx. \tag{6.1}$$

Parameter	Central value $\pm$ Uncertainty
Signal events	503.29 ± 71.9
Background events	23213 ± 167
Gauss $\overline{x}$ $\left[\mathrm{GeV}/c^2\right]$	2.2898 ± 0.000683
Gauss σ $\left[\mathrm{MeV}/c^2\right]$	4.4576 ± 0.764
Exp c $\left[(\mathrm{GeV}/c^2)^{-1}\right]$	1.5587 ± 0.142

Table 6.11: Results of the invariant mass fit of the $\Lambda_c^+ \to pK^-\pi^+$ fixed-target sample with the loose requirements of Table 6.7 applied.

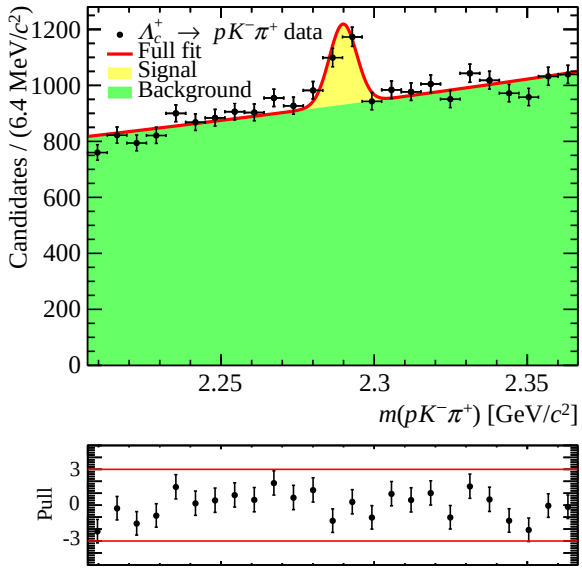

Figure 6.5: Invariant mass distribution of the $\Lambda_c^+ \to pK^-\pi^+$ fixed-target sample with the loose requirements of Table 6.7 applied.

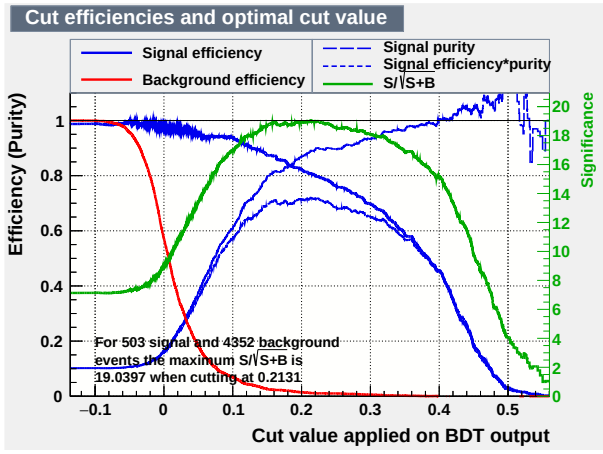

Figure 6.6: Optimisation of the cut on the BDT response.

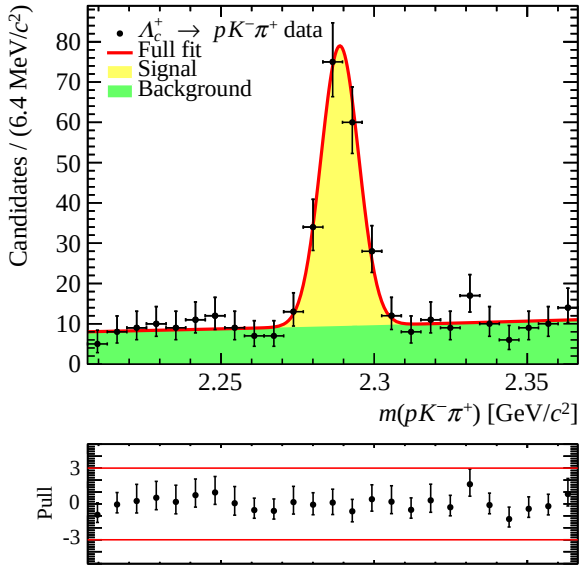

Figure 6.7: Invariant mass distribution of the $\Lambda_c^+ \to pK^-\pi^+$ fixed-target sample with loose requirements (Table 6.7) and $BDT > 0.2131$ cut applied.

values of signal and background $\Lambda_c^+ \to pK^-\pi^+$ yields. The latter are estimated from an invariant mass fit to fixed-target $\Lambda_c^+ \to pK^-\pi^+$ candidates to which the loose requirements of Table 6.10 are applied, Fig. 6.5, obtaining $S = 503 \pm 72$ and $B \approx 4352$ in the $|m(pK^-\pi^+) - m(\Lambda_c^+)_{\rm PDG}| < 15\,{\rm MeV}$ signal region. The invariant mass fit is shown in Fig. 6.5, results reported in Table 6.11. The BDT cut optimisation is presented in Fig. 6.6: a cut value $BDT > 0.2131$ corresponding to a maximum significance of 19.04 is suggested. The invariant mass fit of $\Lambda_c^+ \to pK^-\pi^+$ candidates after application of loose requirements and $BDT > 0.2131$ cut is shown in Fig. 6.7, results reported in Table 6.12, returning a signal yield of 167 ± 15 with a background fraction of $\approx 19\%$ in the signal region, corresponding to a significance of 11.5. The performance of this BDT selection is very similar to the cut-based selection Fig. 6.3, but the former has been achieved with the sole use of topological information, without particle identification nor trigger requirements. The actual significance of the BDT selection is much smaller than the one expected from the optimisation, but this is not surprising as a different BDT response is expected between training and $\Lambda_c^+ \to pK^-\pi^+$ candidates. To obtain a better significance a looser cut value $BDT > 0.07$ is applied: the corresponding invariant mass fit of $\Lambda_c^+ \to pK^-\pi^+$ candidates is shown in Fig. 6.8, results reported in Table 6.13, returning a signal yield of 392 ± 27 with a background fraction of $\approx 42\%$ in the signal region, corresponding to a significance of 15.1. The looser BDT cut allows a better selection with more than double signal yield, at the price of an increased background contamination.

Summarising, the use of a BDT exploiting topological information extracted from $D^+ \to K^-\pi^+\pi^+$ decays is more effective than a simple cut-based selection. The way the BDT is trained and optimised can be improved, since the BDT response is not equal between different D^+ and Λ_c^+ decays, *e.g.* by using simulated $\Lambda_c^+ \to pK^-\pi^+$ decays. The performances of the BDT selection can also be improved by adding particle identification information. Anyway, the important point is that a few hundreds $\Lambda_c^+ \to pK^-\pi^+$

Parameter	Central value ± Uncertainty
Signal events	167.04 ± 15.3
Background events	235.96 ± 17.4
Gauss $\overline{x}$ $\left[\text{GeV}/c^2\right]$	2.2888 ± 0.000609
Gauss σ $\left[\text{MeV}/c^2\right]$	6.1331 ± 0.529
Exp c $\left[(\text{GeV}/c^2)^{-1}\right]$	1.9802 ± 1.41

Table 6.12: Results of the invariant mass fit of the $\Lambda_c^+ \to pK^-\pi^+$ fixed-target sample with loose requirements (Table 6.7) and $BDT > 0.2131$ cut applied.

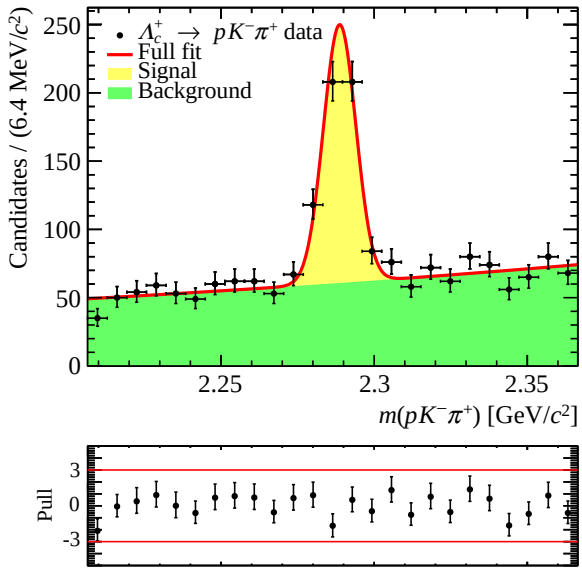

Figure 6.8: Invariant mass distribution of the $\Lambda_c^+ \to pK^-\pi^+$ fixed-target sample with loose requirements (Table 6.7) and $BDT > 0.07$ cut applied.

signal candidates can be selected from the proton-neon data sample, with sufficiently good purity to perform a polarisation measurement, as demonstrated in the following Sec. 6.3.

6.3 Strategy for polarisation measurement

The minimum uncertainty on the Λ_c^+ polarisation can be achieved by exploiting an amplitude model of the $\Lambda_c^+ \to pK^-\pi^+$ decay. The differential decay rate of the $\Lambda_c^+ \to pK^-\pi^+$ decay in terms of the Λ_c^+ polarisation vector $\boldsymbol{P}$ can be written in the helicity formalism as in Eq. (5.18), so that if the decay amplitudes between Λ_c^+ and proton spin states $\mathcal{A}_{s_{\Lambda_c^+},\lambda_p}$ are known, the Λ_c^+ polarisation can be extracted from a maximum-likelihood fit of the decay distribution. The E791 experiment at Fermilab [71] published an amplitude model based on ≈ 1000 events. A far more precise amplitude model can be extracted from the large samples of $\Lambda_c^+ \to pK^-\pi^+$ decay recorded by the LHCb experiment in

Parameter	Central value $\pm$ Uncertainty
Signal events	392.23 ± 27.1
Background events	1520.8 ± 43.1
Gauss $\overline{x}$ $\left[\mathrm{GeV}/c^2\right]$	2.2887 ± 0.000398
Gauss σ $\left[\mathrm{MeV}/c^2\right]$	5.2928 ± 0.374
Exp c $\left[(\mathrm{GeV}/c^2)^{-1}\right]$	2.5642 ± 0.559

Table 6.13: Results of the invariant mass fit of the $\Lambda_c^+ \to pK^-\pi^+$ fixed-target sample with loose requirements (Table 6.7) and $BDT > 0.07$ cut applied.

proton-proton collisions, Chapter 5.

To maximise the precision on the Λ_c^+ polarisation for the low statistics fixed-target data, the amplitude model is fixed to the one obtained from pp collisions, and only the polarisation vector components are determined from the fit. The polarisation frame for fixed-target heavy baryon production depicted in Fig. 1.3 is employed. Since parity conservation requires the Λ_c^+ polarisation to be orthogonal to the production plane, two possible fits can be performed: a single parameter fit in which only the orthogonal component of the polarisation P_y is measured; and a three parameter fit extracting the full polarisation vector, which can be used as a cross-check of the polarisation measurement.

The polarisation extraction via ML fit and the systematic uncertainty associated to the choice of the amplitude model are studied by means of toy experiments, in which Monte Carlo samples generated according to a nominal amplitude model are fit using the same or an alternative simplified amplitude model. The nominal model is the best amplitude fit using the reduced model from LHCb pp collisions data, Fig. 5.17 and Table 5.7. The alternative model is an effective three-resonance model (containing one $\Lambda^* \to pK^-$, one $\Delta^{*++} \to p\pi^+$ and one $K^* \to K^-\pi^+$ contributions) whose parameters (including Breit-Wigner masses and widths) are determined from an amplitude fit to 10'000 $\Lambda_c^+ \to pK^-\pi^+$ candidates of LHCb pp collisions data. The amplitude fit result is displayed in Fig. 6.9, the fit parameters values returned by MINUIT are reported in Table 6.14, and the associated fit fractions in Table 6.15. This effective model is better than the E791 model because the latter employs a narrow $\Lambda^*(1520)$ component which is unable to parametrise the broad structure in $m^2_{pK^-}$ mass observed[2]. Nonetheless, the effective model is still a crude approximation of the real $\Lambda_c^+ \to pK^-\pi^+$ decay distributions, given the large deiations from $\Lambda_c^+ \to pK^-\pi^+$ data phase space distributions, so it provides a conservative estimate for the systematic effect due to the choice of the amplitude model.

Monte Carlo samples are generated for zero Λ_c^+ polarisation, while the polarisation components starting values in the fit are thrown randomly for each toy. From a hundreds of toy experiments the distributions of the extracted polarisation values, the analytical statistical uncertainties from HESSE and the pull $(P_i(\mathrm{fit}) - P_i(\mathrm{gen}))/\sigma(P_i)$ are obtained. In an ideal case, the measured polarisation distribution should be a Gaussian centred around the generated null value, its width representing the actual statistical uncertainty. The analytical computation of the statistical uncertainty from the ML fit is valid only in the large statistics limit; it can be used only if it corresponds to the standard deviation of the polarisation values, otherwise the latter value should be quoted as statistical uncertainty. The pull distributions should be Gaussian distributions with zero mean and

[2]This was already noted by the authors of Ref. [71], who mention that "a model with a spin 1/2 resonance decaying to pK^- having $m = 1.556 \pm 0.019$ GeV and $\Gamma = 279 \pm 74$ MeV reduces the overall χ^2 of the fit".

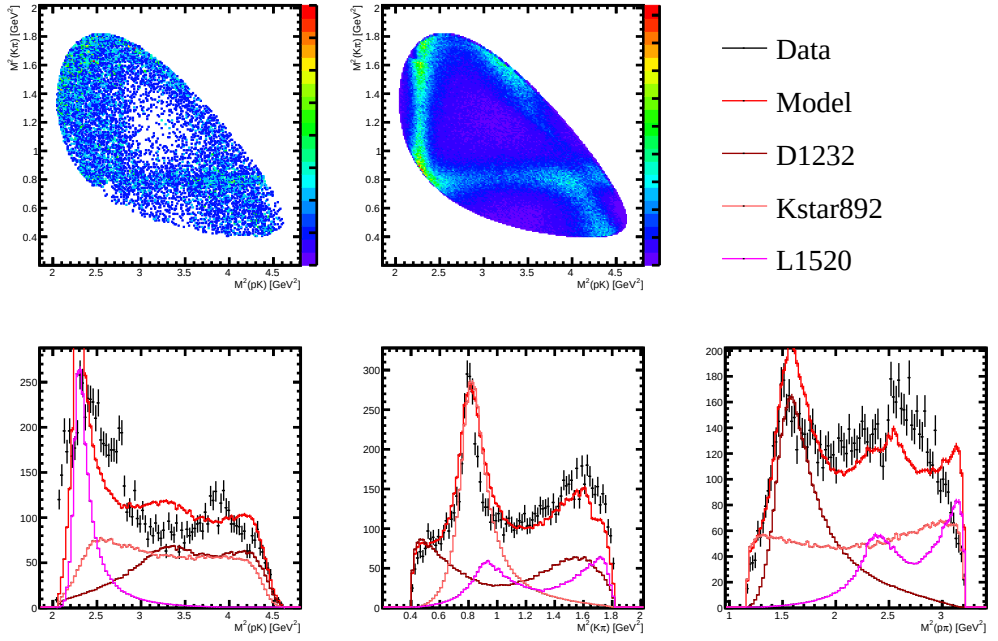

Figure 6.9: Dalitz plot amplitude fit results for the effective three-resonance model on 10'000 $\Lambda_c^+ \to pK^-\pi^+$ candidates.

Parameter	Central value ± Uncertainty	Parameter	Central value ± Uncertainty
MKstar892	0.917853 ± 0.001950	GKstar892	0.120000 ± 0.000169
ML1520	1.539318 ± 0.001561	GL1520	0.160000 ± 0.000541
MD1232	1.300000 ± 0.000271	GD1232	0.299987 ± 0.001111
ArKst892_2	1.511903 ± 0.304827	AiKst892_2	-0.224266 ± 0.195552
ArKst892_3	1.460999 ± 0.322751	AiKst892_3	2.651460 ± 0.294940
ArKst892_4	1.227009 ± 0.289348	AiKst892_4	-2.527752 ± 0.292490
ArL1520_1	-0.173920 ± 0.453407	AiL1520_1	2.740105 ± 0.773901
ArL1520_2	5.093427 ± 0.513726	AiL1520_2	-4.313387 ± 0.698702
ArD1232_1	-5.237213 ± 0.390332	AiD1232_1	-4.624444 ± 0.641536
ArD1232_2	-5.021403 ± 0.929781	AiD1232_2	4.406277 ± 0.886508

Table 6.14: Fit parameters returned by MINUIT for the Dalitz plot amplitude fit with effective three-resonance model on 10'000 $\Lambda_c^+ \to pK^-\pi^+$ candidates. Uncertainties are the 1σ standard deviations returned by HESSE. Fit parameters are defined in Appendix A.3.

Resonance	Fit fraction
Kstar892	0.444850
L1520	0.234014
D1232	0.373394
Sum	1.052257

Table 6.15: Fit fractions for the Dalitz plot amplitude fit with effective three-resonance model on 10'000 $\Lambda_c^+ \to pK^-\pi^+$ candidates.

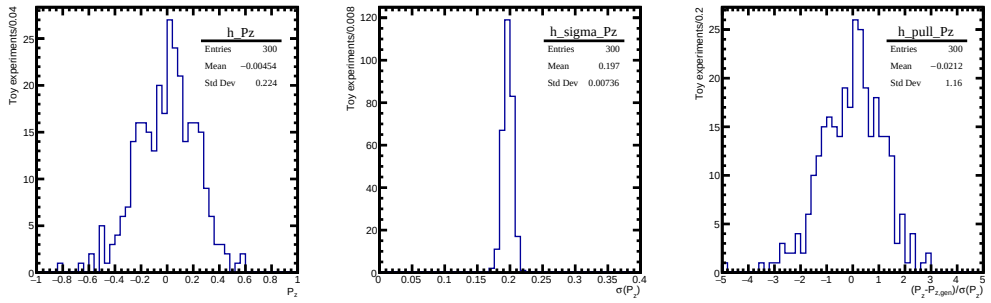

Figure 6.10: Fit validation study for a single polarisation component measurement, done for 300 generated samples of 200 events each, including a 20% flat background component.

unit standard deviation. A significant deviation of the pull distribution from zero would signal a bias in the polarisation measurement.

The validity of the ML framework for a limited number of events is performed considering 300 generated samples of 200 events each, a number considered as a lower limit of the possible $\Lambda_c^+ \to pK^-\pi^+$ yield. The nominal model is used for both generation and fit. Furthermore, a flat background component with an equivalent fraction of 20% of the generated events is added to the $\Lambda_c^+ \to pK^-\pi^+$ amplitude model. The distributions for the measurement of a single polarisation component[3] and the full polarisation vector are reported in Figs. 6.10 and 6.11, respectively. The polarisation distributions have a Gaussian-like shape, centred around the zero generation value, showing a negligible bias given the number of samples. The standard deviation is around 0.21, slightly higher than the analytical uncertainty retrieved by HESSE (see Sec. 5.4) at around 0.19, the first representing the achievable precision on the polarisation with 200 $\Lambda_c^+ \to pK^-\pi^+$ candidates. The pull distributions highlight the absence of bias and the slight underestimation of the statistical uncertainty. No significant differences are seen for the measurement of a single polarisation component. The fit framework is therefore working even at very low statistics. Given that the selections presented in Sec. 6.2.2 can be further optimised, the statistical uncertainty on the polarisation components can be expected to be < 0.2.

The systematic uncertainty associated to the choice of the amplitude model is studied on 1000 generated samples of 1000 events each, a number of events higher than the achievable $\Lambda_c^+ \to pK^-\pi^+$ yield: the reduced statistical uncertainties increase the sensitivity to possible biases. The nominal model is used for generation and the alternative for the ML fits. The distributions for the measurement of the full polarisation vector are shown in Fig. 6.12. The polarisation distributions have a Gaussian-like shape, with a mean value < 0.02 much smaller than the standard deviation. As for the fit model validation, the actual statistical uncertainty on the polarisation components, at $0.07 - 0.08$ level, is slightly higher than the analytical one computed by HESSE. This study demonstrates that the possible polarisation bias is subdominant at the given statistical uncertainty, even for an alternative model very different for the nominal one.

[3]Since detector effects are not included at this stage, any of the polarisation components can be considered for rotational invariance.

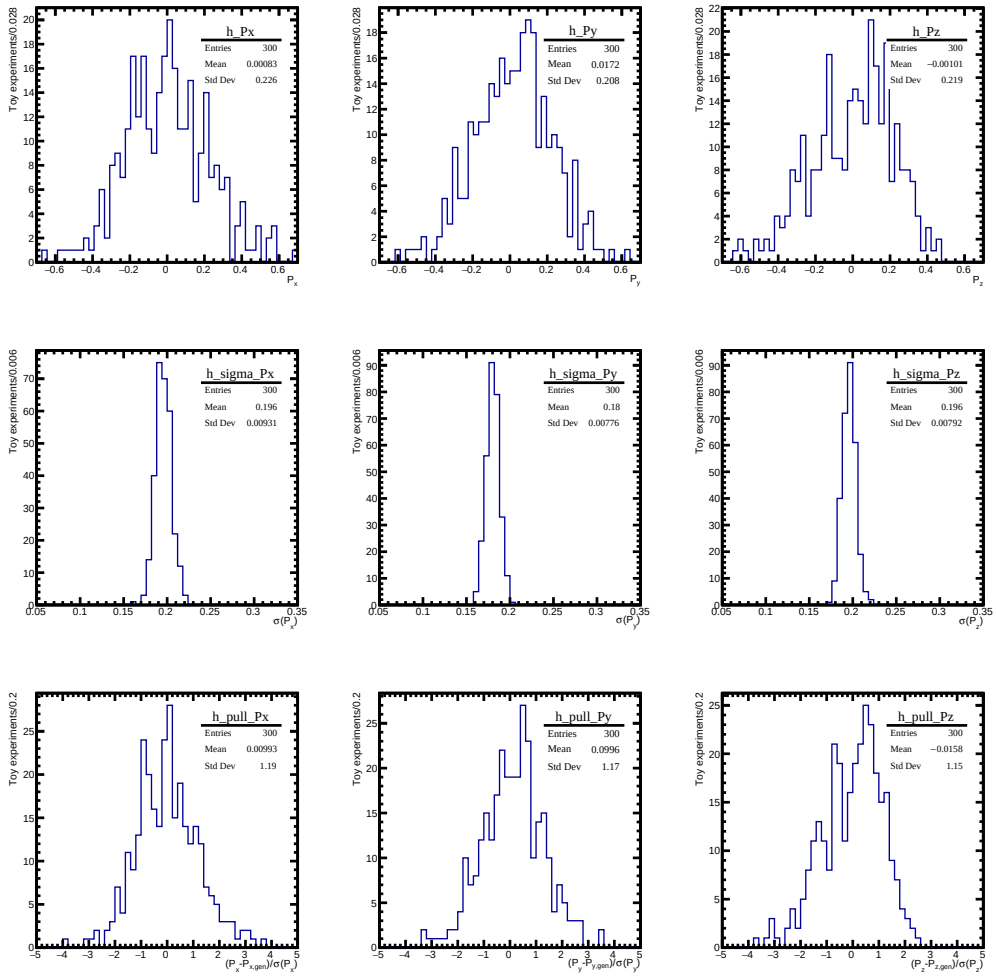

Figure 6.11: Fit validation study for the full polarisation vector measurement, done for 300 generated samples of 200 events each, including a 20% flat background component.

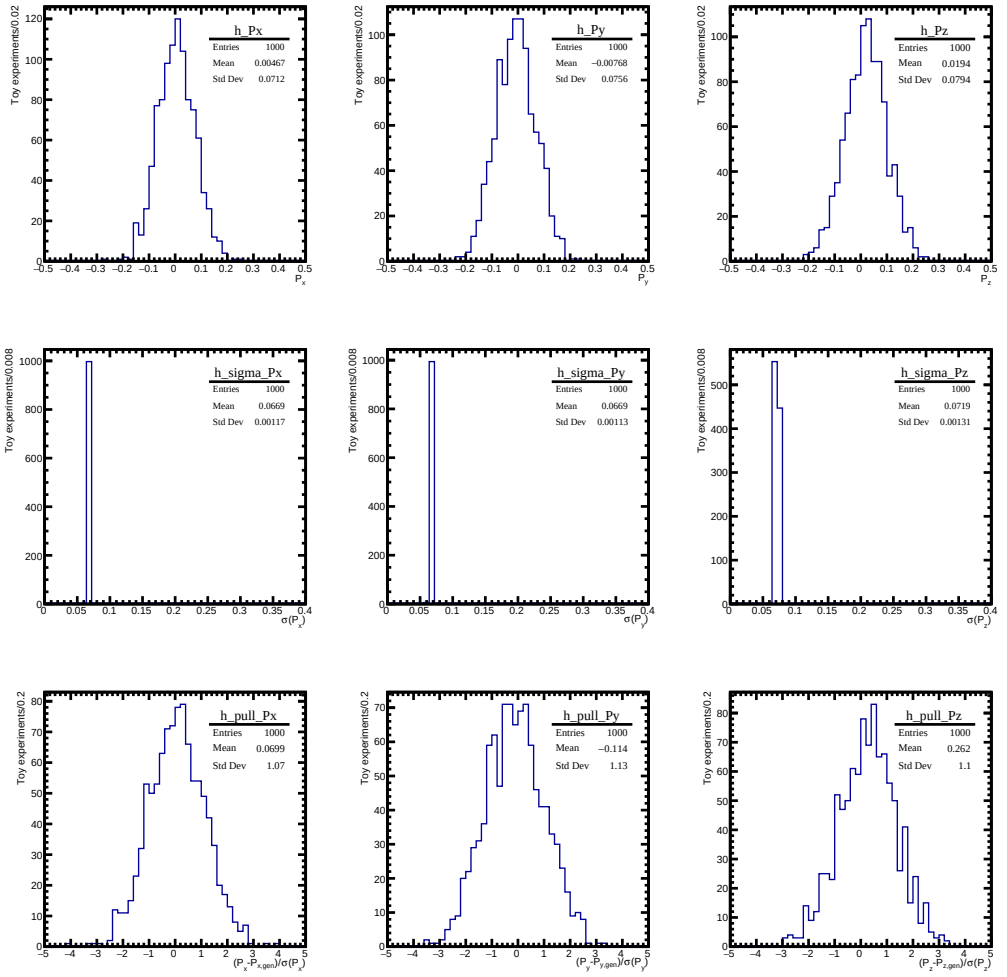

Figure 6.12: Amplitude model systematic uncertainty study for the full polarisation vector measurement, done for 1000 generated samples of 1000 events each, fit using the alternative model.

6.4 Conclusions

The analysis aimed at the measurement of the Λ_c^+ polarisation in proton-neon collisions at $\sqrt{s} = 68.6\,\text{GeV}$ has started. Two essential results, demonstrating the feasibility of the measurement, have been achieved.

First, $\Lambda_c^+ \to pK^-\pi^+$ fixed-target candidates can be distinguished from proton-proton collisions due to ghost charges, and a non-negligible yield can be separated from the combinatorial background. A cut-based and a BDT selection are presented, showing that a few hundreds $\Lambda_c^+ \to pK^-\pi^+$ candidates can be selected with enough purity to perform the polarisation measurement.

Second, it has been demonstrated that the ML fit to extract the polarisation, based on the use of amplitude models derived from LHCb proton-proton collision data, is effective. With a Monte Carlo study in which hundreds of samples are generated and fit, it has been shown that a negligible bias on the polarisation extraction is induced by the ML fit itself and by the choice of a different amplitude model, at the given statistical uncertainty. The statistical uncertainty on the polarisation components, whose actual value will depend on the specific final selection criteria, will be smaller than 0.2, with a systematic effect due to the fit model choice below 0.02.

CHAPTER 7

Summary and prospects

The first part of the thesis presents how the electromagnetic dipole moments of short-lived heavy baryons and τ lepton can be measured for the first time exploiting the spin precession phenomenon for channeled particles in bent crystals. The electromagnetic dipole moments are of particular interest for probing both Beyond the Standard Model physics and low-energy Quantum Chromodynamics effective theories. Spin precession equations are derived for positive and negative particles in planar or axial channeling conditions, for non-zero electric dipole moment contributions. An experimental layout exploiting a beam of 7 TeV protons extracted from the main LHC accelerator beam and directed onto a target-bent crystal device placed in front of the LHCb detector is studied. Such a setup is shown to be able to challenge the current indirect limits on the charm baryon dipole moments. The possibility of selecting polarised τ leptons in a similar experimental layout is demonstrated, and a novel technique to measure the τ^+ polarisation from partially reconstructed $\tau^+ \to \pi^+\pi^-\pi^+\bar{\nu}_\tau$ decay distributions explored. A sensitivity study for a future dedicated experiment is presented, which would able to challenge the SM prediction for the τ^+ anomalous magnetic dipole moment with order 10^{17} protons on target, and searching for the τ^+ electric dipole moment at $10^{-17} e\,\mathrm{cm}$ precision.

Subsequently, the thesis discusses two ongoing data analyses, the amplitude analysis of $\Lambda_c^+ \to pK^-\pi^+$ decays including extraction of the Λ_c^+ polarisation vector and the measurement of the Λ_c^+ polarisation in proton-neon collisions, in light of the possibility to measure the Λ_c^+ baryon electromagnetic dipole moments. The first analysis is needed for the determination of the $\Lambda_c^+ \to pK^-\pi^+$ decay structure and for providing a method to measure the Λ_c^+ polarisation from its decay distributions. The second analysis provides crucial information on the polarisation degree of Λ_c^+ baryons produced in proton-nucleon fixed-target collisions. At the time of writing this thesis, both data analyses performed on LHCb data are still not complete; however, most of the critical aspects have been addressed and some important preliminary results achieved.

The second part of the thesis presents the current status of the amplitude analysis of $\Lambda_c^+ \to pK^-\pi^+$ decays from Λ_b^0 semileptonic production recorded by the LHCb experiment. It is shown how an amplitude model for the $\Lambda_c^+ \to pK^-\pi^+$ decay allowing for the Λ_c^+ baryon polarisation extraction can be written in the helicity formalism. This amplitude model is implemented within the TensorFlowAnalysis software package. The possibility of selecting order one million $\Lambda_c^+ \to pK^-\pi^+$ decays from the LHCb proton-proton collision dataset with negligible background contributions is demonstrated.

Preliminary results are obtained for 2-dimensional "Dalitz plot" invariant mass fits. A decay model well describing the invariant mass decay distributions is found. An unexpected Λ^* contribution is observed with statistical significance of 32.5σ, which can be parametrised by a spin $1/2$ state with mass around 1.97 GeV and width around 140

MeV. Full phase space 5-dimensional amplitude fits are performed, but a problem introducing an unphysical, model-dependent interference pattern is found, which is currently under investigation. The sensitivity to the polarisation of the amplitude model has been preliminarily estimated, found to be similar to that assumed for the measurement of Λ_c^+ baryon dipole moments, this allowing an increase of the useful Λ_c^+ decay statistics by a factor six.

The third part of the thesis demonstrates the feasibility of the Λ_c^+ polarisation measurement in proton-neon collisions at $\sqrt{s} = 68.6\,\mathrm{GeV}$ recorded by the LHCb experiment. A few hundreds $\Lambda_c^+ \to pK^-\pi^+$ fixed-target candidates are distinguished from symmetric proton-proton collisions events and combinatorial background. It is shown that the Λ_c^+ polarisation can be extracted from maximum-likelihood fits with the use of amplitude models derived from LHCb proton-proton collision data. By means of a toy Monte Carlo study, the achievable statistical uncertainty on the polarisation components is estimated to be smaller than 0.2, and the systematic uncertainty due to the amplitude model choice to be below 0.02.

At the time of writing this thesis, the installation of a target-bent crystal device for measuring heavy baryon electromagnetic dipole moments at the LHC is actively discussed witihin the CERN Physics Beyond Colliders initiative and the LHCb Collaboration. The proposal to measure the electromagnetic dipole moments of short-lived particles has become an ERC funded project, SELDOM. The studies presented in the thesis have been an essential contribution towards these achievements.

APPENDIX A

Appendices

A.1 Discrete ambiguities

From Eq. (2.43) one can see that, if all the three components of the final polarisation vector $\mathbf{s}$ are measured, the g and d factors can be extracted along with the initial polarisation s_0, up to discrete ambiguities. If $\{s_0, g', d\}$ is a solution, then

$$\left\{-s_0,\ g' \pm \frac{n\pi}{\gamma\theta_C},\ d\left(1 \pm \frac{n\pi}{\gamma\theta_C}\frac{1}{g'}\frac{\cos\Phi - 1}{\cos\Phi + 1}\right)\right\},$$

$$\left\{s_0,\ g' \pm \frac{m\pi}{\gamma\theta_C},\ d\left(1 \pm \frac{m\pi}{\gamma\theta_C}\frac{1}{g'}\right)\right\}, \tag{A.1}$$

are also solutions, with n (m) an odd (even) integer. A simultaneous fit in bins of γ to the angular distribution Eq. (2.5) is able to resolve the ambiguity.

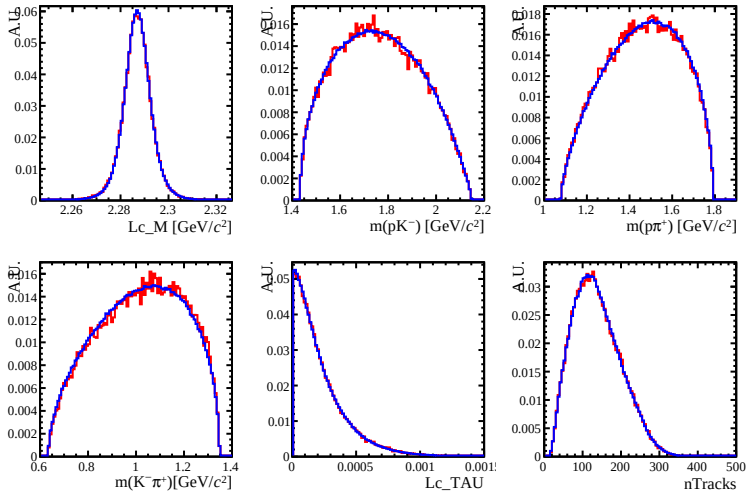

Figure A.1: Comparison between full (red) and ReDecay (blue) simulation two-body invariant mass, Λ_c^+ lifetime, number of tracks distributions.

A.2 ReDecay faster simulation validation for $\Lambda_c^+ \to pK^-\pi^+$ decays

The validity of the *ReDecay* faster simulation [159] for the description of the detector efficiency effects is studied comparing a large set of distributions against the full simulation sample, in which only the flat phase space $\Lambda_c^+ \to pK^-\pi^+$ events are considered, to avoid effects of the full simulation decay model on the distributions. The following distributions are checked: invariant masses, Λ_c^+ lifetime, number of tracks (Fig. A.1), momenta (Fig. A.2), transverse momenta (Fig. A.3), particle identification delta log-likelihoods (Fig. A.4), neural network based ProbNN variables (Fig. A.5) and the one-dimensional projections of the detector efficiency over the $\Lambda_c^+ \to pK^-\pi^+$ phase space (Fig. A.6). No significant discrepancies are visible.

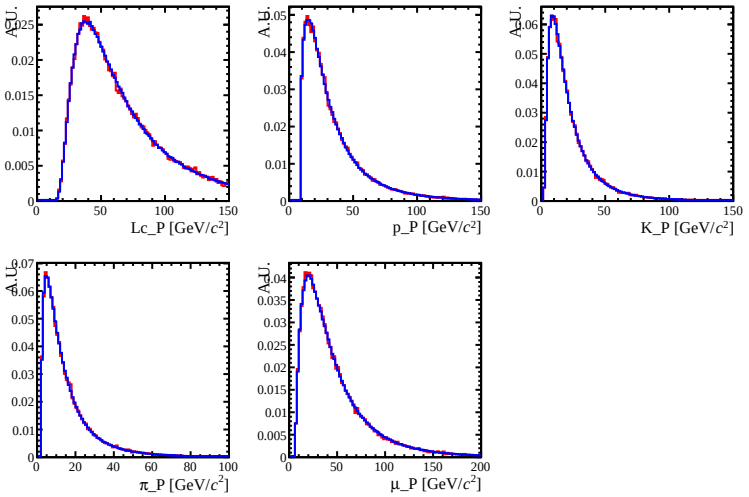

Figure A.2: Comparison between full (red) and ReDecay (blue) simulation momentum distributions.

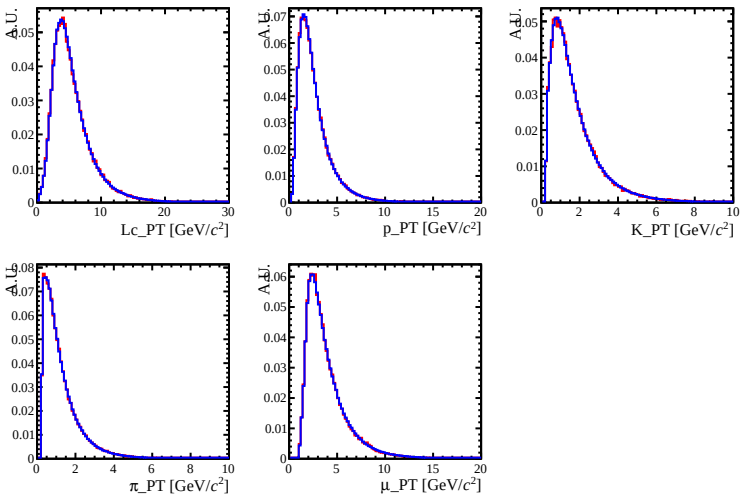

Figure A.3: Comparison between full (red) and ReDecay (blue) simulation transverse momentum distributions.

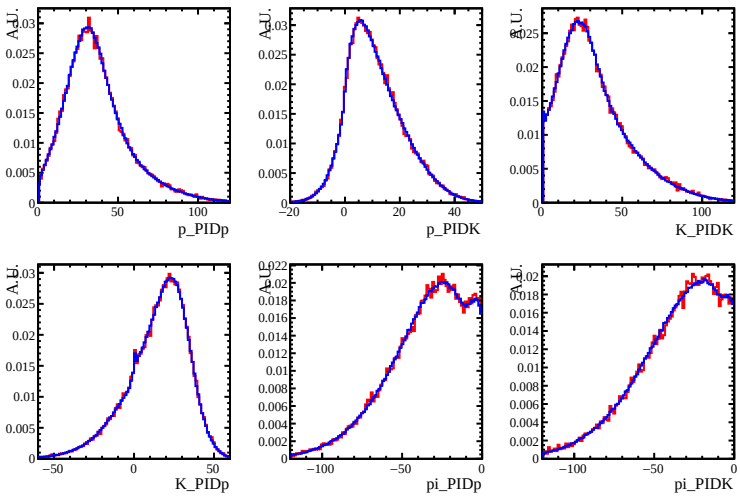

Figure A.4: Comparison between full (red) and ReDecay (blue) simulation PID distributions.

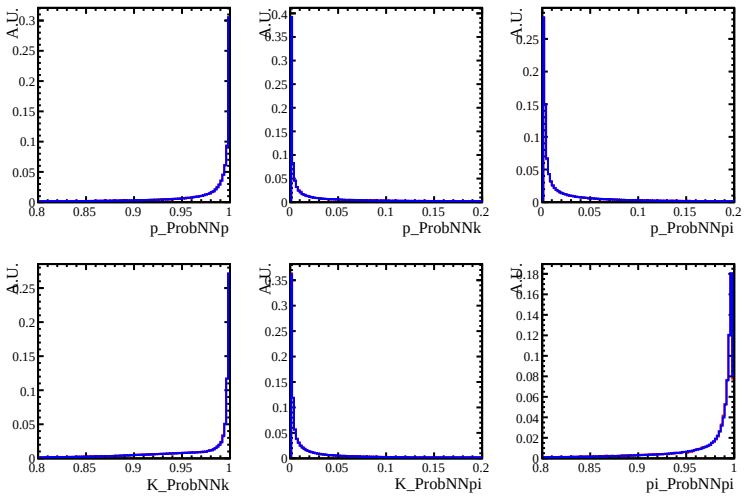

Figure A.5: Comparison between full (red) and ReDecay (blue) simulation ProbNN distributions.

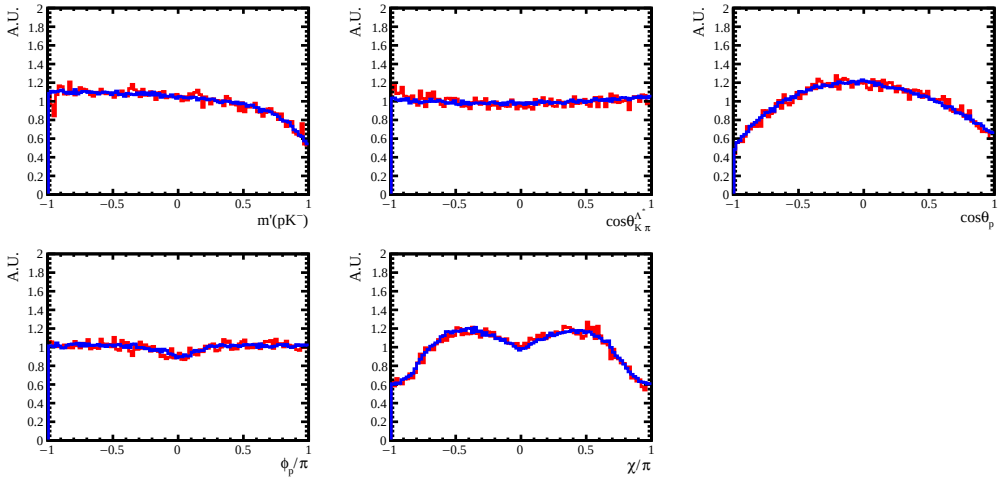

Figure A.6: Comparison between full (red) and ReDecay (blue) simulation Λ_c^+ efficiency distributions in Λ_c^+ phase space.

Resonance type	Coupling number	λ_R	λ_p
Λ^*, Δ^*	1	1/2	
	2	-1/2	
K^*	1	0	-1/2
	2	-1	-1/2
	3	1	1/2
	4	0	1/2
Non resonant	1		-1/2
	2		1/2

Table A.1: Definition of the helicity couplings. λ_R is the resonance helicity in the Λ_c^+ rest frame, λ_p is the proton helicity defined in the resonance rest frame.

A.3 Definition of the amplitude fit parameters

In this appendix, the naming conventions for the amplitude fit parameters are detailed.

Resonances

Resonant states are indicated as L (Λ^*), D (Δ^*), Kst (K^*) and Kswave (non-resonant contribution), followed by their mass identification as assigned by the PDG, Table 5.4.

Lineshape parameters

For most resonances, parametrised using relativistic Breit-Wigner or its modification for sub-threshold resonances, Sec. 5.4.3, the Breit-Wigner mass and width are indicated as M or G (for "Gamma"), respectively, and expressed in GeV units. The LASS parameters scattering length a and effective range r are called a_LASS and r_LASS, respectively, and expressed in GeV^{-1} units.

Helicity couplings

Each complex helicity coupling is introduced in the amplitude fit via two real fit parameters representing its real, Ar, and imaginary, Ai, parts. The number after the resonance specification labels the helicity coupling for specific resonance and proton helicities, as described in Table A.1[1]. The allowed helicity couplings follow from angular momentum conservation, as explained in Sec. 5.2.3.

[1]Helicity couplings for baryonic resonances Λ^* and Δ^* do not depend on proton helicities for parity conservation in their decay.

Bibliography

[1] M. S. Sozzi, *Discrete symmetries and CP violation: from experiment to theory*, Oxford Graduate Texts, Oxford Univ. Press, New York, NY, 2008.

[2] T. D. Lee and C. N. Yang, *Parity nonconservation and a two-component theory of the neutrino*, Phys. Rev. **105** (1957) 1671.

[3] C. S. Wu *et al.*, *Experimental test of parity conservation in beta decay*, Phys. Rev. **105** (1957) 1413.

[4] J. H. Christenson, J. W. Cronin, V. L. Fitch, and R. Turlay, *Evidence for the 2π decay of the K_2^0 meson*, Phys. Rev. Lett. **13** (1964) 138.

[5] A. D. Sakharov, *Violation of CP invariance, C asymmetry, and baryon asymmetry of the universe*, Soviet Physics Uspekhi **34** (1991) 392.

[6] O. W. Greenberg, *CPT violation implies violation of Lorentz invariance*, Phys. Rev. Lett. **89** (2002) 231602, arXiv:hep-ph/0201258.

[7] S. L. Glashow, *Partial-symmetries of weak interactions*, Nuclear Physics **22** (1961), no. 4 579 ; S. Weinberg, *A model of leptons*, Phys. Rev. Lett. **19** (1967) 1264; A. Salam, *Weak and electromagnetic interactions*, Originally printed in N. Svartholm: Elementary particle theory, Proceedings of the Nobel symposium 1968, Lerum, Sweden (1968) 367 ; G. 't Hooft and M. Veltman, *Regularization and renormalization of gauge fields*, Nuclear Physics B **44** (1972), no. 1 189 .

[8] F. Englert and R. Brout, *Broken symmetry and the mass of gauge vector mesons*, Phys. Rev. Lett. **13** (1964) 321; P. W. Higgs, *Broken symmetries and the masses of gauge bosons*, Phys. Rev. Lett. **13** (1964) 508.

[9] N. Cabibbo, *Unitary symmetry and leptonic decays*, Phys. Rev. Lett. **10** (1963) 531.

[10] S. L. Glashow, J. Iliopoulos, and L. Maiani, *Weak interactions with lepton-hadron symmetry*, Phys. Rev. D **2** (1970) 1285.

[11] M. Kobayashi and T. Maskawa, *CP Violation in the renormalizable theory of weak interaction*, Prog. Theo. Phys. **49** (1973) 652.

[12] L. Wolfenstein, *Parametrization of the Kobayashi-Maskawa matrix*, Phys. Rev. Lett. **51** (1983) 1945.

[13] V. A. Kuzmin, V. A. Rubakov, and M. E. Shaposhnikov, *On the Anomalous Electroweak Baryon Number Nonconservation in the Early Universe*, Phys. Lett. **155B** (1985) 36; M. Fukugita and T. Yanagida, *Baryogenesis Without Grand Unification*, Phys. Lett. **B174** (1986) 45.

[14] J. M. Pendlebury *et al.*, *Revised experimental upper limit on the electric dipole moment of the neutron*, Phys. Rev. **D92** (2015), no. 9 092003, arXiv:1509.04411.

[15] R. D. Peccei and H. R. Quinn, *CP conservation in the presence of pseudoparticles*, Phys. Rev. Lett. **38** (1977) 1440.

[16] E. Leader, *Spin in particle physics*, vol. 15, Camb. Monogr. Part. Phys. Nucl. Phys. Cosmol., 2011.

[17] J. S. Bell, *Electromagnetic properties of unstable particles*, Nuovo Cim. C **24** (1962) 452.

[18] F.-K. Guo and U.-G. Meissner, *Baryon electric dipole moments from strong CP violation*, JHEP **12** (2012) 097, arXiv:1210.5887.

[19] M. E. Peskin and D. V. Schroeder, *An Introduction to quantum field theory*, Addison-Wesley, Reading, USA, 1995.

[20] D. Hanneke, S. Fogwell, and G. Gabrielse, *New Measurement of the Electron Magnetic Moment and the Fine Structure Constant*, Phys. Rev. Lett. **100** (2008) 120801, arXiv:0801.1134.

[21] Muon g-2 collaboration, G. W. Bennett *et al.*, *Final Report of the Muon E821 Anomalous Magnetic Moment Measurement at BNL*, Phys. Rev. **D73** (2006) 072003, arXiv:hep-ex/0602035.

[22] M. Davier, *Update of the Hadronic Vacuum Polarisation Contribution to the muon g-2*, Nucl. Part. Phys. Proc. **287-288** (2017) 70, arXiv:1612.02743.

[23] Muon g-2 collaboration, J. Grange *et al.*, *Muon (g-2) Technical Design Report*, arXiv:1501.06858.

[24] Particle Data Group, M. Tanabashi *et al.*, *Review of particle physics*, Phys. Rev. **D98** (2018) 030001.

[25] G. Schneider *et al.*, *Double-trap measurement of the proton magnetic moment at 0.3 parts per billion precision*, Science **358** (2017) 1081.

[26] P. J. Mohr, D. B. Newell, and B. N. Taylor, *CODATA Recommended Values of the Fundamental Physical Constants: 2014*, Rev. Mod. Phys. **88** (2016), no. 3 035009, arXiv:1507.07956.

[27] N. Sharma, H. Dahiya, P. K. Chatley, and M. Gupta, *Spin* $1/2^+$*, spin* $3/2^+$ *and transition magnetic moments of low lying and charmed baryons*, Phys. Rev. **D81** (2010) 073001, arXiv:1003.4338.

[28] ATRAP collaboration, J. DiSciacca *et al.*, *One-Particle Measurement of the Antiproton Magnetic Moment*, Phys. Rev. Lett. **110** (2013), no. 13 130801, arXiv:1301.6310.

[29] R. S. Van Dyck, P. B. Schwinberg, and H. G. Dehmelt, *New high-precision comparison of electron and positron g factors*, Phys. Rev. Lett. **59** (1987) 26.

[30] Muon g-2 collaboration, G. W. Bennett *et al.*, *Measurement of the negative muon anomalous magnetic moment to 0.7 ppm*, Phys. Rev. Lett. **92** (2004) 161802, arXiv:hep-ex/0401008.

[31] S. Ulmer *et al.*, *Technical Design Report BASE*, Tech. Rep. CERN-SPSC-2013-002. SPSC-TDR-002, CERN, 2013.

[32] M. Neubert, *Heavy quark symmetry*, Phys. Rept. **245** (1994) 259, arXiv:hep-ph/9306320.

[33] A. L. Choudhury and V. Joshi, *Magnetic Moments of Charmed Baryons. 1.*, Phys. Rev. **D13** (1976) 3115; D. B. Lichtenberg, *Magnetic Moments of Charmed Baryons in the Quark Model*, Phys. Rev. **D15** (1977) 345; R. J. Johnson and M. Shah-Jahan, *Static and Transition Magnetic Moments of Charmed Baryons in the Quark Model*, Phys. Rev. **D15** (1977) 1400.

[34] F. X. Lee, *Determination of decuplet baryon magnetic moments from QCD sum rules*, Phys. Rev. **D57** (1998) 1801, arXiv:hep-ph/9708323; L. Wang and F. X. Lee, *Octet baryon magnetic moments from QCD sum rules*, Phys. Rev. **D78** (2008) 013003, arXiv:0804.1779.

[35] S.-L. Zhu, W.-Y. P. Hwang, and Z.-S. Yang, *The Sigma(c) and Lambda(c) magnetic moments from QCD spectral sum rules*, Phys. Rev. **D56** (1997) 7273, arXiv:hep-ph/9708411.

[36] G.-J. Wang *et al.*, *Magnetic moments of the spin-$\frac{1}{2}$ singly charmed baryons in chiral perturbation theory*, Phys. Rev. **D98** (2018), no. 5 054026, arXiv:1803.00229; R.-X. Shi, Y. Xiao, and L.-S. Geng, *Magnetic moments of the spin-1/2 singly charmed baryons in covariant baryon chiral perturbation theory*, arXiv:1812.07833.

[37] A. Bernotas and V. Simonis, *Magnetic moments of heavy baryons in the bag model re-examined*, Lith. J. Phys. **53** (2013), no. 84 054026, arXiv:1209.2900; A. Faessler *et al.*, *Magnetic moments of heavy baryons in the relativistic three-quark model*, Phys. Rev. **D73** (2006) 094013, arXiv:hep-ph/0602193; N. Barik and M. Das, *Magnetic moments of confined quarks and baryons in an independent quark model based on dirac equation with power law potential*, Phys. Rev. **D28** (1983) 2823; J. Franklin, D. B. Lichtenberg, W. Namgung, and D. Carydas, *Wave Function Mixing of Flavor Degenerate Baryons*, Phys. Rev. **D24** (1981) 2910.

[38] B. Patel, A. K. Rai, and P. C. Vinodkumar, *Masses and magnetic moments of heavy flavour baryons in hyper central model*, J. Phys. **G35** (2008) 065001, arXiv:0710.3828.

[39] R. Dhir, C. S. Kim, and R. C. Verma, *Magnetic Moments of Bottom Baryons: Effective mass and Screened Charge*, Phys. Rev. **D88** (2013) 094002, arXiv:1309.4057.

[40] QCD Working Group, A. Dainese *et al.*, *Physics Beyond Colliders: QCD Working Group Report*, arXiv:1901.04482.

[41] F. Sala, *A bound on the charm chromo-EDM and its implications*, JHEP **03** (2014) 061, arXiv:1312.2589.

[42] A. G. Grozin, I. B. Khriplovich, and A. S. Rudenko, *Upper limits on electric dipole moments of tau-lepton, heavy quarks, and W-boson*, Nucl. Phys. **B821** (2009) 285, arXiv:0902.3059.

[43] A. E. Blinov and A. S. Rudenko, *Upper Limits on Electric and Weak Dipole Moments of tau-Lepton and Heavy Quarks from e+ e- Annihilation*, Nucl. Phys. Proc. Suppl. **189** (2009) 257, arXiv:0811.2380.

[44] R. Escribano and E. Masso, *Constraints on fermion magnetic and electric moments from LEP-1*, Nucl. Phys. **B429** (1994) 19, arXiv:hep-ph/9403304.

[45] A. Cordero-Cid, J. M. Hernandez, G. Tavares-Velasco, and J. J. Toscano, *Bounding the top and bottom electric dipole moments from neutron experimental data*, J. Phys. **G35** (2008) 025004, arXiv:0712.0154.

[46] S.-M. Zhao *et al.*, *The one loop contributions to c(t) electric dipole moment in the CP violating BLMSSM*, Eur. Phys. J. **C77** (2017), no. 2 102, arXiv:1610.07314; Z. Z. Aydin and U. Erkarslan, *The Charm quark EDM and singlet P wave charmonium production in supersymmetry*, Phys. Rev. **D67** (2003) 036006, arXiv:hep-ph/0204238.

[47] I. B. Khriplovich and A. R. Zhitnitsky, *What Is the Value of the Neutron Electric Dipole Moment in the Kobayashi-Maskawa Model?*, Phys. Lett. **109B** (1982) 490; M. B. Gavela *et al.*, *CP Violation Induced by Penguin Diagrams and the Neutron Electric Dipole Moment*, Phys. Lett. **109B** (1982) 215.

[48] I. B. Khriplovich, *Quark Electric Dipole Moment and Induced θ Term in the Kobayashi-Maskawa Model*, Phys. Lett. **B173** (1986) 193.

[49] M. E. Pospelov and I. B. Khriplovich, *Electric dipole moment of the W boson and the electron in the Kobayashi-Maskawa model*, Sov. J. Nucl. Phys. **53** (1991) 638.

[50] ACME collaboration, V. Andreev *et al.*, *Improved limit on the electric dipole moment of the electron*, Nature **562** (2018), no. 7727 355.

[51] T. Fukuyama, *Searching for New Physics beyond the Standard Model in Electric Dipole Moment*, Int. J. Mod. Phys. **A27** (2012) 1230015, arXiv:1201.4252.

[52] I. B. Khriplovich and S. K. Lamoreaux, *CP violation without strangeness: Electric dipole moments of particles, atoms, and molecules*, Springer, 1997.

[53] M. Pospelov and A. Ritz, *Electric dipole moments as probes of new physics*, Annals Phys. **318** (2005) 119, arXiv:hep-ph/0504231.

[54] J. H. Smith, E. M. Purcell, and N. F. Ramsey, *Experimental limit to the electric dipole moment of the neutron*, Phys. Rev. **108** (1957) 120.

[55] Muon g-2 collaboration, G. W. Bennett *et al.*, *An Improved Limit on the Muon Electric Dipole Moment*, Phys. Rev. **D80** (2009) 052008, arXiv:0811.1207.

[56] V. F. Dmitriev and R. A. Sen'kov, *Schiff moment of the mercury nucleus and the proton dipole moment*, Phys. Rev. Lett. **91** (2003) 212303, arXiv:nucl-th/0306050.

[57] L. Pondrom *et al.*, *New Limit on the Electric Dipole Moment of the Λ Hyperon*, Phys. Rev. **D23** (1981) 814.

[58] J-PARC g-2/EDM collaboration, N. Saito, *A novel precision measurement of muon g-2 and EDM at J-PARC*, AIP Conf. Proc. **1467** (2012) 45.

[59] I. B. Khriplovich, *Feasibility of search for nuclear electric dipole moments at ion storage rings*, Phys. Lett. **B444** (1998) 98, arXiv:hep-ph/9809336; V. Anastassopoulos *et al.*, *A Storage Ring Experiment to Detect a Proton Electric Dipole Moment*, Rev. Sci. Instrum. **87** (2016), no. 11 115116, arXiv:1502.04317; JEDI collaboration, J. Pretz, *Measurement of electric dipole moments at storage rings*, Physica Scripta **2015** (2015), no. T166 014035; F. Abusaif *et al.*, *Feasibility Study for an EDM Storage Ring*, arXiv:1812.08535.

[60] J. Beacham *et al.*, *Physics Beyond Colliders at CERN: Beyond the Standard Model Working Group Report*, arXiv:1901.09966.

[61] C. A. Aidala, S. D. Bass, D. Hasch, and G. K. Mallot, *The Spin Structure of the Nucleon*, Rev. Mod. Phys. **85** (2013) 655, arXiv:1209.2803.

[62] European Muon collaboration, J. Ashman *et al.*, *A Measurement of the Spin Asymmetry and Determination of the Structure Function g(1) in Deep Inelastic Muon-Proton Scattering*, Phys. Lett. **B206** (1988) 364; D. de Florian, R. Sassot, M. Stratmann, and W. Vogelsang, *Global Analysis of Helicity Parton Densities and Their Uncertainties*, Phys. Rev. Lett. **101** (2008) 072001, arXiv:0804.0422; COMPASS collaboration, C. Adolph *et al.*, *The spin structure function g_1^p of the proton and a test of the Bjorken sum rule*, Phys. Lett. **B753** (2016) 18, arXiv:1503.08935.

[63] T. Mannel and G. A. Schuler, *Semileptonic decays of bottom baryons at LEP*, Phys. Lett. **B279** (1992) 194; A. F. Falk and M. E. Peskin, *Production, decay, and polarization of excited heavy hadrons*, Phys. Rev. **D49** (1994) 3320, arXiv:hep-ph/9308241.

[64] M. Galanti *et al.*, *Heavy baryons as polarimeters at colliders*, JHEP **11** (2015) 067, arXiv:1505.02771.

[65] G. Bunce *et al.*, *Λ^0 Hyperon Polarization in Inclusive Production by 300-GeV Protons on Beryllium*, Phys. Rev. Lett. **36** (1976) 1113; K. J. Heller *et al.*, *Polarization of Λ's and $\bar{\Lambda}$'s Produced by 400-GeV Protons*, Phys. Rev. Lett. **41** (1978) 607, [Erratum: Phys. Rev. Lett.45,1043(1980)]; B. Lundberg *et al.*, *Polarization in Inclusive Λ and $\bar{\Lambda}$ Production at Large p_T*, Phys. Rev. **D40** (1989) 3557; B. S. Yuldashev *et al.*, *Neutral strange particle production in p ^{20}Ne and pN interactions at 300-GeV/c*, Phys. Rev. **D43** (1991) 2792; E. J. Ramberg *et al.*, *Polarization of Λ and $\bar{\Lambda}$ produced by 800-GeV protons*, Phys. Lett. **B338** (1994) 403; V. Fanti *et al.*, *A Measurement of the transverse polarization of Λ hyperons produced in inelastic pN reactions at 450-GeV proton energy*, Eur. Phys. J. **C6** (1999) 265; HERA-B collaboration, I. Abt *et al.*, *Polarization of Λ and $\bar{\Lambda}$ in 920-GeV fixed-target proton-nucleus collisions*, Phys. Lett. **B638** (2006) 415, arXiv:hep-ex/0603047.

[66] E761 collaboration, A. Morelos Pineda *et al.*, *Polarization of Σ^+ and $\bar{\Sigma}^-$ hyperons produced by 800-GeV/c protons*, Phys. Rev. Lett. **71** (1993) 2172.

[67] K. J. Heller *et al.*, *Polarization of Ξ^0 and Λ Hyperons Produced by 400-GeV/c Protons*, Phys. Rev. Lett. **51** (1983) 2025.

[68] R. Rameika *et al.*, *Measurements of Production Polarization and Decay Asymmetry for Ξ^- Hyperons*, Phys. Rev. **D33** (1986) 3172; L. H. Trost *et al.*, *New Measurement of the Production Polarization and Magnetic Moment of the Ξ^- Hyperon*, Phys. Rev. **D40** (1989) 1703; P. M. Ho *et al.*, *Production polarization and magnetic moment of $\bar{\Xi}^+$ antihyperons produced by 800-GeV/c protons*, Phys. Rev. Lett. **65** (1990) 1713; J. Duryea

et al., *Polarization of Ξ^- hyperons produced by 800-GeV protons*, Phys. Rev. Lett. **67** (1991) 1193.

[69] K. B. Luk *et al.*, *Polarization of Ω^- hyperons produced in 800-* GeV *proton-beryllium collisions*, Phys. Rev. Lett. **70** (1993) 900.

[70] M. Jezabek, K. Rybicki, and R. Rylko, *Experimental study of spin effects in hadroproduction and decay of Λ_c^+*, Phys. Lett. **B286** (1992) 175.

[71] E791 collaboration, E. M. Aitala *et al.*, *Multidimensional resonance analysis of $\Lambda_c^+ \to pK^-\pi^+$*, Phys. Lett. **B471** (2000) 449, arXiv:hep-ex/9912003.

[72] S. Erhan *et al.*, *Λ^0 Polarization in Proton Proton Interactions at $\sqrt{s} = 53$-GeV and 62-GeV*, Phys. Lett. **82B** (1979) 301.

[73] ATLAS collaboration, G. Aad *et al.*, *Measurement of the transverse polarization of Λ and $\bar{\Lambda}$ hyperons produced in proton-proton collisions at $\sqrt{s} = 7$ TeV using the ATLAS detector*, Phys. Rev. **D91** (2015), no. 3 032004, arXiv:1412.1692.

[74] LHCb collaboration, R. Aaij *et al.*, *Measurements of the $\Lambda_b^0 \to J/\psi\,\Lambda$ decay amplitudes and the Λ_b^0 polarisation in pp collisions at $\sqrt{s} = 7$* TeV, Phys. Lett. **B724** (2013) 27, arXiv:1302.5578; ATLAS, G. Aad *et al.*, *Measurement of the parity-violating asymmetry parameter α_b and the helicity amplitudes for the decay $\Lambda_b^0 \to J/\psi + \Lambda^0$ with the ATLAS detector*, Phys. Rev. **D89** (2014), no. 9 092009, arXiv:1404.1071; CMS collaboration, A. M. Sirunyan *et al.*, *Measurement of the Λ_b polarization and angular parameters in $\Lambda_b \to J/\psi\,\Lambda$ decays from pp collisions at $\sqrt{s} = 7$ and 8 TeV*, Phys. Rev. **D97** (2018), no. 7 072010, arXiv:1802.04867.

[75] LHCb collaboration, R. Aaij *et al.*, *Observation of $J/\psi p$ resonances consistent with pentaquark states in $\Lambda_b^0 \to J/\psi p K^-$ decays*, Phys. Rev. Lett. **115** (2015) 072001, arXiv:1507.03414.

[76] Belle collaboration, Y. Guan *et al.*, *Observation of Transverse $\Lambda/\bar{\Lambda}$ Hyperon Polarization in e^+e^- Annihilation at Belle*, Phys. Rev. Lett. **122** (2019), no. 4 042001, arXiv:1808.05000.

[77] M. Anselmino, D. Boer, U. D'Alesio, and F. Murgia, *Λ polarization from unpolarized quark fragmentation*, Phys. Rev. **D63** (2001) 054029, arXiv:hep-ph/0008186.

[78] BESIII collaboration, M. Ablikim *et al.*, *Polarization and Entanglement in Baryon-Antibaryon Pair Production in Electron-Positron Annihilation*, Nature Phys. **15** (2019) 631, arXiv:1808.08917.

[79] STAR collaboration, J. Adam *et al.*, *Polarization of Λ ($\bar{\Lambda}$) hyperons along the beam direction in Au+Au collisions at $\sqrt{s_{NN}}$ = 200 GeV*, Phys. Rev. Lett. **123** (2019), no. 13 132301, arXiv:1905.11917.

[80] ALICE collaboration, S. Acharya *et al.*, *Global polarization of Λ and $\overline{\Lambda}$ hyperons in Pb-Pb collisions at the LHC*, arXiv:1909.01281.

[81] LHCb collaboration, R. Aaij *et al.*, *Differential branching fraction and angular analysis of $\Lambda_b^0 \to \Lambda\mu^+\mu^-$ decays*, JHEP **06** (2015) 115, Erratum ibid. **09** (2018) 145, arXiv:1503.07138.

[82] R. Dutta, $\Lambda_b \to (\Lambda_c, p)\,\tau\,\nu$ *decays within standard model and beyond*, Phys. Rev. **D93** (2016), no. 5 054003, arXiv:1512.04034; S. Shivashankara, W. Wu, and A. Datta, $\Lambda_b \to \Lambda_c \tau \bar{\nu}_\tau$ *Decay in the Standard Model and with New Physics*, Phys. Rev. **D91** (2015), no. 11 115003, arXiv:1502.07230; X.-Q. Li, Y.-D. Yang, and X. Zhang, $\Lambda_b \to \Lambda_c \tau \overline{\nu}_\tau$ *decay in scalar and vector leptoquark scenarios*, JHEP **02** (2017) 068, arXiv:1611.01635; A. Datta, S. Kamali, S. Meinel, and A. Rashed, *Phenomenology of* $\Lambda_b \to \Lambda_c \tau \overline{\nu}_\tau$ *using lattice QCD calculations*, JHEP **08** (2017) 131, arXiv:1702.02243; E. Di Salvo, F. Fontanelli, and Z. J. Ajaltouni, *Detailed Study of the Decay* $\Lambda_b \to \Lambda_c \tau \bar{\nu}_\tau$, Int. J. Mod. Phys. **A33** (2018), no. 29 1850169, arXiv:1804.05592; A. Ray, S. Sahoo, and R. Mohanta, *Probing new physics in semileptonic* Λ_b *decays*, Phys. Rev. **D99** (2019), no. 1 015015, arXiv:1812.08314; P. Böer, A. Kokulu, J.-N. Toelstede, and D. van Dyk, *Angular Analysis of* $\Lambda_b \to \Lambda_c(\to \Lambda\pi)\ell\bar{\nu}$, arXiv:1907.12554; N. Penalva, E. Hernández, and J. Nieves, *Further tests of lepton flavour universality from the charged lepton energy distribution in* $b \to c$ *semileptonic decays: The case of* $\Lambda_b \to \Lambda_c \ell \bar{\nu}_\ell$, arXiv:1908.02328.

[83] G. Durieux and Y. Grossman, *Probing CP violation systematically in differential distributions*, Phys. Rev. **D92** (2015) 076013, arXiv:1508.03054.

[84] LHCb collaboration, R. Aaij *et al.*, *Study of the* $D^0 p$ *amplitude in* $\Lambda_b^0 \to D^0 p \pi^-$ *decays*, JHEP **05** (2017) 030, arXiv:1701.07873.

[85] M. Jacob and G. C. Wick, *On the general theory of collisions for particles with spin*, Annals Phys. **7** (1959) 404.

[86] J. D. Richman, *An experimenter's guide to the helicity formalism*, CALT-68-1148.

[87] J. D. Jackson, *Classical Electrodynamics*, Wiley, 1998.

[88] F. J. Botella *et al.*, *On the search for the electric dipole moment of strange and charm baryons at LHC*, Eur. Phys. J. **C77** (2017) 181, arXiv:1612.06769.

[89] E. Bagli *et al.*, *Electromagnetic dipole moments of charged baryons with bent crystals at the LHC*, Eur. Phys. J. **C77** (2017) 828, arXiv:1708.08483.

[90] V. G. Baryshevsky, *Spin rotation of ultrarelativistic particles passing through a crystal*, Pis'ma Zh. Tekh. Fiz. **5** (1979) 182.

[91] V. G. Baryshevsky, *The possibility to measure the magnetic moments of short-lived particles (charm and beauty baryons) at LHC and FCC energies using the phenomenon of spin rotation in crystals*, Phys. Lett. **B757** (2016) 426.

[92] UA9 collaboration, L. Burmistrov *et al.*, *Measurement of Short Living Baryon Magnetic Moment using Bent Crystals at SPS and LHC*, Tech. Rep. CERN-SPSC-2016-030. SPSC-EOI-012, CERN, Geneva, Jun, 2016.

[93] V. L. Lyuboshits, *The Spin Rotation at Deflection of Relativistic Charged Particle in Electric Field*, Sov. J. Nucl. Phys. **31** (1980) 509.

[94] D. Mirarchi, A. S. Fomin, S. Redaelli, and W. Scandale, *Layouts for fixed-target experiments and dipole moment measurements of short-living baryons using bent crystals at the LHC*, arXiv:1906.08551.

[95] V. G. Baryshevsky, *Electromagnetic dipole moment and time reversal invariance violating interactions of high energy short-lived particles in bent and straight crystals*, Phys. Rev. Accel. Beams **22** (2019), no. 8 081004, arXiv:1812.00428.

[96] E761 collaboration, D. Chen *et al.*, *First observation of magnetic moment precession of channeled particles in bent crystals*, Phys. Rev. Lett. **69** (1992) 3286.

[97] A. S. Fomin *et al.*, *Feasibility of measuring the magnetic dipole moments of the charm baryons at the LHC using bent crystals*, JHEP **08** (2017) 120, arXiv:1705.03382.

[98] V. G. Baryshevsky, *Spin rotation and depolarization of high-energy particles in crystals at LHC and FCC energies. The possibility to measure the anomalous magnetic moments of short-lived particles and quadrupole moment of Ω -hyperon*, Nucl. Instrum. Meth. **B402** (2017) 5.

[99] J. Lindhard, *Review of Particle Physics*, Kongelige Danske Videnskabernes Selskab **34** (1965) 14.

[100] V. M. Biryukov *et al.*, *Crystal Channeling and Its Application at High-Energy Accelerators*, Springer-Verlag Berlin Heidelberg, 1997.

[101] W. Scandale *et al.*, *Observation of channeling for 6500 GeV/c protons in the crystal assisted collimation setup for LHC*, Phys. Lett. **B758** (2016) 129.

[102] W. Scandale *et al.*, *Observation of channeling and volume reflection in bent crystals for high-energy negative particles*, Phys. Lett. **B681** (2009) 233.

[103] W. Scandale *et al.*, *High-efficiency deflection of high-energy negative particles through axial channeling in a bent crystal*, Phys. Lett. **B680** (2009) 301.

[104] W. Scandale *et al.*, *Volume reflection dependence of 400-GeV/c protons on the bent crystal curvature*, Phys. Rev. Lett. **101** (2008) 234801.

[105] W. Scandale *et al.*, *Deflection of high-energy negative particles in a bent crystal through axial channeling and multiple volume reflection stimulated by doughnut scattering*, Phys. Lett. **B693** (2010) 545.

[106] W. Scandale *et al.*, *Observation of strong leakage reduction in crystal assisted collimation of the SPS beam*, Phys. Lett. **B748** (2015) 451.

[107] L. H. Thomas, *The motion of a spinning electron*, Nature **117** (1926) 514; L. H. Thomas, *The kinematics of an electron with an axis*, Phil. Mag. **3** (1927) 1; V. Bargmann, L. Michel, and V. L. Telegdi, *Precession of the polarization of particles moving in a homogeneous electromagnetic field*, Phys. Rev. Lett. **2** (1959) 435.

[108] T. Fukuyama and A. J. Silenko, *Derivation of Generalized Thomas-Bargmann-Michel-Telegdi Equation for a Particle with Electric Dipole Moment*, Int. J. Mod. Phys. **A28** (2013) 1350147, arXiv:1308.1580; A. J. Silenko, *Spin precession of a particle with an electric dipole moment: contributions from classical electrodynamics and from the Thomas effect*, Phys. Scripta **90** (2015), no. 6 065303, arXiv:1410.6906.

[109] R. H. Good, *Classical Equations of Motion for a Polarized Particle in an Electromagnetic Field*, Phys. Rev. **125** (1962) 2112.

[110] E. M. Metodiev, *Thomas-BMT equation generalized to electric dipole moments and field gradients*, arXiv:1507.04440.

[111] V. G. Baryshevsky, *Spin rotation and depolarization of high-energy particles in crystals at Hadron Collider (LHC) and Future Circular Collider (FCC) energies and the possibility to measure the anomalous magnetic moments of short-lived particles*, arXiv:1504.06702.

[112] LHCb collaboration, R. Aaij *et al.*, *First measurement of charm production in fixed-target configuration at the LHC*, Phys. Rev. Lett. **122** (2019) 132002, arXiv:1810.07907.

[113] L. Gladilin, *Fragmentation fractions of c and b quarks into charmed hadrons at LEP*, Eur. Phys. J. **C75** (2015), no. 1 19, arXiv:1404.3888.

[114] LHCb collaboration, *LHCb Trigger and Online Technical Design Report*, CERN-LHCC-2014-016.

[115] LHCb collaboration, R. Aaij *et al.*, *LHCb detector performance*, Int. J. Mod. Phys. **A30** (2015) 1530022, arXiv:1412.6352.

[116] S. Eidelman and M. Passera, *Theory of the tau lepton anomalous magnetic moment*, Mod. Phys. Lett. **A22** (2007) 159, arXiv:hep-ph/0701260.

[117] A. Pich, *Precision Tau Physics*, Prog. Part. Nucl. Phys. **75** (2014) 41, arXiv:1310.7922.

[118] DELPHI collaboration, J. Abdallah *et al.*, *Study of tau-pair production in photon-photon collisions at LEP and limits on the anomalous electromagnetic moments of the tau lepton*, Eur. Phys. J. **C35** (2004) 159, arXiv:hep-ex/0406010.

[119] Belle collaboration, K. Inami *et al.*, *Search for the electric dipole moment of the tau lepton*, Phys. Lett. **B551** (2003) 16, arXiv:hep-ex/0210066.

[120] J. Fu *et al.*, *Novel method for the direct measurement of the tau lepton dipole moments*, Phys. Rev. Lett. **123** (2019), no. 1 011801, arXiv:1901.04003.

[121] V. B. Berestetskii, E. M. Lifshitz, and L. P. Pitaevskii, *Quantum Electrodynamics*, vol. 4 of *Course of Theoretical Physics*, Butterworth-Heinemann, Oxford, 1982; F. Halzen and A. D. Martin, *Quarks and leptons: An introductory course in modern particle physics*, Wiley, New York, 1984.

[122] A. S. Fomin *et al.*, *Feasibility of τ -lepton electromagnetic dipole moments measurement using bent crystal at the LHC*, JHEP **03** (2019) 156, arXiv:1810.06699.

[123] T. Sjöstrand, S. Mrenna, and P. Skands, *PYTHIA 6.4 physics and manual*, JHEP **05** (2006) 026, arXiv:hep-ph/0603175; T. Sjöstrand, S. Mrenna, and P. Skands, *A brief introduction to PYTHIA 8.1*, Comput. Phys. Commun. **178** (2008) 852, arXiv:0710.3820.

[124] D. J. Lange, *The EvtGen particle decay simulation package*, Nucl. Instrum. Meth. **A462** (2001) 152.

[125] M. Davier, L. Duflot, F. Le Diberder, and A. Rouge, *The Optimal method for the measurement of tau polarization*, Phys. Lett. **B306** (1993) 411.

[126] R. Aaij *et al.*, *Performance of the LHCb Vertex Locator*, JINST **9** (2014) P09007, arXiv:1405.7808.

[127] H. Voss, A. Hoecker, J. Stelzer, and F. Tegenfeldt, *TMVA - Toolkit for Multivariate Data Analysis*, PoS **ACAT** (2007) 040.

[128] S. Dambach, U. Langenegger, and A. Starodumov, *Neutrino reconstruction with topological information*, Nucl. Instrum. Meth. **A569** (2006) 824, arXiv:hep-ph/0607294.

[129] O. S. Bruning *et al.*, *LHC design report Vol.1: the LHC main ring*, tech. rep., 2004. CERN-2004-003-V-1.

[130] LHCb collaboration, A. A. Alves Jr. *et al.*, *The LHCb detector at the LHC*, JINST **3** (2008) S08005.

[131] LHCb collaboration, R. Aaij *et al.*, *Measurement of $\sigma(pp \to b\bar{b}X)$ at $\sqrt{s} = 7$ TeV in the forward region*, Phys. Lett. **B694** (2010) 209, arXiv:1009.2731.

[132] LHCb collaboration, *LHCb VELO (VErtex LOcator): Technical Design Report*, CERN-LHCC-2001-011.

[133] LHCb collaboration, *LHCb inner tracker: Technical Design Report*, CERN-LHCC-2002-029.

[134] LHCb collaboration, *LHCb outer tracker: Technical Design Report*, CERN-LHCC-2001-024.

[135] LHCb collaboration, *LHCb magnet: Technical Design Report*, CERN-LHCC-2000-007.

[136] LHCb collaboration, *LHCb RICH: Technical Design Report*, CERN-LHCC-2000-037.

[137] LHCb collaboration, *LHCb calorimeters: Technical Design Report*, CERN-LHCC-2000-036.

[138] LHCb collaboration, *LHCb muon system: Technical Design Report*, CERN-LHCC-2001-010.

[139] F. Archilli *et al.*, *Performance of the muon identification at LHCb*, JINST **8** (2013) P10020, arXiv:1306.0249.

[140] LHCb, R. Aaij *et al.*, *Design and performance of the LHCb trigger and full real-time reconstruction in Run 2 of the LHC*, JINST **14** (2019), no. 04 P04013, arXiv:1812.10790.

[141] LHCb collaboration, *LHCb online system, data acquisition and experiment control: Technical Design Report*, CERN-LHCC-2001-040.

[142] LHCb collaboration, R. Aaij *et al.*, *Precision luminosity measurements at LHCb*, JINST **9** (2014) P12005, arXiv:1410.0149.

[143] LHCb collaboration, *LHCb SMOG Upgrade*, CERN-LHCC-2019-005.

[144] LHCb collaboration, R. Aaij *et al.*, *Measurement of antiproton production in p He collisions at $\sqrt{s} = 110$ GeV*, Phys. Rev. Lett. **121** (2019) 222001, arXiv:1808.06127.

[145] LHCb collaboration, *LHCb Tracker Upgrade Technical Design Report*, CERN-LHCC-2014-001.

[146] LHCb collaboration, *LHCb PID Upgrade Technical Design Report*, CERN-LHCC-2013-022.

[147] LHCb collaboration, *Expression of Interest for a Phase-II LHCb Upgrade: Opportunities in flavour physics, and beyond, in the HL-LHC era*, CERN-LHCC-2017-003.

[148] G. Barrand *et al.*, *GAUDI: A software architecture and framework for building HEP data processing applications*, Computer Physics Communications **140** (2001), no. 1–2 45 ; *The Gaudi Project*, `http://proj-gaudi.web.cern.ch/proj-gaudi/`.

[149] LHCb collaboration, *The Brunel Project*, `http://lhcbdoc.web.cern.ch/lhcbdoc/brunel/`.

[150] LHCb collaboration, *The DaVinci Project*, `http://lhcbdoc.web.cern.ch/lhcbdoc/davinci/`.

[151] LHCb collaboration, *The Gauss Project*, `http://lhcbdoc.web.cern.ch/lhcbdoc/gauss/`.

[152] P. Golonka and Z. Was, *PHOTOS Monte Carlo: A precision tool for QED corrections in Z and W decays*, Eur. Phys. J. **C45** (2006) 97, `arXiv:hep-ph/0506026`.

[153] T. Pierog *et al.*, *EPOS LHC: Test of collective hadronization with data measured at the CERN Large Hadron Collider*, Phys. Rev. **C92** (2015), no. 3 034906, `arXiv:1306.0121`.

[154] Geant4 collaboration, S. Agostinelli *et al.*, *Geant4: A simulation toolkit*, Nucl. Instrum. Meth. **A506** (2003) 250; Geant4 collaboration, J. Allison *et al.*, *Geant4 developments and applications*, IEEE Trans. Nucl. Sci. **53** (2006) 270.

[155] LHCb collaboration, *The Boole Project*, `http://lhcbdoc.web.cern.ch/lhcbdoc/boole/`.

[156] D. Marangotto, *Angular and CP-Violation Analyses of $\bar{B} \to D^{*+} l^- \bar{\nu}_l$ Decays at Hadron Collider Experiments*, Adv. High Energy Phys. **2019** (2019) 5274609, `arXiv:1812.08144`; D. Hill, M. John, W. Ke, and A. Poluektov, *Model-independent method for measuring the angular coefficients of $B^0 \to D^{*-}\tau^+\nu_\tau$ decays*, `arXiv:1908.04643`; M. Ferrillo, A. Mathad, P. Owen, and N. Serra, *Probing effects of new physics in $\Lambda_b^0 \to \Lambda_c^+ \mu^- \bar{\nu}_\mu$ decays*, `arXiv:1909.04608`.

[157] M. Mikhasenko *et al.*, *Dalitz-plot decomposition for three-body decays*, `arXiv:1910.04566`.

[158] W. D. Hulsbergen, *Decay chain fitting with a Kalman filter*, Nucl. Instrum. Meth. **A552** (2005) 566, `arXiv:physics/0503191`.

[159] D. Müller, M. Clemencic, G. Corti, and M. Gersabeck, *ReDecay: A novel approach to speed up the simulation at LHCb*, Eur. Phys. J. **C78** (2018), no. 12 1009, `arXiv:1810.10362`.

[160] M. Pivk and F. R. Le Diberder, *sPlot: A statistical tool to unfold data distributions*, Nucl. Instrum. Meth. **A555** (2005) 356, `arXiv:physics/0402083`.

[161] *TensorFlowAnalysis: A collection of useful functions and example scripts for performing amplitude fits using TensorFlow*, `https://gitlab.cern.ch/poluekt/TensorFlowAnalysis`.

[162] M. Abadi *et al.*, *TensorFlow: Large-scale machine learning on heterogeneous systems*, `https://www.tensorflow.org`.

[163] F. James and M. Roos, *Minuit: A System for Function Minimization and Analysis of the Parameter Errors and Correlations*, Comput. Phys. Commun. **10** (1975) 343.

[164] N. D. Gagunashvili, *Comparison of weighted and unweighted histograms*, PoS **ACAT** (2007) 054, `arXiv:physics/0605123`.

[165] R. Brun and F. Rademakers, *ROOT: An object oriented data analysis framework*, Nucl. Instrum. Meth. **A389** (1997) 81.

[166] J. M. Blatt and V. F. Weisskopf, *Theoretical nuclear physics*, Springer, New York, 1952. doi: 10.1007/978-1-4612-9959-2.

[167] F. Von Hippel and C. Quigg, *Centrifugal-barrier effects in resonance partial decay widths, shapes, and production amplitudes*, Phys. Rev. **D5** (1972) 624.

[168] D. Aston *et al.*, *A Study of $K^-\,\pi^+$ Scattering in the Reaction $K^-p \to K^-\pi^+n$ at 11-GeV/c*, Nucl. Phys. **B296** (1988) 493.

[169] J. Back *et al.*, LAURA^{++}*: A Dalitz plot fitter*, Comput. Phys. Commun. **231** (2018) 198, `arXiv:1711.09854`.

[170] S. M. Flatté, *Coupled - Channel Analysis of the $\pi\eta$ and $K\bar{K}$ Systems Near $K\bar{K}$ Threshold*, Phys. Lett. **63B** (1976) 224.

[171] S. S. Wilks, *The large-sample distribution of the likelihood ratio for testing composite hypotheses*, Ann. Math. Stat. **9** (1938) 60.

[172] D. Marangotto, *Helicity formalism revisited for polarised particle decays*, `arXiv:1911.10025`.

[173] G. R. Goldstein, *Polarization of inclusively produced Λ_c^+ in a QCD based hybrid model*, `arXiv:hep-ph/9907573`.

Acknowledgements

No achievement is the work of a single person. I dedicate this thesis to all the people who contributed to it.

I thank my supervisor Nicola, who started and leads the crazy path towards the measurement of unstable particles dipole moments at the LHC.

I thank my colleagues of the LHCb Milano group Andrea, Elisabetta, Jinlin, Paolo, Salvatore; of the LHCb IFIC València group Fernando, Joan, Louis, and Elisabeth from the LHCb LAL Orsay group, for sharing this path together.

I thank Andrea, Enrico, Laura, Vincenzo from INFN Ferrara and Gianluca from INFN Roma for joining this effort with their experience on bent crystals. A thank also to Marcello for fostering the even more crazy idea of measuring the τ lepton dipole moments.

A thank for the careful revision and evaluation of the thesis to Alessandro, Fernando, Guy, Tomasz and Vincenzo.

A big thank to the LHCb Collaboration, not only for the impressive work performed by each individual in all the aspects (hardware, computing, running) needed for producing the amazing datasets employed in this thesis, but also for the support and encouragement given to the dipole moment experiment proposal.

A special thank goes to my parents, who supported me (also in the sense of the Italian *sopportare*) in the difficulties of the work.

Finally, a big thank to Physics, *L'amor che move il sole e l'altre stelle*.